

# **Quantum effects in nonresonant x-ray scattering**

**Dissertation**

**zur Erlangung des Doktorgrades an der Fakultät für  
Mathematik, Informatik und Naturwissenschaften  
Fachbereich Physik  
der Universität Hamburg**

vorgelegt von

**Jan Malte Slowik**

Hamburg

2015

Tag der Disputation: 12. Oktober 2015

Folgende Gutachter empfehlen die Annahme der Dissertation:

Prof. Dr. Robin Santra – I. Institut für Theoretische Physik, Universität Hamburg und  
Center for Free-Electron Laser Science, DESY, Hamburg.

Prof. Dr. Michael Thorwart – I. Institut für Theoretische Physik, Universität Hamburg.

Prof. Dr. Harry Quiney – School of Physics, University of Melbourne.

## Abstract – Quantum effects in nonresonant x-ray scattering

Due to their versatile properties, x rays are a unique tool to investigate the structure and dynamics of matter. X-ray scattering is the fundamental principle of many imaging techniques. Examples are x-ray crystallography, which recently celebrated one hundred years and is currently the leading method in structure determination of proteins, as well as X-ray phase contrast imaging (PCI), which is an imaging technique with countless applications in biology, medicine, etc.

The technological development of X-ray free electron lasers (XFEL) has brought x-ray imaging at the edge of a new scientific revolution. XFELs offer ultrashort x-ray pulses with unprecedented high x-ray fluence and excellent spatial coherence properties. These properties make them an outstanding radiation source for x-ray scattering experiments, providing ultrafast temporal resolution as well as atomic spatial resolution. However, the radiation-matter interaction in XFEL experiments also advances into a novel regime. This demands a sound theoretical fundament to describe and explore the new experimental possibilities. This dissertation is dedicated to the theoretical study of nonresonant x-ray scattering.

As the first topic, I consider the near-field imaging by propagation based x-ray phase contrast imaging (PCI). I devise a novel theory of PCI, in which radiation and matter are quantized. Remarkably, the crucial interference term automatically excludes contributions from inelastic scattering. This explains the success of the classical description thus far.

The second topic of the thesis is the x-ray imaging of coherent electronic motion, where quantum effects become particularly apparent. The electron density of coherent electronic wave packets – important in charge transfer and bond breaking – varies in time, typically on femto- or attosecond time scales. In the near future, XFELs are envisaged to provide attosecond x-ray pulses, opening the possibility for time-resolved ultrafast x-ray scattering experiments. In the quantum theory it has however been revealed that x-ray scattering patterns of electronic motion are related to complex spatio-temporal correlations, instead of the instantaneous electron density. I scrutinize the time-resolved scattering pattern from coherent electronic wave packets. I show that time-resolved PCI recovers the instantaneous electron density of electronic motion. For the far-field diffraction scattering pattern, I analyze the influence of photon energy resolution of the detector. Moreover, I demonstrate that x-ray scattering from a crystal of identical wave packets also recovers the instantaneous electron density. I point out that a generalized electron density propagator of the wave packet can be reconstructed from a scattering experiment. Finally, I propose time-resolved Compton scattering of electronic wave packets. I show that x-ray scattering with large energy transfer can be used to recover the instantaneous momentum space density of the target.

The third topic of this dissertation is Compton scattering in single molecule coherent diffractive imaging (CDI). The structure determination of single macromolecules via CDI is one of the key applications of XFELs. The structure of the molecule can be reconstructed from the elastic diffraction pattern. Inelastic x-ray scattering generates a background signal, which I determine for typical high-intensity imaging conditions. I find that at high x-ray fluence the background signal becomes dominating, posing a problem for high resolution imaging. The strong ionization by the x-ray pulse may ionize several electrons per atom. Scattering from these free electrons makes a major contribution to the background signal. I present and discuss detailed numerical studies for different x-ray fluence and photon energy.

# Zusammenfassung – Quanteneffekte der nichtresonanten Röntgenstreuung

Aufgrund ihrer vielseitigen Eigenschaften ist Röntgenstrahlung ein einzigartiges Werkzeug zur Untersuchung der Struktur und Dynamik der Materie. Röntgenstreuung ist das grundlegende Prinzip vieler Abbildungsverfahren, wie z.B. die Röntgenkristallographie, gerade einhundert Jahre alt und gegenwärtig die führende Methode zur Strukturaufklärung von Proteinen, sowie die Phasenkontrastabbildung, ein Abbildungsverfahren mit vielen Anwendungen in der Biologie, Medizin, etc.

Die technische Entwicklung der Röntgen-Freie-Elektronen-Laser (XFEL) ermöglicht eine Revolution in der Röntgenbildgebung. XFELs erzeugen ultrakurze Röntgenpulse mit beispiellos hoher Fluenz und exzellenter räumlicher Kohärenz. Diese Eigenschaften machen XFELs zu einer hervorragenden Lichtquelle für Röntgenstreuexperimente mit ultraschneller zeitlicher und atomarer räumlicher Auflösung. Allerdings dringen die Licht-Materie-Wechselwirkung in XFEL-Experimenten in ein völlig neues Regime vor. Zur Beschreibung und Erkundung neuer experimenteller Möglichkeiten wird daher ein tragfähiges theoretisches Fundament benötigt. Diese Dissertation widmet sich der theoretischen Untersuchung der nichtresonanten Röntgenstreuung.

Als erstes Thema betrachte ich die Nahfeld-Bildgebung mit propagationsbasierter Phasenkontrast-Röntgenabbildung. Ich entwickle eine neue Theorie für dieses Verfahren, in der Strahlung und Materie quantisiert sind. Interessanterweise schließt der entscheidende Interferenzterm automatisch inelastische Streuung aus. Dies erklärt den bisherigen Erfolg der klassischen Beschreibung.

Ein zweites Thema dieser Arbeit ist die Abbildung kohärenter elektronischer Bewegung, wo Quanteneffekte besonders auffällig sind. Die Elektronendichte kohärenter elektronischer Wellenpakete – wichtig im Ladungstransfer und dem Aufbrechen von Bindungen – variiert in der Zeit, typischerweise auf Zeitskalen von Femto- oder Attosekunden. In naher Zukunft werden XFELs Attosekunden-Röntgenpulse generieren können und damit die Möglichkeit zeitaufgelöster ultraschneller Röntgenstreuung eröffnen. Allerdings hat die Quantentheorie gezeigt, dass das Streubild elektronischer Wellenpakete von komplexen Korrelationen in Raum und Zeit abhängt und nicht von der instantanen Elektronendichte. Ich untersuche das zeitabhängigen Streubild kohärenter elektronischer Wellenpakete eingehend. Ich zeige, dass mit zeitaufgelöster Phasenkontrastabbildung die instantane Elektronendichte abgebildet wird. Im Fall der Fernfeld-Abbildung analysiere ich den Einfluss der Energieauflösung des Detektors. Zudem lege ich dar, dass Röntgenstreuung an Kristallstrukturen von identischen Wellenpaketen die instantane Elektronendichte abbildet. Ich zeige auf, dass man einen verallgemeinerten Elektronendichte-Propagator aus Streuexperimenten rekonstruieren kann. Schließlich schlage ich zeitaufgelöste Comptonstreuung an elektronischen Wellenpaketen vor. Ich zeige, dass Röntgenstreuung mit großem Energieübertrag genutzt werden kann, um die instantane Impulsdichte des Objekts abzubilden.

Ein drittes Thema dieser Arbeit ist Comptonstreuung bei der kohärenten Diffraktionsabbildung von einzelnen Molekülen. Die Strukturaufklärung von einzelnen Molekülen mittels kohärenter Diffraktion ist eine der Schlüssellandwendungen von XFELs. Die Struktur von Molekülen kann aus dem elastischen Streubild rekonstruiert werden. Inelastische Streuung trägt ein Hintergrundsignal bei, das ich für typische Bedingungen der Hochintensitäts-Abbildung bestimme. Ich beobachte, dass bei großer Röntgenfluenz das Hintergrundsignal dominierend wird, was ein Problem für die Abbildung mit hoher Auflösung darstellt. Die starke Ionisierung durch den Röntgenpuls kann mehrere Elektronen pro Atom ionisieren. Die Streuung an diesen freien Elektronen macht einen Großteil des Hintergrundsignal aus. Ich präsentiere und diskutiere detaillierte numerische Studien für verschiedene Röntgenfluenzen und Photonenenergien.

# List of publications

## Research Articles

- [1] X-RAY PHASE-CONTRAST IMAGING: THE QUANTUM PERSPECTIVE  
Jan Malte Slowik and Robin Santra  
[J. Phys. B: At. Mol. Opt. Phys.](#) **46** 164016 (2013).
- [2] PROPOSED IMAGING OF THE ULTRAFAST ELECTRONIC MOTION IN SAMPLES USING X-RAY PHASE CONTRAST  
Gopal Dixit, Jan Malte Slowik and Robin Santra  
[Phys. Rev. Lett.](#) **110**, 137403 (2013).
- [3] THEORY OF TIME-RESOLVED NONRESONANT X-RAY SCATTERING FOR IMAGING ULTRAFAST COHERENT ELECTRON MOTION  
Gopal Dixit, Jan Malte Slowik and Robin Santra  
[Phys. Rev. A](#) **89**, 043409 (2014).
- [4] INCOHERENT X-RAY SCATTERING IN SINGLE MOLECULE IMAGING  
Jan Malte Slowik, Sang-Kil Son, Gopal Dixit, Zoltan Jurek and Robin Santra  
[New J. Phys.](#) **16**, 073042 (2014).

## Other

- [5] COMMENT ON “HOW TO OBSERVE COHERENT ELECTRON DYNAMICS DIRECTLY”  
Robin Santra, Gopal Dixit, and Jan Malte Slowik  
[Phys. Rev. Lett.](#) **113**, 189301 (2014).
- FILMING DANCING ELECTRONS WITH A HIGH SPEED X-RAY CAMERA  
Gopal Dixit, Jan Malte Slowik and Robin Santra  
[DESY Photon Science 2013 - Highlights and Annual Report](#), p. 33.



# Contents

<b>Abstract</b>	<b>iii</b>
<b>Zusammenfassung</b>	<b>iv</b>
<b>List of Publications</b>	<b>v</b>
<b>1. Introduction</b>	<b>1</b>
1.1. X-ray free electron lasers and nonresonant x-ray scattering . . . . .	1
1.2. Outline of content and contributions . . . . .	4
<b>I. Theoretical formalism</b>	<b>7</b>
<b>2. Theoretical formalism</b>	<b>9</b>
2.1. Theory of radiation-matter interaction . . . . .	9
2.1.1. Canonical quantization . . . . .	9
2.1.2. Quantized electronic system . . . . .	12
2.1.3. Quantized radiation field . . . . .	15
2.1.4. Radiation-matter interaction Hamiltonian . . . . .	16
2.2. Time evolution . . . . .	18
2.2.1. Schrödinger and Interaction picture . . . . .	18
2.2.2. Perturbation theory . . . . .	21
2.2.3. Fermi's golden rule . . . . .	23
<b>II. Near field imaging: x-ray phase contrast</b>	<b>25</b>
<b>3. About x-ray phase contrast imaging</b>	<b>27</b>
3.1. Introduction and applications . . . . .	27
3.2. Classical theory of phase contrast imaging . . . . .	28
3.2.1. Classical scattering of a light pulse . . . . .	29
3.2.2. Quasi-stationary pulses . . . . .	30

3.2.3.	Propagation and intensity in the Fresnel regime . . . . .	31
3.2.4.	Phase contrast . . . . .	33
<b>4.</b>	<b>Quantum theory of x-ray phase contrast imaging</b>	<b>37</b>
4.1.	Motivation . . . . .	37
4.2.	Formalism and intensity observable . . . . .	38
4.3.	The (0,1) term of the Poynting operator . . . . .	40
4.A.	Calculation of the matrix element . . . . .	44
4.B.	Propagation of the correlation function . . . . .	45
4.C.	Calculation of the phase contrast term . . . . .	46
<b>5.</b>	<b>Time-resolved phase contrast imaging of wave packets</b>	<b>49</b>
5.1.	Motivation . . . . .	49
5.2.	Time-resolved PCI: theory and examples . . . . .	50
5.2.1.	Theory of time-resolved PCI . . . . .	50
5.2.2.	Application to hydrogen wave packets . . . . .	51
5.3.	Challenges and opportunities of time-resolved PCI . . . . .	55
<b>III.</b>	<b>Far field imaging: coherent and incoherent x-ray scattering</b>	<b>57</b>
<b>6.</b>	<b>X-ray scattering and the far-field diffraction pattern</b>	<b>59</b>
6.1.	The (0,1) term of the Poynting operator . . . . .	59
6.2.	The (1,1) term of the Poynting operator . . . . .	60
6.3.	The projection observable . . . . .	65
<b>7.</b>	<b>Time-resolved imaging of coherent electronic motion</b>	<b>69</b>
7.1.	Motivation . . . . .	69
7.2.	The time-resolved x-ray scattering of electronic wave packets . . . . .	71
7.2.1.	Theory of time-resolved x-ray scattering . . . . .	71
7.2.2.	Application to the hydrogen 3d-4f wave packet . . . . .	75
7.3.	Unravelling the time-resolved diffraction pattern . . . . .	76
7.3.1.	Dynamical structure factor and influence of energy resolution . . . . .	76
7.3.2.	Crystals: Recovering the instantaneous electron density . . . . .	80
7.4.	Recovering the electron density propagator . . . . .	83
7.4.1.	Motivation: The time-resolved imaging by Abbamonte . . . . .	83
7.4.2.	Relation of electron density propagator and generalized DSF . . . . .	84
7.4.3.	Linear response theory and scattering induced dynamics . . . . .	85
7.5.	Momentum space imaging: Ultrafast time-resolved Compton scattering . . . . .	87
7.5.1.	Introduction . . . . .	87
7.5.2.	Time-resolved Compton scattering . . . . .	88

---

7.5.3.	Connection of real- and momentum space densities . . . . .	92
7.5.4.	Application to hydrogen 3d-4f wave packet . . . . .	93
<b>8.</b>	<b>Compton scattering in single molecule coherent diffractive imaging</b>	<b>97</b>
8.1.	Introduction . . . . .	97
8.2.	Formalism of high-intensity x-ray scattering . . . . .	101
8.2.1.	The regime of ionization induced extreme matter states . . . . .	101
8.2.2.	Differential scattering probability . . . . .	103
8.2.3.	Rate equation approach for electronic system . . . . .	106
8.3.	Form and structure factors . . . . .	107
8.3.1.	Formalism . . . . .	107
8.3.2.	Static structure factor in the Waller-Hartree approach . . . . .	110
8.3.3.	Static structure factor from explicit integration . . . . .	110
8.3.4.	The XATOM toolkit . . . . .	112
8.4.	Coherent and incoherent scattering from atomic carbon . . . . .	113
8.4.1.	The spectrum of scattered photons . . . . .	113
8.4.2.	Comparison of Waller-Hartree approach and direct integration . . . . .	113
8.4.3.	Scattering pattern of a single carbon atom . . . . .	115
8.5.	Coherent and incoherent scattering in single molecule imaging . . . . .	120
8.A.	Differential scattering probability considering high-intensity ionization dynamics . . . . .	125
8.B.	Averaging of $S(\mathbf{Q})$ and simplification for numerical implementation . . . . .	131
8.C.	Molecular scattering pattern . . . . .	135
8.D.	Photon count distribution . . . . .	136
<b>9.</b>	<b>Summary and final remarks</b>	<b>141</b>
	<b>Acknowledgements</b>	<b>145</b>
	<b>Eidesstattliche Versicherung</b>	<b>147</b>
	<b>Bibliography</b>	<b>149</b>



# Chapter 1.

## Introduction

The Road goes ever on and on  
Down from the door where it began.  
Now far ahead the Road has gone,  
And I must follow, if I can,  
Pursuing it with eager feet,  
Until it joins some larger way  
Where many paths and errands meet.  
And whither then? I cannot say.

---

*(From J.R.R. Tolkien's "The Lord of the Rings")*

### 1.1. X-ray free electron lasers and nonresonant x-ray scattering

This dissertation uncovers fundamental and practical aspects of nonresonant x-ray scattering with ultrashort, high-intensity x-ray pulses by means of a rigorous quantum mechanical formulation.

X-ray free electron lasers (XFELs) have begun to influence many areas of science in a revolutionary way. XFELs are an unprecedentedly bright source of coherent and ultrafast x-ray pulses. They offer new possibilities to explore atoms, clusters, molecules, proteins, crystals, solids or plasmas. The ultrafast time resolution promises to glimpse into the microcosm through direct observation of nuclear motion on the pico- to femtosecond time scale or even electronic motion on the femto- to attosecond time scale. There is the ambition to shoot molecular movies, i.e., to capture ultrafast physical processes and chemical reactions in real-time.

Experiments at XFELs can exploit the ultrafast time-resolution as well as the inherent properties of x rays: short wavelength, high penetration-depth, access to core and valence electrons, element specificity up to orbital specificity, sensitivity to chemical environment and molecular geometry, and sensitivity to orbital and spin magnetic moment. The unprecedentedly high x-ray intensity offers novel opportunities in x-ray imaging with atomic resolution. These properties make XFELs an excellent tool to investigate the structure and dynamics of matter. The disciplines with applications range from atomic and molecular physics, plasma physics, femtochemistry and chemical analysis to structural biology and biochemistry, etc. The experimental methods to utilize XFEL radiation are manifold. To give a rough idea, there are to name resonant, nonresonant and magnetic x-ray scattering, the multifaceted x-ray absorption and fluorescence spectroscopies, as well as photoelectron and ion spectroscopies.

There are several XFELs in operation and some more under construction at present [6–11]. In the hard x-ray regime LCLS (USA, since 2009) and SACLA (Japan, since 2012) are in operation, while the European XFEL (Germany, expected 2017), the SwissFEL (Switzerland, expected 2017) and PAL-XFEL (South Korea, expected 2015) are under construction. In the soft x-ray and VUV regime FLASH (Germany, since 2005) and FERMI FEL (Italy, since 2010) are operational with extensions in commissioning.

This dissertation focuses on imaging methods based on nonresonant x-ray scattering. In the following, I introduce the three main topics of this dissertation.

### **Quantum theory of phase contrast imaging**

In the recent past, the power of x-ray imaging has unfolded with the emergence of coherent synchrotron radiation at storage ring light sources. These third generation light sources have spread globally and their number is still progressing. X-ray phase contrast imaging (PCI) is among their outstanding scientific achievements. This near-field imaging method has opened the road to image biological and medical samples, which otherwise would be transparent to x rays. Organic matter mostly consists of light elements which do not yield sufficient absorption contrast for x-ray imaging. A quantum mechanical formulation of PCI has so far been missing. A modern theoretical fundament is of interest on its own and it is indispensable to fathom novel developments of this technique. Moreover, such a formulation provides better understanding of the theoretical formalism itself. In this dissertation, I give a rigorous quantum mechanical description of x-ray PCI.

### **Time-resolved imaging of coherent electronic motion**

Since the technology of XFELs is rapidly evolving, XFELs are believed to produce hard x-ray pulses with attosecond duration in the near future. The research field of attosecond physics is still young and mostly taking place in the regime of optical photon energies. Attosecond XFELs will make electron dynamics on the atomic scale accessible to real-time and, possibly, real-space imaging. An imaginable application is the direct investigation of electronic processes in chemical reactions, such as chemical bonding. Unravelling the details of coherent electronic motion is scientifically equally challenging and appealing, e.g., to understand the energy and charge transport in light harvesting molecules. Because attosecond physics is a young research field, technological and scientific progress are still two sides of the same coin. Thus, theory is a valuable tool to gauge and steer upcoming scientific and technological developments. As a consequence, the full potential of imaging methods should be assessed from rigorous theoretical predictions. Recently, it was discovered by Dixit, Vendrell and Santra that x-ray scattering of coherent electronic motion does not recover instantaneous snapshots of the electron density. I analyze this surprising effect in more detail. In this dissertation, methods for imaging coherent electronic motion by nonresonant x-ray scattering are studied. Different methods to image coherent electronic wave packets in real-space and real-time are devised. For example, time-resolved x-ray PCI of wave packets is explored. Moreover, I propose time-resolved Compton scattering on electronic wave packets to obtain momentum-space information in real-time.

### **Inelastic scattering in single molecule coherent diffractive imaging**

The XFELs, that are already operational or under construction, offer new opportunities in nonresonant x-ray imaging. In particular, they facilitate imaging with atomic spatial resolution. Nonresonant x-ray scattering is the basic principle of x-ray crystallography and coherent diffractive imaging (CDI). X-ray crystallography, that recently turned 100 years old, has been a tremendous scientific success so far. The majority of known protein structures has been resolved by x-ray crystallography. However, crystallography is suffering from a severe shortcoming: the unavailability of crystals with sufficient quality for many interesting biomolecules. Serial femtosecond crystallography (SFX) is a brand-new imaging method. SFX exploits the high intensity of XFELs to image very small crystals that are easier to grow, but may have only nanometer dimensions. Another key application of XFELs will be CDI of single molecules. Imaging of single molecules promises to supersede the need for crystals at all. These novel imaging methods are expected to have an enduring impact on structural biology. It is commonly believed that from the knowledge of molecular structures their function can be better understood and controlled. Hence,

the basic research on molecular structures may ultimately have a profound impact on society, e.g., through novel drugs targeting these molecules or through novel energy harvesting materials.

In this dissertation, potential challenges and limitations for single molecule CDI with atomic resolution are investigated. Any target in the highly intense XFEL radiation field underlies strong ionization leading ultimately to its destruction. Thus, the high intensity regime of XFEL radiation plays a crucial role and has to be considered in the theoretical modelling of single molecule CDI experiments. Moreover, it is well known that the quantum mechanical formulation of nonresonant x-ray scattering includes inelastic x-ray scattering. I fathom the role of this inelastic scattering in coherent diffractive imaging. In numerical studies the x-ray scattering pattern in typical CDI conditions is estimated. The background signal from inelastic scattering on bound and free electrons is quantified. By varying x-ray fluence and photon energy optimal machine parameters for CDI are assessed.

## 1.2. Outline of content and contributions

### Content

This dissertation is organized in 9 chapters, which are grouped into 3 parts. The main results can be found in Chapters 4, 5, 7, 8.

Part I is an introduction to the theoretical formalism. In Chapter 2 I recapitulate the fundament of nonrelativistic quantum electrodynamics: the canonical quantization of the coupled radiation matter system. Most importantly, the radiation-matter interaction Hamiltonian is presented, which is used throughout the thesis. Moreover, I summarize the treatment of dynamics, introducing the time evolution representations. In particular, the widely used perturbation theory in the interaction picture is presented.

Part II deals with near field x-ray phase contrast imaging, it comprises Chapters 3, 4, 5. More technically, I analyze in this part the (0,1) order terms of the perturbation theory of the expectation value of intensity.

In Chapter 3 I present the classical theory of x-ray phase contrast. In this chapter I put the classical theory on the basis of optical scattering. This approach is more similar to the quantized theory than using diffraction or coherence theory. Moreover, I introduce the statistical properties of the x-ray pulse and anticipate some calculations that are equal in the quantum theory.

In Chapter 4 I present the first<sup>1</sup> quantum theory of x-ray phase contrast imaging.

---

<sup>1</sup>To the best of my knowledge.

This chapter is based on my published article [1]. As a suitable observable I introduce the Poynting operator. Then, I calculate the (0,1)-term of the expectation value and demonstrate that it recovers the phase contrast effect.

Chapter 5 extends the theory of phase contrast imaging developed in Chap. 4 to time-resolved imaging of coherent electronic wave packets. This chapter is based on my co-authored article [2]. Here, I present the extension of the theory to the time-dependent case. I illustrate this case with the examples of the 3d-4f and 3p-4p wave packets of hydrogen.

Part III turns towards the far-field x-ray imaging, in the Chapters 6, 7, 8. In technical terms, the far-field scattering pattern arises from the (1,1) order terms of the expectation value.

In Chapter 6 I demonstrate that the (1,1) term of the expectation value of the Poynting operator agrees with the more standard differential scattering probability from Fermi's golden rule. Moreover, I show that the (0,1) term is negligible in the far-field. This chapter establishes the tie between Parts II and III in terms of different order of perturbation theory.

Chapter 7 deals with the time-resolved x-ray imaging of coherent electronic motion. The chapter starts with a short motivation in Sec. 7.1 and recapitulation of relevant results in the literature in Section 7.2. Sections 7.3 and 7.4 are based on my co-authored article [3]. In Section 7.3 the influence of photon energy resolution on the time-resolved diffraction pattern is investigated. Moreover, I demonstrate that, using a crystal of identical wave packets, time-resolved crystallography can recover the instantaneous electron density of a wave packet. In Section 7.4 I extend the reconstruction of the electron density propagator à la Abbamonte to the time dependent case. The relation to the linear response of scattering induced density fluctuations is discussed. Finally, I explore in Section 7.5 the prospects of time-resolved Compton scattering. These results have not yet been published elsewhere. I demonstrate that one can recover the instantaneous electron momentum density of a wave packet. I illustrate these findings with the help of the 3d-4f wave packet of hydrogen, for which I calculated the electron momentum density and the resulting scattering patterns in Q-space.

Chapter 8 deals with inelastic scattering in coherent diffractive imaging of single molecules imaging with atomic resolution. This chapter is based on my article [4]. I examine the coherent and incoherent scattering signal from carbon atoms, including the electronic radiation damage. In this chapter, I present results of my calculations of the scattered photon spectrum, number of scattered photons for single carbon atoms. These results are used to estimate the scattering pattern of carbon clusters.

### Contributions

[1] Slowik, Santra, J. Phys. B **46** 164016 (2013):

I have performed the research and wrote the article under the supervision of Prof. Robin Santra.

[2] Dixit, Slowik, Santra, Phys. Rev. Lett. **110**, 137403 (2013):

This article is a joint work with Dr. Gopal Dixit and Prof. Robin Santra. I have developed the theory for the article. Moreover, I have contributed to the writing of the article.

[3] Dixit, Slowik, Santra, Phys. Rev. A **89**, 043409 (2014):.

Another joint work with Dr. Gopal Dixit and Prof. Robin Santra. I have contributed to formulate the theory in this article and I have contributed to the writing of the article.

[4] Slowik, Son, Dixit, Jurek and Santra, New J. Phys. **16**, 073042 (2014):

This work is a collaboration with Dr. Sang-Kil Son, Dr. Gopal Dixit, Dr. Zoltan Jurek, and Prof. Robin Santra. I have programmed a compton scattering module for the XATOM-toolkit. I performed the calculations, prepared the figures and wrote the article.

# Part I.

## **Theoretical formalism**



# Chapter 2.

## Theoretical formalism

In this chapter I introduce the theoretical framework and the notation used throughout the thesis. I do not present proofs and only some intermediate steps. The theoretical framework has been presented in [12, 13], more information can be found in the textbooks [14–22].

### 2.1. Theory of radiation-matter interaction

The formalism of second quantization offers for our purposes an elegant and simple approach to the electronic many-body problem. In this thesis matter and radiation will be treated as fields. Particles, the electrons and photons, are represented as excitations of the fields. In this way, the formalism is very flexible. It does not depend on a fixed number of particles. Moreover, calculations are simplified by the introduction of creation and annihilation operators.

In this dissertation only situations are encountered, where relativistic effects play no role. This is the case, when the x-ray photon energy is much smaller than the electron rest mass (511 keV) and all considered nuclei are sufficiently light to neglect relativistic electronic structure effects. Furthermore, we will assume that the radiation interacts with the electrons only. This assumption relies on the fact that nuclei are about 1000 times heavier than electrons; heuristically, they are too inert to react with the field. Additionally, nuclear resonance absorption can be neglected for light elements in the considered photon energy range.

If not mentioned otherwise we will employ atomic units, i.e., electron mass  $m_e = 1$ , electron charge  $e = -1$ , reduced Planck constant  $\hbar = 1$ , and speed of light in vacuum  $c = \alpha^{-1}$ , with the fine-structure constant  $\alpha \approx \frac{1}{137}$ .

#### 2.1.1. Canonical quantization

I sketch the quantization procedure for the combined system of charges and radiation field. For a detailed account of the quantization procedure I refer the reader to the

literature [e.g., 13, 14, 16, 18]. One starts from a classical system, where the charged particles and the electromagnetic field are coupled by the Maxwell-Lorentz equations

$$\nabla \cdot \mathbf{E} = 4\pi\rho, \quad (2.1a)$$

$$\nabla \cdot \mathbf{B} = 0, \quad (2.1b)$$

$$\nabla \times \mathbf{B} = 4\pi\alpha \mathbf{j} + \alpha \frac{\partial \mathbf{E}}{\partial t}, \quad (2.1c)$$

$$\nabla \times \mathbf{E} = -\alpha \frac{\partial \mathbf{B}}{\partial t}, \quad (2.1d)$$

$$m_n \ddot{\mathbf{q}}_n = e_n (\mathbf{E} + \alpha \dot{\mathbf{q}}_n \times \mathbf{B}), \quad (2.1e)$$

where the last equation describes the Lorentz force acting on the particles, and the first four equations are the Maxwell equations. Charge density  $\rho$  and current  $\mathbf{j}$  are given by

$$\rho(\mathbf{x}, t) = \sum_n e_n \delta(\mathbf{x} - \mathbf{q}_n(t)), \quad (2.1f)$$

$$\mathbf{j}(\mathbf{x}, t) = \sum_n e_n \dot{\mathbf{q}}_n(t) \delta(\mathbf{x} - \mathbf{q}_n(t)). \quad (2.1g)$$

$m_n$ ,  $e_n$ ,  $\mathbf{q}_n$ , and  $\dot{\mathbf{q}}_n$  denote the mass, charge, position, and velocity of the  $n$ -th particle, respectively.

The quantization strategy is to determine the proper dynamical variables, then to find a Lagrangian such that the Euler-Lagrange equations reproduce the Maxwell-Lorentz equations for the system. From this Lagrangian one obtains the so-called minimal coupling Hamiltonian, to be quantized by promoting variables to operators with a suitable set of commutation relations.

The dynamical variables of the system of charges are the particle positions  $\mathbf{q}_n$  and velocities  $\dot{\mathbf{q}}_n$ . The electromagnetic field is fixed by its vector potential  $\mathbf{A}$  and scalar potential  $\mathcal{U}$ , which are required to satisfy

$$\mathbf{B} = \nabla \times \mathbf{A}, \quad (2.2)$$

$$\mathbf{E} = -\nabla\mathcal{U} - \alpha \frac{\partial \mathbf{A}}{\partial t}. \quad (2.3)$$

In this way the electromagnetic potentials are defined uniquely only up to a gauge transformation. Choosing a particular gauge is therefore necessary to obtain gauge invariant results. Since we do not need a relativistically covariant theory, we will from now on adopt the extremely useful Coulomb gauge

$$\nabla \cdot \mathbf{A} = 0. \quad (2.4)$$

This gauge makes the vector potential purely transverse. Moreover,  $\mathbf{A}$  is the dynamical variable of the radiation field. Note that the scalar potential is a redundant variable, according to Eqs. (2.1a) and (2.3),  $\mathcal{U}$  can be expressed by Poisson's equation

$$\nabla^2 \mathcal{U} = -4\pi\rho. \quad (2.5)$$

This also shows that the scalar potential corresponds to the Coulomb potential generated by the particles. Therefore, we can include the Coulomb interaction into the potential of the particle system. The Lagrangian of the coupled system can be written as

$$L(\{\mathbf{q}_n, \dot{\mathbf{q}}_n\}, t, \mathbf{A}, \dot{\mathbf{A}}, \{\partial_j \mathbf{A}_i\}) = L_{\text{part}} + \int d^3x \mathcal{L}_{\text{rad}} + \int d^3x \mathcal{L}_{\text{int}}. \quad (2.6)$$

$L_{\text{part}}$  and  $\mathcal{L}_{\text{rad}}$  depend only on particles and radiation, respectively,

$$L_{\text{part}} = \sum_n \frac{m_n}{2} \dot{\mathbf{q}}_n^2 - V_{\text{Coul}} = \sum_n \frac{m_n}{2} \dot{\mathbf{q}}_n^2 - \frac{1}{2} \sum_{k,l; k \neq l} \frac{e_k e_l}{|\mathbf{q}_k - \mathbf{q}_l|}, \quad (2.7)$$

$$\mathcal{L}_{\text{rad}} = \frac{1}{8\pi} (\alpha^2 \dot{\mathbf{A}}^2 - (\nabla \times \mathbf{A})^2). \quad (2.8)$$

$\mathcal{L}_{\text{int}}$  determines the interaction of particle and field system, such that it reproduces the equations of motion (2.1)

$$\mathcal{L}_{\text{int}} = \alpha \mathbf{j} \cdot \mathbf{A}. \quad (2.9)$$

Note that we neglect the self interaction terms in the Coulomb interaction of the particles. The conjugate momenta of the dynamical variables are

$$\mathbf{p}_n = m_n \dot{\mathbf{q}}_n + e_n \alpha \mathbf{A}(\mathbf{q}_n), \quad \mathbf{\Pi} = \frac{\alpha^2}{4\pi} \dot{\mathbf{A}} = -\frac{\alpha}{4\pi} \mathbf{E}^\perp. \quad (2.10)$$

From this Lagrangian one can construct the Hamiltonian

$$H = \sum_n \frac{1}{2m_n} (\mathbf{p}_n - e_n \alpha \mathbf{A}(\mathbf{q}_n))^2 + V_{\text{Coul}} + \frac{1}{8\pi} \int d^3x \left( \left( \frac{4\pi}{\alpha} \mathbf{\Pi}(\mathbf{x}) \right)^2 + \left( \nabla \times \mathbf{A}(\mathbf{x}) \right)^2 \right). \quad (2.11)$$

Observe that one would obtain exactly this Hamiltonian by substituting  $\mathbf{p}_n \rightarrow \mathbf{p}_n - e_n \alpha \mathbf{A}(\mathbf{q}_n)$  in the uncoupled Hamiltonians of particles and radiation. This procedure and the resulting Hamiltonian have been named the principle of minimal coupling and the minimal coupling Hamiltonian, respectively. The Hamiltonian can now easily be written as a sum of the uncoupled particle and radiation Hamiltonians plus an interaction term, coupling particles and radiation,

$$H = H_{\text{part}} + H_{\text{rad}} + H_{\text{int}}, \quad (2.12)$$

with

$$H_{\text{part}} = \sum_n \frac{\mathbf{p}_n^2}{2m_n} + V_{\text{Coul}}, \quad (2.13)$$

$$H_{\text{rad}} = \frac{1}{8\pi} \int d^3x \left( \left( \frac{4\pi}{\alpha} \boldsymbol{\Pi}(\mathbf{x}) \right)^2 + (\nabla \times \mathbf{A}(\mathbf{x}))^2 \right) \quad (2.14)$$

$$H_{\text{int}} = - \sum_n \frac{e_n \alpha}{2m_n} \left( \mathbf{p}_n \cdot \mathbf{A}(\mathbf{q}_n) + \mathbf{A}(\mathbf{q}_n) \cdot \mathbf{p}_n \right) + \sum_n \frac{e_n^2 \alpha^2}{2m_n} \mathbf{A}^2(\mathbf{q}_n). \quad (2.15)$$

From the classical Hamiltonian we obtain the quantum theory by promoting variables to operators and introducing canonical commutation relations between the variables and the canonical momenta. This procedure yields time-independent Schrödinger picture operators. For the particles we introduce the well known quantization relations

$$\left[ (\hat{\mathbf{q}}_n)_i, (\hat{\mathbf{q}}_m)_j \right] = 0 = \left[ (\hat{\mathbf{p}}_n)_i, (\hat{\mathbf{p}}_m)_j \right], \quad (2.16a)$$

$$\left[ (\hat{\mathbf{q}}_n)_i, (\hat{\mathbf{p}}_m)_j \right] = i\delta_{mn}\delta_{ij}. \quad (2.16b)$$

Before writing down the commutation relations for the radiation field we note that because of the Coulomb gauge condition in Eq. (2.4) the three components of the vector potential are not independent. Therefore, instead of a delta function the transverse delta dyadic  $\delta^\perp(\mathbf{x} - \mathbf{x}')$  appears in the commutation relations. The commutation relations read

$$\left[ \hat{\mathbf{A}}_i(\mathbf{x}), \hat{\mathbf{A}}_j(\mathbf{x}') \right] = 0 = \left[ \hat{\boldsymbol{\Pi}}_i(\mathbf{x}), \hat{\boldsymbol{\Pi}}_j(\mathbf{x}') \right], \quad (2.17a)$$

$$\left[ \hat{\mathbf{A}}_i(\mathbf{x}), \hat{\boldsymbol{\Pi}}_j(\mathbf{x}') \right] = i\delta_{ij}^\perp(\mathbf{x} - \mathbf{x}'). \quad (2.17b)$$

Like the classical Hamiltonian the Hamilton operator can be separated into  $\hat{H} = \hat{H}_{\text{part}} + \hat{H}_{\text{rad}} + \hat{H}_{\text{int}}$ . In the following, we analyze these three terms in more detail.

### 2.1.2. Quantized electronic system

Atoms and molecules consist of electrons and nuclei, which are charged particles that interact via the Coulomb interaction. We will treat the electronic many-body problem in the formalism of second quantization [13, 19, 20]. This has several advantages, e.g., the number of electrons enters only in the state of the system, not in the formalism. Moreover, the antisymmetry of fermionic wave functions can be introduced via the anticommutation relations in the formalism and no additional (anti)symmetry conditions for the states are required.

The particle Hamiltonian can be written as the sum of the nuclear kinetic energy  $\hat{T}_N$ , the nucleus-nucleus repulsion  $\hat{V}_{NN}$  and the electronic Hamiltonian  $\hat{H}_{\text{el}}$

$$\hat{H}_{\text{part}} = \hat{T}_N + \hat{V}_{NN} + \hat{H}_{\text{el}}, \quad (2.18)$$

where

$$\hat{T}_N = -\frac{1}{2} \sum_n \frac{\nabla_n^2}{M_n} \quad (2.19)$$

$$\hat{V}_{NN} = \sum_{n < n'} \frac{Z_n Z_{n'}}{|\mathbf{R}_n - \mathbf{R}_{n'}|}. \quad (2.20)$$

Here,  $\mathbf{R}_n$ ,  $M_n$ ,  $Z_n$  are the position, mass and charge of the  $n$ th nucleus, respectively. The kinetic energy of the electrons, the Coulomb attraction of electrons and nuclei and the electron-electron repulsion are included in the electronic Hamiltonian

$$\begin{aligned} \hat{H}_{\text{el}} = & \int d^3x \hat{\psi}^\dagger(\mathbf{x}) \left[ -\frac{1}{2} \nabla^2 - \sum_n \frac{Z_n}{|\mathbf{x} - \mathbf{R}_n|} \right] \hat{\psi}(\mathbf{x}) \\ & + \frac{1}{2} \iint d^3x d^3x' \hat{\psi}^\dagger(\mathbf{x}) \hat{\psi}^\dagger(\mathbf{x}') \frac{1}{|\mathbf{x} - \mathbf{x}'|} \hat{\psi}(\mathbf{x}') \hat{\psi}(\mathbf{x}). \end{aligned} \quad (2.21)$$

The electron field operator has two-components

$$\hat{\psi}(\mathbf{x}) = \begin{pmatrix} \hat{\psi}_{+1/2}(\mathbf{x}) \\ \hat{\psi}_{-1/2}(\mathbf{x}) \end{pmatrix}, \quad (2.22)$$

with spinor-like behaviour under spin rotations. The operators  $\hat{\psi}_\sigma^\dagger(\mathbf{x})$  [ $\hat{\psi}_\sigma(\mathbf{x})$ ] act on the fermionic Fock-space and create [annihilate] an electron with spin  $\sigma$  at position  $\mathbf{x}$ . Since electrons are fermions, the field operators satisfy the anticommutation relations

$$\{\hat{\psi}_\sigma(\mathbf{x}), \hat{\psi}_{\sigma'}(\mathbf{x}')\} = 0 = \{\hat{\psi}_\sigma^\dagger(\mathbf{x}), \hat{\psi}_{\sigma'}^\dagger(\mathbf{x}')\}, \quad (2.23a)$$

$$\{\hat{\psi}_\sigma(\mathbf{x}), \hat{\psi}_{\sigma'}^\dagger(\mathbf{x}')\} = \delta_{\sigma, \sigma'} \delta(\mathbf{x} - \mathbf{x}'). \quad (2.23b)$$

Often the field operators are expressed in terms of creation and annihilation operators for a given spin-orbital basis. The spin-orbitals  $\varphi_p(\mathbf{x})$  form an orthonormal basis of the one-particle Hilbert space, the index  $p$  comprises a complete set of spatial and spin quantum numbers. For example  $p = (n, l, m, s)$  with  $(n, l, m)$  as spatial quantum numbers and  $s$  the spin quantum number. The spin orbital and its conjugate transpose then have the form

$$\varphi_p(\mathbf{x}) = \varphi_{(n, l, m)}(\mathbf{x}) \begin{pmatrix} \delta_{s, +1/2} \\ \delta_{s, -1/2} \end{pmatrix} \quad \text{and} \quad \varphi_p^\dagger(\mathbf{x}) = \varphi_{(n, l, m)}^*(\mathbf{x}) \begin{pmatrix} \delta_{s, +1/2} & \delta_{s, -1/2} \end{pmatrix}. \quad (2.24)$$

Here, we do not specify the nature of the spin-orbitals. Usually they are chosen as eigenfunctions of a one-body operator, e.g., a mean-field operator such as the Fock operator, to approximate the  $N_{\text{el}}$ -electron ground state. We can now define the corresponding creation operator  $\hat{c}_p^\dagger$  by its action on Slater determinants

$$\hat{c}_p^\dagger |\text{vacc}\rangle = |\varphi_p\rangle, \quad (2.25)$$

$$\hat{c}_p^\dagger |\varphi_{p_1} \cdots \varphi_{p_N}\rangle = |\varphi_p \varphi_{p_1} \cdots \varphi_{p_N}\rangle. \quad (2.26)$$

The adjoint operator of the creation operator  $\hat{c}_p = (\hat{c}_p^\dagger)^\dagger$  is called the annihilation operator because

$$\hat{c}_p |\varphi_p \varphi_{p_1} \cdots \varphi_{p_N}\rangle = |\varphi_{p_1} \cdots \varphi_{p_N}\rangle. \quad (2.27)$$

Using the completeness relation  $\int d^3x |\mathbf{x}\rangle \langle \mathbf{x}| = \mathbb{1}$  we obtain

$$\begin{aligned} \hat{c}_p^\dagger |\varphi_{p_1} \cdots \varphi_{p_N}\rangle &= |\varphi_p \varphi_{p_1} \cdots \varphi_{p_N}\rangle \\ &= (N+1)^{-1/2} \mathcal{A} \left( \int d^3x |\mathbf{x}\rangle \langle \mathbf{x}| \varphi_p \right) |\varphi_{p_1} \cdots \varphi_{p_N}\rangle \\ &= (N+1)^{-1/2} \int d^3x \langle \mathbf{x}| \varphi_p \rangle \mathcal{A} (|\mathbf{x}\rangle |\varphi_{p_1} \cdots \varphi_{p_N}\rangle) \\ &= \int d^3x \varphi_p(\mathbf{x}) \hat{\psi}^\dagger(\mathbf{x}) |\varphi_{p_1} \cdots \varphi_{p_N}\rangle, \end{aligned}$$

where  $\mathcal{A}$  is the antisymmetrization operator. Because this is valid for arbitrary basis states, we obtain

$$\hat{c}_p^\dagger = \int d^3x \langle \mathbf{x}| \varphi_p \rangle \hat{\psi}^\dagger(\mathbf{x}) = \int d^3x \varphi_p(\mathbf{x}) \hat{\psi}^\dagger(\mathbf{x}), \quad (2.28a)$$

and for the adjoint

$$\hat{c}_p = \int d^3x \langle \varphi_p | \mathbf{x} \rangle \hat{\psi}(\mathbf{x}) = \int d^3x \varphi_p^\dagger(\mathbf{x}) \hat{\psi}(\mathbf{x}). \quad (2.28b)$$

From the anticommutation relations of the field operators, one can now derive the anticommutation relations of the creation and annihilation operators

$$\{\hat{c}_p, \hat{c}_q\} = 0 = \{\hat{c}_p^\dagger, \hat{c}_q^\dagger\}, \quad (2.29a)$$

$$\{\hat{c}_p, \hat{c}_q^\dagger\} = \delta_{p,q}. \quad (2.29b)$$

Using the completeness of the spin-orbital basis yields the expansion of field operators

$$\hat{\psi}^\dagger(\mathbf{x}) = \sum_p \varphi_p^\dagger(\mathbf{x}) \hat{c}_p^\dagger, \quad (2.30a)$$

$$\hat{\psi}(\mathbf{x}) = \sum_p \varphi_p(\mathbf{x}) \hat{c}_p. \quad (2.30b)$$

### 2.1.3. Quantized radiation field

In Section 2.1.1 we have seen that the vector potential is the dynamical variable of the radiation field. Recall that we have adopted the Coulomb gauge, see Eq. (2.4). The Hamiltonian of the radiation field takes the form

$$\hat{H}_{\text{rad}} = \frac{1}{8\pi} \int d^3x \left( \left( \frac{4\pi}{\alpha} \hat{\Pi}(\mathbf{x}) \right)^2 + \left( \nabla \times \hat{\mathbf{A}}(\mathbf{x}) \right)^2 \right). \quad (2.31)$$

In order to quantize the radiation field, we consider the free Maxwell-field in a box of volume  $V$  with imposed periodic boundary conditions. Then the classical vector potential can be expanded in terms of plane wave modes  $(\mathbf{k}, \lambda)$ , called photon modes. They are characterized by wave vector  $\mathbf{k}$  and polarization vector  $\boldsymbol{\epsilon}_{\mathbf{k},\lambda}$  ( $\lambda = 1$  or  $2$ ). The wave and polarization vectors satisfy the transversality and orthogonality conditions  $\mathbf{k} \cdot \boldsymbol{\epsilon}_{\mathbf{k},\lambda} = 0$ , and  $\boldsymbol{\epsilon}_{\mathbf{k},1}^* \cdot \boldsymbol{\epsilon}_{\mathbf{k},2} = 0$ .

Promoting the Fourier coefficients of the plane waves to operators  $\hat{a}_{\mathbf{k},\lambda}$  and  $\hat{a}_{\mathbf{k},\lambda}^\dagger$ , we can express the vector potential operator  $\hat{\mathbf{A}}$  in the Schrödinger picture as

$$\hat{\mathbf{A}}(\mathbf{x}) = \sum_{\mathbf{k},\lambda} \sqrt{\frac{2\pi}{V\omega_{\mathbf{k}}\alpha^2}} \left\{ \hat{a}_{\mathbf{k},\lambda} \boldsymbol{\epsilon}_{\mathbf{k},\lambda} e^{i\mathbf{k}\cdot\mathbf{x}} + \hat{a}_{\mathbf{k},\lambda}^\dagger \boldsymbol{\epsilon}_{\mathbf{k},\lambda}^* e^{-i\mathbf{k}\cdot\mathbf{x}} \right\}. \quad (2.32)$$

These operators can be expressed in terms of the vector potential and its canonical momentum as

$$\hat{a}_{\mathbf{k},\lambda} = \int_V d^3x \boldsymbol{\epsilon}_{\mathbf{k},\lambda}^* \cdot \left( \sqrt{\frac{\omega_{\mathbf{k}}\alpha^2}{8\pi V}} \hat{\mathbf{A}}(\mathbf{x}) + i \sqrt{\frac{2\pi}{V\omega_{\mathbf{k}}\alpha^2}} \hat{\Pi}(\mathbf{x}) \right) e^{-i\mathbf{k}\cdot\mathbf{x}}, \quad (2.33)$$

$$\hat{a}_{\mathbf{k},\lambda}^\dagger = \int_V d^3x \boldsymbol{\epsilon}_{\mathbf{k},\lambda} \cdot \left( \sqrt{\frac{\omega_{\mathbf{k}}\alpha^2}{8\pi V}} \hat{\mathbf{A}}(\mathbf{x}) - i \sqrt{\frac{2\pi}{V\omega_{\mathbf{k}}\alpha^2}} \hat{\Pi}(\mathbf{x}) \right) e^{i\mathbf{k}\cdot\mathbf{x}}. \quad (2.34)$$

The quantum analogue of the mode expansion of the classical fields  $\mathbf{E} = -\alpha \frac{\partial \mathbf{A}}{\partial t}$  and  $\mathbf{B} = \nabla \times \mathbf{A}$  are

$$\hat{\mathbf{E}}(\mathbf{x}) = \hat{\mathbf{E}}^+(\mathbf{x}) + \hat{\mathbf{E}}^-(\mathbf{x}) = i \sum_{\mathbf{k},\lambda} \sqrt{\frac{2\pi\omega_{\mathbf{k}}}{V}} \left\{ \hat{a}_{\mathbf{k},\lambda} \boldsymbol{\epsilon}_{\mathbf{k},\lambda} e^{i\mathbf{k}\cdot\mathbf{x}} - \hat{a}_{\mathbf{k},\lambda}^\dagger \boldsymbol{\epsilon}_{\mathbf{k},\lambda}^* e^{-i\mathbf{k}\cdot\mathbf{x}} \right\} \quad (2.35)$$

$$\begin{aligned} \hat{\mathbf{B}}(\mathbf{x}) &= \hat{\mathbf{B}}^+(\mathbf{x}) + \hat{\mathbf{B}}^-(\mathbf{x}) \\ &= i \sum_{\mathbf{k},\lambda} \sqrt{\frac{2\pi}{V\omega_{\mathbf{k}}\alpha^2}} \left\{ \hat{a}_{\mathbf{k},\lambda} (\mathbf{k} \times \boldsymbol{\epsilon}_{\mathbf{k},\lambda}) e^{i\mathbf{k}\cdot\mathbf{x}} - \hat{a}_{\mathbf{k},\lambda}^\dagger (\mathbf{k} \times \boldsymbol{\epsilon}_{\mathbf{k},\lambda}^*) e^{-i\mathbf{k}\cdot\mathbf{x}} \right\}. \end{aligned} \quad (2.36)$$

where  $\hat{\mathbf{E}}^\pm, \hat{\mathbf{B}}^\pm$  denote the positive and negative frequency parts of the electric and the magnetic field operator, respectively. The commutation relations of the operators

$\hat{a}_{\mathbf{k},\lambda}$  and  $\hat{a}_{\mathbf{k},\lambda}^\dagger$  follow from the commutation relations of the canonical variables in Eq. (2.17)

$$\left[ \hat{a}_{\mathbf{k},\lambda}, \hat{a}_{\mathbf{l},\mu} \right] = 0 = \left[ \hat{a}_{\mathbf{k},\lambda}^\dagger, \hat{a}_{\mathbf{l},\mu}^\dagger \right]. \quad (2.37a)$$

$$\left[ \hat{a}_{\mathbf{k},\lambda}, \hat{a}_{\mathbf{l},\mu}^\dagger \right] = \delta_{\mathbf{k},\mathbf{l}} \delta_{\lambda,\mu}. \quad (2.37b)$$

These are the commutation relations for bosonic creation and annihilation operators. In fact, one finds that the quantized Maxwell field can be represented as an infinite collection of independent harmonic oscillators. The Hamiltonian can be expressed as

$$\hat{H}_{\text{rad}} = \sum_{\mathbf{k},\lambda} \omega_{\mathbf{k}} \left( \hat{a}_{\mathbf{k},\lambda}^\dagger \hat{a}_{\mathbf{k},\lambda} + \frac{1}{2} \right). \quad (2.38)$$

There is one harmonic oscillator per mode  $(\mathbf{k}, \lambda)$ , and  $\hat{a}_{\mathbf{k},\lambda}^\dagger$  [ $\hat{a}_{\mathbf{k},\lambda}$ ] is the corresponding creation [annihilation] operator. The excitations of the Maxwell field are the photons with energy  $\omega_{\mathbf{k}}$ . Usually we will neglect the last term in the Hamiltonian, which gives the (infinite) vacuum energy.

The number operator of photons occupying a given mode  $(\mathbf{k}, \lambda)$  is simply  $\hat{a}_{\mathbf{k},\lambda}^\dagger \hat{a}_{\mathbf{k},\lambda}$ . Its eigenstate  $|n_{\mathbf{k},\lambda}\rangle$  is a singlemode Fock state with  $n_{\mathbf{k},\lambda}$  photons in the mode  $(\mathbf{k}, \lambda)$ . We will often use the multimode Fock states as a basis for the photonic Fock space. Let  $\{n\} = \{n_{\mathbf{k}_1,1}, n_{\mathbf{k}_1,2}, n_{\mathbf{k}_2,1}, n_{\mathbf{k}_2,2}, \dots\}$  be a sequence of occupation numbers for all photon modes, with total photon number  $N = \sum_{\mathbf{k},\lambda} n_{\mathbf{k},\lambda}$ . The corresponding multimode Fock state is defined by

$$|\{n\}\rangle = \prod_{\mathbf{k},\lambda} |n_{\mathbf{k},\lambda}\rangle. \quad (2.39)$$

#### 2.1.4. Radiation-matter interaction Hamiltonian

The interaction Hamiltonian of classical fields has been introduced in Eq. (2.15). Before writing down the corresponding Hamilton operator, we observe that within the Coulomb gauge

$$-i\nabla \cdot \left[ \hat{\mathbf{A}}(\mathbf{x})\varphi(\mathbf{x}) \right] = -i\hat{\mathbf{A}}(\mathbf{x}) \cdot \nabla\varphi(\mathbf{x}) - i \left[ \nabla \cdot \hat{\mathbf{A}}(\mathbf{x}) \right] \varphi(\mathbf{x}) = -i\hat{\mathbf{A}}(\mathbf{x}) \cdot \nabla\varphi(\mathbf{x}),$$

and consequently the particle momentum  $\hat{\mathbf{p}} = -i\nabla$  and the vector potential operator commute

$$[\hat{\mathbf{p}}, \hat{\mathbf{A}}] = 0. \quad (2.40)$$

Furthermore, recall that we neglect any interaction of the radiation with the nuclei. Thus, we will only write down the Hamilton operator for the interaction of electrons

(charge  $e = -1$ ) and the radiation field. The interaction Hamilton operator has the form

$$\hat{H}_{\text{int}} = \alpha \int d^3x \hat{\psi}^\dagger(\mathbf{x}) \frac{\nabla}{i} \cdot \hat{\mathbf{A}}(\mathbf{x}) \hat{\psi}(\mathbf{x}) + \frac{\alpha^2}{2} \int d^3x \hat{\psi}^\dagger(\mathbf{x}) \hat{\mathbf{A}}^2(\mathbf{x}) \hat{\psi}(\mathbf{x}). \quad (2.41)$$

We call the first term on the right hand side the “ $\mathbf{p} \cdot \mathbf{A}$ ” Hamiltonian. To the second term we refer as the “ $\mathbf{A}^2$ ” Hamiltonian.

To develop some intuition of their physical consequences we have a closer look at these terms. The “ $\mathbf{p} \cdot \mathbf{A}$ ” Hamiltonian

$$\hat{H}_{\hat{\mathbf{p}} \cdot \hat{\mathbf{A}}} = \alpha \int d^3x \hat{\psi}^\dagger(\mathbf{x}) \frac{\nabla}{i} \cdot \hat{\mathbf{A}}(\mathbf{x}) \hat{\psi}(\mathbf{x}) \quad (2.42)$$

is linear in the vector potential. The vector potential  $\hat{\mathbf{A}}$  is a sum of a photon creation  $\hat{a}_{\mathbf{k},\lambda}^\dagger$  and an annihilation operator  $\hat{a}_{\mathbf{k},\lambda}$  (see Eq. (2.32)). In perturbation theory (cf. Sec. 2.2.2) the first order is linear in the interaction Hamiltonian  $\hat{H}_{\hat{\mathbf{p}} \cdot \hat{\mathbf{A}}}$ . Consequently, there are terms proportional to  $\hat{c}_p^\dagger \hat{c}_q \hat{a}_{\mathbf{k},\lambda}^\dagger$  and  $\hat{c}_p^\dagger \hat{c}_q \hat{a}_{\mathbf{k},\lambda}$ , i.e., one photon is created or annihilated and one spin-orbital is changed. In fact, the “ $\mathbf{p} \cdot \mathbf{A}$ ” interaction in first order perturbation theory describes the x-ray absorption and emission by bound electrons. The second order perturbation theory can be thought of as a two-step process involving a (virtual) intermediate state. First, one photon from a mode  $(\mathbf{k}, \lambda)$  is absorbed and secondly a photon is emitted in the mode  $(\mathbf{l}, \mu)$ . In this way, the “ $\mathbf{p} \cdot \mathbf{A}$ ” Hamiltonian induces x-ray scattering in second order perturbation theory. Because an intermediate state is involved this kind of scattering is called “resonant x-ray scattering” [21, 23–25].

The “ $\mathbf{A}^2$ ” Hamiltonian

$$\hat{H}_{\hat{\mathbf{A}}^2} = \frac{\alpha^2}{2} \int d^3x \hat{\psi}^\dagger(\mathbf{x}) \hat{\mathbf{A}}^2(\mathbf{x}) \hat{\psi}(\mathbf{x}) = \frac{\alpha^2}{2} \int d^3x \hat{\mathbf{A}}^2(\mathbf{x}) \hat{n}(\mathbf{x}) \quad (2.43)$$

is, in contrast, quadratic in  $\hat{\mathbf{A}}$ . This Hamiltonian couples the radiation field directly to the electron density operator  $\hat{n}(\mathbf{x}) = \hat{\psi}^\dagger(\mathbf{x}) \hat{\psi}(\mathbf{x})$ . In first order perturbation theory there appear terms proportional to

$$\hat{c}_p^\dagger \left( \hat{a}_{\mathbf{k},\lambda}^\dagger + \hat{a}_{\mathbf{k},\lambda} \right)^2 \hat{c}_q = \hat{c}_p^\dagger \left( \hat{a}_{\mathbf{k},\lambda}^\dagger \hat{a}_{\mathbf{k},\lambda}^\dagger + \hat{a}_{\mathbf{k},\lambda} \hat{a}_{\mathbf{k},\lambda}^\dagger + \hat{a}_{\mathbf{k},\lambda}^\dagger \hat{a}_{\mathbf{k},\lambda} + \hat{a}_{\mathbf{k},\lambda} \hat{a}_{\mathbf{k},\lambda} \right) \hat{c}_q.$$

Terms where two photons are created or annihilated constitute nonlinear two-photon contributions. More importantly, this Hamiltonian describes the processes where a photon in the mode  $(\mathbf{k}, \lambda)$  is created and a photon in the mode  $(\mathbf{l}, \mu)$  is annihilated. Hence, this term describes x-ray scattering in first order perturbation theory. The x-ray scattering may be elastic or inelastic because the electronic state may remain

unchanged ( $p = q$ ) or may change ( $p \neq q$ ). The “ $\mathbf{A}^2$  scattering” is also called “non-resonant scattering”, because it is a first order process involving no intermediate (or resonant) electronic states.

Finally, there remain some remarks on the interaction Hamiltonian. In quantum optics it is usually convenient to make the long-wavelength approximation and, introducing gauge transformations to velocity or length gauge (Göppert-Mayer gauge), to obtain the electric dipole (or higher-order multipolar) Hamiltonian [14, 18, 26]. We avoid the long-wavelength approximation, because the wavelength of x rays is on the order of atomic dimensions.

Moreover, there are no interaction terms involving the electron spin. The minimal coupling Hamiltonian considered here couples only charges to the radiation field. Terms coupling spin and magnetic field, as well as terms involving spin-orbit coupling can be derived from a fully relativistic treatment [21, 27, 28]. They give rise to magnetic scattering, an interesting x-ray technique to investigate spin systems. However, because these terms appear only in higher order perturbation theory, they will not be considered in this dissertation.

## 2.2. Time evolution

### 2.2.1. Schrödinger and Interaction picture

In this section I discuss the dynamics of the system, for details I refer to Ref. [20]. So far, we have used the *Schrödinger picture*, where the time evolution of the system is completely represented by the time dependence of the states. In the Schrödinger picture the time evolution is governed by the Schrödinger equation

$$i\frac{\partial}{\partial t}|\Psi(t)\rangle = \hat{H}|\Psi(t)\rangle. \quad (2.44)$$

For a time-independent Hamiltonian one readily defines a time evolution operator

$$\hat{U}_S(t, t_0) = e^{-i\hat{H}(t-t_0)}, \quad (2.45)$$

such that  $\hat{U}_S(t, t_0)$  evolves states from time  $t_0$  to time  $t$ :

$$|\Psi(t)\rangle = \hat{U}_S(t, t_0)|\Psi(t_0)\rangle. \quad (2.46)$$

This operator has several properties that are required to induce a physical time evolution:

- It satisfies the initial condition  $\hat{U}_S(t_0, t_0) = \mathbb{1}$ .

- It has the group property  $\hat{U}_S(t, t_1)\hat{U}_S(t_1, t_0) = \hat{U}_S(t, t_0)$ , i.e., the time evolution can be applied consecutively.
- It is a unitary operator  $\hat{U}_S^\dagger(t, t_0) = \hat{U}_S^{-1}(t, t_0) = \hat{U}_S(t_0, t)$ . Thus, it preserves the norm of the states and the transition probabilities (scalar product) between the states.

If the state of the system at time  $t$  is specified by a density matrix operator  $\hat{\rho}(t_0) = \sum_{i,j} \rho_{i,j} |\Psi_j(t_0)\rangle \langle \Psi_i(t_0)|$  the density matrix operator evolves in time according to

$$\hat{\rho}(t) = \hat{U}_S(t, t_0) \hat{\rho}(t_0) \hat{U}_S^\dagger(t, t_0) . \quad (2.47)$$

In this thesis we will usually encounter the case that the Hamiltonian can be separated into two parts

$$\hat{H} = \hat{H}_0 + \hat{H}_{\text{int}} , \quad (2.48)$$

a simple Hamiltonian  $\hat{H}_0$  that can be easily solved or has known solutions, usually describing the free or unperturbed system, and an interaction Hamiltonian  $\hat{H}_{\text{int}}$  that induces a perturbation and causes the interesting time evolution. In this situation the *interaction picture* turns out to be very useful. We define the interaction picture state vector

$$|\Psi_I(t)\rangle = e^{i\hat{H}_0 t} |\Psi(t)\rangle , \quad (2.49)$$

which results in the equation of motion

$$i \frac{\partial}{\partial t} |\Psi_I(t)\rangle = -e^{i\hat{H}_0 t} \hat{H}_0 |\Psi(t)\rangle + e^{i\hat{H}_0 t} i \frac{\partial}{\partial t} |\Psi(t)\rangle \quad (2.50)$$

$$= e^{i\hat{H}_0 t} \left[ -\hat{H}_0 + \hat{H} \right] e^{-i\hat{H}_0 t} |\Psi_I(t)\rangle \quad (2.51)$$

$$= \hat{H}_{\text{int}}(t) |\Psi_I(t)\rangle . \quad (2.52)$$

In the last equation we have introduced the time-dependent interaction Hamiltonian  $\hat{H}_{\text{int}}(t) = e^{i\hat{H}_0 t} \hat{H}_{\text{int}} e^{-i\hat{H}_0 t}$ . In general operators become time dependent in the interaction picture

$$\hat{O}_I(t) = e^{i\hat{H}_0 t} \hat{O} e^{-i\hat{H}_0 t} . \quad (2.53)$$

This definition is made plausible by writing out an arbitrary matrix element in the Schrödinger picture

$$\langle \Phi(t) | \hat{O} | \Psi(t) \rangle = \langle \Phi_I(t) | e^{i\hat{H}_0 t} \hat{O} e^{-i\hat{H}_0 t} | \Psi_I(t) \rangle \quad (2.54)$$

$$= \langle \Phi_I(t) | \hat{O}_I(t) | \Psi_I(t) \rangle . \quad (2.55)$$

Thus, states and operators depend on time in the interaction picture. The equation of motion for operators in the interaction picture follows directly from Eq. (2.53)

$$i\frac{\partial}{\partial t}\hat{O}_I(t) = [\hat{O}_I(t), \hat{H}_0]. \quad (2.56)$$

As in the Schrödinger picture, we introduce a time evolution operator that satisfies the initial condition, group property and unitarity mentioned above. The time evolution operator propagates vector states

$$\hat{U}_I(t, t_0)|\Psi_I(t_0)\rangle = |\Psi_I(t)\rangle, \quad (2.57)$$

and density matrix operators

$$\hat{\rho}_I(t) = \hat{U}_I(t, t_0)\hat{\rho}_I(t_0)\hat{U}_I^\dagger(t, t_0). \quad (2.58)$$

From Eq. (2.52) follows the equation of motion

$$i\frac{\partial}{\partial t}\hat{U}_I(t, t_0) = \hat{H}_{\text{int}}(t)\hat{U}_I(t, t_0). \quad (2.59)$$

There is a crucial difference to the Schrödinger picture: The Hamiltonian is time dependent. The key advantage of the interaction picture is the separation of free time evolution and interaction induced perturbations. The time evolution of operators depends only on  $\hat{H}_0$ , whereas states are propagated with respect to the interaction Hamiltonian  $\hat{H}_{\text{int}}$ .

Typically, the interaction picture is used with an initial state that has been prepared at  $t_0 \rightarrow -\infty$  without the influence of any interaction. To turn off the interaction we introduce a switching function  $f_\epsilon(t)$  in the Hamiltonian

$$\hat{H} = \hat{H}_0 + f_\epsilon(t)\hat{H}_{\text{int}}. \quad (2.60)$$

The switching function should be chosen such that  $f_\epsilon \rightarrow 0$  for  $t \rightarrow \pm\infty$ , so that the interaction part in the Hamiltonian vanishes. At time  $t = 0$  we wish to have the full interaction strength, thus we require  $f_\epsilon(0) = 1$ . Finally, we need  $\lim_{\epsilon \rightarrow 0} f_\epsilon(t) = 1$  because we want to obtain the original Hamiltonian. Of course, all physical quantities should be calculated in the limit  $\epsilon \rightarrow 0$ . We will use the very common *adiabatic switching*

$$f_\epsilon(t) = e^{-\epsilon|t|}. \quad (2.61)$$

In the limit that  $t_0$  approaches  $-\infty$  the Hamiltonian becomes simply  $\hat{H}_0$ . Assume that we can choose the eigenstate  $|\Phi\rangle$  of the free Hamiltonian  $\hat{H}_0$ , with energy  $E_0$ , as the initial state. Then the initial state in the Schrödinger picture is

$$|\Psi(t_0)\rangle = e^{-i\hat{E}_0 t_0} |\Phi\rangle. \quad (2.62)$$

In the interaction picture this is simply the time-independent eigenstate of the free Hamiltonian

$$|\Psi_I(t_0)\rangle = e^{i\hat{H}_0 t_0} |\Psi(t_0)\rangle = |\Phi\rangle. \quad (2.63)$$

When the interaction is turned on the state evolves with respect to the interaction  $f_\epsilon(t)\hat{H}_{\text{int}}$ . Since the previous steps also hold for time-dependent interactions one only needs to solve the Eq. (2.59). The state at finite times is then obtained from

$$|\Psi_I(t)\rangle = \hat{U}_I(t, t_0)|\Phi\rangle. \quad (2.64)$$

In the following we will assume that all states are well defined in the limit  $\epsilon \rightarrow 0$ , a problem that is accounted for by the Gell-Mann and Low theorem [20]. In the case of x-ray pulses it is often not even necessary to introduce a switching function. The electric field of the pulse is vanishing at infinite times at the position of the sample, i.e., the interaction is automatically switched off.

### 2.2.2. Perturbation theory

In the previous section we have seen that the crucial problem in interaction picture dynamics is to solve the equation of motion (2.59). We need a time evolution operator<sup>1</sup> that satisfies

$$i\frac{\partial}{\partial t}\hat{U}_\epsilon(t, t_0) = f_\epsilon(t)\hat{H}_{\text{int}}(t)\hat{U}_\epsilon(t, t_0). \quad (2.65)$$

Using the initial condition of  $\hat{U}_\epsilon$ , we can reformulate the last result as an integral equation

$$\hat{U}_\epsilon(t, t_0) = \mathbb{1} - i \int_{t_0}^t dt' f_\epsilon(t')\hat{H}_{\text{int}}(t')\hat{U}_\epsilon(t', t_0). \quad (2.66)$$

Taking care of the operator ordering the integration can be iterated

$$\hat{U}_\epsilon(t, t_0) = \mathbb{1} - i \int_{t_0}^t dt' f_\epsilon(t')\hat{H}_{\text{int}}(t') \quad (2.67)$$

$$+ i^2 \int_{t_0}^t dt' \int_{t_0}^{t'} dt'' f_\epsilon(t')f_\epsilon(t'')\hat{H}_{\text{int}}(t')\hat{H}_{\text{int}}(t'') \quad (2.68)$$

$$- i^3 \int_{t_0}^t dt' \int_{t_0}^{t'} dt'' \int_{t_0}^{t''} dt''' f_\epsilon(t')f_\epsilon(t'')f_\epsilon(t''')\hat{H}_{\text{int}}(t')\hat{H}_{\text{int}}(t'')\hat{H}_{\text{int}}(t''') \quad (2.69)$$

+ ...

Introducing the time-ordering symbol  $\mathcal{T}$  the expansion can be written as [20]

$$\hat{U}_\epsilon(t, t_0) = \mathcal{T} \exp\left(-i \int_{t_0}^t dt' f_\epsilon(t')\hat{H}_{\text{int}}(t')\right). \quad (2.70)$$

<sup>1</sup>From now on we work exclusively in the interaction picture. Thus, we drop using the index  $I$ .

However, for our purposes it is sufficient to consider only the first order expansion in Eq. (2.67).

We can now expand the expectation value of an observable in first order perturbation theory. The most general initial state at  $t_0 \rightarrow -\infty$  is a density matrix

$$\hat{\rho}_{\text{in}} = \sum_{i,j} \rho_{i,j} |\Phi_j\rangle \langle \Phi_i|, \quad (2.71)$$

where  $\Phi_i$  are eigenstates of  $\hat{H}_0$ . The expectation value of the (Schrödinger picture) observable  $\hat{O}$  at a time  $t$  is

$$\langle \hat{O} \rangle_t = \text{Tr} \left( \hat{\rho}(t) \hat{O}(t) \right) \quad (2.72)$$

$$= \lim_{\epsilon \rightarrow 0} \lim_{t_0 \rightarrow -\infty} \text{Tr} \left( \hat{U}_\epsilon(t, t_0) \hat{\rho}_{\text{in}} \hat{U}_\epsilon^\dagger(t, t_0) \hat{O}(t) \right). \quad (2.73)$$

Inserting the first order expansion of the time evolution we obtain

$$\langle \hat{O} \rangle_t^{1\text{st}} = \lim_{\epsilon \rightarrow 0} \left[ \text{Tr} \left( \hat{\rho}_{\text{in}} \hat{O}(t) \right) + \right. \quad (2.74)$$

$$+ i \int_{-\infty}^t dt' f_\epsilon(t') \left\{ \text{Tr} \left( \hat{\rho}_{\text{in}} \hat{H}_{\text{int}}(t') \hat{O}(t) \right) - \text{Tr} \left( \hat{H}_{\text{int}}(t') \hat{\rho}_{\text{in}} \hat{O}(t) \right) \right\} \quad (2.75)$$

$$\left. + \int_{-\infty}^t dt' \int_{-\infty}^t dt'' f_\epsilon(t') f_\epsilon(t'') \text{Tr} \left( \hat{H}_{\text{int}}(t') \hat{\rho}_{\text{in}} \hat{H}_{\text{int}}(t'') \hat{O}(t) \right) \right]. \quad (2.76)$$

To simplify the second term on the right hand side, note the trace property

$$\begin{aligned} \text{Tr}(\hat{A} \hat{\rho}_{\text{in}} \hat{B}) &= \sum_M \sum_{i,j} \rho_{i,j} \langle \Phi_M | \hat{A} | \Phi_j \rangle \langle \Phi_i | \hat{B} | \Phi_M \rangle \\ &= \sum_{i,j} \rho_{i,j} \langle \Phi_i | \hat{B} \hat{A} | \Phi_j \rangle = \sum_{i,j} \rho_{i,j} \left( \langle \Phi_j | \hat{A}^\dagger \hat{B}^\dagger | \Phi_i \rangle \right)^* \\ &= \left( \sum_{i,j} \rho_{j,i} \langle \Phi_M | \Phi_i \rangle \langle \Phi_j | \hat{A}^\dagger \hat{B}^\dagger | \Phi_M \rangle \right)^* = \text{Tr}(\hat{\rho}_{\text{in}} \hat{A}^\dagger \hat{B}^\dagger)^*, \end{aligned}$$

where the star denotes complex conjugation.  $\hat{H}_{\text{int}}$  and  $\hat{O}(t)$  are self-adjoint operators enabling us to rewrite the second term in the fashion  $i\{z - z^*\} = 2 \text{Re}(iz)$ . Then, we get for the first order perturbation theory expression of the expectation value

$$\begin{aligned} \langle \hat{O} \rangle_t^{1\text{st}} &= \lim_{\epsilon \rightarrow 0} \left[ \text{Tr} \left( \hat{\rho}_{\text{in}} \hat{O}(t) \right) + 2 \text{Re} \left( i \int_{-\infty}^t dt' f_\epsilon(t') \text{Tr} \left( \hat{\rho}_{\text{in}} \hat{H}_{\text{int}}(t') \hat{O}(t) \right) \right) \right. \\ &\quad \left. + \int_{-\infty}^t dt' \int_{-\infty}^t dt'' f_\epsilon(t') f_\epsilon(t'') \text{Tr} \left( \hat{H}_{\text{int}}(t') \hat{\rho}_{\text{in}} \hat{H}_{\text{int}}(t'') \hat{O}(t) \right) \right]. \quad (2.77) \end{aligned}$$

We denote the terms on the right hand side by

$$\langle \hat{\mathcal{O}} \rangle_t^{\text{1st}} = \langle \hat{\mathcal{O}} \rangle_t^{(0,0)} + \langle \hat{\mathcal{O}} \rangle_t^{(0,1)} + \langle \hat{\mathcal{O}} \rangle_t^{(1,1)}, \quad (2.78)$$

and refer to them as the (0,0), (0,1), and (1,1) term, respectively. One immediately sees that the (0,0) term represents the expectation value of  $\hat{\mathcal{O}}$  in the initial state, without any interaction. The physical meaning of the (0,1) and (1,1) terms will be discussed in the next chapters in the context of x-ray scattering.

### 2.2.3. Fermi's golden rule

A quite generally used method to calculate transition rates between different states is Fermi's golden rule. Assume that initially ( $t_0 \rightarrow -\infty$ ) the system is in an eigenstate of  $\hat{H}_0$

$$\lim_{t_0 \rightarrow -\infty} |\Psi(t_0)\rangle = |\Phi_I\rangle \quad (2.79)$$

which is a stationary state. We are interested in transitions, where long after the scattering  $t \rightarrow \infty$  the system is found in an eigenstate  $|\Phi_F\rangle$  of  $\hat{H}_0$ , that is different from the initial state, i.e.,  $\langle \Phi_F | \Phi_I \rangle = 0$ . The probability amplitude for such a transition is

$$S_{FI} = \lim_{t \rightarrow +\infty} \langle \Phi_F | \Psi(t) \rangle = \lim_{t \rightarrow +\infty} \langle \Phi_F | \hat{U}(t, t_0) | \Phi_I \rangle. \quad (2.80)$$

Employing adiabatic switching and first order perturbation theory this expression becomes

$$S_{FI} = -i \lim_{\epsilon \rightarrow 0} \int_{-\infty}^{\infty} dt e^{i(E_F - E_I)t} e^{-\epsilon|t|} \langle \Phi_F | \hat{H}_{\text{int}} | \Phi_I \rangle \quad (2.81)$$

$$= -2\pi i \delta(E_F - E_I) \langle \Phi_F | \hat{H}_{\text{int}} | \Phi_I \rangle. \quad (2.82)$$

Before we can obtain a probability  $|S_{FI}|^2$  from this amplitude, we have to explain how to handle the delta function. The delta function ensures that the total energy in the transition is preserved. In all realistic experiments, however, the transitions occur in a finite time interval  $T$ . Thus one may use the following trick[12, 29]

$$[\delta(E_F - E_I)]^2 = \delta(E_F - E_I) \int_{-T/2}^{T/2} \frac{dt}{2\pi} e^{i(E_F - E_I)t} = \delta(E_F - E_I) \frac{T}{2\pi}. \quad (2.83)$$

Finally, we obtain a formula for the transition rate, known as Fermi's golden rule,

$$\Gamma_{FI} = \frac{|S_{FI}|^2}{T} = 2\pi \delta(E_F - E_I) \left| \langle \Phi_F | \hat{H}_{\text{int}} | \Phi_I \rangle \right|^2. \quad (2.84)$$

We could also express the initial state as a density matrix  $\hat{\rho}_{\text{in}} = |\Phi_I\rangle\langle\Phi_I|$  and we can consider the projection onto the final state as an observable  $\hat{\mathcal{O}} = |\Phi_F\rangle\langle\Phi_F|$ . Then the last expression becomes

$$\Gamma_{FI} = 2\pi \delta(E_F - E_I) \text{Tr}(\hat{H}_{\text{int}}\hat{\rho}_{\text{in}}\hat{H}_{\text{int}}\hat{\mathcal{O}}). \quad (2.85)$$

Using Eq. (2.83) one finds that the transition rate  $\Gamma_{FI}$  from Fermi's golden rule corresponds to the (1,1) term in first order perturbation theory for the projection operator observable divided by the interaction time  $T$

$$\lim_{t \rightarrow \infty} \langle \hat{\mathcal{O}} \rangle_t^{(1,1)} = \int dt' \int dt'' \text{Tr}(\hat{H}_{\text{int}}(t')\hat{\rho}_{\text{in}}\hat{H}_{\text{int}}(t'')\hat{\mathcal{O}}) \quad (2.86)$$

$$= \int dt' e^{i(E_F - E_I)t'} \int dt'' e^{-i(E_F - E_I)t''} \langle \Phi_F | \hat{H}_{\text{int}} | \Phi_I \rangle \langle \Phi_I | \hat{H}_{\text{int}} | \Phi_F \rangle \quad (2.87)$$

$$= \Gamma_{FI} T. \quad (2.88)$$

## Part II.

# Near field imaging: x-ray phase contrast



# Chapter 3.

## About x-ray phase contrast imaging

In this chapter I introduce x-ray phase contrast imaging. The classical expressions for propagation-based x-ray phase contrast imaging are derived for pulsed x-ray sources. The derivation is based on an optical scattering scheme.

### 3.1. Introduction and applications

Several imaging methods exploit the phase variation of coherent radiation propagating through an object. These phase contrast imaging (PCI) methods provide images irrespective of the absorption properties of the target. Different concepts of PCI have been established, such as propagation based PCI, Zernike PCI, differential PCI, interferometric PCI, etc. Different types of radiation may be used, e.g., x rays [30, 31], visible light [32–35], electrons [36, 37], and neutrons [38, 39]. The invention of optical phase contrast microscopy earned F. Zernike the Nobel prize in 1953 [40, 41]. This technique has also been extended to electron [42] and soft x-ray microscopy [43].

Microscopy techniques are, however, not easily transferable to hard x-ray imaging, because of the difficulties in producing suitable x-ray focusing optics. For hard x rays the propagation based PCI scheme is more convenient. The principle of this setup is simple: The wavefront of an x-ray pulse will be distorted, when it propagates through an object. After free propagation for some distance, these phase changes may cause intensity variations of the wave field. Typically, Fresnel diffraction of the radiation field describes this effect, see Fig. 3.1. Even completely transparent (nonabsorbing) objects may be imaged.

Since its discovery in 1995 [45, 46] using synchrotron radiation, hard x-ray PCI has seen a rapid development. Along with the advent of coherent x-ray sources, it has spread into many areas of science and become an indispensable tool in nondestructive imaging. Very soon after its discovery, it was also realized that spatial coherence is crucial, opening the way to use conventional laboratory x-ray sources [47]. X-ray PCI has been accomplished using synchrotron radiation [45–47], x-ray microscopes [43],

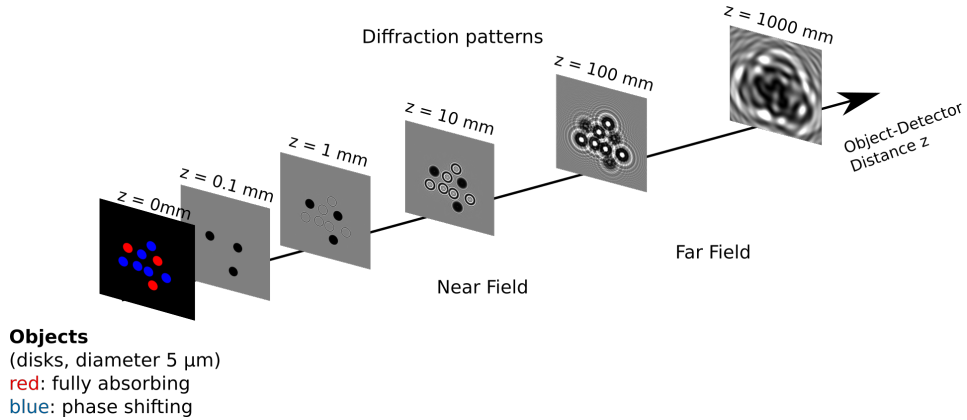


Figure 3.1.: Sketch of the principle of propagation based x-ray PCI. The Fresnel diffraction pattern is shown after some propagation distance: directly behind the object only absorbing samples show any contrast, after some propagation distance the shape of the phase shifting objects become visible.

Simulations for fully absorbing and purely phase shifting disks with  $5 \mu\text{m}$  diameter and a monochromatic plane wave with 12.4 keV photon energy [44].

Images adapted from Timm Weitkamp (under CC BY 3.0 DE license).

and x-ray tubes [48]. Because organic materials often contain few heavy elements and consequently are highly transparent to x rays, x-ray PCI has proven to be particularly useful in the biological and medical sciences [30, 49]. The vast amount of applications of x-ray PCI range from computed tomography of biological tissue [50], mammography [51], imaging of lipid monolayers [52, 53], in vivo studies of muscle complexes in insects [54], to studies of paleontological fish [55, 56], and revealing letters in archaeological papyri from Herculaneum [57].

### 3.2. Classical theory of phase contrast imaging

The classical formulation of x-ray phase contrast imaging is commonly based on the macroscopic index of refraction and scalar diffraction theory [31, 58], the propagation of coherence functions [30], or the transport-of-intensity equation [59–61]. I present a theory of propagation based PCI in terms of optical scattering. This approach is closely related to the formalism of photon scattering in the next chapter. In particular, the appearance and treatment of the correlation functions is revealed.

### 3.2.1. Classical scattering of a light pulse

The scattering of a classical electromagnetic field is treated in [31, 62]. The scattering medium is described by a time-independent complex refractive index  $n_\omega(\mathbf{x})$ . Moreover, it is assumed that: (i) the medium is non-magnetic; (ii) the electrical permittivity, and therefore the index of refraction, is time-independent and slowly varying over spatial lengths comparable to the wavelength of the field; (iii) we can describe the radiation by a scalar field  $E(\mathbf{x}, t)$ .

Let the light pulse be described by the complex scalar function  $E_{\text{in}}(\mathbf{x}, t)$ . The physical electric field is real. The function  $E_{\text{in}}(\mathbf{x}, t)$  is the corresponding complex analytic signal [15], which can be spectrally decomposed into its monochromatic components

$$E_{\text{in}}(\mathbf{x}, t) = \frac{1}{\sqrt{2\pi}} \int_0^\infty E_{\text{in}}(\mathbf{x}, \omega) e^{i\omega t} d\omega. \quad (3.1)$$

Each monochromatic component satisfies the inhomogeneous Helmholtz equation [31, 62]

$$(\nabla^2 + k^2) E(\mathbf{x}, \omega) = k^2 (1 - n_\omega^2(\mathbf{x})) E(\mathbf{x}, \omega), \quad (3.2)$$

where  $k = \alpha\omega$ . Within the first Born approximation, we find the solution to the inhomogeneous Helmholtz equation

$$E(\mathbf{x}, \omega) = E_{\text{in}}(\mathbf{x}, \omega) - \frac{k^2}{4\pi} \int d^3x' \frac{e^{ik|\mathbf{x}-\mathbf{x}'|}}{|\mathbf{x}-\mathbf{x}'|} (1 - n_\omega^2(\mathbf{x}')) E_{\text{in}}(\mathbf{x}', \omega). \quad (3.3)$$

Recall that the correlation function  $\Gamma(\mathbf{r}_1, \mathbf{r}_2, t_1, t_2)$  and the cross spectral density  $W(\mathbf{r}_1, \mathbf{r}_2, \omega_1, \omega_2)$  of the light field are defined by [15]

$$\Gamma(\mathbf{r}_1, \mathbf{r}_2, t_1, t_2) = \langle E^*(\mathbf{r}_1, t_1) E(\mathbf{r}_2, t_2) \rangle \quad (3.4)$$

$$= \frac{1}{2\pi} \iint d\omega_1 d\omega_2 \langle E^*(\mathbf{r}_1, \omega_1) E(\mathbf{r}_2, \omega_2) \rangle e^{-i(\omega_2 t_2 - \omega_1 t_1)} \quad (3.5)$$

$$= \frac{1}{2\pi} \iint d\omega_1 d\omega_2 W(\mathbf{r}_1, \mathbf{r}_2, \omega_1, \omega_2) e^{-i(\omega_2 t_2 - \omega_1 t_1)}, \quad (3.6)$$

where  $\langle \cdot \rangle$  denotes an average over the ensemble of pulses. The intensity at position  $\mathbf{r}$  is

$$I(\mathbf{r}, t) = \Gamma(\mathbf{r}, \mathbf{r}, t, t) = \langle E^*(\mathbf{r}, t) E(\mathbf{r}, t) \rangle \quad (3.7)$$

$$= \left\langle \frac{1}{2\pi} \iint d\omega_1 d\omega_2 E^*(\mathbf{r}, \omega_1) E(\mathbf{r}, \omega_2) e^{-i(\omega_2 - \omega_1)t} \right\rangle. \quad (3.8)$$

The target is assumed to scatter weakly and to absorb no radiation. In this case the index of refraction is  $n_\omega(\mathbf{x}) = 1 - \delta_\omega(\mathbf{x})$ , where  $\delta_\omega$  is typically very small for

x rays [63]. Thus, only terms of first order in  $\delta_\omega$  need to be considered. This means  $1 - n_\omega^2(\mathbf{x}) \approx 2\delta_\omega(\mathbf{x})$ , and

$$\begin{aligned}
 I(\mathbf{r}, t) &= \frac{1}{2\pi} \iint d\omega_1 d\omega_2 \langle E_{\text{in}}^*(\mathbf{r}, \omega_1) E_{\text{in}}(\mathbf{r}, \omega_2) \rangle e^{-i(\omega_2 - \omega_1)t} \\
 &\quad - 2 \operatorname{Re} \left\{ \frac{1}{2\pi} \iint d\omega_1 d\omega_2 \frac{k_2^2}{4\pi} \int d^3x' \frac{e^{ik_2|\mathbf{r}-\mathbf{x}'|}}{|\mathbf{r}-\mathbf{x}'|} 2\delta_{\omega_2}(\mathbf{x}') \right. \\
 &\quad \left. \times \langle E_{\text{in}}^*(\mathbf{r}, \omega_1) E_{\text{in}}(\mathbf{x}', \omega_2) \rangle e^{-i(\omega_2 - \omega_1)t} \right\} \\
 &= I_{\text{in}}(\mathbf{r}, t) - \frac{1}{2\pi^2} \operatorname{Re} \left\{ \iint d\omega_1 d\omega_2 \int d^3x' k_2^2 \frac{e^{ik_2|\mathbf{r}-\mathbf{x}'|}}{|\mathbf{r}-\mathbf{x}'|} \delta_{\omega_2}(\mathbf{x}') \right. \\
 &\quad \left. \times W(\mathbf{r}, \mathbf{x}', \omega_1, \omega_2) e^{-i(\omega_2 - \omega_1)t} \right\}, \tag{3.9}
 \end{aligned}$$

where  $I_{\text{in}}(\mathbf{r}, t)$  denotes the intensity of the unscattered pulse.

### 3.2.2. Quasi-stationary pulses

In the following, let us consider a plane-wave x-ray pulse and let us assume that its intensity profile varies on a much longer timescale than its temporal coherence properties. Then we can make the assumption that the statistical properties of the x-ray pulse have a quasi-stationary form [64, 65]. For  $\mathbf{x}_1, \mathbf{x}_2$  in the common plane  $x_{z,1} = 0 = x_{z,2}$  (orthogonal to the propagation direction and at the origin), we assume

$$\Gamma(\mathbf{x}_1, \mathbf{x}_2, t_1, t_2) = I\left(\frac{t_1+t_2}{2}\right) \gamma_{\text{sp}}(\mathbf{x}_1, \mathbf{x}_2) \gamma_{\text{tp}}(t_1 - t_2), \tag{3.11}$$

where  $\gamma_{\text{sp}}$  describes the transversal and  $\gamma_{\text{tp}}$  the longitudinal correlations and  $I$  is an intensity envelope. We will assume the following transversal (or spatial) correlation function with the coherence length  $l_c$

$$\gamma_{\text{sp}}(\mathbf{x}, \mathbf{x}') = e^{-|\mathbf{x}_\perp - \mathbf{x}'_\perp|^2 / l_c^2}, \tag{3.12}$$

where  $\mathbf{x} = (\mathbf{x}_\perp, 0)$ .

Write  $t = \frac{t_1+t_2}{2}$  and  $\tau = t_1 - t_2$ , as well as  $\omega = \frac{\omega_1+\omega_2}{2}$  and  $\bar{\omega} = \omega_1 - \omega_2$ . Then the cross-spectral density becomes [64]

$$W(\mathbf{x}_1, \mathbf{x}_2, \omega, \bar{\omega}) = \gamma_{\text{sp}}(\mathbf{x}_1, \mathbf{x}_2) W_1(\omega) W_2(\bar{\omega}), \tag{3.13}$$

where we have introduced the Fourier transforms

$$W_1(\omega) = \frac{1}{\sqrt{2\pi}} \int \gamma_{\text{tp}}(\tau) e^{i\omega\tau} d\tau, \tag{3.14a}$$

$$W_2(\bar{\omega}) = \frac{1}{\sqrt{2\pi}} \int I(t) e^{i\bar{\omega}t} dt. \tag{3.14b}$$

From these equations we see, that for very long pulses

$$W_2(\bar{\omega}) \rightarrow \delta(\bar{\omega}), \quad \text{for } T \rightarrow \infty, \quad (3.15)$$

i.e., for long pulse duration  $T$  we recover the case of a stationary field, where the frequency components are uncorrelated. We assume a Gaussian shape of the longitudinal (or temporal) coherence function

$$\gamma_{\text{tp}}(\tau) = \frac{1}{\sqrt{2\pi}} e^{-\frac{\tau^2}{\tau_c^2}} e^{-i\omega_{\text{in}}\tau}, \quad (3.16)$$

where the width  $\tau_c$  of the temporal coherence function is called the coherence time. From the Fourier relationship in Eq. (3.14a) follows that the spectral bandwidth of the radiation field is  $\Delta\omega = 1/\tau_c$ . For sufficiently long coherence time  $\tau_c$  one recovers the (quasi)monochromatic case ( $\Delta\omega \ll \omega_{\text{in}}$ )

$$W_1(\omega) \rightarrow \delta(\omega - \omega_{\text{in}}), \quad \text{for } \tau_c \rightarrow \infty. \quad (3.17)$$

In the following we will always assume the pulse duration  $T$  to be much larger than the coherence time  $\tau_c$

$$\tau_c \ll T. \quad (3.18)$$

### 3.2.3. Propagation and intensity in the Fresnel regime

When the field  $E(\mathbf{x}, \omega)$  is known in the plane  $x_z = 0$ , the field can be calculated at position  $\mathbf{r}$  by the Rayleigh-Sommerfeld diffraction integral [31, 62]

$$E(\mathbf{r}, \omega) = \frac{-1}{2\pi} \int_{x_z=0} d^2\mathbf{x} E(\mathbf{x}, \omega) \frac{\partial}{\partial z} \left[ \frac{e^{ik|\mathbf{r}-\mathbf{x}|}}{|\mathbf{r}-\mathbf{x}|} \right]. \quad (3.19)$$

Consequently, there is also a propagation equation for the cross-spectral density [15]. This is particularly helpful because the correlation function and cross-spectral density are typically known only in the interaction region. Combining this with the definition of the cross-spectral density, it follows that  $W$  can be propagated from the plane  $x_z = 0$  to the point  $\mathbf{r}$

$$W(\mathbf{r}, \mathbf{x}', \omega, \bar{\omega}) = -\frac{1}{2\pi} \int_{x_z=0} d^2\mathbf{x} W(\mathbf{x}, \mathbf{x}', \omega, \bar{\omega}) \frac{\partial}{\partial z} \left[ \frac{e^{-i\alpha(\omega+\bar{\omega}/2)|\mathbf{r}-\mathbf{x}|}}{|\mathbf{r}-\mathbf{x}|} \right]. \quad (3.20)$$

Now, inserting the last result into in Eq. (3.10), the term in braces becomes

$$\begin{aligned} & \frac{1}{2\pi} \iint d\omega d\bar{\omega} \frac{\alpha^2(\omega - \bar{\omega}/2)^2}{4\pi} \int d^3x' \frac{e^{i\alpha(\omega - \bar{\omega}/2)|\mathbf{r}-\mathbf{x}'|}}{|\mathbf{r}-\mathbf{x}'|} \delta_{(\omega - \bar{\omega}/2)}(\mathbf{x}') \\ & \times \frac{-1}{2\pi} \int_{x_z=0} d^2\mathbf{x} W(\mathbf{x}, \mathbf{x}', \omega, \bar{\omega}) \frac{\partial}{\partial z} \left[ \frac{e^{-i\alpha(\omega+\bar{\omega}/2)|\mathbf{r}-\mathbf{x}|}}{|\mathbf{r}-\mathbf{x}|} \right] e^{i\bar{\omega}t}. \end{aligned} \quad (3.21)$$

At this point, we have to introduce the essential requirement for phase-contrast imaging. The detector at  $\mathbf{r} = (\mathbf{r}_\perp, z)$  must be placed in the near field, also called the Fresnel regime. We introduce the Fresnel approximation

$$\frac{e^{-ik|\mathbf{r}-\mathbf{x}'|}}{|\mathbf{r}-\mathbf{x}'|} \approx \frac{e^{-ik(z-x'_z + \frac{|\mathbf{r}_\perp-\mathbf{x}'_\perp|^2}{2z})}}{z}, \quad (3.22)$$

where  $\mathbf{x}' = (\mathbf{x}'_\perp, x'_z)$  is a point in the target. As a rule of thumb, the Fresnel regime is characterized by the Fresnel number

$$F \gtrsim 1, \quad \text{where} \quad F = \frac{D^2}{z\lambda},$$

with  $D$  the characteristic size of the object,  $\lambda$  the wavelength.

Moreover, we will use the projection approximation. This means we assume that the sample is so thin that the field propagating through the sample is not deviated much from the path of a plane wave. Thus, we will consider the cross-spectral density only in a single plane. Let the plane  $z = 0$  be directly behind the sample. For all points  $\mathbf{x}'$  of the sample and  $\mathbf{x} = (\mathbf{x}_\perp, 0)$ , we set

$$W(\mathbf{x}, \mathbf{x}', \omega, \bar{\omega}) \approx W(\mathbf{x}_\perp, \mathbf{x}'_\perp, \omega, \bar{\omega}) e^{i\alpha(\omega-\bar{\omega}/2)x'_z}. \quad (3.23)$$

With these approximations and inserting the cross-spectral density  $W(\mathbf{x}, \mathbf{x}', \omega, \bar{\omega})$  from Eq. (3.13), the term in (3.21) becomes

$$\begin{aligned} & \frac{i\alpha^3}{8\pi^3 z^2} \iint d\omega d\bar{\omega} (\omega - \frac{\bar{\omega}}{2})^2 (\omega + \frac{\bar{\omega}}{2}) \int d^3 x' e^{i\alpha(\omega-\frac{\bar{\omega}}{2})(z+\frac{|\mathbf{r}_\perp-\mathbf{x}'_\perp|^2}{2z})} \delta_{(\omega-\bar{\omega}/2)}(\mathbf{x}') \\ & \times \int_{x_z=0} d^2 \mathbf{x} \gamma_{\text{sp}}(\mathbf{x}, \mathbf{x}') W_1(\omega) W_2(\bar{\omega}) e^{-i\alpha(\omega+\frac{\bar{\omega}}{2})(z+\frac{|\mathbf{r}_\perp-\mathbf{x}_\perp|^2}{2z})} e^{i\bar{\omega}t}. \end{aligned}$$

For long pulse duration  $W_2(\bar{\omega}) \rightarrow \delta(\bar{\omega})$ . Thus, we consider only terms with  $\bar{\omega} \approx 0$ , when performing the  $\bar{\omega}$  integral,

$$\begin{aligned} & \frac{i}{4\pi^2 z^2} I(t - \alpha z) \int_{x_z=0} d^3 x' \int d^2 \mathbf{x} \gamma_{\text{sp}}(\mathbf{x}, \mathbf{x}') \\ & \times \frac{1}{\sqrt{2\pi}} \int d\omega \alpha^3 \omega^3 W_1(\omega) \delta_\omega(\mathbf{x}') e^{i\alpha\omega(\frac{|\mathbf{r}_\perp-\mathbf{x}'_\perp|^2}{2z} - \frac{|\mathbf{r}_\perp-\mathbf{x}_\perp|^2}{2z})}. \end{aligned}$$

$I(t)$  is the intensity envelope of the pulse. Finally, we have to perform the  $\omega$  integral. The phase factor can be regarded as constant, due to the small bandwidth of a quasi-

monochromatic pulse. Hence, we obtain

$$I(\mathbf{r}, t) = I_{\text{in}}(\mathbf{r}, t) - I(t - \alpha z) \left( \frac{k_{\text{in}}}{2\pi z} \right)^2 2 \operatorname{Re} \left\{ i \int d^3 x' k_{\text{in}} \delta_{\omega_{\text{in}}}(\mathbf{x}') \right. \\ \left. \times \int_{x_z=0} d^2 \mathbf{x} \gamma_{\text{sp}}(\mathbf{x}, \mathbf{x}') e^{\frac{ik_{\text{in}}}{2z} (|\mathbf{r}_{\perp} - \mathbf{x}'_{\perp}|^2 - |\mathbf{r}_{\perp} - \mathbf{x}_{\perp}|^2)} \right\}. \quad (3.24)$$

The intensity of the beam without any scattering can be calculated analogously, yielding the intensity envelope at the retarded time  $t - \alpha z$

$$I_{\text{in}}(\mathbf{r}, t) = I(t - \alpha z) =: I_{\text{in}}(t). \quad (3.25)$$

The spatial coherence function from Eq. (3.12) is independent of  $x'_z$ . The intensity in Eq. (3.24) depends only on the projection  $\int dx'_z \delta_{\omega_{\text{in}}}(\mathbf{x}')$  of  $\delta_{\omega_{\text{in}}}$ . We can introduce the phase shift function  $\varphi$  (cp. Eq. (2.40) in Ref. [31])

$$\varphi(\mathbf{x}'_{\perp}) = -k_{\text{in}} \int dx'_z \delta_{\omega_{\text{in}}}(\mathbf{x}'). \quad (3.26)$$

The expression for the intensity at the detector simplifies to

$$I(\mathbf{r}, t) = I_{\text{in}}(t) \left( 1 + \left( \frac{k_{\text{in}}}{2\pi z} \right)^2 2 \operatorname{Re} \left\{ i \int d^2 \mathbf{x}_{\perp} \int d^2 \mathbf{x}'_{\perp} \varphi(\mathbf{x}'_{\perp}) \right. \right. \\ \left. \left. \times \gamma_{\text{sp}}(\mathbf{x}_{\perp} - \mathbf{x}'_{\perp}) e^{\frac{ik_{\text{in}}}{2z} (|\mathbf{r}_{\perp} - \mathbf{x}'_{\perp}|^2 - |\mathbf{r}_{\perp} - \mathbf{x}_{\perp}|^2)} \right\} \right). \quad (3.27)$$

### 3.2.4. Phase contrast

The phase contrast effect is not obvious from the final expression for the intensity in the Fresnel regime. This subsection presents a derivation (based on [30]) that results in an expression that makes this effect more obvious. We define new variables

$$\mathbf{a} := \frac{1}{2}(\mathbf{x}'_{\perp} + \mathbf{x}_{\perp}) \quad \mathbf{b} := \mathbf{x}_{\perp} - \mathbf{x}'_{\perp}, \quad (3.28)$$

that have the useful property

$$|\mathbf{r}_{\perp} - \mathbf{x}'_{\perp}|^2 - |\mathbf{r}_{\perp} - \mathbf{x}_{\perp}|^2 = x'^2_{\perp} - x^2_{\perp} - 2\mathbf{r}_{\perp} \cdot (\mathbf{x}'_{\perp} - \mathbf{x}_{\perp}) = -2(\mathbf{a} - \mathbf{r}_{\perp}) \cdot \mathbf{b}. \quad (3.29)$$

Inserting the the new variables into Eq. (3.27) we obtain

$$I(\mathbf{r}, t) = I_{\text{in}}(t) \left( 1 + \left( \frac{k_{\text{in}}}{2\pi z} \right)^2 \int d^2 \mathbf{b} \gamma_{\text{sp}}(\mathbf{b}) \right. \\ \left. \times i \int d^2 \mathbf{a} \left[ \varphi(\mathbf{a} - \frac{1}{2}\mathbf{b}) e^{-i\frac{k_{\text{in}}}{z}(\mathbf{a} - \mathbf{r}_{\perp}) \cdot \mathbf{b}} - \varphi(\mathbf{a} - \frac{1}{2}\mathbf{b}) e^{i\frac{k_{\text{in}}}{z}(\mathbf{a} - \mathbf{r}_{\perp}) \cdot \mathbf{b}} \right] \right). \quad (3.30)$$

This can be significantly simplified by redefining the variable  $\mathbf{a} := \mathbf{a} - \frac{1}{2}\mathbf{b}$ , and by subsequently redefining  $\mathbf{b} := -\mathbf{b}$  in the first summand only

$$I(\mathbf{r}, t) = I_{\text{in}}(t) \left( 1 + \left( \frac{k_{\text{in}}}{2\pi z} \right)^2 \int d^2\mathbf{b} \gamma_{\text{sp}}(\mathbf{b}) e^{-i\frac{k_{\text{in}}}{z}\mathbf{r}_{\perp} \cdot \mathbf{b}} \right. \\ \left. \times (-2) \sin\left(\frac{k_{\text{in}}}{2z}b^2\right) \int d^2\mathbf{a} \varphi(\mathbf{a}) e^{i\frac{k_{\text{in}}}{z}\mathbf{a} \cdot \mathbf{b}} \right). \quad (3.31)$$

Evaluating the last integral yields an expression depending on the Fourier transform  $\mathcal{F}\varphi(\mathbf{k})$  of the phase function

$$I(\mathbf{r}, t) = I_{\text{in}}(t) \left( 1 - 4\pi \left( \frac{k_{\text{in}}}{2\pi z} \right)^2 \times \right. \\ \left. \times \int d^2\mathbf{b} \gamma_{\text{sp}}(\mathbf{b}) \sin\left(\frac{k_{\text{in}}}{2z}b^2\right) \mathcal{F}\varphi\left(\frac{k_{\text{in}}}{z}\mathbf{b}\right) e^{-i\frac{k_{\text{in}}}{z}\mathbf{r}_{\perp} \cdot \mathbf{b}} \right). \quad (3.32)$$

We linearize the sine to simplify the previous expressions

$$I(\mathbf{r}, t) = I_{\text{in}}(t) \left( 1 - \frac{k_{\text{in}}^3}{2\pi z^3} \int d^2\mathbf{b} e^{-\mathbf{b}^2/l_c^2} b^2 \mathcal{F}\varphi\left(\frac{k_{\text{in}}}{z}\mathbf{b}\right) e^{-i\frac{k_{\text{in}}}{z}\mathbf{r}_{\perp} \cdot \mathbf{b}} \right). \quad (3.33)$$

The linearization is justified because for a given pixel size  $p$  of the detector one can only image spatial frequencies up to  $\pi/p$  in reciprocal space.  $\tilde{\varphi}$  will then only be measured up to a maximal spatial frequency  $|\mathbf{b}| \leq \frac{\pi z}{k_{\text{in}} p}$ . The argument of the sine has then a maximal value of  $\frac{\pi}{2} \frac{z\lambda_{\text{in}}}{p^2}$ . The resolution for imaging in the Fresnel regime is limited by the pixel size. Requiring the smallest resolvable feature  $D \approx p$  to be in the Fresnel regime  $D^2/z\lambda_{\text{in}} \gtrsim 1$ , yields that the argument of the sine is less than  $\frac{\pi}{2}$ . The last equation can then be expressed as

$$I(\mathbf{r}, t) = I_{\text{in}}(t) \left( 1 - \frac{z}{2\pi k_{\text{in}}} \int d^2\mathbf{b} e^{-z^2\mathbf{b}^2/k_{\text{in}}^2 l_c^2} \mathcal{F}(\nabla^2\varphi)(\mathbf{b}) e^{-i\mathbf{r}_{\perp} \cdot \mathbf{b}} \right) \quad (3.34)$$

and since the Fourier transform takes products into convolutions the last integral evaluates to

$$I(\mathbf{r}, t) = I_{\text{in}}(t) \left( 1 - \frac{z}{\pi k_{\text{in}}} \int d^2\mathbf{y} e^{-\mathbf{y}^2} \nabla^2\varphi\left(\mathbf{r}_{\perp} - \frac{2z}{k_{\text{in}} l_c}\mathbf{y}\right) \right). \quad (3.35)$$

The intensity depends on a convolution of the Laplacian of the phase function and a rapidly decaying Gaussian. In order for the convolution to be constrained to a single pixel of size  $p$ , the spatial coherence length  $l_c$  of the pulse has to be sufficiently large

$$\left( \frac{2z}{k_{\text{in}} p} \right)^2 \ll l_c^2. \quad (3.36)$$

When the convolution evaluates the Laplacian of the phase shift  $\Delta\varphi$  only within a single pixel, we can set the Laplacian of the phase function constant within the pixel

$$\int d^2\mathbf{y} e^{-\mathbf{y}^2} \nabla^2\varphi(\mathbf{r}_\perp - \frac{2z}{k_{\text{in}}l_c}\mathbf{y}) \approx \nabla^2\varphi(\mathbf{r}_\perp) \int d^2\mathbf{y} e^{-\mathbf{y}^2} = \pi\nabla^2\varphi(\mathbf{r}_\perp). \quad (3.37)$$

The final result for the intensity in the Fresnel regime is

$$I(\mathbf{r}, t) = I_{\text{in}}(t) \left( 1 - \frac{z}{k_{\text{in}}^*} \nabla^2\varphi(\mathbf{r}_\perp) \right). \quad (3.38)$$

We have obtained the common expression for the intensity in the Fresnel regime [30, 31]. The intensity is time-dependent but otherwise the result is equal for stationary radiation. We encounter the phase contrast effect, because the Laplacian highlights edges in the phase shift function. There is an intensity pattern, that reflects the shape of the target, although x-ray absorption by the target has been completely neglected. The distance of the detector to the target is important, because the contrast vanishes for  $z \rightarrow 0$ , when the propagation distance is too small.



# Chapter 4.

## Quantum theory of x-ray phase contrast imaging

In this chapter, I present the quantum theory of PCI published in the article [1]:  
SLOWIK, SANTRA *J. Phys. B* **46** 164016 (2013).

### 4.1. Motivation

The tremendous scientific impact of x-ray PCI has been presented in the last chapter. Despite its success there has been no quantum formulation of PCI available. In the last chapter a theoretical formalism for a pulsed x-ray source based on optical scattering was presented. The classical formalism incorporates the matter through the macroscopic index of refraction, disregarding its quantum nature. The interactions of radiation and matter are often subsumed in a phase shift function. The classical formulations of PCI [30, 31, 58–61] have been quite successful so far. However, they completely neglect physical effects like inelastic x-ray scattering. A thorough comprehension of all physical effects certainly makes a modern theoretical fundament of x-ray PCI highly desirable. Only within a formalism without internal contradictions, all possibilities and limitations of the technique may be explored. However, the classical and the semiclassical description of radiation-matter interaction cannot properly account for all physical effects [66, 67]. Most notably, the semiclassical theory cannot correctly describe inelastic Compton scattering [68, 69]. On the other hand, at first thought one might wonder whether the quantum formalism requires a phase operator. From quantum optics it is, however, well known that an observable phase operator is not trivially defined [15, 17].

In this chapter, the theoretical description of PCI is based on a full quantum theory of matter and radiation. The full quantum theory yields an elegant and rigorous formulation of PCI. Thus, the subject whether a semiclassical description may suffice is not touched on. Treating imaging in the near-field (Fresnel) regime by photon scattering is in itself conceptually interesting. The standard approach for x-ray

scattering uses Fermi's golden rule. In this way, the correct scattering probabilities are obtained, but no distinction between near-field and far-field observation is made. How to distinguish between near-field and far-field regime? Why do the transition probabilities from Fermi's golden rule work very well for far-field scattering? A careful analysis of the formalism will clarify these questions. In particular, the crucial role of the observable will be revealed. In the process we will identify suitable observables to describe x-ray PCI.

## 4.2. Formalism and intensity observable

The theoretical formalism introduced in Chapter 2 is used [12, 13]. Before defining the observable, I recall the major points for the reader's convenience.

The electrons of the system are governed by the electronic Hamiltonian  $\hat{H}_{\text{el}}$ , see Eq. (2.21).  $\hat{H}_{\text{el}}$  comprises the kinetic energy of the electrons, the electron-nucleus attraction and the electron-electron repulsion. In second quantization the electrons are excitations of the quantum field  $\hat{\psi}$ . The nuclei are assumed to be fixed in space and we exclusively focus on electron-photon interactions. The Hamiltonian of the free radiation field is  $\hat{H}_{\text{rad}}$ , see Eq. (2.38). The radiation field is described by the vector potential operator  $\hat{\mathbf{A}}$ , which can be expressed in terms of photon creation and annihilation operators as

$$\hat{\mathbf{A}}(\mathbf{x}) = \sum_{\mathbf{k}, \lambda} \sqrt{\frac{2\pi}{V\omega_{\mathbf{k}}\alpha^2}} \left\{ \hat{a}_{\mathbf{k}, \lambda} \boldsymbol{\epsilon}_{\mathbf{k}, \lambda} e^{i\mathbf{k}\cdot\mathbf{x}} + \hat{a}_{\mathbf{k}, \lambda}^\dagger \boldsymbol{\epsilon}_{\mathbf{k}, \lambda}^* e^{-i\mathbf{k}\cdot\mathbf{x}} \right\}. \quad (4.1)$$

The radiation-matter interaction is governed by the minimal coupling Hamiltonian, see Eq. (2.41). At hard x-ray photon energies the scattering is dominated by the  $\mathbf{A}^2$  term. Therefore, we consider the interaction Hamiltonian

$$\hat{H}_{\text{int}} = \frac{\alpha^2}{2} \int d^3x \hat{\psi}^\dagger(\mathbf{x}) \hat{\mathbf{A}}^2(\mathbf{x}) \hat{\psi}(\mathbf{x}). \quad (4.2)$$

Because in a scattering process the number of photons is conserved we take only the photon-number-conserving parts of  $\mathbf{A}^2$  into account. We may neglect the  $\mathbf{p} \cdot \mathbf{A}$  term, since in first-order perturbation theory it describes photon absorption, but phase contrast imaging is usually utilized with weakly absorbing samples. As was discussed in Sec. 2.1.4, in second order perturbation theory the  $\mathbf{p} \cdot \mathbf{A}$  term gives rise to resonant scattering or dispersive corrections. However, at sufficiently high photon energy, away from inner-shell absorption edges, resonant effects are negligible [12].

We describe the evolution of the system in the interaction picture, introduced in Sec. 2.2. We describe the state of the radiation-matter system by a density matrix

$\hat{\rho}$ , which follows the interaction picture time evolution

$$\hat{\rho}(t) = \lim_{t_0 \rightarrow -\infty} \hat{U}(t, t_0) \hat{\rho}_{\text{in}} \hat{U}^\dagger(t, t_0). \quad (4.3)$$

The radiation and matter systems are prepared independently long before the scattering at  $t_0 \rightarrow -\infty$  in the initial state

$$\hat{\rho}_{\text{in}} = \hat{\rho}_{\text{in}}^X \otimes \hat{\rho}_{\text{in}}^{\text{el}}. \quad (4.4)$$

Take the initial state of the electronic system to be a pure state  $|\Psi_{\text{el}}\rangle$

$$\hat{\rho}_{\text{in}}^{\text{el}} = |\Psi_{\text{el}}\rangle \langle \Psi_{\text{el}}|. \quad (4.5)$$

This may either be a stationary state (e.g. the molecular ground state) or a non-stationary state (e.g. an electronic wave packet). The generalization to mixed states (e.g. thermal equilibrium states) is straightforward. The density operator of the incoming x-ray pulse is [12, 17, 70]

$$\hat{\rho}_{\text{in}}^X = \sum_{\{n\}, \{\bar{n}\}} \rho_{\{n\}, \{\bar{n}\}}^X |\{n\}\rangle \langle \{\bar{n}\}|, \quad (4.6)$$

where  $|\{n\}\rangle = \prod_{\mathbf{k}, \lambda} |n_{\mathbf{k}, \lambda}\rangle$  denotes the basis of multimode Fock states.  $\{n\} = (n_{\mathbf{k}_1, 1}, n_{\mathbf{k}_1, 2}, n_{\mathbf{k}_2, 1}, n_{\mathbf{k}_2, 2}, \dots)$  is the set of occupation numbers of all photon modes. The total photon number is  $N = \sum_{\mathbf{k}, \lambda} n_{\mathbf{k}, \lambda}$ . The basis of multimode Fock states is a basis of energy eigenstates  $\hat{H}_{\text{rad}} |\{n\}\rangle = E_{\{n\}} |\{n\}\rangle$ . At this point it is not necessary to specify the exact form of the density operator for the x-ray pulse. The statistical properties of the x-ray pulse will be specified by the first-order correlation function.

As mentioned in the introduction the choice of the observable is essential for describing x-ray PCI. In a typical experimental situation of PCI a Pixel array detector is placed in the x-ray beam. The detector measures incoming intensity or the radiation energy that irradiates each detector pixel. The Poynting operator measures the incident energy per unit area and unit time. The quantum-mechanical Poynting operator is defined by the Hermitian operator [17]

$$\hat{\mathbf{S}}(\mathbf{x}) = \frac{1}{4\pi\alpha} \cdot \frac{1}{2} \left( \hat{\mathbf{E}}^-(\mathbf{x}) \times \hat{\mathbf{B}}^+(\mathbf{x}) - \hat{\mathbf{B}}^-(\mathbf{x}) \times \hat{\mathbf{E}}^+(\mathbf{x}) \right), \quad (4.7)$$

where  $\hat{E}^\pm$  and  $\hat{B}^\pm$  are the the positive and negative frequency parts of the electric and the magnetic field operator as defined in Eqs. (2.35), (2.36). In terms of creation and annihilation operators the Poynting operator may be written as

$$\hat{\mathbf{S}}(\mathbf{x}) = \frac{1}{4V\alpha} \sum_{\mathbf{k}, \lambda} \sum_{\mathbf{l}, \mu} \sqrt{\omega_{\mathbf{k}} \omega_{\mathbf{l}}} \hat{a}_{\mathbf{k}, \lambda}^\dagger \hat{a}_{\mathbf{l}, \mu} (\mathbf{e}_{\mathbf{l}} + \mathbf{e}_{\mathbf{k}}) (\boldsymbol{\epsilon}_{\mathbf{k}, \lambda}^* \cdot \boldsymbol{\epsilon}_{\mathbf{l}, \mu}) e^{-i(\mathbf{k}-\mathbf{l}) \cdot \mathbf{x}}, \quad (4.8)$$

where  $\mathbf{e}_{\mathbf{k}} = \frac{\mathbf{k}}{|\mathbf{k}|}$ . The energy flux through the surface of a detector pixel is a well-motivated choice for an observable. To describe the effective area of the pixel in the incoming radiation beam, let the unit vector  $\mathbf{d}$  be a normal vector to an infinitesimal pixel on the detector. We describe intensity measurements of the detector at position  $\mathbf{r}$  by the observable

$$\hat{\mathcal{O}} = \hat{\mathbf{S}}(\mathbf{r}) \cdot \mathbf{d} . \quad (4.9)$$

This observable evolves in time according to  $\hat{\mathcal{O}}(t) = e^{i\hat{H}_{\text{rad}}t} \hat{\mathcal{O}} e^{-i\hat{H}_{\text{rad}}t}$ . The expectation value at time  $t$  is

$$\langle \hat{\mathcal{O}} \rangle_t = \text{Tr}(\hat{\rho}(t)\hat{\mathcal{O}}(t)) . \quad (4.10)$$

In the following, we use the short-hand notation

$$I(\mathbf{r}, t) = \langle \hat{\mathbf{S}}(\mathbf{r}) \cdot \mathbf{d} \rangle_t \quad (4.11)$$

for the expectation value of the intensity observable.

Note that this observable is in general different from the usual photoelectric detection probability  $\hat{E}^- \hat{E}^+$  [15, 71] because it depends on the propagation direction of the photon modes. However, under the assumptions made in this work the differences in the result are negligible [17].

### 4.3. The (0,1) term of the Poynting operator

The time evolution operator  $\hat{U}(t, t_0)$  satisfies  $i\frac{\partial}{\partial t}\hat{U}(t, t_0) = \hat{H}_{\text{int}}(t)\hat{U}(t, t_0)$ . We employ first-order perturbation theory with respect to  $\hat{H}_{\text{int}}$  as introduced in Sec. 2.2.2. The first-order perturbation theory corresponds to the first Born approximation in the classical derivation. In consequence x-ray photons are scattered only once from the electronic system, which is a useful approximation for weak scatterers. The time evolution operator expanded to first-order is

$$\lim_{t_0 \rightarrow -\infty} \hat{U}(t, t_0) = \hat{1} - i \int_{-\infty}^t dt' e^{i\hat{H}_0 t'} \hat{H}_{\text{int}} e^{-i\hat{H}_0 t'} , \quad (4.12)$$

where  $\hat{H}_0 = \hat{H}_{\text{el}} + \hat{H}_{\text{rad}}$ . The expectation value of the intensity observable  $\hat{\mathcal{O}} = \hat{\mathbf{S}}(\mathbf{r}) \cdot \mathbf{d}$  becomes, cf. Eq. (2.77),

$$I(\mathbf{r}, t) = \text{Tr}(\hat{\rho}_{\text{in}}\hat{\mathcal{O}}(t)) + 2 \text{Re} \left\{ i \int_{-\infty}^t dt' \text{Tr}[\hat{\rho}_{\text{in}}\hat{H}_{\text{int}}(t')\hat{\mathcal{O}}(t)] \right\} \quad (4.13)$$

$$\begin{aligned} &+ \int_{-\infty}^t \int_{-\infty}^t dt' dt'' \text{Tr}[\hat{H}_{\text{int}}(t'')\hat{\rho}_{\text{in}}\hat{H}_{\text{int}}(t')\hat{\mathcal{O}}(t)] \\ &= I_{\text{in}}(t) + I_{\varphi}(t) + \text{higher order terms} . \end{aligned} \quad (4.14)$$

We remark that setting the adiabatic switching parameter  $\epsilon$  to zero does not affect the results.

The (0,0) term is the first term in Eq. (4.13), denoted by  $I_{\text{in}}(t)$ . We can directly identify  $I_{\text{in}}(t)$  as the expectation value of the (instantaneous) intensity in the initial state. Because there is no interaction or scattering involved,  $I_{\text{in}}(t)$  describes the intensity of the incoming x-ray field.

The (0,1) term is the second term in Eq. (4.13), denoted by  $I_{\varphi}(t)$ . We will demonstrate that  $I_{\varphi}(t)$  accounts for the phase contrast effect. In particular, we will show that the expectation value  $I(\mathbf{r}, t) = I_{\text{in}}(t) + I_{\varphi}(t)$  depends on the electron density of the sample and how it is highlighted when the detector is placed in the near-field. Matrix elements of the form  $\langle S | \hat{O}(t) | I \rangle$  describe the measurement of the interference of the two states  $|I\rangle$  and  $|S\rangle$  by the observable  $\hat{O}$ .  $I_{\varphi}$  describes the intensity pattern due to the interference of the incoming and scattered x-ray fields. In order that  $I_{\varphi}$  does not vanish, it is crucial that the observable can simultaneously detect the incoming and the scattered fields.

The (1,1) term is the last term in Eq. (4.13). It is a term of higher order in  $\alpha^2$ . Thus, with respect to the (0,0) and (0,1) term, the (1,1) term can be neglected. This is consistent with the physical situation of near field imaging, where the detector is placed in the illuminated beam. However, it is important to note that this term is responsible for the intensity distribution of the scattered light in the far field, as will be discussed in Chapter 6.

Now, we demonstrate that  $I_{\varphi}$  describes the phase contrast effect. Because the electronic state of the system remains unobserved we can separate electronic and radiation degrees of freedom. Inserting the Hamiltonian, the initial state, and the observable – given in Eqs. (4.2), (4.4), (4.9) – the matrix element can be written

$$\begin{aligned} \text{Tr}(\hat{\rho}_{\text{in}} \hat{H}_{\text{int}}(t') \hat{O}(t)) &= \frac{\alpha^2}{2} \int d^3 x' \langle \Psi_{\text{el}} | e^{i\hat{H}_{\text{el}} t'} \hat{\psi}^\dagger(\mathbf{x}') \hat{\psi}(\mathbf{x}') e^{-i\hat{H}_{\text{el}} t'} | \Psi_{\text{el}} \rangle \\ &\times \text{Tr}_{\text{rad}} \left( \rho_{\text{in}}^X e^{i\hat{H}_{\text{rad}} t'} \hat{\mathbf{A}}^2(\mathbf{x}') e^{-i\hat{H}_{\text{rad}}(t'-t)} \hat{\mathbf{S}}(\mathbf{r}) \cdot \mathbf{d} e^{-i\hat{H}_{\text{rad}} t} \right), \end{aligned} \quad (4.15)$$

where  $\text{Tr}_{\text{rad}}$  denotes the trace of the radiation system only. As a first result, we obtain that  $I_{\varphi}$  depends on the electronic system only via the electron density

$$\rho(\mathbf{x}', t') = \langle \Psi_{\text{el}} | e^{i\hat{H}_{\text{el}} t'} \hat{\psi}^\dagger(\mathbf{x}') \hat{\psi}(\mathbf{x}') e^{-i\hat{H}_{\text{el}} t'} | \Psi_{\text{el}} \rangle. \quad (4.16)$$

This means electronic excitations do not contribute to the interference term  $I_{\varphi}$ . Therefore,  $I_{\varphi}$  contains only contributions from electronically elastic scattering. Remarkably, for this interaction Hamiltonian this is a simple consequence of the fact that the observable does not act on the electronic state.

The right hand side of (4.15) can be related to the statistical properties of the incoming radiation field. Assuming that a scalar description of the radiation system

is sufficient, let the incoming x-ray field have a mean wave vector  $\mathbf{k}_{\text{in}}$  with  $|\mathbf{k}_{\text{in}}| = k_{\text{in}} = \alpha\omega_{\text{in}}$  and a mean polarization vector  $\boldsymbol{\epsilon}_{\text{in}} = \boldsymbol{\epsilon}_{\mathbf{k}_{\text{in}},\lambda_{\text{in}}}$ . Then we can use the simplified first-order correlation function of the incoming radiation field [15, 17, 70, 71]

$$G^{(1)}(\mathbf{x}', t', \mathbf{r}, t) \equiv \text{Tr}(\hat{\rho}_{\text{in}}^X \hat{\mathbf{E}}^-(\mathbf{x}', t') \hat{\mathbf{E}}^+(\mathbf{r}, t)) \quad (4.17)$$

$$= \frac{2\pi\omega_{\text{in}}}{V} \sum_{\mathbf{k},\lambda} \sum_{\mathbf{l},\mu} \text{Tr}(\hat{\rho}_{\text{in}}^X \hat{a}_{\mathbf{k},\lambda}^\dagger \hat{a}_{\mathbf{l},\mu}) e^{i(\omega_{\mathbf{k}}t' - \mathbf{k}\cdot\mathbf{x}')} e^{-i(\omega_{\mathbf{l}}t - \mathbf{l}\cdot\mathbf{r})}. \quad (4.18)$$

Furthermore we assume: i) that the incoming x-ray field has a small bandwidth; ii) that all modes propagate with small angular spread in the direction  $\mathbf{e}_{\text{in}} = \frac{\mathbf{k}_{\text{in}}}{|\mathbf{k}_{\text{in}}|}$ ; and iii) that they are equally polarized, i.e.,

$$\omega_{\mathbf{k}} \approx \omega_{\text{in}} \approx \omega_{\mathbf{l}}, \quad \mathbf{e}_{\mathbf{k}} \approx \mathbf{e}_{\text{in}} \approx \mathbf{e}_{\mathbf{l}}, \quad \boldsymbol{\epsilon}_{\mathbf{k},\lambda} \approx \boldsymbol{\epsilon}_{\text{in}} \approx \boldsymbol{\epsilon}_{\mathbf{l},\mu}. \quad (4.19)$$

Now, we can express (4.15) in terms of the first-order correlation function:

$$\begin{aligned} \text{Tr}(\hat{\rho}_{\text{in}} \hat{H}_{\text{int}}(t') \hat{\mathcal{O}}(t)) &= \sum_{\mathbf{k},\lambda} \int d^3x' \rho(\mathbf{x}', t') e^{-i\mathbf{k}\cdot(\mathbf{r}-\mathbf{x}')} e^{i\omega_{\mathbf{k}}(t-t')} \\ &\quad \times |\boldsymbol{\epsilon}_{\text{in}}^* \cdot \boldsymbol{\epsilon}_{\mathbf{k},\lambda}|^2 (\mathbf{e}_{\mathbf{k}} + \mathbf{e}_{\text{in}}) \cdot \mathbf{d} \\ &\quad \times \frac{1}{4Vk_{\text{in}}} G^{(1)}(\mathbf{x}', t', \mathbf{r}, t). \end{aligned} \quad (4.20)$$

The detailed derivation of this expression can be found in Appendix 4.A.

From (4.20) it follows that the interference term  $I_\varphi$  depends on the correlation function at position and time of the scattering event  $(\mathbf{x}', t')$  and the measurement  $(\mathbf{r}, t)$ . We encounter the same problem as in the classical derivation in Chapter 3, namely that this correlation is usually unknown. Typically, only the correlation function in a plane can be determined experimentally. However, as in Sec. 3.2.3, we can use the propagation properties of  $G^{(1)}$  [15, 72] to determine  $G^{(1)}(\mathbf{x}', t', \mathbf{r}, t)$ . We then only need to know  $G^{(1)}$  in one plane. We call this plane the exit plane, and choose it perpendicular to the propagation direction and close to the object, see Fig. 4.1. We think of the exit plane to be right behind the object for macroscopic (or mesoscopic) objects. For continuous electron densities of microscopic objects like single atoms or molecules, we may use any plane that is close to (or within) the maximal density. We choose the coordinates system such that the exit plane has  $x_z = 0$ . The projection of any vector  $\mathbf{x} = (x_x, x_y, x_z) = (\mathbf{x}_\perp, x_z)$  onto the exit plane is  $(\mathbf{x}_\perp, 0)$ .

As in the previous chapter, we use the correlation function of a quasi-stationary, quasi-monochromatic field, see Sec. 3.2.2. This is a good choice for x-ray free electron laser pulses or synchrotron radiation. In the exit plane it has the form [64]

$$G^{(1)}(\mathbf{x}', t_1, \mathbf{x}, t_2) = 4\pi\alpha I\left(\frac{t_1+t_2}{2}\right) \gamma_{\text{sp}}(|\mathbf{x}_\perp - \mathbf{x}'_\perp|) \gamma_{\text{tp}}(t_1 - t_2), \quad (4.21)$$

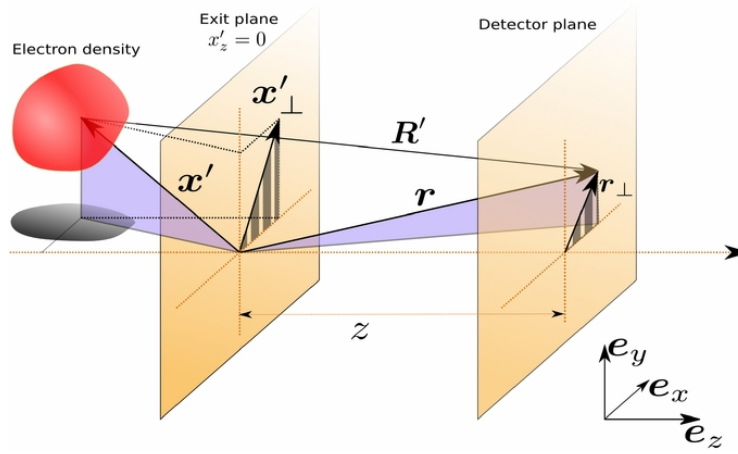


Figure 4.1.: An illustration of the chosen coordinates. Position vectors within the electron density distribution of the sample are denoted by  $\mathbf{x}'$ , and their projection onto the exit plane directly behind the object is denoted by  $\mathbf{x}'_{\perp}$ . The detector is placed at  $\mathbf{r}$ , at a distance  $z$  in the direction of propagation and  $\mathbf{r}_{\perp}$  perpendicular to it.  $\mathbf{R}'$  is the direction from the point of scattering to the detector.

Figure taken from (Slowik, Santra J. Phys. B **46**, 164016) [1].

© 2013 IOP Publishing Ltd.

where  $I$  denotes the average intensity, and  $\gamma_{\text{sp}}$  and  $\gamma_{\text{tp}}$  denote the spatial and temporal coherence functions, respectively. Recall, we assume the coherence time  $\tau_c$  to be much shorter than the pulse duration. The spectral bandwidth of the radiation field is  $\Delta\omega = 1/\tau_c$ . The width of the spatial coherence function is called the coherence length  $l_c$ .

Let the detector be placed at the position  $\mathbf{r} = (\mathbf{r}_{\perp}, z)$ . It is crucial that the detector is in the near-field (Fresnel) regime of the object. Then,  $G^{(1)}(\mathbf{x}', t', \mathbf{r}, t)$  [see (4.34)] can be determined by Fresnel propagation.

The sum over all photon modes  $(\mathbf{k}, \lambda)$  in (4.20) describes photons scattered in all directions. This is a consequence of the Poynting operator, which is able to detect all photon modes. We make no assumptions on the scattering angles of the photons. In general, there is no constraint to small scattering angles following from the form factors of single atoms. A careful analysis of (4.20), performed in Appendix 4.C, reveals that only photon modes contribute, that are scattered directly towards the detector. That is, in the limit  $\lambda_{\text{in}} \ll z$ , the wave vector points directly to the detector. Moreover, polarization effects are negligible if the detector is placed paraxially (at small angles from the optical axis) downstream from the sample. In case the initial electronic state is not a stationary state, we assume the electron density to

vary slowly on time scales of the coherence time of the pulse.

Finally, we insert the model for  $G^{(1)}$  and (4.20) into the expression for  $I_\varphi$  in Eq. (4.13). This yields the phase-contrast term

$$I_\varphi(t) = 2 \operatorname{Re} \left\{ i \frac{\alpha^2 k_{\text{in}}}{2\pi z^2} I_{\text{in}}(t) \int d^3 x' \rho(\mathbf{x}', t - \alpha z) \right. \\ \left. \times \int d^2 x_\perp \gamma_{\text{sp}}(|\mathbf{x}_\perp - \mathbf{x}'_\perp|) e^{\frac{i k_{\text{in}}}{2z} (|\mathbf{r}_\perp - \mathbf{x}_\perp|^2 - |\mathbf{r}_\perp - \mathbf{x}'_\perp|^2)} \right\}, \quad (4.22)$$

where  $I_{\text{in}}(t) = I(t - \alpha z) \mathbf{e}_{\text{in}} \cdot \mathbf{d}$  is the intensity of the incoming radiation. Observe, that finally we have obtained an expression for  $I_\varphi$  that is equivalent to the classical expression, cf. Eq. (3.24). According to (4.22), PCI encodes the projection of the expectation value of the electron density  $\rho_\perp(\mathbf{x}_\perp, t) = \int dx_z \rho(\mathbf{x}, t)$ .

As in the classical theory, one can recast (4.22) into a term that highlights the density distribution of the target. The same arguments as in Sec. 3.2.4 yield (cf. Sec. 4.2 in [30])

$$I_\varphi(t) = \frac{2\pi\alpha^2 z}{k_{\text{in}}^2} I_{\text{in}}(t) \nabla^2 \rho_\perp(\mathbf{r}_\perp, t - \alpha z). \quad (4.23)$$

PCI yields a real space image, where edges of the projected electron density distribution are particularly emphasized. We may express the electron density by the phase shift function  $\varphi$  [31, 63]

$$\rho_\perp(\mathbf{r}_\perp, t) = -\frac{k_{\text{in}}}{2\pi\alpha^2} \varphi(\mathbf{r}_\perp, t). \quad (4.24)$$

This recovers the classical expression of PCI (Eq. (3.38)) as the expectation value of a suitable intensity observable in the full quantum theory

$$I(\mathbf{r}, t) = I_{\text{in}}(t) + I_\varphi(t) = I_{\text{in}}(t) \left\{ 1 - \frac{z}{k_{\text{in}}} \nabla^2 \varphi(\mathbf{r}_\perp, t - \alpha z) \right\}. \quad (4.25)$$

## 4.A. Calculation of the matrix element

In this appendix, it is shown how the right hand side of Eq. (4.15) can be expressed in terms of  $G^{(1)}$ . To simplify the trace term

$$\operatorname{Tr}_{\text{rad}} \left( \rho_{\text{in}}^X e^{i\hat{H}_{\text{rad}} t'} \hat{\mathbf{A}}^2(\mathbf{x}') e^{-i\hat{H}_{\text{rad}}(t'-t)} \hat{\mathbf{S}}(\mathbf{r}) \cdot \mathbf{d} e^{-i\hat{H}_{\text{rad}} t} \right)$$

we insert the expansions of  $\hat{\mathbf{A}}^2$  and  $\hat{\mathbf{S}}(\mathbf{r}) \cdot \mathbf{d}$  in terms of creation and annihilation operators, given in (4.1) and (4.8). We express the initial state in the basis of

multimode Fock states, see Eq. (4.6). Moreover, we consider only the normal ordered one-photon contributions from  $\hat{\mathbf{A}}^2$ .

The matrix elements that appear have the form

$$\begin{aligned}
 & \sum_{\{\bar{n}\},\{n\}} \rho_{\{n\},\{\bar{n}\}}^X \langle \{\bar{n}\} | e^{i\hat{H}_{\text{rad}}t'} \hat{\mathbf{A}}^2(\mathbf{x}') e^{-iH_{\text{rad}}(t'-t)} \hat{\mathbf{S}}(\mathbf{r}) \cdot \mathbf{d} e^{-i\hat{H}_{\text{rad}}t} | \{n\} \rangle \\
 &= \frac{\pi}{V^2 \alpha^3} \sum_{\mathbf{p},\alpha} \sum_{\mathbf{q},\beta} \sum_{\mathbf{k},\lambda} \sum_{\mathbf{l},\mu} \sqrt{\frac{\omega_{\mathbf{k}}\omega_{\mathbf{l}}}{\omega_{\mathbf{p}}\omega_{\mathbf{q}}}} e^{i(\mathbf{q}-\mathbf{p})\cdot\mathbf{x}'} e^{-i(\mathbf{k}-\mathbf{l})\cdot\mathbf{r}} e^{i(E_{\{\bar{n}\}}t' - E_{\{n\}}t)} \\
 & \quad \times e^{-i(E_{\{n\}} - \omega_1 + \omega_{\mathbf{k}})(t'-t)} \langle \{\bar{n}\} | \hat{a}_{\mathbf{p},\alpha}^\dagger \hat{a}_{\mathbf{q},\beta} \hat{a}_{\mathbf{k},\lambda}^\dagger \hat{a}_{\mathbf{l},\mu} | \{n\} \rangle \\
 & \quad \times (\boldsymbol{\epsilon}_{\mathbf{p},\alpha}^* \cdot \boldsymbol{\epsilon}_{\mathbf{q},\beta}) (\boldsymbol{\epsilon}_{\mathbf{k},\lambda}^* \cdot \boldsymbol{\epsilon}_{\mathbf{l},\mu}) (\mathbf{e}_{\mathbf{k}} + \mathbf{e}_{\mathbf{l}}) \cdot \mathbf{d} .
 \end{aligned} \tag{4.26}$$

The nonzero contributions give rise to phase factors

$$e^{i(E_{\{\bar{n}\}}t' - E_{\{n\}}t)} e^{-i(E_{\{n\}} - \omega_1 + \omega_{\mathbf{k}})(t'-t)} = e^{i((\omega_{\mathbf{p}} - \omega_{\mathbf{q}})t' + (\omega_{\mathbf{k}} - \omega_1)t)} . \tag{4.27}$$

Applying the commutation relations from Eq. (2.37) yields

$$\begin{aligned}
 \text{Tr}(\hat{\rho}_{\text{in}} \hat{H}_{\text{int}}(t') \hat{\mathcal{O}}(t)) &= \frac{\pi}{2V^2 \alpha} \sum_{\mathbf{p},\alpha} \sum_{\mathbf{q},\beta} \sum_{\mathbf{k},\lambda} \sum_{\mathbf{l},\mu} \int d^3x' \rho(\mathbf{x}', t') \\
 & \quad \times \sqrt{\frac{\omega_{\mathbf{k}}\omega_{\mathbf{l}}}{\omega_{\mathbf{p}}\omega_{\mathbf{q}}}} e^{i((\omega_{\mathbf{p}} - \omega_{\mathbf{q}})t' + (\omega_{\mathbf{k}} - \omega_1)t)} e^{i(\mathbf{q}-\mathbf{p})\cdot\mathbf{x}'} e^{-i(\mathbf{k}-\mathbf{l})\cdot\mathbf{r}} \\
 & \quad \times \left[ \text{Tr} \left( \hat{\rho}_{\text{in}}^X \hat{a}_{\mathbf{p},\alpha}^\dagger \hat{a}_{\mathbf{k},\lambda}^\dagger \hat{a}_{\mathbf{q},\beta} \hat{a}_{\mathbf{l},\mu} \right) + \delta_{\mathbf{k},\mathbf{q}} \delta_{\lambda,\beta} \text{Tr} \left( \hat{\rho}_{\text{in}}^X \hat{a}_{\mathbf{p},\alpha}^\dagger \hat{a}_{\mathbf{l},\mu} \right) \right] \\
 & \quad \times (\boldsymbol{\epsilon}_{\mathbf{p},\alpha}^* \cdot \boldsymbol{\epsilon}_{\mathbf{q},\beta}) (\boldsymbol{\epsilon}_{\mathbf{k},\lambda}^* \cdot \boldsymbol{\epsilon}_{\mathbf{l},\mu}) (\mathbf{e}_{\mathbf{k}} + \mathbf{e}_{\mathbf{l}}) \cdot \mathbf{d} .
 \end{aligned} \tag{4.28}$$

First, we take a look at the term with  $\delta_{\mathbf{k},\mathbf{q}} \delta_{\lambda,\beta} \text{Tr}(\hat{\rho}_{\text{in}}^X \hat{a}_{\mathbf{p},\alpha}^\dagger \hat{a}_{\mathbf{l},\mu})$ . The summation over  $\mathbf{q}, \beta$  can be performed. Combined with the assumptions in (4.19) the trace term gives the first order correlation function of the field  $G^{(1)}$ . Thus, this term yields the desired Eq. (4.20). Finally, we analyze the term with  $\text{Tr}(\hat{\rho}_{\text{in}}^X \hat{a}_{\mathbf{p},\alpha}^\dagger \hat{a}_{\mathbf{k},\lambda}^\dagger \hat{a}_{\mathbf{q},\beta} \hat{a}_{\mathbf{l},\mu})$ . One finds that an interchange of the indices  $(\mathbf{p}, \alpha)$  with  $(\mathbf{q}, \beta)$  and  $(\mathbf{k}, \lambda)$  with  $(\mathbf{l}, \mu)$  corresponds to complex conjugation of the summand. In the last step, one uses the trace property  $\text{Tr}(\hat{\rho} \hat{A}) = \text{Tr}(\hat{\rho} \hat{A}^\dagger)^*$ , where  $\hat{A}$  is any operator. As a consequence, each summand and its complex conjugate are added, resulting in a real sum. This term does not contribute to  $I_\varphi$ , because of the imaginary factor in the real part.

## 4.B. Propagation of the correlation function

The Fourier transform of  $G^{(1)}$  is called the (two frequency) cross spectral density [73]

$$\mathcal{W}^{(1)}(\mathbf{x}', \omega_1, \mathbf{x}, \omega_2) = \frac{1}{2\pi} \iint dt_1 dt_2 G^{(1)}(\mathbf{x}', t_1, \mathbf{x}, t_2) e^{i(\omega_2 t_2 - \omega_1 t_1)} . \tag{4.29}$$

We recall from Sec. 3.2.2 that the cross spectral density in the quasi-stationary model has the form [64, 65]

$$\mathcal{W}^{(1)}(\mathbf{x}', \omega + \frac{\bar{\omega}}{2}, \mathbf{x}, \omega - \frac{\bar{\omega}}{2}) = 4\pi\alpha \gamma_{\text{sp}}(|\mathbf{x}_{\perp} - \mathbf{x}'_{\perp}|) W_1(\omega) W_2(\bar{\omega}), \quad (4.30)$$

where  $W_1$  is the Fourier transform of  $\gamma_{\text{tp}}$ , and  $W_2$  is the Fourier transform of the pulse  $I(t)$ .

In vacuum the cross spectral density  $\mathcal{W}^{(1)}(\mathbf{x}', \omega_1, \mathbf{r}_{\perp}, \omega_2)$  has to satisfy the homogeneous wave equation, like the classical cross spectral density. We can describe the propagation of  $\mathcal{W}^{(1)}$  in the second pair of variables by a Rayleigh-Sommerfeld diffraction integral [15, 72]. We use this to determine  $\mathcal{W}^{(1)}$  at the point  $\mathbf{r} = (\mathbf{r}_{\perp}, z)$  from its values in the exit plane

$$\mathcal{W}^{(1)}(\mathbf{x}', \omega_1, \mathbf{r}, \omega_2) = -\frac{1}{2\pi} \int_{x_z=0} d^2x_{\perp} \mathcal{W}^{(1)}(\mathbf{x}', \omega_1, \mathbf{x}, \omega_2) \frac{\partial}{\partial z} \left[ \frac{e^{ik_2|\mathbf{r}-\mathbf{x}|}}{|\mathbf{r}-\mathbf{x}|} \right]. \quad (4.31)$$

In analogy to the classical theory, we assume the detector in the Fresnel regime

$$\frac{\partial}{\partial z} \frac{e^{ik_{\text{in}}|\mathbf{r}-\mathbf{x}|}}{|\mathbf{r}-\mathbf{x}|} \approx \frac{ik_{\text{in}}}{z} e^{ik_{\text{in}} \left( z + \frac{|\mathbf{r}_{\perp} - \mathbf{x}_{\perp}|^2}{2z} \right)}, \quad (4.32)$$

is valid for  $k_{\text{in}} = \alpha\omega_{\text{in}}$ . We assume as well a thin object

$$\mathcal{W}^{(1)}(\mathbf{x}', \omega_1, \mathbf{r}, \omega_2) = e^{-ik_1 x'_z} \mathcal{W}^{(1)}(\mathbf{x}'_{\perp}, \omega_1, \mathbf{r}_{\perp}, \omega_2). \quad (4.33)$$

Moreover, we assume that the coherence time is large enough that the pulse is quasi-monochromatic  $\Delta\omega/\omega_{\text{in}} \ll 1$  and that  $\alpha\Delta\omega \frac{|\mathbf{r}_{\perp} - \mathbf{x}_{\perp}|^2}{2z} \ll 1$ . Combining these assumptions we get the first-order correlation function from  $\mathcal{W}^{(1)}$

$$\begin{aligned} G^{(1)}(\mathbf{x}', t', \mathbf{r}, t) &= -2i\alpha \frac{k_{\text{in}}}{z} e^{-ik_{\text{in}} x'_z} I\left(\frac{t+t'-\alpha z}{2}\right) \gamma_{\text{tp}}(t' - t + \alpha z) \\ &\times \int_{x_z=0} d^2x_{\perp} \gamma_{\text{sp}}(|\mathbf{x}_{\perp} - \mathbf{x}'_{\perp}|) e^{\frac{ik_{\text{in}}}{2z} |\mathbf{r}_{\perp} - \mathbf{x}_{\perp}|^2}. \end{aligned} \quad (4.34)$$

## 4.C. Calculation of the phase contrast term

We calculate the phase-contrast term  $I_{\varphi}$

$$I_{\varphi}(t) = 2 \operatorname{Re} \left\{ i \int_{-\infty}^t dt' \operatorname{Tr}[\hat{\rho}_{\text{in}} \hat{H}_{\text{int}}(t') \hat{O}(t)] \right\}.$$

The appearing trace term has been simplified in Eq. (4.20) and depends on the first-order correlation function  $G^{(1)}(\mathbf{x}', t', \mathbf{r}, t)$ . In Appendix 4.A we have determined  $G^{(1)}(\mathbf{x}', t', \mathbf{r}, t)$  from its values in the exit plane given in Eq. (4.21).

When inserting the correlation function in Eq. (4.34) into Eq. (4.20) the time integral has the form

$$\int_{-\infty}^t dt' \rho(\mathbf{x}', t') I\left(\frac{t+t'-\alpha z}{2}\right) \gamma_{\text{tp}}(t' - t + \alpha z) e^{i\omega_{\mathbf{k}}(t-t')}.$$

The temporal coherence function  $\gamma_{\text{tp}}$  vanishes for times much larger than  $\tau_c$ . We assume that the pulse intensity and the electron density vary slowly on the time scale  $\tau_c$ . Then we have  $I\left(\frac{t+t'-\alpha z}{2}\right)\rho(\mathbf{x}', t') \approx I(t - \alpha z)\rho(\mathbf{x}', t - \alpha z)$ , because  $\gamma_{\text{tp}}$  is centered around  $t' = t - \alpha z$ . Moreover, the temporal coherence function  $\gamma_{\text{tp}}$  decays fast enough to treat the time integral as the Fourier transform  $W_1$  of  $\gamma_{\text{tp}}$ . The fast decay of  $\gamma_{\text{tp}}$  in the last step is satisfied if the distance of the detector is much larger than the path covered by the radiation in the time  $\tau_c$ , i.e.,  $\alpha z \gg \tau_c$ .

Letting the quantization volume approach infinity, we replace  $\sum_{\mathbf{k}}$  by  $\frac{V}{(2\pi)^3} \int d^3k$ . Thus

$$I_\varphi = 2 \operatorname{Re} \left\{ \frac{\alpha\sqrt{2\pi}}{2(2\pi)^3} I(t - \alpha z) \int d^3x' \rho(\mathbf{x}', t - \alpha z) F(\mathbf{x}') \int d^3k G(\mathbf{k}, \mathbf{x}') \right\}, \quad (4.35)$$

where

$$F(\mathbf{x}') = z^{-1} e^{-ik_{\text{in}}x'_z} \int d^2x_\perp e^{ik_{\text{in}} \frac{|\mathbf{r}_\perp - \mathbf{x}_\perp|^2}{2z}} \gamma_{\text{sp}}(|\mathbf{x}_\perp - \mathbf{x}'_\perp|) \quad (4.36)$$

$$G(\mathbf{k}, \mathbf{x}') = W_1(\omega_{\mathbf{k}}) e^{i\omega_{\mathbf{k}}\alpha z} e^{-i\mathbf{k}\cdot(\mathbf{r}-\mathbf{x}')} \sum_{\lambda} |\boldsymbol{\epsilon}_{\text{in}}^* \cdot \boldsymbol{\epsilon}_{\mathbf{k},\lambda}|^2 (\mathbf{e}_{\mathbf{k}} + \mathbf{e}_{\text{in}}) \cdot \mathbf{d}. \quad (4.37)$$

Finally, we only have to perform the integration over all wavevectors  $\mathbf{k}$ , which represent photons scattered in all directions. We will now see that only photons scattered directly into the detector contribute. Because we consider only forward scattering, we can write  $\mathbf{k} = \alpha\omega_{\mathbf{k}}(\kappa_x, \kappa_y, \sqrt{1 - \kappa_x^2 - \kappa_y^2})$ , with  $\kappa_x = \frac{k_x}{\alpha\omega_{\mathbf{k}}}$  and  $\kappa_y = \frac{k_y}{\alpha\omega_{\mathbf{k}}}$ . The integral over  $\mathbf{k}$  becomes

$$\begin{aligned} \int d^3k G(\mathbf{k}, \mathbf{x}') &= \int d\omega_{\mathbf{k}} \alpha^3 \omega_{\mathbf{k}}^2 W_1(\omega_{\mathbf{k}}) e^{i\omega_{\mathbf{k}}\alpha z} \\ &\times \iint_{\sqrt{\kappa_x^2 + \kappa_y^2} \leq 1} d\kappa_x d\kappa_y \frac{\sum_{\lambda} |\boldsymbol{\epsilon}_{\text{in}}^* \cdot \boldsymbol{\epsilon}_{\mathbf{k},\lambda}|^2 (\mathbf{e}_{\mathbf{k}} + \mathbf{e}_{\text{in}}) \cdot \mathbf{d}}{\sqrt{1 - \kappa_x^2 - \kappa_y^2}} e^{-i\alpha\omega_{\mathbf{k}}R' \mathbf{e}_{\mathbf{k}} \cdot \mathbf{e}_{\mathbf{R}'}} , \end{aligned} \quad (4.38)$$

where we denoted  $\mathbf{R}' = \mathbf{r} - \mathbf{x}'$  and  $R' = |\mathbf{R}'|$ . The double integral can be treated with the method of stationary phase [e.g., see Sec. 3.3.4. in [15]]. In the limit  $\alpha\omega_{\mathbf{k}}R' \rightarrow \infty$ , when the detector is many wavelengths away from the object, we find that only the wave vectors  $\mathbf{k}$  pointing in the direction  $\mathbf{R}'/R'$  contribute. We obtain

$$\int d^3k G(\mathbf{k}, \mathbf{x}') = 2\pi i \int d\omega_{\mathbf{k}} \alpha^2 \omega_{\mathbf{k}} W_1(\omega_{\mathbf{k}}) e^{i\omega_{\mathbf{k}}\alpha z} \times \sum_{\lambda} |\boldsymbol{\epsilon}_{\text{in}}^* \cdot \boldsymbol{\epsilon}_{\mathbf{R}',\lambda}|^2 (\mathbf{e}_{\mathbf{R}'} + \mathbf{e}_{\text{in}}) \cdot \mathbf{d} \frac{e^{-i\alpha\omega_{\mathbf{k}}R'}}{R'}. \quad (4.39)$$

In the last expression, we used that the polarization vectors  $\boldsymbol{\epsilon}_{\mathbf{k},\lambda}$  and the directions  $\mathbf{e}_{\mathbf{k}}$  depend only on  $\mathbf{k}/k$ . We denote by  $\boldsymbol{\epsilon}_{\mathbf{R}',\lambda}$  and  $\mathbf{e}_{\mathbf{R}',\lambda}$  the polarization and direction vectors for a wave vector  $\mathbf{k}$  pointing in the direction  $\mathbf{R}'/R'$ . Because the x-ray pulse is sufficiently monochromatic  $W_1(\omega_{\mathbf{k}})$  is centered at  $\omega_{\text{in}}$  with narrow width  $\Delta\omega$ , such that  $\alpha\Delta\omega \frac{|\mathbf{r}_{\perp} - \mathbf{x}'_{\perp}|^2}{2z} \ll 1$ . Application of the Fresnel approximation

$$R'^{-1} e^{-i\alpha\omega_{\mathbf{k}}R'} \approx z^{-1} e^{-i\alpha\omega_{\mathbf{k}}(z - x'_z + \frac{|\mathbf{r}_{\perp} - \mathbf{x}'_{\perp}|^2}{2z})}, \quad (4.40)$$

yields

$$\int d^3k G(\mathbf{k}, \mathbf{x}') = (\sqrt{2\pi})^3 \frac{i\alpha^2 \omega_{\text{in}}}{z} e^{ik_{\text{in}}\alpha x'_z} e^{-i\alpha\omega_{\text{in}} \frac{|\mathbf{r}_{\perp} - \mathbf{x}'_{\perp}|^2}{2z}} \times \sum_{\lambda} |\boldsymbol{\epsilon}_{\text{in}}^* \cdot \boldsymbol{\epsilon}_{\mathbf{R}',\lambda}|^2 (\mathbf{e}_{\mathbf{R}'} + \mathbf{e}_{\text{in}}) \cdot \mathbf{d} \quad (4.41)$$

Making the paraxial approximation, suitable for typical experiments, we assume  $\mathbf{R}' = \mathbf{r} - \mathbf{x}' = \mathbf{r}_{\perp} - \mathbf{x}'_{\perp} + (z - x'_z)\mathbf{e}_{\text{in}} \approx z\mathbf{e}_{\text{in}}$ . This means  $\mathbf{e}_{\mathbf{R}'} \approx \mathbf{e}_{\text{in}}$  and we can neglect the contributions from polarization and propagation direction

$$\sum_{\lambda} |\boldsymbol{\epsilon}_{\text{in}}^* \cdot \boldsymbol{\epsilon}_{\mathbf{R}',\lambda}|^2 (\mathbf{e}_{\mathbf{R}'} + \mathbf{e}_{\text{in}}) \cdot \mathbf{d} \approx 2\mathbf{e}_{\text{in}} \cdot \mathbf{d}, \quad (4.42)$$

because they vary slowly with the angle between  $\mathbf{e}_{\mathbf{R}'}$  and  $\mathbf{e}_{\text{in}}$ . Inserting Eqs. (4.41) with (4.42) into (4.35), we obtain (4.22).

# Chapter 5.

## Time-resolved phase contrast imaging of wave packets

In this chapter I present the proposal of time resolved PCI for imaging coherent electronic motion, published in the article [2]:

DIXIT, SLOWIK, SANTRA *Phys. Rev. Lett.* **110**, 137403 (2013).

### 5.1. Motivation

An electronic wave packet is a superposition of stationary electronic states. The wave packet is nonstationary and gives rise to ultrafast electronic motion. Electronic motion has a wide range of applications and implications in ultrafast science [74–77]. Recently, the first experiments, using attosecond light pulses, have been able to investigate electronic motion in real time [78–87], cf. Sec. 7.1.

In this work, I investigate the application of x-ray imaging to investigate electronic motion. Fundamental understanding of imaging techniques is vital to identify suitable methods for investigation of electronic motion. A great advantage of ultrafast x-ray scattering would be the access to simultaneous real space and real time information. Surprisingly, the far-field scattering of nonstationary electronic states is more involved than in the stationary case. In Ref. [88] it was demonstrated that the far-field diffraction pattern of an electronic wave packet does not encode the instantaneous electron density. (An in-depth discussion of the far-field imaging problem of electronic wave packets is given in Chapter 7.) Thus, the question is brought up whether it is possible at all to recover the instantaneous electron density of electronic wave packets by x-ray scattering. In this chapter, I demonstrate that time-resolved x-ray phase contrast imaging does not suffer from the limitations of far-field x-ray imaging. In Section 5.2, I demonstrate that time-resolved x-ray phase contrast imaging can – in principle – recover the instantaneous electron density. In particular, I present the example of an electronic wave packet in hydrogen. In Section 5.3 I will discuss the formidable challenges that an experimental realization will have to overcome.

## 5.2. Time-resolved PCI: theory and examples

### 5.2.1. Theory of time-resolved PCI

I present the theoretical description of an ultrafast phase-contrast imaging experiment using the pump-probe scheme, aiming at real-time and real-space information of an electronic wave packet [2]. The pump-probe scheme is the prevalent method to investigate ultrafast processes. First, one triggers the dynamics to be investigated in the pump step. Subsequently, the dynamics is examined by another interaction with an ultrafast radiation pulse in the probe step. Performing the measurement repeatedly, one gains access to the evolution of the system by controlling the time delay between pump and probe interaction.

The scope here is to image electron dynamics with an ultrafast x-ray pulse in a pump-probe setup. The details of the pump step are not considered, typically, an attosecond laser pulse is used as the pump. An ultrashort x-ray pulse serves as the probe pulse. There have been several proposals how to generate attosecond x-ray pulses with x-ray free-electron lasers [89–93]. Thus, in the foreseeable future such x-ray light sources should become available.

The quantum theory of phase contrast imaging has been presented in Chapter 4. I recall the main points, placing more emphasis on time-dependent electronic states. There are two important assumptions: First, the x-ray photon energies have to be far-away from all inner-shell absorption edges. Secondly, the photon counting detector has to be placed in the near-field. The attentive reader may have noticed that nonstationary states were not explicitly excluded in the last chapter. The initial state of the electronic system has been simply assumed to be a general pure state

$$\hat{\rho}_{\text{in}}^{\text{el}} = |\Psi_{\text{el}}\rangle\langle\Psi_{\text{el}}|, \quad (5.1)$$

which are not necessarily stationary. For example, we may consider an electronic wave packet composed of the coherent superposition of two energy eigenstates

$$|\Psi_{\text{el}}\rangle = c_1|\varphi_1\rangle + c_2|\varphi_2\rangle, \quad \text{with } |c_1|^2 + |c_2|^2 = 1, \quad (5.2)$$

where  $\hat{H}_{\text{el}}|\varphi_i\rangle = E_i|\varphi_i\rangle$  for  $i = 1$  or  $2$ . The electron density of this superposition oscillates with a period  $T_{\text{el}} = 2\pi/|E_2 - E_1|$ . For simplicity, let us assume here a superposition of two energy eigenstates.

Remarkably, any inelastic transitions were excluded from the phase contrast term in Eq. (4.15). This is of particular interest for time-resolved imaging because the inelastic transitions are the root of the problem in the far-field imaging of electronic motion, see [88] and Chapter 7. In time-resolved PCI only the instantaneous electron density

$$\rho(\mathbf{x}', t') = \langle\Psi_{\text{el}}|\psi^\dagger(\mathbf{x}', t')\psi(\mathbf{x}', t')|\Psi_{\text{el}}\rangle$$

contributes to the phase contrast term

$$I_\varphi(t) = \alpha^2 \operatorname{Re} \left\{ i \int_{-\infty}^t dt' \int d^3x' \rho(\mathbf{x}', t') \operatorname{Tr}_{\text{rad}} \left( \rho_{\text{in}}^X \hat{\mathbf{A}}^2(\mathbf{x}', t') \hat{\mathbf{S}}(\mathbf{r}, t) \cdot \mathbf{d} \right) \right\}. \quad (5.3)$$

According to the pump-probe scheme, we assume that the x-ray pulse is short enough to “freeze” the wave packet dynamics. Concretely, we require the x-ray pulse duration  $T_{\text{rad}}$  to be much shorter than the oscillation period of the electron wave packet

$$T_{\text{rad}} \ll T_{\text{el}}. \quad (5.4)$$

Furthermore, we assume that the x-ray probe pulse probes the electronic wave packet after a pump-probe delay time  $\tau$ . In Chapter 4 the expectation value of the Poynting vector in the Fresnel regime has been calculated. This expectation value describes the instantaneous intensity observed by a detector at a distance  $\Delta$  in the near field (cf. Eq. (4.25))

$$I(\mathbf{r}, t) = I_{\text{in}}(t) \left\{ 1 + 2\pi\alpha^2 \frac{\Delta}{k_{\text{in}}^2} \nabla^2 \rho_{\perp}(\mathbf{r}_{\perp}, t - \alpha\Delta) \right\}. \quad (5.5)$$

In contrast to the previous chapter, here the x-ray pulse is chosen to propagate in  $y$ -direction. In this way, the quantization axis for the wave packet in the example is the more usual  $z$ -axis. The electron density is integrated along the propagation axis of the x-ray pulse

$$\rho_{\perp}(\mathbf{r}_{\perp}, \tau) = \int dy \rho(r_x, y, r_z, \tau). \quad (5.6)$$

The signal measured by the detector is the integration of the instantaneous signal over the pulse duration. The x-ray pulse has to be sufficiently short ( $T_{\text{rad}} \ll T_{\text{el}}$ ) to image the wave packet “frozen” at the pump-probe delay  $\tau$ . Thus, time-integration yields

$$I^{\text{tot}}(\mathbf{r}) = I_{\text{in}}^{\text{tot}} \left\{ 1 + 2\pi\alpha^2 \frac{\Delta}{k_{\text{in}}^2} \nabla^2 \rho_{\perp}(\mathbf{r}_{\perp}, \tau) \right\}. \quad (5.7)$$

Remarkably, the result depends on the Laplacian of the projection of the instantaneous electron density  $\rho_{\perp}(\mathbf{r}_{\perp}, \tau)$ . The phase contrast image of a nonstationary electronic state is not fundamentally different from the image of a stationary state, it only has an additional dependence on the pump-probe delay  $\tau$ .

### 5.2.2. Application to hydrogen wave packets

To breathe life into the previous discussion, I consider concrete wave packets. I use the same wave packet as in [88], in order to facilitate direct comparison with the

far-field image. Considering a coherent electronic wave packet in atomic hydrogen has the advantage that multiparticle contributions have not to be taken into account [94]. Specifically, take the coherent superposition of the hydrogen 3d and 4f states with vanishing magnetic quantum number

$$|\Psi_{\text{el}}\rangle = \frac{1}{\sqrt{2}}|\varphi_{3,2,0}\rangle + \frac{1}{\sqrt{2}}|\varphi_{4,3,0}\rangle. \quad (5.8)$$

This is the example that has been used in [2]. The energy spacing of the 3d and 4f states (0.66 eV) amounts to an oscillation period of  $T_{\text{el}} = 6.25$  fs of the wave packet. This oscillation period is of the order of typical time scales of electronic motion in complex molecular systems [95–97]. The instantaneous electron density of this wave packet is

$$\begin{aligned} \rho(\mathbf{x}, \tau) = & \frac{1}{2} \left( |\varphi_{3,2,0}(\mathbf{x})|^2 + |\varphi_{4,3,0}(\mathbf{x})|^2 \right) \\ & + \text{Re} \left\{ e^{-i(E_{3d}-E_{4f})\tau} \varphi_{4,3,0}^*(\mathbf{x}) \varphi_{3,2,0}(\mathbf{x}) \right\}. \end{aligned} \quad (5.9)$$

Fig. 5.1 shows a two-dimensional slice of the instantaneous electron density. The projected electron density  $\rho_{\perp}(\mathbf{x}, \tau)$  is obtained by integration along the propagation direction of the x rays, here the  $y$ -direction. Fig. 5.2 shows the projected electron density  $\rho_{\perp}$  for different values of  $\tau$ . The structure of the wave packet is encoded in the phase contrast image through the Laplacian of the projected electron density  $\nabla^2 \rho_{\perp}(\mathbf{x}, \tau)$ , cf. Eq. (5.7). This Laplacian is displayed in Fig. 5.3. Clearly, the Laplacian follows the time-evolution of the wave packet. The projected electron densities at times  $\tau = T/2$  and  $\tau = 3T/4$  coincide and consequently also their Laplacians are indistinguishable. As one would naively expect,  $\nabla^2 \rho_{\perp}(\mathbf{x}, \tau)$  at  $\tau = 0$  and  $\tau = T/2$  are clearly distinguishable from each other. This shows that, from the PCI image alone, one can recover the oscillation period. Although not surprising, this behaviour is in stark contrast to the far-field image of the wave packet [88], see Chapter 7.

In the same way, one may also treat the hydrogen 3p-4p wave packet, which has served as an example for ultrafast electron diffraction in Ref. [98],

$$|\Psi_{\text{el}}\rangle = \frac{1}{\sqrt{2}}|\varphi_{3,1,0}\rangle + \frac{1}{\sqrt{2}}|\varphi_{4,1,0}\rangle. \quad (5.10)$$

This wave packet has the same oscillation period of  $T = 6.25$  fs as the 3d-4f wave packet. The oscillation of the electron density can be described as a “breathing motion”. The electron density expands and contracts. Fig. 5.4 shows 2-d slices through the instantaneous electron density. The integrated electron density of the wave packet (along the  $x$ -direction in this case) is shown in Fig. 5.5. Finally, the Laplacian of the integrated electron density is presented in Fig. 5.6. As in the previous example, the PCI image reflects the wave packet oscillation.

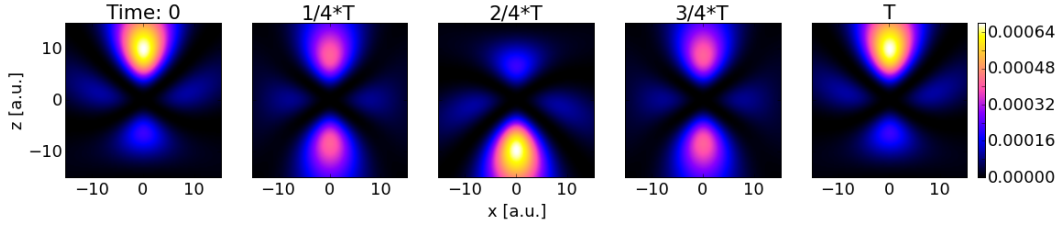


Figure 5.1.: 2-d cut ( $y = 0$ ) through the instantaneous electron density  $\rho(\mathbf{x}, t)$  of the 3d-4f wave packet of atomic hydrogen, at five instants in steps of fourths of the oscillation period  $T$ . The  $x, z$ -axes extend from -15 to 15 atomic units.

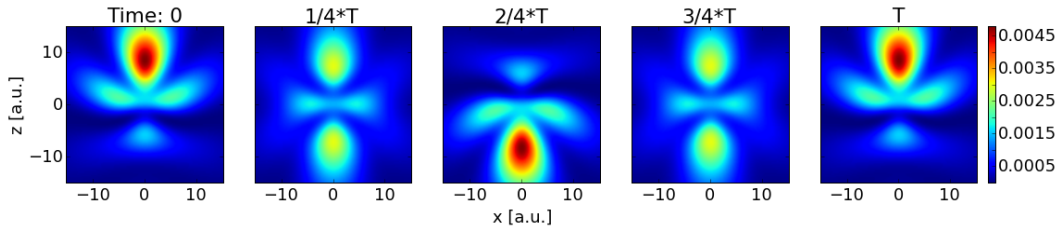


Figure 5.2.: The (along the  $y$ -axis) integrated instantaneous electron density  $\rho_{\perp}(\mathbf{r}_{\perp}, t)$  of the 3d-4f wave packet of atomic hydrogen.

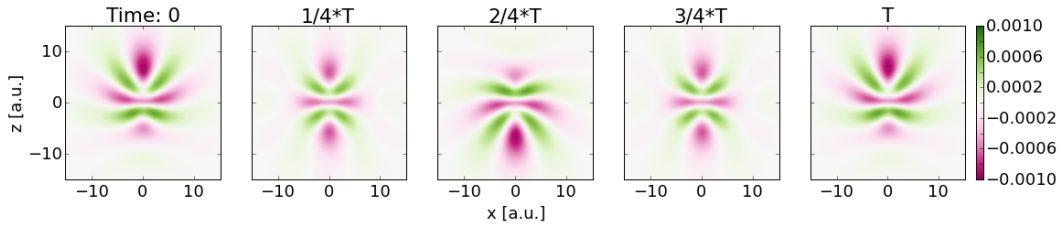


Figure 5.3.: The Laplacian of the integrated instantaneous electron density  $\nabla^2 \rho_{\perp}(\mathbf{r}_{\perp}, t)$  of the 3d-4f wave packet of atomic hydrogen.

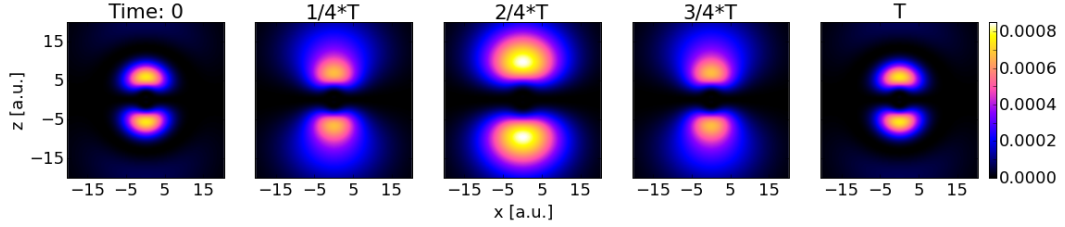


Figure 5.4.: 2-d cut ( $y = 0$ ) through the instantaneous electron density  $\rho(\mathbf{x}, t)$  of the 3p-4p wave packet of atomic hydrogen, at five instants in steps of fourths of the oscillation period  $T$ . The  $x, z$ -axes extend from -20 to 20 atomic units.

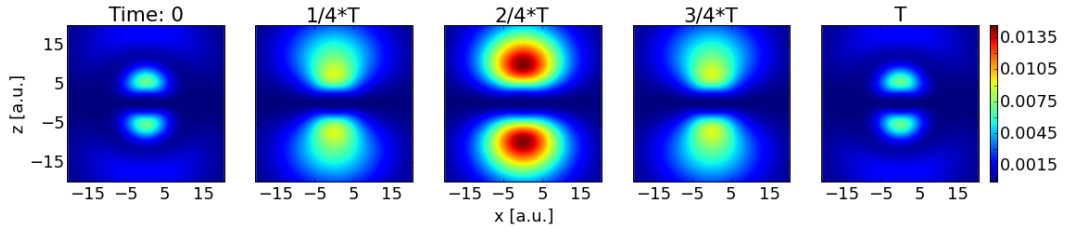


Figure 5.5.: The (along the  $y$ -axis) integrated instantaneous electron density  $\rho_{\perp}(\mathbf{r}_{\perp}, t)$  of the 3p-4p wave packet of atomic hydrogen.

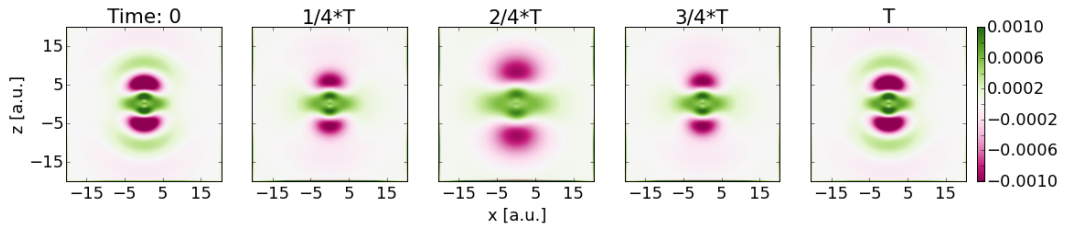


Figure 5.6.: The Laplacian of the integrated instantaneous electron density  $\nabla^2 \rho_{\perp}(\mathbf{r}_{\perp}, t)$  of the 3p-4p wave packet of atomic hydrogen.

### 5.3. Challenges and opportunities of time-resolved PCI

The experimental realization of time-resolved PCI of electronic wave packets faces some serious challenges. In the introduction it was already mentioned that ultrafast x-ray sources have yet to be developed. Proposals to generate attosecond sources from free electron lasers exist [89–92]. The recent technological progress in x-ray sources, such as free electron lasers or x-ray plasma sources, has been rapid. Thus, the radiation source seems not to be the major bottleneck for experimental realization of this imaging scheme.

A serious issue of time-resolved PCI appears to be the availability of suitable x-ray detectors. The problem is that phase contrast imaging produces real space images, which are of the size of the object. Obviously, the hydrogen wave packet serves as a toy model, as it would require detector pixels of (sub)atomic size. Thus, one would even reach the physical limit of detector size. Yet, for larger (macro-)molecules the extension of coherent electronic wave packets would be on the (sub-)nanometer scale. Nowadays, the available detectors have pixel sizes on the order of hundred microns ( $\mu\text{m}$ ) [99, 100]. A glimmer of hope may be the use of diverging x-ray beams to gain some magnification on the detector plane [47]. However, this would require an extremely fine x-ray focus. Moreover, the detector distance may become extremely small. In order for the detector to be in the near-field, one should have a Fresnel number  $F = \frac{D^2}{\Delta\lambda} \gtrsim 1$ , where  $D$  is the extension of the wave packet and  $\Delta$  the detector distance. In the case of  $D = 1$  nm and assuming the x-ray wavelength of  $\lambda = 1$  Å ( $0.01$  Å) the detector distance should be less than 10 nm ( $1$   $\mu\text{m}$ ).

Another challenge to be faced is the problem of sufficient contrast. From Eq. (5.7) one sees that the Laplacian of the projected electron density is added to the intensity signal of the incoming beam. Usually, one would need very intense x-ray beams to collect sufficient scattering data. The phase contrast signal may be much weaker than the beam. In practice, it may become extremely difficult to subtract the background signal.

Moreover, radiation damage in form of photoionization is a problem that has been neglected so far. This is, however, a problem that is independent of the imaging technique and has to be faced in the far field as well.

Having mentioned the obstacles, it remains to offer some incentives to overcome them. The direct imaging of the Laplacian of the projected instantaneous electron density  $\nabla^2\rho_{\perp}(\mathbf{x}, \tau)$  has already been highlighted. Obviously,  $\rho(\mathbf{x}, \tau)$  is of more direct physical interest. Solving the Poisson equation yields the projected (2d) instantaneous electron density  $\rho_{\perp}(\mathbf{x}, \tau)$ . It is possible to reconstruct the complete 3d instantaneous electron density  $\rho(\mathbf{x}, \tau)$  by using tomographic methods [101]. Tomography requires individual images corresponding to rotations of the wave packet around the quantization axis. The (3d) instantaneous electron density can also be

directly reconstructed from a set of the 2d projections  $\rho_{\theta\perp}$  ( $\theta$  labels the rotation angle) [102]. The reconstruction algorithm has the form of a filtered backprojection. According to the Fourier projection theorem [103], the Fourier transform of a data function  $g_{\theta} = \nabla^2 \rho_{\theta\perp}$  corresponds to a rotated plane in Fourier space of the 3D object. The 3d electron density is recovered by integrating over all rotation angles,

$$\rho(\mathbf{r}, \tau) = \frac{1}{4\pi^2} \int_0^\pi d\theta \mathcal{F}^{-1}[Q\mathcal{F}[g_{\theta}]](x_{\theta}, y), \quad (5.11)$$

after multiplication with the filter function  $Q(k_{x_{\theta}}, k_y) = |k_{x_{\theta}}|/(k_{x_{\theta}}^2 + k_y^2)$  in Fourier space. Here,  $x_{\theta} = x \cos \theta + z \sin \theta$  and  $\mathcal{F}$  denotes the 2d Fourier transform.

Interestingly, a set of 2d phase contrast images also opens a possibility to obtain the 3d Laplacian  $\nabla^2 \rho(\mathbf{r}, \tau)$  of  $\rho(\mathbf{x}, \tau)$ . This can be achieved by a filtered backprojection with  $Q(k_{x_{\theta}}, k_y) = |k_{x_{\theta}}|$ . The 3d Laplacian contains important physical information. It highlights internal and external boundaries of the wave packet, e.g., boundaries of zero electron density flux. According to Bader's theory of atoms in molecules [104, 105] this is a useful quantity that carries information about the complex bonding and topology of the charge distributions in molecules.

## Part III.

### **Far field imaging: coherent and incoherent x-ray scattering**



# Chapter 6.

## X-ray scattering and the far-field diffraction pattern

This chapter is a technical preparation for the following chapters and connects Part II and Part III. Previously, near-field imaging has been considered. In this part, I analyze the far-field scattering pattern, especially needed for coherent diffractive imaging and inelastic x-ray scattering. In this chapter, I present the far-field expectation value of the Poynting operator and compare it to the transition rate from Fermi's golden rule. This chapter is rather technical, the physical consequences and applications are in the focus of the following chapters.

### 6.1. The (0,1) term of the Poynting operator

In Chapter 4, I have introduced the Poynting operator as the observable for x-ray photon detection. For phase-contrast imaging in the near-field, the lowest order perturbation theory term, the (0,1) term, turned out to be the relevant term. In this section, I demonstrate that the (0,1) term vanishes in the far-field.

The (0,1) term of the Poynting operator results in Eq. (4.22) to

$$I_{\varphi}(t) = 2 \operatorname{Re} \left\{ i \frac{\alpha^2 k_{\text{in}}}{2\pi z^2} I_{\text{in}}(t) \int d^3 x' \rho(\mathbf{x}', t - \alpha z) \right. \\ \left. \times \int d^2 x_{\perp} \gamma_{\text{sp}}(|\mathbf{x}_{\perp} - \mathbf{x}'_{\perp}|) e^{\frac{ik_{\text{in}}}{2z} (|\mathbf{r}_{\perp} - \mathbf{x}_{\perp}|^2 - |\mathbf{r}_{\perp} - \mathbf{x}'_{\perp}|^2)} \right\}. \quad (6.1)$$

The final phase factor results from the Fresnel approximation for the near-field. The Fresnel approximation has been applied once in propagating the correlation function yielding Eq. (4.34). The Fresnel approximation had to be used a second time, when all scattered photon modes were integrated to obtain Eq. (4.41).

In the far field the quadratic phase terms are negligible. Then all integrands are real and the phase contrast term vanishes. In more detail, the far-field approximation

is [62]

$$e^{ik_{\text{in}}|\mathbf{r}-\mathbf{x}|}/|\mathbf{r}-\mathbf{x}| \approx \frac{e^{ik_{\text{in}}r}}{r} e^{-ik_{\text{in}}\mathbf{s}\cdot\mathbf{x}}, \quad (6.2)$$

where  $r = |\mathbf{r}|$  and  $\mathbf{s} = \mathbf{r}/r$ . Using the paraxial approximation  $s_z \approx 1$ , and introducing  $\boldsymbol{\xi}_{\perp} = \mathbf{x}_{\perp} - \mathbf{x}'_{\perp}$ , we find

$$I_{\varphi}(t) = 2 \operatorname{Re} \left\{ i \frac{\alpha^2 k_{\text{in}}}{2\pi z^2} I_{\text{in}}(t) \int d^3 x' \rho(\mathbf{x}', t - \alpha z) \int d^2 \xi_{\perp} \gamma_{\text{sp}}(|\boldsymbol{\xi}_{\perp}|) e^{ik_{\text{in}}\mathbf{s}_{\perp} \cdot \boldsymbol{\xi}_{\perp}} \right\} \quad (6.3)$$

$$= 2 \operatorname{Re} \left\{ i \frac{\alpha^2 k_{\text{in}}}{2\pi z^2} I_{\text{in}}(t) N_{\text{el}} \widetilde{\gamma}_{\text{sp}}(k_{\text{in}}\mathbf{s}_{\perp}) \right\}. \quad (6.4)$$

The number of electrons  $N_{\text{el}}$  results from the integral over the electron density. The Fourier transform  $\widetilde{\gamma}_{\text{sp}}$  is real because the spatial coherence function is radially symmetric. Consequently, the real part vanishes and  $I_{\varphi} = 0$ . This term is negligible even for not perfectly radially symmetric spatial coherence. If the coherence length is sufficiently large,  $\widetilde{\gamma}_{\text{sp}}$  has basically only contributions in the forward direction. In summary, the (0,1) term can be completely neglected in the far-field intensity pattern.

## 6.2. The (1,1) term of the Poynting operator

In first-order perturbation theory, there is also the (1,1) term. In this section, I demonstrate that this term accounts for the far-field x-ray diffraction pattern. Commonly, the method to derive the far-field diffraction pattern is to choose a projection operator as the observable. However, it has some conceptual shortcomings. The projection operator does not at all specify the position of the detector and is not obviously limited to the far-field. Here, the Poynting operator is used again as the observable. The connection between both approaches will be clarified in the next section.

As in Section 4.2, the operator

$$\hat{\mathcal{O}} = \hat{\mathbf{S}}(\mathbf{r}) \cdot \mathbf{d} \quad (6.5)$$

serves as the observable for the intensity at the detector at position  $\mathbf{r}$ . The (1,1) term has been established in Eq. (2.77) and takes the form

$$\langle \hat{\mathbf{S}}(\mathbf{r}) \cdot \mathbf{d} \rangle_t^{(1,1)} = \int_{-\infty}^t dt' \int_{-\infty}^t dt'' \operatorname{Tr} \left( \hat{H}_{\text{int}}(t'') \hat{\rho}_{\text{in}} \hat{H}_{\text{int}}(t') \hat{\mathbf{S}}(\mathbf{r}) \cdot \mathbf{d}(t) \right), \quad (6.6)$$

where it is again appropriate to set the adiabatic switching parameter  $\epsilon$  to zero. As before, we consider the  $\mathbf{A}^2$ -interaction

$$\hat{H}_{\text{int}} = \frac{\alpha^2}{2} \int d^3x \hat{\mathbf{A}}^2(\mathbf{x}) \hat{n}(\mathbf{x}), \quad (6.7)$$

assuming that the x-ray photon energy is sufficiently far above all absorption edges. The initial state of the radiation and matter system is

$$\hat{\rho}_{\text{in}} = \hat{\rho}_{\text{in}}^X \otimes \hat{\rho}_{\text{in}}^{\text{el}}. \quad (6.8)$$

This yields

$$\begin{aligned} \langle \hat{\mathbf{S}}(\mathbf{r}) \cdot \mathbf{d} \rangle_t^{(1,1)} &= \left(\frac{\alpha^2}{2}\right)^2 \int_{-\infty}^t dt' \int_{-\infty}^t dt'' \iint d^3x' d^3x'' \text{Tr}_{\text{el}} \left( \hat{n}(\mathbf{x}'', t'') \hat{\rho}_{\text{in}}^{\text{el}} \hat{n}(\mathbf{x}', t') \right) \\ &\quad \text{Tr}_{\text{rad}} \left( \hat{\mathbf{A}}^2(\mathbf{x}'', t'') \hat{\rho}_{\text{in}}^X \hat{\mathbf{A}}^2(\mathbf{x}', t') \hat{\mathbf{S}}(\mathbf{r}) \cdot \mathbf{d}(t) \right). \end{aligned} \quad (6.9)$$

Expressing  $\hat{\mathbf{A}}$  and  $\hat{\mathbf{S}}$  in terms of photon creation and annihilation operators (see Eqs. (4.1), (4.8)), the matrix elements are of the form

$$\sum_{\{n\}, \{\bar{n}\}} \rho_{\{n\}, \{\bar{n}\}}^X \langle \{\bar{n}\} | \hat{a}_{\mathbf{k}, \lambda}^\dagger \hat{a}_{\mathbf{l}, \mu} \hat{a}_{\mathbf{p}, \alpha}^\dagger \hat{a}_{\mathbf{q}, \beta} \hat{a}_{\mathbf{m}, \zeta}^\dagger \hat{a}_{\mathbf{n}, \eta} | \{n\} \rangle. \quad (6.10)$$

Normal ordering yields

$$\begin{aligned} \hat{a}_{\mathbf{k}}^\dagger \hat{a}_{\mathbf{l}} \hat{a}_{\mathbf{p}}^\dagger \hat{a}_{\mathbf{q}} \hat{a}_{\mathbf{m}}^\dagger \hat{a}_{\mathbf{n}} &= \hat{a}_{\mathbf{k}}^\dagger \hat{a}_{\mathbf{n}} \delta_{p,l} \delta_{q,m} \\ &\quad + \hat{a}_{\mathbf{k}}^\dagger \hat{a}_{\mathbf{m}}^\dagger \hat{a}_{\mathbf{q}} \hat{a}_{\mathbf{n}} \delta_{p,l} + \hat{a}_{\mathbf{k}}^\dagger \hat{a}_{\mathbf{p}}^\dagger \hat{a}_{\mathbf{l}} \hat{a}_{\mathbf{n}} \delta_{q,m} + \hat{a}_{\mathbf{k}}^\dagger \hat{a}_{\mathbf{p}}^\dagger \hat{a}_{\mathbf{q}} \hat{a}_{\mathbf{n}} \delta_{l,m} \\ &\quad + \hat{a}_{\mathbf{k}}^\dagger \hat{a}_{\mathbf{p}}^\dagger \hat{a}_{\mathbf{m}}^\dagger \hat{a}_{\mathbf{l}} \hat{a}_{\mathbf{q}} \hat{a}_{\mathbf{n}}. \end{aligned}$$

Photon scattering in first order perturbation theory is a single photon scattering theory. In particular, we neglect all terms where more than one photon has been changed from the incoming beam. Thus, only the term stemming from the  $\hat{a}_{\mathbf{k}}^\dagger \hat{a}_{\mathbf{n}} \delta_{p,l} \delta_{q,m}$  part of the matrix element is considered. Physically, we neglect all terms where the detector measures vacuum fluctuations instead of scattered photons. In this way we avoid to deal with the infinities that arise from vacuum fluctuations. Eventually, we find the expression for the trace of the photonic system

$$\begin{aligned} &\text{Tr}_{\text{rad}} \left( \hat{\mathbf{A}}^2(\mathbf{x}'', t'') \hat{\rho}_{\text{in}}^X \hat{\mathbf{A}}^2(\mathbf{x}', t') \hat{\mathbf{S}}(\mathbf{r}) \cdot \mathbf{d}(t) \right) \\ &= \sum_{\mathbf{l}, \mu} \sum_{\mathbf{q}, \beta} \frac{(2\pi)^2}{V^3 \alpha^5} (\mathbf{e}_{\mathbf{l}} + \mathbf{e}_{\mathbf{q}}) \cdot \mathbf{d} e^{i\mathbf{l} \cdot \mathbf{x}' - i\mathbf{q} \cdot \mathbf{x}''} e^{i\omega_{\mathbf{l}}(t-t')} e^{-i\omega_{\mathbf{q}}(t-t'')} \\ &\quad \times \sum_{\mathbf{k}, \lambda} \sum_{\mathbf{n}, \eta} \frac{1}{\sqrt{\omega_{\mathbf{k}} \omega_{\mathbf{n}}}} \text{Tr}_{\text{rad}} \left( \rho_{\text{in}}^X \hat{a}_{\mathbf{k}, \lambda}^\dagger \hat{a}_{\mathbf{n}, \eta} \right) e^{i\omega_{\mathbf{k}} t' - i\mathbf{k} \cdot \mathbf{x}'} e^{i\omega_{\mathbf{n}} t'' + i\mathbf{n} \cdot \mathbf{x}''} \\ &\quad \times (\boldsymbol{\epsilon}_{\mathbf{k}, \lambda}^* \cdot \boldsymbol{\epsilon}_{\mathbf{l}, \mu}) (\boldsymbol{\epsilon}_{\mathbf{l}, \mu}^* \cdot \boldsymbol{\epsilon}_{\mathbf{q}, \beta}) (\boldsymbol{\epsilon}_{\mathbf{q}, \beta}^* \cdot \boldsymbol{\epsilon}_{\mathbf{n}, \eta}). \end{aligned} \quad (6.11)$$

We assume that the x-ray pulse has a narrow bandwidth as well as a small angular spread in the interaction region and is linearly polarized. Then, the second line of the right hand side can be expressed by the first order correlation function  $G^{(1)}$  of the radiation field [15, 17, 70, 71].  $G^{(1)}$  has been defined in Eq. 4.18. Relabel  $(\mathbf{l}, \mu) = (\mathbf{k}_1, \lambda_1)$ , and  $(\mathbf{q}, \beta) = (\mathbf{k}_2, \lambda_2)$  and replace  $\sum_{\mathbf{k}, \lambda}$  by  $\sum_{\lambda} \frac{V}{(2\pi)^3} \int d^3k$ . After some trivial steps we obtain

$$\begin{aligned} & \text{Tr}_{\text{rad}} \left( \hat{\mathbf{A}}^2(\mathbf{x}'', t'') \hat{\rho}_{\text{in}}^X \hat{\mathbf{A}}^2(\mathbf{x}', t') \hat{\mathbf{S}}(\mathbf{r}) \cdot \mathbf{d}(t) \right) \\ &= (2\pi)^{-5} \alpha^{-5} \omega_{\text{in}}^{-2} G^{(1)}(\mathbf{x}', t', \mathbf{x}'', t'') \\ & \times \int d^3k_1 \int d^3k_2 e^{-i\mathbf{k}_1 \cdot (\mathbf{r} - \mathbf{x}')} e^{-i\mathbf{k}_2 \cdot (\mathbf{r} - \mathbf{x}'')} e^{i\omega_{\mathbf{k}_1}(t-t')} e^{-i\omega_{\mathbf{k}_2}(t-t'')} \\ & \times (\mathbf{e}_{\mathbf{k}_1} + \mathbf{e}_{\mathbf{k}_2}) \cdot \mathbf{d} (\boldsymbol{\epsilon}_{\mathbf{k}_{\text{in}}, \lambda_{\text{in}}}^* \cdot \boldsymbol{\epsilon}_{\mathbf{k}_1, \lambda_{\text{in}}}) (\boldsymbol{\epsilon}_{\mathbf{k}_1, \lambda_{\text{in}}}^* \cdot \boldsymbol{\epsilon}_{\mathbf{k}_2, \lambda_{\text{in}}}) (\boldsymbol{\epsilon}_{\mathbf{k}_2, \lambda_{\text{in}}}^* \cdot \boldsymbol{\epsilon}_{\mathbf{k}_{\text{in}}, \lambda_{\text{in}}}). \end{aligned} \quad (6.12)$$

Now, we can use the dispersion relation for photons  $|\mathbf{k}| = \alpha\omega_{\mathbf{k}}$  to introduce coordinates  $(k_x, k_y, \omega_{\mathbf{k}})$  with  $d^3k = \frac{\alpha^2 \omega_{\mathbf{k}}}{k_z} d\omega_{\mathbf{k}} dk_x dk_y$ . Then, we can perform the  $k_1, k_2$ -integrations. The  $k_1$ -integral from Eq. (6.12) has the form

$$\begin{aligned} & \int d\omega_{\mathbf{k}_1} \alpha^2 \omega_{\mathbf{k}_1} \iint_{\sqrt{k_x^2 + k_y^2} \leq \alpha \omega_{\mathbf{k}_1}} dk_x dk_y \frac{e^{i\omega_{\mathbf{k}_1}(t-t')}}{\sqrt{\alpha^2 \omega_{\mathbf{k}_1}^2 - k_x^2 - k_y^2}} e^{-i\mathbf{k}_1 \cdot (\mathbf{r} - \mathbf{x}')} \\ & \times (\mathbf{e}_{\mathbf{k}_1} + \mathbf{e}_{\mathbf{k}_2}) \cdot \mathbf{d} (\boldsymbol{\epsilon}_{\mathbf{k}_{\text{in}}, \lambda_{\text{in}}}^* \cdot \boldsymbol{\epsilon}_{\mathbf{k}_1, \lambda_{\text{in}}}) (\boldsymbol{\epsilon}_{\mathbf{k}_1, \lambda_{\text{in}}}^* \cdot \boldsymbol{\epsilon}_{\mathbf{k}_2, \lambda_{\text{in}}}). \end{aligned} \quad (6.13)$$

In the far field, this integral can be treated with the method of stationary phase [15]. This method gives an asymptotic formula for integrals of the type

$$I(x, y, z) = \iint_{p^2 + q^2 \leq 1} a(p, q) e^{ik_0(px + qy + mz)} dp dq, \quad (6.14)$$

where  $z \geq 0$  and  $m = \sqrt{1 - p^2 - q^2}$ . In the limit  $k_0 r \rightarrow \infty$ , where  $r = \sqrt{x^2 + y^2 + z^2}$ , this integral yields

$$I(x, y, z) \sim \frac{2\pi i}{k_0} \frac{z}{r} a\left(\frac{x}{r}, \frac{y}{r}\right) \frac{e^{ik_0 r}}{r}, \quad \text{for } k_0 r \rightarrow \infty. \quad (6.15)$$

In the limit  $\alpha\omega_{\mathbf{k}_1} |\mathbf{r} - \mathbf{x}'| \rightarrow \infty$ , we obtain for the integral in Eq. (6.13)

$$\int d\omega_{\mathbf{k}_1} \alpha^2 \omega_{\mathbf{k}_1} (-2\pi i) \frac{e^{-i\alpha\omega_{\mathbf{k}_1} R}}{R} (\mathbf{e}_{\mathbf{R}} + \mathbf{e}_{\mathbf{k}_2}) \cdot \mathbf{d} (\boldsymbol{\epsilon}_{\mathbf{k}_{\text{in}}, \lambda_{\text{in}}}^* \cdot \boldsymbol{\epsilon}_{\mathbf{R}, \lambda_{\text{in}}}) (\boldsymbol{\epsilon}_{\mathbf{R}, \lambda_{\text{in}}}^* \cdot \boldsymbol{\epsilon}_{\mathbf{k}_2, \lambda_{\text{in}}}), \quad (6.16)$$

where  $\mathbf{R} = \mathbf{r} - \mathbf{x}'$ ,  $R = |\mathbf{R}|$ . We remark that, in order to obtain this result, we have performed the  $k$ -integral over all possible scattered photon modes with all possible directions. In the limit that the detector is far away from the object

(w.r.t. the wavelength of the incoming radiation), we find that only one photon mode contributes. A far-field detector at a given position will only be sensitive to the photon modes scattered into the direction of the detector.

Performing the  $k_1$  and the  $k_2$  integration Eq. (6.12) becomes

$$\begin{aligned}
 & \text{Tr}_{\text{rad}} \left( \hat{\mathbf{A}}^2(\mathbf{x}'', t'') \hat{\rho}_{\text{in}}^X \hat{\mathbf{A}}^2(\mathbf{x}', t') \hat{\mathbf{S}}(\mathbf{r}) \cdot \mathbf{d}(t) \right) \\
 &= \frac{1}{(2\pi)^3 \alpha} G^{(1)}(\mathbf{x}', t', \mathbf{x}'', t'') (\mathbf{e}_{\mathbf{r}-\mathbf{x}'} + \mathbf{e}_{\mathbf{r}-\mathbf{x}''}) \cdot \mathbf{d} \\
 & \times (\boldsymbol{\epsilon}_{\mathbf{k}_{\text{in}}, \lambda_{\text{in}}}^* \cdot \boldsymbol{\epsilon}_{\mathbf{r}-\mathbf{x}', \lambda_{\text{in}}}) (\boldsymbol{\epsilon}_{\mathbf{r}-\mathbf{x}', \lambda_{\text{in}}}^* \cdot \boldsymbol{\epsilon}_{\mathbf{r}-\mathbf{x}'', \lambda_{\text{in}}}) (\boldsymbol{\epsilon}_{\mathbf{r}-\mathbf{x}'', \lambda_{\text{in}}}^* \cdot \boldsymbol{\epsilon}_{\mathbf{k}_{\text{in}}, \lambda_{\text{in}}}) \\
 & \times \iint d\omega_{\mathbf{k}_1} d\omega_{\mathbf{k}_2} \frac{\omega_{\mathbf{k}_1} \omega_{\mathbf{k}_2}}{\omega_{\text{in}}^2} \frac{e^{-i\alpha\omega_{\mathbf{k}_1} |\mathbf{r}-\mathbf{x}'|}}{|\mathbf{r}-\mathbf{x}'|} \frac{e^{i\alpha\omega_{\mathbf{k}_2} |\mathbf{r}-\mathbf{x}''|}}{|\mathbf{r}-\mathbf{x}''|} e^{i\omega_{\mathbf{k}_1} (t-t')} e^{-i\omega_{\mathbf{k}_2} (t-t'')} .
 \end{aligned} \tag{6.17}$$

For a small object that is far away from the detector, the direction pointing to the detector does not change much within the object. Then, we can make the simplifying assumptions

$$\begin{aligned}
 |\mathbf{r}-\mathbf{x}| &\approx \mathbf{r}-\mathbf{s} \cdot \mathbf{x}, & \text{where } \mathbf{s} &= \mathbf{r}/r, \\
 \mathbf{e}_{\mathbf{r}-\mathbf{x}} &\approx \mathbf{e}_{\mathbf{s}}, \\
 \boldsymbol{\epsilon}_{\mathbf{r}-\mathbf{x}, \lambda_{\text{in}}} &\approx \boldsymbol{\epsilon}_{\mathbf{s}, \lambda_{\text{in}}}.
 \end{aligned}$$

Finally,

$$\begin{aligned}
 & \text{Tr}_{\text{rad}} \left( \hat{\mathbf{A}}^2(\mathbf{x}'', t'') \hat{\rho}_{\text{in}}^X \hat{\mathbf{A}}^2(\mathbf{x}', t') \hat{\mathbf{S}}(\mathbf{r}) \cdot \mathbf{d}(t) \right) \\
 &\approx \frac{1}{(2\pi)^3 \alpha} G^{(1)}(\mathbf{x}', t', \mathbf{x}'', t'') 2\mathbf{e}_{\mathbf{s}} \cdot \mathbf{d} \left| \boldsymbol{\epsilon}_{\mathbf{k}_{\text{in}}, \lambda_{\text{in}}}^* \cdot \boldsymbol{\epsilon}_{\mathbf{s}, \lambda_{\text{in}}} \right|^2 \\
 & \times \iint d\omega_{\mathbf{k}_1} d\omega_{\mathbf{k}_2} \frac{\omega_{\mathbf{k}_1} \omega_{\mathbf{k}_2}}{\omega_{\text{in}}^2} \frac{e^{i\alpha(\omega_{\mathbf{k}_2} - \omega_{\mathbf{k}_1})r}}{r^2} e^{i\alpha(\omega_{\mathbf{k}_1} \mathbf{s} \cdot \mathbf{x}' - \omega_{\mathbf{k}_2} \mathbf{s} \cdot \mathbf{x}'')} e^{i\omega_{\mathbf{k}_1} (t-t')} e^{-i\omega_{\mathbf{k}_2} (t-t'')} .
 \end{aligned} \tag{6.18}$$

At this point, we need to specify the concrete model for the correlation function of the radiation field. We use the same quasi-stationary, quasi-monochromatic correlation function as in Sec. 3.2.2 and 4.3

$$G^{(1)}(\mathbf{x}', t', \mathbf{x}'', t'') = 4\pi\alpha I\left(\frac{t'+t''}{2}\right) \gamma_{\text{sp}}(|\mathbf{x}'_{\perp} - \mathbf{x}''_{\perp}|) \gamma_{\text{tp}}(t' - t'') e^{-i\mathbf{k}_{\text{in}}(\mathbf{x}' - \mathbf{x}'')} . \tag{6.19}$$

We assume that the spatial coherence length of the radiation is much larger than the object, such that for all points within the object

$$\gamma_{\text{sp}}(|\mathbf{x}'_{\perp} - \mathbf{x}''_{\perp}|) \approx 1 .$$

Moreover, we introduce

$$\theta = \frac{t' + t''}{2} \quad \text{and} \quad \tau = t' - t'' , \tag{6.20}$$

and assume that, within the object, the correlations propagate like plane waves, such that

$$G^{(1)}(\mathbf{x}', \mathbf{x}'', \theta, \tau) = 4\pi\alpha I(\theta) e^{-\tau^2/\tau_c^2} e^{i\omega_{\text{in}}\tau} e^{-i\mathbf{k}_{\text{in}}(\mathbf{x}'-\mathbf{x}'')}, \quad (6.21)$$

where  $\tau_c$  is the coherence time of the radiation field.

Inserting the trace term (6.18) into Eq. (6.9) yields

$$\begin{aligned} \langle \hat{\mathbf{S}}(\mathbf{r}) \cdot \mathbf{d} \rangle_t^{(1,1)} &= \frac{\alpha^4}{8\pi^2 r^2} 2\mathbf{e}_{\mathbf{s}} \cdot \mathbf{d} \left| \boldsymbol{\epsilon}_{\mathbf{k}_{\text{in}}, \lambda_{\text{in}}}^* \cdot \boldsymbol{\epsilon}_{\mathbf{s}, \lambda_{\text{in}}} \right|^2 \iint d^3x' d^3x'' \\ &\times \text{Tr}_{\text{el}} \left( \hat{\rho}_{\text{in}}^{\text{el}} \hat{n}(\mathbf{x}', \theta + \frac{\tau}{2}) \hat{n}(\mathbf{x}'', \theta - \frac{\tau}{2}) \right) e^{-i\mathbf{k}_{\text{in}}(\mathbf{x}'-\mathbf{x}'')} \\ &\times \int_{-\infty}^t d\theta \int d\bar{\omega} I(\theta) e^{-i\bar{\omega}(\theta-t+\alpha r - \frac{\alpha}{2}\mathbf{s} \cdot (\mathbf{x}'+\mathbf{x}''))} \\ &\times \int_{-\infty}^{\infty} d\tau \int d\omega \frac{\omega^2 - \bar{\omega}^2}{\omega_{\text{in}}^2} e^{i(\omega_{\text{in}}-\omega)\tau} e^{-\tau^2/\tau_c^2} e^{i\alpha\omega\mathbf{s} \cdot (\mathbf{x}'-\mathbf{x}'')}, \end{aligned} \quad (6.22)$$

where we have introduced the variables

$$\omega = \frac{\omega_{\mathbf{k}_1} + \omega_{\mathbf{k}_2}}{2} \quad \text{and} \quad \bar{\omega} = \omega_{\mathbf{k}_1} - \omega_{\mathbf{k}_2}. \quad (6.23)$$

For the purpose of this chapter we assume the electronic system is in a pure, stationary state  $|\Psi_a\rangle$ ,

$$\rho_{\text{in}}^{\text{el}} = |\Psi_a\rangle\langle\Psi_a|. \quad (6.24)$$

Thus, we can simplify the trace of the electronic system

$$\text{Tr}_{\text{el}} \left( \hat{\rho}_{\text{in}}^{\text{el}} \hat{n}(\mathbf{x}', \theta + \frac{\tau}{2}) \hat{n}(\mathbf{x}'', \theta - \frac{\tau}{2}) \right) = \langle \Psi_a | \hat{n}(\mathbf{x}', \theta + \frac{\tau}{2}) \hat{n}(\mathbf{x}'', \theta - \frac{\tau}{2}) | \Psi_a \rangle \quad (6.25)$$

$$= \sum_f e^{i(E_a - E_f)\tau} \langle \Psi_a | \hat{n}(\mathbf{x}') | \Psi_f \rangle \langle \Psi_f | \hat{n}(\mathbf{x}'') | \Psi_a \rangle, \quad (6.26)$$

where we have introduced a summation over a complete, orthogonal basis of stationary states.

The Fourier transform of  $I(\theta)$  was defined in in Eq. (3.14b). We find

$$\begin{aligned} \langle \hat{\mathbf{S}}(\mathbf{r}) \cdot \mathbf{d} \rangle_t^{(1,1)} &= \frac{\alpha^4}{8\pi^2 r^2} 2\mathbf{e}_{\mathbf{s}} \cdot \mathbf{d} \left| \boldsymbol{\epsilon}_{\mathbf{k}_{\text{in}}, \lambda_{\text{in}}}^* \cdot \boldsymbol{\epsilon}_{\mathbf{s}, \lambda_{\text{in}}} \right|^2 \iint d^3x' d^3x'' \\ &\times \sum_f \langle \Psi_a | \hat{n}(\mathbf{x}') | \Psi_f \rangle \langle \Psi_f | \hat{n}(\mathbf{x}'') | \Psi_a \rangle e^{-i\mathbf{k}_{\text{in}}(\mathbf{x}'-\mathbf{x}'')} \\ &\times \int d\bar{\omega} \sqrt{2\pi} W_2(\bar{\omega}) e^{i\bar{\omega}(t-\alpha r + \frac{\alpha}{2}\mathbf{s} \cdot (\mathbf{x}'+\mathbf{x}''))} \\ &\times \int d\omega \frac{\omega^2 - \bar{\omega}^2}{\omega_{\text{in}}^2} \sqrt{2\pi} W_1(\omega - \omega_{\text{in}} + E_f - E_a) e^{i\alpha\omega\mathbf{s} \cdot (\mathbf{x}'-\mathbf{x}'')}. \end{aligned} \quad (6.27)$$

For a sufficiently large pulse duration we can neglect all frequency correlations and  $W_2$  becomes very narrow and centered around  $\bar{\omega} \approx 0$ . Also, we assume that the detector is so far away that  $\mathbf{s} \cdot \frac{(\mathbf{x}' + \mathbf{x}'')}{2} \ll r$ . Furthermore, we require the pulse to be quasi-monochromatic. This means  $W_1$ , representing the bandwidth of the pulse, can be assumed to be a delta function, implementing the energy conservation during the scattering process. Thus,

$$\begin{aligned} \langle \hat{\mathbf{S}}(\mathbf{r}) \cdot \mathbf{d} \rangle_t^{(1,1)} &= \left( \frac{d\sigma}{d\Omega} \right)_{\text{Th}} \mathbf{e}_s \cdot \mathbf{d} \frac{I(t - \alpha r)}{r^2} \\ &\times \sum_f \frac{\omega_f^2}{\omega_{\text{in}}^2} \iint d^3x' d^3x'' \langle \Psi_a | \hat{n}(\mathbf{x}') | \Psi_f \rangle \langle \Psi_f | \hat{n}(\mathbf{x}'') | \Psi_a \rangle e^{i\mathbf{Q}(\mathbf{x}'' - \mathbf{x}')} , \end{aligned} \quad (6.28)$$

where the final photon energy is  $\omega_f = \omega_{\text{in}} - E_f - E_a$ , the momentum transfer is  $\mathbf{Q} = \mathbf{k}_{\text{in}} - \mathbf{k}_f = \mathbf{k}_{\text{in}} - \alpha\omega_f \mathbf{s}$ , and the Thomson cross section is

$$\left( \frac{d\sigma}{d\Omega} \right)_{\text{Th}} = \alpha^4 \left| \boldsymbol{\epsilon}_{\mathbf{k}_{\text{in}}, \lambda_{\text{in}}}^* \cdot \boldsymbol{\epsilon}_{\mathbf{k}_f, \lambda_{\text{in}}} \right|^2 . \quad (6.29)$$

It should be emphasized that in the case of elastic scattering, when  $|\Psi_f\rangle = |\Psi_a\rangle$ , we have found the well-known relationship of scattering pattern and Fourier transform of electron density

$$\langle \hat{\mathbf{S}}(\mathbf{r}) \cdot \mathbf{d} \rangle_t^{(1,1)} = \left( \frac{d\sigma}{d\Omega} \right)_{\text{Th}} \frac{I(t - \alpha r)}{r^2} \mathbf{e}_s \cdot \mathbf{d} \left| \int d^3x \langle \Psi_a | \hat{n}(\mathbf{x}) | \Psi_a \rangle e^{i\mathbf{Q}\mathbf{x}} \right|^2 . \quad (6.30)$$

$\langle \hat{\mathbf{S}}(\mathbf{r}) \cdot \mathbf{d} \rangle_t^{(1,1)}$  is the expectation value at the instant  $t$ . It depends on the retarded intensity at the time of scattering,  $\alpha r$  is the time a photon travels from the target to the detector. Any real measurement would correspond to a time-integration of such instantaneous expectation values. Moreover, this expectation value depends on the inverse square of the detector distance. This expresses the intensity fall off of a spherical wave upon propagation. Moreover, the orientation of the detector influences the size of the area which the radiation propagates through. The term  $\mathbf{e}_s \cdot \mathbf{d}$  reflects that. Note, we have not made any a priori assumption on the direction of scattered photons.

### 6.3. The projection observable

In this section I derive the (1,1) term for the projection operator onto a scattered photon mode. Using the projection operator is the common approach to calculate the far-field diffraction pattern [21, 63, 70, 106]. In the previous section we have used the Poynting operator as the observable. Its expectation value gives the value of the energy flowing through a unit area per unit time. The energy of the radiation

field is transported in form of photons and, thus, it is a reasonable observable for photon detection. This poses the question, what the (1,1) term of the projection operator corresponds to.

In the last section, we learned that for each given point in the far field only one photon mode is crucial for the intensity of the radiation field. Therefore, it is crucial to determine the populations of the photon modes in the scattered radiation field. In other words, we ask what is the probability that an incoming photon is scattered into a final photon mode. As we have seen in Sec. 2.2.3, one can calculate transition probabilities by Fermi's Golden Rule. It was demonstrated that these transition rates correspond to the (1,1) term of a projection operator. In short, we consider projection operators to determine transition rates to scattered photon modes. Because the intensity at each point on the detector depends only on a single mode, we obtain the diffraction pattern from this quantity.

We employ the same formalism as in the previous section. The projection operator is defined by

$$\hat{O} = \hat{P}_{\mathbf{k}_s, \lambda_s} \otimes \hat{\mathbf{1}}_{\text{el}}. \quad (6.31)$$

For the projector we may use the short hand notation

$$\hat{P}_{\mathbf{k}_s, \lambda_s} = |1_{\mathbf{k}_s, \lambda_s}\rangle \langle 1_{\mathbf{k}_s, \lambda_s}|, \quad (6.32)$$

where  $|1_{\mathbf{k}_s, \lambda_s}\rangle$  is the Fock state with one photon in the mode  $(\mathbf{k}_s, \lambda_s)$ , for the multimode Fock state expression  $\hat{P}_{\mathbf{k}_s, \lambda_s} = \sum_{\{n'\}} |\{n'\}\rangle \langle \{n'\}|$ , where  $\{n'\}$  are the multimode Fock states with  $n_{\mathbf{k}_s, \lambda_s} = 1$ . A single photon in the scattered mode is sufficient because we assume that the scattering occurs only into previously unoccupied modes.

According to Eq. (2.86), the transition rate  $\Gamma_{FI}$  for a scattering a photon into the mode  $(\mathbf{k}_s, \lambda_s)$  satisfies

$$\Gamma_{FI} T = \langle \hat{P}_{\mathbf{k}_s, \lambda_s} \otimes \hat{\mathbf{1}}_{\text{el}} \rangle_{t \rightarrow \infty}^{(1,1)}. \quad (6.33)$$

This yields the differential scattering probability (DSP) to scatter a photon into a given solid angle  $d\Omega$ , where we have to sum over all wave vectors  $\mathbf{k}_s$  pointing into the direction of  $d\Omega$

$$\frac{dP}{d\Omega} = \sum_{\mathbf{k}_s \rightarrow d\Omega, \lambda_s} \langle \hat{P}_{\mathbf{k}_s, \lambda_s} \otimes \hat{\mathbf{1}}_{\text{el}} \rangle_{t \rightarrow \infty}^{(1,1)} \quad (6.34)$$

$$= \sum_{\lambda_s} \frac{V \alpha^3}{(2\pi)^3} \int \omega_{\mathbf{k}_s}^2 d\omega_{\mathbf{k}_s} \langle \hat{P}_{\mathbf{k}_s, \lambda_s} \otimes \hat{\mathbf{1}}_{\text{el}} \rangle_{t \rightarrow \infty}^{(1,1)}. \quad (6.35)$$

The crucial expression for the DSP is

$$\begin{aligned} \langle \hat{P}_{\mathbf{k}_s, \lambda_s} \otimes \hat{\mathbb{1}}_{\text{el}} \rangle_{t \rightarrow \infty}^{(1,1)} &= \lim_{t \rightarrow \infty} \left( \frac{\alpha^2}{2} \right)^2 \iint d^3 x' d^3 x'' \int_{-\infty}^t dt' \int_{-\infty}^t dt'' \\ &\text{Tr}_{\text{el}} \left( \hat{n}(\mathbf{x}'', t'') \hat{\rho}_{\text{in}}^{\text{el}} \hat{n}(\mathbf{x}', t') \right) \text{Tr}_{\text{rad}} \left( \hat{\mathbf{A}}^2(\mathbf{x}'', t'') \hat{\rho}_{\text{in}}^X \hat{\mathbf{A}}^2(\mathbf{x}', t') \hat{P}_{\mathbf{k}_s, \lambda_s}(t) \right). \end{aligned} \quad (6.36)$$

In the case of the projection operator, the expressions become simpler than in the previous section

$$\begin{aligned} &\text{Tr}_{\text{rad}} \left( \hat{\mathbf{A}}^2(\mathbf{x}'', t'') \hat{\rho}_{\text{in}}^X \hat{\mathbf{A}}^2(\mathbf{x}', t') \hat{P}_{\mathbf{k}_s, \lambda_s}(t) \right) \\ &= \langle 1_{\mathbf{k}_s, \lambda_s} | \hat{\mathbf{A}}^2(\mathbf{x}'', t'') \hat{\rho}_{\text{in}}^X \hat{\mathbf{A}}^2(\mathbf{x}', t') | 1_{\mathbf{k}_s, \lambda_s} \rangle. \\ &= \left( \frac{4\pi}{V\alpha^2} \right)^2 \frac{1}{\omega_{\mathbf{k}_s}} \sum_{\mathbf{k}, \lambda} \sum_{1, \mu} \frac{1}{\sqrt{\omega_{\mathbf{k}} \omega_1}} e^{-i\mathbf{k}_s \cdot (\mathbf{x}'' - \mathbf{x}')} e^{i\omega_{\mathbf{k}_s}(t'' - t')} \\ &\quad \times \sum_{\{n\}, \{\bar{n}\}} \rho_{\{n\}, \{\bar{n}\}}^X \langle 1_{\mathbf{k}_s, \lambda_s} | \hat{a}_{\mathbf{k}_s, \lambda_s}^\dagger \hat{a}_{\mathbf{k}, \lambda} | \{n\} \rangle \langle \{\bar{n}\} | \hat{a}_{1, \mu}^\dagger \hat{a}_{\mathbf{k}_s, \lambda_s} | 1_{\mathbf{k}_s, \lambda_s} \rangle \\ &\quad \times e^{-i(\mathbf{k} \cdot \mathbf{x}'' - \omega_{\mathbf{k}} t'')} e^{i(1 \cdot \mathbf{x}' - \omega_1 t')} (\boldsymbol{\epsilon}_{\mathbf{k}_s, \lambda_s}^* \cdot \boldsymbol{\epsilon}_{\mathbf{k}, \lambda}) (\boldsymbol{\epsilon}_{1, \mu}^* \cdot \boldsymbol{\epsilon}_{\mathbf{k}_s, \lambda_s}) \\ &= \frac{8\pi}{V\alpha^4 \omega_{\mathbf{k}_s} \omega_{\text{in}}^2} |\boldsymbol{\epsilon}_{\mathbf{k}_s, \lambda_s}^* \cdot \boldsymbol{\epsilon}_{\mathbf{k}_{\text{in}}, \lambda_{\text{in}}}|^2 G^{(1)}(\mathbf{x}', t', \mathbf{x}'', t'') e^{-i\mathbf{k}_s \cdot (\mathbf{x}'' - \mathbf{x}')} e^{i\omega_{\mathbf{k}_s}(t'' - t')}, \end{aligned}$$

where in the last step we have made the same assumptions on the pulse as in the last section. Consequently, the DSP becomes

$$\begin{aligned} \frac{dP}{d\Omega} &= \sum_{\lambda_s} \frac{\alpha^3}{(2\pi)^2 \omega_{\text{in}}} |\boldsymbol{\epsilon}_{\mathbf{k}_s, \lambda_s}^* \cdot \boldsymbol{\epsilon}_{\mathbf{k}_{\text{in}}, \lambda_{\text{in}}}|^2 \int \frac{\omega_{\mathbf{k}_s}}{\omega_{\text{in}}} d\omega_{\mathbf{k}_s} \\ &\quad \times \iint d^3 x' d^3 x'' \int dt' \int dt'' G^{(1)}(\mathbf{x}', t', \mathbf{x}'', t'') \\ &\quad \times \text{Tr}_{\text{el}} \left( \hat{n}(\mathbf{x}'', t'') \hat{\rho}_{\text{in}}^{\text{el}} \hat{n}(\mathbf{x}', t') \right) e^{-i\mathbf{k}_s \cdot (\mathbf{x}'' - \mathbf{x}')} e^{i\omega_{\mathbf{k}_s}(t'' - t')}. \end{aligned} \quad (6.37)$$

As in the previous section, we assume that the x-ray pulse is quasi-stationary, quasi-monochromatic and introduce new variables

$$G^{(1)}(\mathbf{x}', \mathbf{x}'', \theta, \tau) = 4\pi\alpha I(\theta) e^{-\tau^2/\tau_c^2} e^{i\omega_{\text{in}}\tau} e^{-i\mathbf{k}_{\text{in}}(\mathbf{x}' - \mathbf{x}'')},$$

also we assume again that the electronic system is in a stationary state

$$\hat{\rho}_{\text{in}}^{\text{el}} = |\Psi_a\rangle \langle \Psi_a|.$$

Under these assumptions the DSP becomes

$$\begin{aligned} \frac{dP}{d\Omega} &= \mathcal{F} \left( \frac{d\sigma}{d\Omega} \right)_{\text{Th}} \int \frac{\omega_{\mathbf{k}_s}}{\omega_{\text{in}}} d\omega_{\mathbf{k}_s} \sum_f \frac{\tau_c}{\sqrt{\pi}} e^{-\tau_c^2(\omega_{\text{in}} - \omega_{\mathbf{k}_s} - (E_f - E_a))^2/4} \\ &\quad \times \iint d^3 x' d^3 x'' \langle \Psi_f | \hat{n}(\mathbf{x}'') | \Psi_a \rangle \langle \Psi_a | \hat{n}(\mathbf{x}') | \Psi_f \rangle e^{i\mathbf{Q} \cdot (\mathbf{x}'' - \mathbf{x}')}, \end{aligned} \quad (6.38)$$

where  $(\frac{d\sigma}{d\Omega})_{\text{Th}} = \alpha^4 \sum_{\lambda_s} |\boldsymbol{\epsilon}_{\mathbf{k}_s, \lambda_s}^* \cdot \boldsymbol{\epsilon}_{\mathbf{k}_{\text{in}}, \lambda_{\text{in}}}|^2$  is the Thomson cross section and  $\mathcal{F} = \int d\theta \frac{I(\theta)}{\omega_{\text{in}}}$  is the photon fluence of the incoming x-ray pulse.

Neglecting the bandwidth of the pulse, yields  $\omega_{\mathbf{k}_s} = \omega_{\text{in}} - (E_f - E_a)$  and

$$\frac{dP}{d\Omega} = \mathcal{F} \left( \frac{d\sigma}{d\Omega} \right)_{\text{Th}} \sum_f \frac{\omega_f}{\omega_{\text{in}}} \left| \int d^3x \langle \Psi_f | \hat{n}(\mathbf{x}) | \Psi_a \rangle e^{i\mathbf{Q} \cdot \mathbf{x}} \right|^2. \quad (6.39)$$

For elastic scattering, we obtain the DSP

$$\frac{dP}{d\Omega} = \mathcal{F} \left( \frac{d\sigma}{d\Omega} \right)_{\text{Th}} \left| \int d^3x \langle \Psi_a | \hat{n}(\mathbf{x}) | \Psi_a \rangle e^{i\mathbf{Q} \cdot \mathbf{x}} \right|^2. \quad (6.40)$$

Finally, we can compare the (1,1) term of the Poynting operator in Eq. (6.28) with the present result in Eq. (6.39). First, one notices that the latter yields an expression that is already time-integrated, whereas the former yields an instantaneous intensity. More importantly, the Poynting operator depends on the detector orientation  $\mathbf{d}$  and the detector distance  $r$ . This reflects that the Poynting operator models a detector placed at a given position, in contrast to the projection observable that analyzes the mode composition of the scattered radiation field. Moreover, there is a difference of prefactors between the two results. The expectation value of the Poynting operator gives an energy flux. Thus, the energy flux of the incoming beam  $I(t)$  is multiplied with the energy ratio  $\omega_f/\omega_{\text{in}}$ . The DSP, on the other hand, corresponds to a probability and is a number. The time integrated flux  $\int d\theta I(\theta)$  is the energy  $N_{\text{ph}}\omega_{\text{in}}$  per unit area, such that the DSP depends on the number of photons  $N_{\text{ph}}$  in the incoming pulse.

# Chapter 7.

## Time-resolved imaging of coherent electronic motion

In this chapter I scrutinize the time-resolved x-ray scattering from ultrafast coherent electronic motion in the far-field.

In Sec. 7.2 I introduce the problems emerging in time-resolved x-ray diffraction experiments.

In Sections 7.3 and 7.4 I present results that were obtained in collaboration with G. Dixit and R. Santra. These results were published in the article [3]:

DIXIT, SLOWIK, SANTRA *Phys. Rev. A* **89**, 043409 (2014).

In Sec. 7.3 the influence of photon energy resolution is investigated. In Sec. 7.4 I discuss the connection to the time-resolved imaging scheme by Abbamonte and coworkers.

Finally, in Sec. 7.5 I propose time-resolved Compton scattering in the regime of the impulse approximation to investigate electronic wave packets. The results of this section are not yet published.

### 7.1. Motivation

Coherent electronic motion is a fundamental electronic processes in ultrafast science [74]. It is, for example, held responsible for charge and energy transfer in molecules like biological light-harvesting complexes. Moreover, coherent electronic motion plays a leading role in chemical bond breaking and formation during chemical reactions. A thorough understanding of coherent electronic motion requires to unravel the electronic dynamics in real-time. The electronic structure of atomic and molecular systems can be studied with x-ray radiation. With the advent of X-ray free-electron lasers, a radiation source emerged that combines ultrafast time-resolution with atomic spatial resolution. The imaging of coherent electronic motion in real-time has recently seen a lot of progress in experiment [78–87] and in theory [3, 88, 94, 98, 107–112].

In this chapter, x-ray imaging of coherent electronic motion in real-time and real-space is investigated. X-rays are a versatile tool to image electronic structure of atomic and molecular systems. X-ray scattering is a well-established and widespread method to explore atomic-scale structure of matter in real-space. X-rays have a sufficiently small wavelength to gain atomic resolution. The field of x-ray crystallography, for example, is an extremely fruitful application of x-ray diffraction [113, 114] that yields atomic resolution images of molecules. Even single molecule imaging with atomic scale resolution is envisaged in the near future. Moreover, the appeal of x-ray diffraction to gain atomic-scale structural information is the relation of the diffraction pattern with the electron density of the target. In Eq. (6.40) we found the diffraction pattern of elastic scattering from a stationary electronic state

$$\frac{dP}{d\Omega} = \mathcal{F} \left( \frac{d\sigma}{d\Omega} \right)_{\text{Th}} \left| \int d^3x \langle \Psi_a | \hat{n}(\mathbf{x}) | \Psi_a \rangle e^{i\mathbf{Q} \cdot \mathbf{x}} \right|^2. \quad (7.1)$$

This diffraction pattern encodes the modulus square of the Fourier transformation of the electron density. In many cases this allows the reconstruction of the electron density.

Furthermore, ultrashort x-ray pulses broaden the horizon of x-ray imaging to the time domain. Ultrafast XUV-imaging experiments have been performed in the energy domain [79, 87] yielding ultrafast time-resolution. Ultrafast x-ray diffraction to image ultrafast molecular dynamics has been proposed more than fifteen years ago [115, 116] for imaging nuclear dynamics in chemical reactions. First formulations with a quantized radiation field were given in [107, 117]. Time-resolved x-ray diffraction of nonstationary states differs drastically from diffraction off stationary states. In the nonstationary case, inelastic scattering is not negligible and changes the diffraction pattern [117, 118]. X-ray scattering experiments with ultrafast time-resolution are typically performed in a pump-probe setup. The principle of the pump-probe scheme is very simple. In a first step, the dynamics are triggered by exciting the sample into a nonstationary state. Typically, this is done using an ultrashort optical or x-ray pulse, called the pump pulse. In the second step, one performs the measurement after a well-defined delay time. Here, we consider x-ray diffraction of an ultrafast x-ray pulse, called probe pulse. This pump-probe experiment is performed repeatedly for different delay times. For each delay time one records the diffraction pattern. Evaluation of the diffraction data for different delay times yields the information on the dynamics.

One strives for time-resolved real-space information of coherent electronic dynamics. Surprisingly, the real-space and real-time imaging of electronic wave packets by coherent diffraction of x-rays or electrons turned out to be more difficult than the imaging of stationary electronic systems [88, 91, 98]. This situation is even more intricate than in the case of nuclear dynamics. The time-scale of electronic motion is typically so fast that ultrafast pulses with a considerable bandwidth are inevitable

and whether transitions occurred elastically or inelastically becomes energetically indistinguishable. The first analysis of the x-ray diffraction pattern from a coherent electronic wave packet was presented in Ref. [88]. Subsequently, the result was extended to a two-electron system [94]. A comparable result was established for electron diffraction [98]. The diffraction pattern does not simply encode the instantaneous electron density, but more complicated spatio-temporal electron density-density correlations [3, 88, 98, 111]. Even mimicking the case of elastic scattering by high energy resolving detectors, one does not recover the simple classical diffraction pattern. This chapter is intended to shine some light on the question which physical information is encoded in the diffraction pattern of time-resolved x-ray diffraction.

## 7.2. The time-resolved x-ray scattering of electronic wave packets

### 7.2.1. Theory of time-resolved x-ray scattering

#### The differential scattering probability

In this paragraph, I recall the derivation of the differential scattering probability (DSP) from [88]. Assume the wave packet has been created by a suitable pump-pulse and is specified by the density operator

$$\hat{\rho}_{\text{in}}^{\text{el}} = |\Psi_{\text{el}}\rangle\langle\Psi_{\text{el}}| = \sum_{i,j} \rho_{i,j} |\Psi_i\rangle\langle\Psi_j|. \quad (7.2)$$

The DSP in Eq. (6.37) contains the crucial term  $\text{Tr}_{\text{el}}(\hat{n}(\mathbf{x}'', t'') \hat{\rho}_{\text{in}}^{\text{el}} \hat{n}(\mathbf{x}', t'))$  which after the usual change of variables  $\theta = \frac{t'+t''}{2}$  and  $\tau = t' - t''$ , becomes

$$\begin{aligned} & \sum_f \langle\Psi_f|\hat{n}(\mathbf{x}'', \theta - \frac{\tau}{2})|\Psi_{\text{el}}\rangle\langle\Psi_{\text{el}}|\hat{n}(\mathbf{x}', \theta + \frac{\tau}{2})|\Psi_f\rangle \\ & = \sum_f e^{-iE_f\tau} \langle\Psi_f|\hat{n}(\mathbf{x}'') e^{-i\hat{H}_{\text{el}}(\theta-\tau/2)} |\Psi_{\text{el}}\rangle\langle\Psi_{\text{el}}| e^{i\hat{H}_{\text{el}}(\theta+\tau/2)} \hat{n}(\mathbf{x}')|\Psi_f\rangle. \end{aligned} \quad (7.3)$$

One of the premises for the pump-probe scheme is that the probe pulse duration is much shorter than the dynamics one wishes to snapshot. Consequently, we require the x-ray pulse duration  $T_{\text{rad}}$  to be short enough to “freeze” the wave packet, i.e., we assume that wave packet dynamics can be neglected on time scales of  $T_{\text{rad}}$ . As before (see Sections 3.2.2 and 6.3), we assume a quasi-stationary, quasi-monochromatic correlation function for the x-ray pulse that is coherent over the extent of the object

$$G^{(1)}(\mathbf{x}', \mathbf{x}'', \theta, \tau) = 4\pi\alpha I(\theta) e^{-\tau^2/\tau_c^2} e^{i\omega_{\text{in}}\tau} e^{-i\mathbf{k}_{\text{in}}(\mathbf{x}'-\mathbf{x}'')}. \quad (7.4)$$

Note that in Ref. [88] an ensemble of coherent Gaussian pulses was used, which has a very similar correlation function

$$G^{(1)}(\mathbf{x}', \mathbf{x}'', \theta, \tau) = 2\pi\alpha I(\theta) e^{-2\ln 2 \tau^2/T_{\text{rad}}^2} e^{i\omega_{\text{in}}\tau} e^{-i\mathbf{k}_{\text{in}}\cdot(\mathbf{x}'-\mathbf{x}'')}. \quad (7.5)$$

However, for the quasi-stationary ensemble of partially coherent pulses the coherence time  $\tau_c$  is much shorter than the pulse duration. In both cases, the correlation function vanishes for  $\tau$ -values that exceed the pulse duration.

It is assumed that the probe pulse intensity  $I(\theta)$  is centered at the pump-probe delay time  $\tau_{\text{delay}}$ . We denote  $\exp(-i\hat{H}_{\text{el}}\tau_{\text{delay}})|\Psi_{\text{el}}\rangle$  by  $|\Psi_{\text{el}}(\tau_{\text{delay}})\rangle$ . Let  $E_{\text{el}}$  denote the expectation value for the energy of the wave packet. If the pulse duration is short enough to freeze the wave packet, then  $|E_i - E_j| \ll 1/\tau_c$  must hold for all energies  $E_i, E_j$  of eigenstates contained in the wave packet. Then this must also hold for the expectation value  $|E_i - E_{\text{el}}| \ll 1/\tau_c$ . Consequently, the time-evolution of the wave packet can be approximated

$$e^{i\hat{H}_{\text{el}}\tau/2} |\Psi_{\text{el}}\rangle \langle \Psi_{\text{el}}| e^{i\hat{H}_{\text{el}}\tau/2} = \sum_{i,j} \rho_{i,j} e^{i(E_i+E_j)\tau/2} |\Psi_i\rangle \langle \Psi_j| \quad (7.6)$$

$$\approx e^{iE_{\text{el}}\tau} |\Psi_{\text{el}}\rangle \langle \Psi_{\text{el}}|. \quad (7.7)$$

From (6.37) one obtains the DSP

$$\begin{aligned} \frac{dP}{d\Omega} &= \mathcal{F} \left( \frac{d\sigma}{d\Omega} \right)_{\text{Th}} \int \frac{\omega_{\mathbf{k}_s}}{\omega_{\text{in}}} d\omega_{\mathbf{k}_s} \sum_f \frac{\tau_c}{\sqrt{\pi}} e^{-\tau_c^2(\omega_{\text{in}}-\omega_{\mathbf{k}_s}+E_{\text{el}}-E_f)^2/4} \iint d^3x' d^3x'' \\ &\times \langle \Psi_f | \hat{n}(\mathbf{x}'') | \Psi_{\text{el}}(\tau_{\text{delay}}) \rangle \langle \Psi_{\text{el}}(\tau_{\text{delay}}) | \hat{n}(\mathbf{x}') | \Psi_f \rangle e^{i\mathbf{Q}\cdot(\mathbf{x}''-\mathbf{x}')}. \end{aligned} \quad (7.8)$$

Introducing the function of the Hamiltonian  $C(\hat{H}_{\text{el}}) = \frac{\tau_c}{\sqrt{\pi}} e^{-\tau_c^2(\omega_{\text{in}}-\omega_{\mathbf{k}_s}+E_{\text{el}}-\hat{H}_{\text{el}})^2/4}$  the last result takes the form

$$\begin{aligned} \frac{dP}{d\Omega} &= \mathcal{F} \left( \frac{d\sigma}{d\Omega} \right)_{\text{Th}} \int \frac{\omega_{\mathbf{k}_s}}{\omega_{\text{in}}} d\omega_{\mathbf{k}_s} \\ &\times \iint d^3x' d^3x'' \langle \Psi_{\text{el}}(\tau_{\text{delay}}) | \hat{n}(\mathbf{x}') C(\hat{H}_{\text{el}}) \hat{n}(\mathbf{x}'') | \Psi_{\text{el}}(\tau_{\text{delay}}) \rangle e^{i\mathbf{Q}\cdot(\mathbf{x}''-\mathbf{x}')}. \end{aligned} \quad (7.9)$$

In the case of a stationary electronic state, a simple Fourier transform relationship between the DSP and the electron density holds, see Eq. (6.40). The preceding results, however, lead to the surprising conclusion that the simple Fourier transform relationship is not valid when imaging coherent electronic wave packets. In the present case of time-resolved imaging of ultrafast coherent electronic dynamics the situation is more intricate. There is an essential difference: the ultrashort probe pulse unavoidably requires a broad bandwidth. As a consequence, the bandwidth of the pulse cannot be neglected. At least the inelastic scattering where the energy

transfer is smaller than the bandwidth of the pulse has to be taken into account. Can one somehow select only the elastic scattering contributions? Consider the case of energy filtering the final photon energy or measuring the final electronic state. This would not completely exclude inelastic scattering, because it could only reduce the set of final electronic states to all states in the subspace spanned by the states  $|\Psi_i\rangle$  contained in the wave packet  $|\Psi_{\text{el}}\rangle = \sum_i c_i |\Psi_i\rangle$ . Recall that the pulse was required to “freeze” the wave packet, i.e.,  $|E_i - E_j| \ll \Delta\omega$ . Going a step further, consider the case where the scattering does not affect the wave packet, i.e., after the scattering process the electronic system is still in the wave packet state  $|\Psi_f\rangle = |\Psi_{\text{el}}\rangle$ . Is the scattering process then purely elastic? No, electronic transitions between the states of the wave packet may have occurred in the scattering process. The energy transfer from these transitions to the photon lies within the bandwidth of the pulse. Although this is a case of coherent scattering, it does not need to be elastic, see Sec. 7.3.2.

### Measurements with photon energy resolution

In order to minimize the contributions of inelastic scattering, the authors of Ref. [88] assumed the photon detector to be energy resolving and considered only quasielastic scattering. Energy resolution can be incorporated in the model by introducing a spectral window function  $W_{\Delta E}(\omega_{\mathbf{k}_s})$  into the observable

$$\hat{O} = W_{\Delta E}(\omega_{\mathbf{k}_s}) \hat{P}_{\mathbf{k}_s, \lambda_s} \otimes \hat{\mathbb{1}}_{\text{el}}. \quad (7.10)$$

The spectral window function  $W_{\Delta E}$  is centered at  $\omega_{\text{in}}$ , has a width  $\Delta E$ , and takes values between 0 and 1.  $W_{\Delta E}(\omega_{\mathbf{k}_s})$  is zero if the detector is completely unresponsive to photons of the given photon energy and is equal to one if the detector counts all photons of the given photon energy.

Introducing a spectral window function with  $\Delta E$  much narrower than the bandwidth reduces the contributions from inelastic scattering. Only the scattering events with final photon energy  $\omega_{\mathbf{k}_s}$  in the interval  $\omega_{\text{in}} \pm \Delta E$  are accepted. The final expression in Eq. (7.9) simplifies to the main result of [88]

$$\frac{dP}{d\Omega} = \mathcal{F} \left( \frac{d\sigma}{d\Omega} \right)_{\text{Th}} \iint d^3x' d^3x'' \langle \hat{n}(\mathbf{x}') C(\hat{H}_{\text{el}}) \hat{n}(\mathbf{x}'') \rangle_{\tau_{\text{delay}}} e^{i\mathbf{Q} \cdot (\mathbf{x}'' - \mathbf{x}')}, \quad (7.11)$$

where  $\langle \dots \rangle_{\tau_{\text{delay}}}$  denotes the expectation value with respect to  $|\Psi_{\text{el}}(\tau_{\text{delay}})\rangle$  and  $C(\hat{H}_{\text{el}}) = \frac{\tau_c}{\sqrt{\pi}} e^{-\tau_c^2 (E_{\text{el}} - \hat{H}_{\text{el}})^2 / 4}$ . In the next subsection we illustrate the consequences of this DSP by means of a concrete example.

### Uniqueness of pixels in reciprocal space

The x-ray scattering pattern contains information about the reciprocal space of the target (Q-space). The scattering pattern is sampled by the detector pixels.

If the scattering is purely elastic, the size of the target determines the required sampling frequency in reciprocal space. In coherent diffractive imaging the pixel size determines the field-of-view, which obviously should comprise the complete wave packet. This constrains the Q-space pixel size to  $\Delta Q_{\max} = \frac{\pi}{D}$ , for an object of size  $D$ . Thus, the detector geometry and the detector pixel size limit the maximal extension of the target, cf. [119].

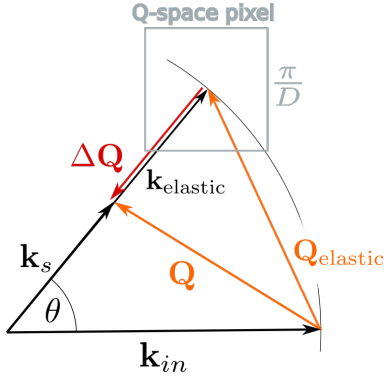


Figure 7.1.: Momentum transfer vectors of elastic  $\mathbf{Q}_{\text{elastic}}$  and inelastic scattering  $\mathbf{Q}$ :  $\mathbf{Q}$  does not point into the same Q-space pixel as  $\mathbf{Q}_{\text{elastic}}$ .

Here, we discuss an additional limitation on the target size. Each detector pixel detects the scattering signal of photons with  $\mathbf{k}_s$  pointing into the pixel, cf. Chap. 6. The momentum transfer vector  $\mathbf{Q} = \mathbf{k}_{\text{in}} - \mathbf{k}_s$  depends on the direction and magnitude of  $\mathbf{k}_s$ . This means, the signal in a given detector pixel may correspond to vectors  $\mathbf{Q}$  that cover a large region in reciprocal space. As a consequence, the signal of a detector pixel may not correspond to a single Q-space pixel (see Fig. 7.1). For a meaningful mapping between reciprocal space and scattering signal one needs a one-to-one correspondence of Q-space pixels and detector pixels. Hence, we require sufficiently large Q-space pixels, such that the scattering signal in one detector pixel corresponds to only one Q-space pixel. However, the maximal Q-space pixel size is  $\Delta Q_{\max} = \frac{\pi}{D}$ . Thus, the wave packet has to be sufficiently small for both conditions to

be fulfilled.

I present a simple estimation of the maximal extension of the wave packet. In the case when a spectral window function with width  $\Delta E$  is used, we have at worst  $k_s = |\mathbf{k}_s| = k_{\text{in}} - \alpha \Delta E$  and  $Q = |\mathbf{Q}| = \sqrt{k_{\text{in}}^2 + k_s^2 - 2k_{\text{in}}k_s \cos \theta}$ . The momentum transfer change  $\Delta Q = |\mathbf{Q}_{\text{elastic}} - \mathbf{Q}|$  is

$$\Delta Q = \frac{Q_{\text{elastic}}^2}{2k_{\text{in}}} - \sqrt{\left(\frac{Q_{\text{elastic}}^2}{2k_{\text{in}}}\right)^2 - Q_{\text{elastic}}^2 + Q^2}, \quad (7.12)$$

where the momentum transfer in elastic scattering is  $Q_{\text{elastic}} = 2k_{\text{in}} \sin(\theta/2)$ . From the condition that the maximal  $\Delta Q$  should be less than half the maximal pixel size

$$\Delta Q \leq \frac{\pi}{2D}, \quad (7.13)$$

one obtains the maximal possible size of the wave packet  $D$ . Consider a 4 keV x-ray pulse and a maximal scattering angle of  $\theta = 60^\circ$  and  $\Delta E \approx 1$  eV, corresponding

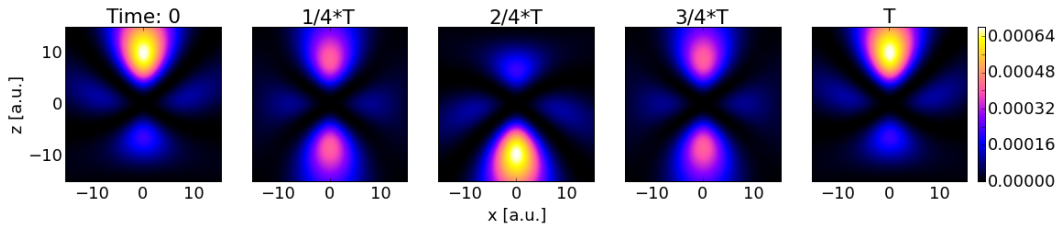


Figure 7.2.: The hydrogen 3d-4f wave packet: the instantaneous electron density sliced in the  $x, z$ -plane for  $y = 0$ . (Figure identical to Fig. 5.1)

to the bandwidth of a 1 fs pulse. The condition (7.13) is then fulfilled for  $D$  up to about 300 nm.

The situation is different without energy resolution. In this case one needs to estimate the maximal photon energy shift. The photon energy of the peak of the spectrum can be estimated by Compton's formula [120]:

$$\omega_{\text{peak}} = \frac{\omega_{\text{in}}}{1 + \alpha^2 \omega_{\text{in}} (1 - \cos \theta)}. \quad (7.14)$$

Because the spectrum is approximately symmetric one may take  $\Delta\omega$  as twice the Compton shift  $\omega_{\text{in}} - \omega_{\text{peak}}$ . With the same parameters, condition (7.13) is valid only for wave packets up to about 10 nm.

### 7.2.2. Application to the hydrogen 3d-4f wave packet

In Ref. [88] the DSP of a coherent electronic wave packet was explicitly calculated for the 3d-4f wave packet of hydrogen, which we have already encountered in Sec. 5.2.2. The wave packet is an equal superposition of the 3d and 4f eigenstates of atomic hydrogen with vanishing magnetic quantum number

$$|\Psi_{\text{el}}\rangle = \frac{1}{\sqrt{2}}|\varphi_{3,2,0}\rangle + \frac{1}{\sqrt{2}}|\varphi_{4,3,0}\rangle. \quad (7.15)$$

The wave packet has rotational symmetry around the quantization axis (here  $z$ -axis). A two-dimensional slice through the origin of the instantaneous electron density of the wave packet is shown in Fig. 7.2. The electron density of the wave packet oscillates with a period of  $T = 6.25$  fs up and down along the  $z$ -axis. The wave packet has an extension of about 14–17 Å along the  $z$ -axis and 7.5–9 Å along the  $x$ - and  $y$ -axes.

This wave packet is a convenient choice to illustrate the consequences of the differential scattering probability from quantum theory

$$\frac{dP}{d\Omega} = \mathcal{F} \left( \frac{d\sigma}{d\Omega} \right)_{\text{Th}} \iint d^3x' d^3x'' \langle \hat{n}(\mathbf{x}') C(\hat{H}_{\text{el}}) \hat{n}(\mathbf{x}'') \rangle_{\tau_{\text{delay}}} e^{i\mathbf{Q} \cdot (\mathbf{x}'' - \mathbf{x}')}. \quad (7.16)$$

In Ref. [88] the quantum theory has been compared with the semiclassical expression

$$\frac{dP}{d\Omega} = \mathcal{F} \left( \frac{d\sigma}{d\Omega} \right)_{\text{Th}} \left| \int d^3x \langle \hat{n}(\mathbf{x}) \rangle_{\tau_{\text{delay}}} e^{i\mathbf{Q} \cdot \mathbf{x}} \right|^2, \quad (7.17)$$

which depends only on the instantaneous electron density of the wave packet. Note that simply inserting the instantaneous electron density of the wave packet into DSP of a stationary target, Eq. (6.40), also yields Eq. (7.17).

The main result of Ref. [88] is shown in Fig. 7.3, where a 1 fs x-ray pulse with 4 keV photon energy and  $\sim 1$  eV bandwidth was assumed. To reduce contributions from inelastic scattering a spectral window function with width  $\Delta E = 0.5$  eV was used. The upper panel in Fig. 7.3 shows the DSP from Eq. (7.16) calculated for values in the  $Q_x, Q_z$ -plane. The lower panel shows the DSP from Eq. (7.17). One immediately notices that quantum and semiclassical theory yield completely different scattering signals. The scattering signal from Eq. (7.16) exhibits higher intensities due to inelastic scattering contributions. More importantly, the two results differ in the oscillation period of the patterns. The diffraction pattern in the upper panel has the same oscillation period as the wave packet, whereas the signal from Eq. (7.17) in the lower panel has half the period. Moreover, the signal from Eq. (7.16) is, unlike the semiclassical scattering signal, not centrosymmetric, i.e., it does not obey Friedel's law. In conclusion, Fig. 7.3 shows that the scattering pattern from an electronic wave packet encodes complex electron density correlations and not simply the Fourier transform of the instantaneous electron density.

## 7.3. Unravelling the time-resolved diffraction pattern

### 7.3.1. Dynamical structure factor and influence of energy resolution

In the previous section, it was demonstrated that the x-ray scattering pattern of electronic wave packets is more complex than the x-ray scattering pattern of stationary systems. Unfortunately, we have no direct physical interpretation of the scattering pattern at hand. Moreover, it is not clear how to reconstruct the wave packet from the scattering pattern. The aim of this section is a better understanding of the scattering pattern in physical terms. In the example of the last section, the spectral window function was chosen to mimic elastic coherent diffractive imaging. I explore the consequence of this energy resolution.

The DSP for the time-resolved imaging of a coherent electronic wave packet has been derived in Eq. (7.8). Introducing the spectral window function  $W_{\Delta E}(\omega_{\mathbf{k}_s})$  and

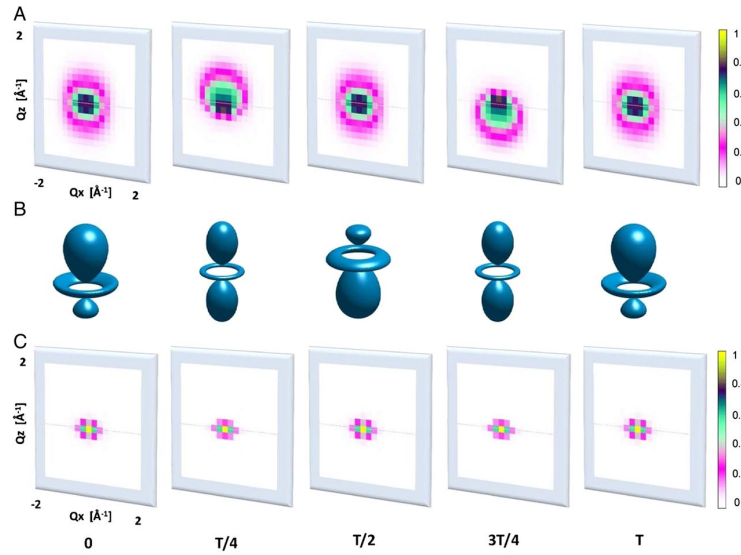


Figure 7.3.: Scattering patterns in the  $Q_x$ - $Q_z$  plane ( $Q_y = 0$ ) of the 3d-4f wave packet at pump-probe delay times 0,  $T/4$ ,  $T/2$ ,  $3T/4$ , and  $T$ .

(A) QED scattering patterns obtained from Eq. (7.16),

(B) Instantaneous electron density (isosurface enclosing  $\sim 26\%$  of the total probability), and

(C) Semiclassical scattering patterns obtained from Eq. (7.17).

The wavepacket is exposed to a 1 fs X-ray pulse with 4 keV photons. A spectral window function with width  $\Delta E = 0.5$  eV is assumed. The intensities of the patterns are shown in units of  $(\frac{d\sigma}{d\Omega})_{Th}$  in both cases.

Figure taken from (Dixit, Vendrell, Santra PNAS **109**, 11636) [88].

© 2012 Dixit, Vendrell, Santra.

rearranging the expression, it can be written as

$$\begin{aligned} \frac{dP}{d\Omega} &= \mathcal{F} \left( \frac{d\sigma}{d\Omega} \right)_{\text{Th}} \int d\omega_{\mathbf{k}_s} W_{\Delta E}(\omega_{\mathbf{k}_s}) \frac{\omega_{\mathbf{k}_s}}{\omega_{\text{in}}} \\ &\times \sum_f \frac{\tau_c}{\sqrt{\pi}} e^{-\tau_c^2(\omega_{\text{in}} - \omega_{\mathbf{k}_s} + E_{\text{el}} - E_f)^2/4} \left| \int d^3x \langle \Psi_f | \hat{n}(\mathbf{x}, \tau_{\text{delay}}) | \Psi_{\text{el}} \rangle e^{i\mathbf{Q} \cdot \mathbf{x}} \right|^2. \end{aligned} \quad (7.18)$$

The last equation suggests the definition of a generalized dynamical structure factor (DSF) [3]

$$\tilde{S}(\mathbf{Q}, \omega, \tau_{\text{delay}}) = \sum_f \frac{\tau_c}{\sqrt{\pi}} e^{-\tau_c^2(\omega_{\text{in}} - \omega_{\mathbf{k}_s} + E_{\text{el}} - E_f)^2/4} \left| \int d^3x \langle \Psi_f | \hat{n}(\mathbf{x}, \tau_{\text{delay}}) | \Psi_{\text{el}} \rangle e^{i\mathbf{Q} \cdot \mathbf{x}} \right|^2,$$

such that the DSP becomes

$$\frac{dP}{d\Omega} = \mathcal{F} \left( \frac{d\sigma}{d\Omega} \right)_{\text{Th}} \int d\omega_{\mathbf{k}_s} W_{\Delta E}(\omega_{\mathbf{k}_s}) \frac{\omega_{\mathbf{k}_s}}{\omega_{\text{in}}} \tilde{S}(\mathbf{Q}, \omega, \tau_{\text{delay}}). \quad (7.19)$$

The generalized DSF depends on the momentum transfer  $\mathbf{Q}$ , the energy transfer  $\omega = \omega_{\text{in}} - \omega_{\mathbf{k}_s}$ , and the pump-probe delay time  $\tau_{\text{delay}}$ .

In the case of a stationary target the DSP expressed in terms of  $S(\mathbf{Q}, \omega)$  is [21]

$$\frac{dP}{d\Omega} = \mathcal{F} \left( \frac{d\sigma}{d\Omega} \right)_{\text{Th}} \int d\omega_{\mathbf{k}_s} W_{\Delta E}(\omega_{\mathbf{k}_s}) \frac{\omega_{\mathbf{k}_s}}{\omega_{\text{in}}} S(\mathbf{Q}, \omega). \quad (7.20)$$

The DSF of a stationary target is time-independent. In fact, the DSF is the Fourier transform of the van Hove correlation function [121] and

$$S(\mathbf{Q}, \omega) = \sum_f \delta(\omega + E_i - E_f) \left| \int d^3x \langle \Psi_f | \hat{n}(\mathbf{x}) | \Psi_i \rangle e^{i\mathbf{Q} \cdot \mathbf{x}} \right|^2. \quad (7.21)$$

Note that in the case of a stationary target, the x-ray pulse does not need to be ultrafast. By making the pulse duration and the coherence time  $\tau_c$  sufficiently large, the bandwidth of the pulse can, in principle, be made arbitrarily small – recall that  $\Delta\omega = 1/\tau_c$ , cf. Sec. 3.2.2. In this limit the generalized DSF recovers the usual DSF for stationary targets

$$\tilde{S}(\mathbf{Q}, \omega, \tau_{\text{delay}}) \xrightarrow{\tau_c \rightarrow \infty} S(\mathbf{Q}, \omega) \quad \text{for a stationary target.} \quad (7.22)$$

In the following, we analyze the role of the spectral window function, i.e., the role of photon energy resolution in the measurement.

### No energy resolution

The case of no energy resolution is certainly the easiest to realize experimentally: the x-ray photon detector counts the photons, but does not resolve the photon energy. Typically, the pixel array detectors used for coherent diffractive imaging at x-ray free electron lasers fall into this category [99, 100]. In the formalism, this case corresponds to a constant spectral window function. Thus, let us assume  $\Delta E$  to be broad enough to include all scattered photon energies and  $W_{\Delta E}(\omega_{\mathbf{k}_s})$  constant over the range of  $\Delta E$ . Moreover, let us assume the target size and the spectrum of scattered photon energies to be such that the uniqueness of pixels in Q-space is guaranteed, cf. the last paragraph of Sec. 7.2.1. Since we consider x-ray pulses with photon energies far above the absorption edges of the system, we may assume the photon energy to be much higher than the energy transfer  $\omega_{\text{in}} \gg |E_{\text{el}} - E_f|$ . The crucial integral over photon energies in Eq. (7.18) may be approximated

$$\int_0^{\infty} d\omega_{\mathbf{k}_s} \frac{\omega_{\mathbf{k}_s}}{\omega_{\text{in}}} \frac{\tau_c}{\sqrt{\pi}} e^{-\tau_c^2(\omega_{\text{in}} - \omega_{\mathbf{k}_s} + E_{\text{el}} - E_f)^2/4} \approx 1. \quad (7.23)$$

From Eq. (7.18) we obtain the DSP [3]

$$\frac{dP}{d\Omega} = \mathcal{F} \left( \frac{d\sigma}{d\Omega} \right)_{\text{Th}} \sum_f \left| \int d^3x \langle \Psi_f | \hat{n}(\mathbf{x}, \tau_{\text{delay}}) | \Psi_{\text{el}} \rangle e^{i\mathbf{Q}\cdot\mathbf{x}} \right|^2. \quad (7.24)$$

Observe that this result depends on the pump-probe delay  $\tau_{\text{delay}}$ , otherwise it equals the result for the stationary case. This is remarkable because it opens the possibility to measure wave packet dynamics without energy resolution. In particular, it is well-known that the stationary DSP encodes the pair-correlation function of the system [121]. Electron-correlation effects have been investigated experimentally by inelastic x-ray scattering [21, 122–125]. First ultrafast time-resolved measurements have been performed on phonons [126]. The result in Eq. (7.24) suggests that time-resolved measurements of time-dependent electronic correlations in electronic motion are feasible.

### High energy resolution

Consider a setup where the photon detector measures, in addition to the scattering pattern, spectral information with high photon energy resolution. In particular, let us consider the case where the energy resolution is finer than the bandwidth of the incoming x-ray pulse. Let the photon energy that the detector observes be  $\omega_{\text{obs}}$ . This situation is modelled by a spectral window function  $W_{\Delta E}(\omega_{\mathbf{k}_s} - \omega_{\text{obs}})$  with

$$\int_0^{\infty} d\omega_{\mathbf{k}_s} W_{\Delta E}(\omega_{\mathbf{k}_s} - \omega_{\text{obs}}) = \Delta E. \quad (7.25)$$

Because we consider the energy resolution  $\Delta E$  much finer than the bandwidth, we may assume for the detected photon energies  $|\omega_{\mathbf{k}_s} - \omega_{\text{obs}}| \leq \Delta E$  that

$$e^{-\tau_c^2(\omega_{\text{in}} - \omega_{\mathbf{k}_s} + E_{\text{el}} - E_f)^2/4} \approx e^{-\tau_c^2(\omega_{\text{in}} - \omega_{\text{obs}} + E_{\text{el}} - E_f)^2/4} .$$

This yields the approximation for the photon energy integral

$$\begin{aligned} & \int_0^\infty d\omega_{\mathbf{k}_s} W_{\Delta E}(\omega_{\mathbf{k}_s} - \omega_{\text{obs}}) \frac{\omega_{\mathbf{k}_s}}{\omega_{\text{in}}} \frac{\tau_c}{\sqrt{\pi}} e^{-\tau_c^2(\omega_{\text{in}} - \omega_{\mathbf{k}_s} + E_{\text{el}} - E_f)^2/4} \\ & \approx \Delta E \frac{\tau_c}{\sqrt{\pi}} e^{-\tau_c^2(\omega_{\text{in}} - \omega_{\text{obs}} + E_{\text{el}} - E_f)^2/4} , \end{aligned} \quad (7.26)$$

where  $\omega_{\text{obs}} \approx \omega_{\text{in}}$  was used. Substituting into Eq. (7.18) yields the DSP [3]

$$\begin{aligned} \frac{dP}{d\Omega} &= \mathcal{F} \left( \frac{d\sigma}{d\Omega} \right)_{\text{Th}} \Delta E \\ & \times \sum_f \frac{\tau_c}{\sqrt{\pi}} e^{-\tau_c^2(\omega_{\text{in}} - \omega_{\text{obs}} + E_{\text{el}} - E_f)^2/4} \left| \int d^3x \langle \Psi_f | \hat{n}(\mathbf{x}, \tau_{\text{delay}}) | \Psi_{\text{el}} \rangle e^{i\mathbf{Q} \cdot \mathbf{x}} \right|^2 \\ & = \mathcal{F} \left( \frac{d\sigma}{d\Omega} \right)_{\text{Th}} \Delta E \tilde{S}(\mathbf{Q}, \omega_{\text{in}} - \omega_{\text{obs}}, \tau_{\text{delay}}) . \end{aligned} \quad (7.27)$$

$$(7.28)$$

This result shows that with high energy resolution one can measure the generalized DSF  $\tilde{S}(\mathbf{Q}, \omega, \tau_{\text{delay}})$  by varying  $\omega_{\text{obs}}$ . In the case  $\omega_{\text{obs}} = \omega_{\text{in}}$  one measures  $\tilde{S}(\mathbf{Q}, 0, \tau_{\text{delay}})$ . This special case of quasielastic scattering comes closest to what could be considered as time-resolved coherent diffractive imaging of the wave packet. However, this special case does not recover the elastic diffraction pattern of the instantaneous electron density. As demonstrated in the last section, due to the unavoidable inelastic transitions within the inevitable bandwidth of the pulse, the scattering signal depends on the spatio-temporal density-density correlation of the wave packet.

### 7.3.2. Crystals: Recovering the instantaneous electron density

Is there no way to recover the instantaneous electron density by x-ray scattering from a coherent electronic wave packet? If the wave packet is not disturbed by the scattering, i.e., the initial and final state of the scattering process are equal, the scattering pattern depends only on the instantaneous electron density. However, in Section 7.2.1 we have already stated that it is impossible to filter out these terms energetically. But there is another way to select the scattering terms for which initial and final state are indistinguishable. X-ray diffraction from a crystal can distinguish the coherent from the incoherent scattering terms, as will be shown in the following.

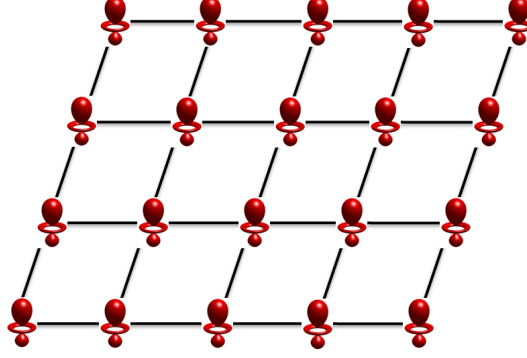


Figure 7.4.: A two-dimensional view of a crystal made of identical atoms prepared in exactly the same quantum superposition and with identical phase.”

Figure taken from (Dixit, Slowik, Santra, PRA **89**, 043409) [3].

© 2014 American Physical Society.

Assume we are given a crystal, where at each lattice site a realization of the wave packet is prepared. Let all these wave packets be excited simultaneously, all with the same phase. Furthermore, we assume that all sub-units of the crystal are noninteracting.

To select the coherent and incoherent scattering signal, we decompose the final states into projections onto the wave packet and the orthogonal complement. We project states onto the wave packet with  $|\Psi_{\text{el}}\rangle\langle\Psi_{\text{el}}|$  and onto the orthogonal complement with  $\mathbb{1} - |\Psi_{\text{el}}\rangle\langle\Psi_{\text{el}}|$ . Thus, from the set of energy eigenstates  $\{|\Psi_f\rangle\}_f$  we obtain another complete set of final states  $\{|\Psi_{\text{el}}\rangle, |\Psi_f^\perp\rangle\}_f$ , containing the wave packet  $|\Psi_{\text{el}}\rangle$  and the orthogonal vectors  $|\Psi_f^\perp\rangle$ , obtained from normalizing  $(1 - \langle\Psi_{\text{el}}|\Psi_f\rangle)|\Psi_{\text{el}}\rangle$ . We do not require photon energy resolution in the measurement. Inserting the new basis of final states into the DSP of a single wave packet from Eq. (7.24), we separate the terms where the final state is still the wave packet or the electronic state changes

$$\begin{aligned} \frac{dP}{d\Omega} = \mathcal{F} \left( \frac{d\sigma}{d\Omega} \right)_{\text{Th}} & \left| \int d^3x \langle\Psi_{\text{el}}|\hat{n}(\mathbf{x}, \tau_{\text{delay}})|\Psi_{\text{el}}\rangle e^{i\mathbf{Q}\cdot\mathbf{x}} \right|^2 \\ & + \mathcal{F} \left( \frac{d\sigma}{d\Omega} \right)_{\text{Th}} \sum_f \left| \int d^3x \langle\Psi_f^\perp|\hat{n}(\mathbf{x}, \tau_{\text{delay}})|\Psi_{\text{el}}\rangle e^{i\mathbf{Q}\cdot\mathbf{x}} \right|^2. \end{aligned} \quad (7.29)$$

The sub-units of the crystal are assumed to be mutually independent. The electronic state of the entire crystal factorizes into the states of the individual wave packets. Let there be  $N$  lattice sites, specified by the lattice vectors  $\mathbf{R}_n$ . Then the initial

state is given by

$$|\Psi_{\text{el}}\rangle_{\text{crystal}} = \bigotimes_{n=1}^N |\Psi_{\text{el}}\rangle,$$

and the final states can be expressed as

$$|\Psi_f^{(i)}\rangle_{\text{crystal}} = |\Psi_{\text{el}}^{(1)}\rangle \otimes \cdots \otimes |\Psi_{\text{el}}^{(i-1)}\rangle \otimes |\Psi_f^\perp\rangle \otimes |\Psi_{\text{el}}^{(i+1)}\rangle \otimes \cdots \otimes |\Psi_{\text{el}}^{(N)}\rangle.$$

From this we find the DSP for the entire crystal [3]

$$\begin{aligned} \frac{dP}{d\Omega} = & \mathcal{F}\left(\frac{d\sigma}{d\Omega}\right)_{\text{Th}} \left| \sum_{n=1}^N e^{i\mathbf{Q}\cdot\mathbf{R}_n} \int d^3x \langle \Psi_{\text{el}} | \hat{n}(\mathbf{x}, \tau_{\text{delay}}) | \Psi_{\text{el}} \rangle e^{i\mathbf{Q}\cdot\mathbf{x}} \right|^2 \\ & + \mathcal{F}\left(\frac{d\sigma}{d\Omega}\right)_{\text{Th}} \sum_{i=1}^N \sum_f \left| \int d^3x \langle \Psi_f^\perp | \hat{n}(\mathbf{x}, \tau_{\text{delay}}) | \Psi_{\text{el}}^{(i)} \rangle e^{i\mathbf{Q}\cdot(\mathbf{x}+\mathbf{R}_i)} \right|^2. \end{aligned} \quad (7.30)$$

The first term on the right hand side gives rise to Bragg reflections [63, 106]. It describes coherent scattering because initial and final state are equal and it is impossible to decide from which lattice site the scattering occurred. According to the Laue condition the lattice sum allows scattering only at momentum transfer  $\mathbf{Q}$  that is equal to a reciprocal lattice vector, and one has  $e^{i\mathbf{Q}\cdot\mathbf{R}_n} = 1$ . Hence, the Bragg intensity of the coherent scattering signal scales with  $N^2$ .

The second term in Eq. (7.30) describes the incoherent scattering signal. An electron transition to a state different from the wave packet is induced at a particular lattice site. Therefore, the sum over final states in Eq. (7.30) involves a sum over the different lattice sites. Because the site where the wave packet was destroyed can be distinguished from the other sites, the corresponding contributions sum up incoherently. Consequently, the intensity of the incoherent signal scales with  $N$ .

Thus, for sufficiently large crystals (large  $N$ ) the time-resolved x-ray scattering signal is dominated by the coherent scattering signal. Therefore, the scattering signal is the typical Bragg diffraction pattern from the instantaneous electron density.

In the previous discussion we have made the very strong assumption that in the pump step all lattice sites are excited to the wave packet. Fortunately, this may not be necessary in experiment. In fact, it has been argued that weak excitation may be even advantageous [127]. The signal from the excited system may be heterodyned against the background signal from the ground state. Experiments have shown that in certain cases even very small fractions of excitations are sufficient to image ultrafast electron charge relocalizations in crystals [82, 83, 128]. To sketch the basic idea of this approach, assume only a small fraction of the sub-units has been excited into the wave packet state and the majority of sub-units is in the ground state. In

this case we start from a mixture of ground state and wave packet state as initial state

$$\hat{\rho}_{\text{in}}^{\text{el}} = \eta |\Psi_{\text{el}}\rangle \langle \Psi_{\text{el}}| + (1 - \eta) |\Psi_0\rangle \langle \Psi_0|, \quad (7.31)$$

where  $\eta \ll 1$  is the fraction of excited unit cells. The intensity of the coherent scattering is then proportional to

$$\begin{aligned} |\eta F_{\text{wp}}(\mathbf{Q}, \tau_{\text{delay}}) + (1 - \eta) F_0(\mathbf{Q})|^2 = & \left| \eta \int d^3x \langle \Psi_{\text{el}} | \hat{n}(\mathbf{x}, \tau_{\text{delay}}) | \Psi_{\text{el}} \rangle e^{i\mathbf{Q}\cdot\mathbf{x}} \right. \\ & \left. + (1 - \eta) \int d^3x \langle \Psi_0 | \hat{n}(\mathbf{x}) | \Psi_0 \rangle e^{i\mathbf{Q}\cdot\mathbf{x}} \right|^2. \end{aligned} \quad (7.32)$$

We assume the form factor of the ground state  $F_0(\mathbf{Q})$  to be known. Taking the difference of measurements with and without excitation, one may recover the change of the form factor  $\Delta F(\mathbf{Q}, \tau_{\text{delay}}) = F_{\text{wp}}(\mathbf{Q}, \tau_{\text{delay}}) - F_0(\mathbf{Q})$ . When the fraction of excited unit cells is small, we may take from Eq. (7.32) only the part linear in  $\eta$ . This yields an implicit equation for  $\Delta F(\mathbf{Q}, \tau_{\text{delay}})$  [82, 83, 128]

$$\frac{|\eta F_{\text{wp}} + (1 - \eta) F_0|^2 - |F_0|^2}{F_0^*} \approx \eta \left( \Delta F + \Delta F^* e^{2i\varphi_0} \right), \quad (7.33)$$

where  $\varphi_0$  is the complex phase of  $F_0$  and we have omitted the arguments. In some circumstances (e.g., when ground and excited state have inversion symmetry) the phase of  $\Delta F$  can be reconstructed, which makes it possible to recover the change of electron density  $\Delta n(\mathbf{x}, \tau_{\text{delay}}) = \langle \Psi_{\text{el}} | \hat{n}(\mathbf{x}, \tau_{\text{delay}}) | \Psi_{\text{el}} \rangle - \langle \Psi_0 | \hat{n}(\mathbf{x}) | \Psi_0 \rangle$ .

## 7.4. Recovering the electron density propagator

### 7.4.1. Motivation: The time-resolved imaging by Abbamonte

In Sec. 7.3.1 I have demonstrated that time-resolved x-ray scattering with high energy resolution yields the generalized DSF  $\tilde{S}(\mathbf{Q}, \omega, \tau_{\text{delay}})$ . In the case of stationary targets, it is well known [21, 129] that the DSF  $S(\mathbf{Q}, \omega)$  is related to the propagator of the electron density of the system by

$$\text{Im}[\chi(\mathbf{Q}, \omega)] = -\pi(S(\mathbf{Q}, \omega) - S(\mathbf{Q}, -\omega)). \quad (7.34)$$

For a target in thermal equilibrium this is a formulation of the Fluctuation-Dissipation theorem [21, 129]. Abbamonte and co-workers have devised a method to recover the electron density propagator from measurements of the DSF  $S(\mathbf{Q}, \omega)$  [130]. This propagator determines the complete linear response behaviour of the system to disturbances of the electron density. This method accomplishes a temporal resolution of 20 as ( $1 \text{ as} = 10^{-18} \text{ s}$ ) and has measured the valence plasmon in liquid water

[131] and the charge-transfer exciton in LiF [132]. Notably, this makes it possible to investigate processes that are faster than the imaging x-ray pulse duration. In the next subsection I will explore the content of information that can be extracted from the generalized DSF  $\tilde{S}(\mathbf{Q}, \omega, \tau_{\text{delay}})$ .

### 7.4.2. Relation of electron density propagator and generalized DSF

The (retarded) electron density propagator

$$\chi(\mathbf{x}, t, \mathbf{x}', t') = -i \langle \Psi | [\hat{n}(\mathbf{x}, t), \hat{n}(\mathbf{x}', t')] | \Psi \rangle \Theta(t - t'), \quad (7.35)$$

propagates disturbances in the electron density from  $\mathbf{x}', t'$  to  $\mathbf{x}, t$ . The propagator characterizes electron dynamics of the system. The Heaviside step function  $\Theta(t - t')$  ensures causality. To connect the dynamical properties of the system with the temporal coherence of the probe pulse, we define the generalized propagator

$$\tilde{\chi}(\mathbf{x}, t, \mathbf{x}', t') = -i \gamma_{\text{tp}}(t - t') \langle \Psi | [\hat{n}(\mathbf{x}, t), \hat{n}(\mathbf{x}', t')] | \Psi \rangle \Theta(t - t'), \quad (7.36)$$

where  $\gamma_{\text{tp}}(t - t') = e^{-(t-t')^2/\tau_c^2}$  describes the temporal coherence of the x-ray pulse. Observe that this propagator vanishes when  $t - t'$  is much larger than the coherence time  $\tau_c$  of the pulse, in particular when  $t - t'$  is much larger than the pulse duration. For the case of a coherent electronic wave packet  $|\Psi_{\text{el}}\rangle$ , we assume that we image the system at a pump probe delay time  $\tau_{\text{delay}}$  with a pulse duration short enough to freeze the wave packet. Moreover, we consider only the propagation of disturbances on time scales much shorter than the wave packet motion. That means we assume  $|t - \tau_{\text{delay}}|$  and  $|t' - \tau_{\text{delay}}|$  to be small with respect to the wave packet motion. We introduce the coordinates  $\tau = t - t'$  and  $\theta = (t + t')/2 \approx \tau_{\text{delay}}$ . Then we can write the generalized propagator

$$\begin{aligned} \tilde{\chi}(\mathbf{x}, \mathbf{x}', \tau, \tau_{\text{delay}}) &= \\ &= -i \gamma_{\text{tp}}(\tau) \Theta(\tau) \sum_f \left( \langle \Psi_{\text{el}} | \hat{n}(\mathbf{x}, \tau_{\text{delay}}) | \Psi_f \rangle \langle \Psi_f | \hat{n}(\mathbf{x}', \tau_{\text{delay}}) | \Psi_{\text{el}} \rangle e^{i(E_{\text{el}} - E_f)\tau} \right. \\ &\quad \left. - \langle \Psi_{\text{el}} | \hat{n}(\mathbf{x}', \tau_{\text{delay}}) | \Psi_f \rangle \langle \Psi_f | \hat{n}(\mathbf{x}, \tau_{\text{delay}}) | \Psi_{\text{el}} \rangle e^{-i(E_{\text{el}} - E_f)\tau} \right). \end{aligned} \quad (7.37)$$

$E_{\text{el}}$  is the energy expectation value of the wave packet. Fourier transformation with respect to  $\mathbf{x}, \mathbf{x}'$  and  $\tau$  yields

$$\tilde{\chi}(\mathbf{Q}, \mathbf{Q}', \omega, \tau_{\text{delay}}) = \iiint d\tau d^3\mathbf{x} d^3\mathbf{x}' e^{i\omega\tau} e^{i\mathbf{Q}\cdot\mathbf{x}} e^{i\mathbf{Q}'\cdot\mathbf{x}'} \tilde{\chi}(\mathbf{x}, \mathbf{x}', \tau, \tau_{\text{delay}}) \quad (7.38)$$

$$\begin{aligned} &= -i \sum_f \iint d^3\mathbf{x} d^3\mathbf{x}' e^{i(\mathbf{Q}\cdot\mathbf{x} + \mathbf{Q}'\cdot\mathbf{x}')} \int_0^\infty d\tau e^{-\tau^2/\tau_c^2} \\ &\quad \times \left( e^{i(\omega + E_{\text{el}} - E_f)\tau} \langle \Psi_{\text{el}} | \hat{n}(\mathbf{x}, \tau_{\text{delay}}) | \Psi_f \rangle \langle \Psi_f | \hat{n}(\mathbf{x}', \tau_{\text{delay}}) | \Psi_{\text{el}} \rangle - \text{c.c.} \right). \end{aligned} \quad (7.39)$$

Now, one can easily determine the imaginary part of  $\tilde{\chi}(\mathbf{Q}, -\mathbf{Q}, \omega, \tau_{\text{delay}})$

$$\text{Im} \left[ \tilde{\chi}(\mathbf{Q}, -\mathbf{Q}, \omega, \tau_{\text{delay}}) \right] = -\pi \sum_f \frac{\tau_c}{\sqrt{\pi}} \left| \int d^3\mathbf{x} \langle \Psi_f | \hat{n}(\mathbf{x}, \tau_{\text{delay}}) | \Psi_{\text{el}} \rangle e^{i\mathbf{Q}\cdot\mathbf{x}} \right|^2 \quad (7.40)$$

$$\times \left( e^{-\tau_c^2(\omega + E_{\text{el}} - E_f)^2/4} - e^{-\tau_c^2(\omega + E_{\text{el}} - E_f)^2/4} \right) \\ = -\pi \left( \tilde{S}(\mathbf{Q}, \omega, \tau_{\text{delay}}) - \tilde{S}(\mathbf{Q}, -\omega, \tau_{\text{delay}}) \right). \quad (7.41)$$

This establishes the relation between the generalized DSF, which can be measured in experiment, and the imaginary part of the generalized density propagator. The relation has a close similarity to the Fluctuation-Dissipation theorem, although the wave packet is not in a thermal equilibrium state.  $\text{Im}[\tilde{\chi}(\mathbf{Q}, -\mathbf{Q}, \omega, \tau_{\text{delay}})]$  is experimentally accessible. To obtain the full  $\tilde{\chi}(\mathbf{Q}, -\mathbf{Q}, \omega, \tau_{\text{delay}})$  one can apply Abbamonte's four step recipe [130, 131]. If the temporal coherence function is known or if the time propagation is much shorter than the pulse duration ( $\tau \ll \tau_l$ ) the exact density propagator  $\chi$  can be recovered.

In order to reconstruct the propagator in real space one has to perform the inverse Fourier transform. However, the generalized DSF only provides the diagonal terms, where  $\mathbf{Q}' = -\mathbf{Q}$ . From the diagonal terms one recovers the full electron density propagator for homogeneous systems [133]. In the case of an inhomogeneous system one obtains the generalized propagator  $\tilde{\chi}(\mathbf{x}, \mathbf{x}', \tau, \tau_{\text{delay}})$  averaged over all possible source locations  $\mathbf{x}'$  [133]. A method to measure the nondiagonal terms was proposed in [134]. Thus, in principle it is possible to reconstruct the generalized electron density propagator in real-space.

### 7.4.3. Linear response theory and scattering induced dynamics

The DSP for the x-ray scattering pattern of the wave packet, given in Eq. (7.3), depends on electron density fluctuations of the form

$$\langle \Psi_{\text{el}} | \hat{n}(\mathbf{x}', \theta + \frac{\tau}{2}) \hat{n}(\mathbf{x}'', \theta - \frac{\tau}{2}) | \Psi_{\text{el}} \rangle =: n_{\text{corr}}(\mathbf{x}', \mathbf{x}'', \theta, \tau). \quad (7.42)$$

This expression describes the correlation of the electron density at position  $\mathbf{x}'$  at time  $\theta + \frac{\tau}{2}$  and position  $\mathbf{x}''$  at time  $\theta - \frac{\tau}{2}$ . In the stationary case the crucial term is the van Hove correlation function  $\langle \Psi | \hat{n}(\mathbf{x}', 0) \hat{n}(\mathbf{x}'', \tau) | \Psi \rangle$  [21, 121]. In the case of the wave packet,  $n_{\text{corr}}$  correlates two points at time difference  $\tau$ , i.e., on a time scale much faster than the x-ray pulse duration. The electron density propagator is only related to the imaginary part of the correlation function

$$\chi(\mathbf{x}', \theta + \frac{\tau}{2}, \mathbf{x}'', \theta - \frac{\tau}{2}) = 2 \Theta(\tau) \text{Im} \left( n_{\text{corr}}(\mathbf{x}', \mathbf{x}'', \theta, \tau) \right). \quad (7.43)$$

On the one hand, the propagator contains not enough information to fully reconstruct the correlations. On the other hand, one may regard the electron density

fluctuations in the DSP as partly due to (scattering induced) electron density dynamics. But, the propagator characterizes the electron dynamics on time scales faster than the pulse duration. Therefore, one may ask whether the electron density propagator obtained from experiment through  $\tilde{S}(\mathbf{Q}, \omega, \tau_{\text{delay}})$  can be used to calculate the electron density dynamics induced by the scattering process. We determine the linear density response of an electronic wave packet to the scattering process [3]. The linear density response can be written as

$$\delta n(\mathbf{x}, t) = \text{Tr}[\hat{n}(\mathbf{x}, t) \delta \hat{\rho}(t)], \quad (7.44)$$

where  $\delta \hat{\rho}(t)$  is the change of the system within linear response theory. According to usual perturbation theory (see Eq. (2.75)), we can write the first order terms of the electronic state as

$$\delta \hat{\rho}(t) = \hat{\rho}^{(0,1)}(t) + \hat{\rho}^{(1,0)}(t) \quad (7.45)$$

$$= \int_{-\infty}^t dt' \hat{\rho}_{\text{in}} \hat{H}_{\text{int}}(t') + \int_{-\infty}^t dt' \hat{H}_{\text{int}}(t') \hat{\rho}_{\text{in}}. \quad (7.46)$$

In the present case of  $\hat{\mathbf{A}}^2$  scattering the interaction Hamiltonian is

$$\hat{H}_{\text{int}} = \frac{\alpha^2}{2} \int d^3x \hat{\mathbf{A}}^2(\mathbf{x}) \hat{n}(\mathbf{x}), \quad (7.47)$$

and the linear-order density response becomes

$$\delta n(\mathbf{x}, t) = -i \frac{\alpha^2}{2} \int_{-\infty}^t dt' \int d^3x' \text{Tr}[\hat{\rho}_{\text{in}}^{\text{rad}} \hat{\mathbf{A}}^2(\mathbf{x}', t')] \langle \Psi_{\text{el}} | [\hat{n}(\mathbf{x}, t), \hat{n}(\mathbf{x}', t')] | \Psi_{\text{el}} \rangle. \quad (7.48)$$

Expressing the vector field in terms of  $\hat{\mathbf{E}}^{\pm}$ , defined in Eq. (2.35), we obtain trace terms with  $\hat{\mathbf{E}}^{\pm}(\mathbf{x}', t') \hat{\mathbf{E}}^{\mp}(\mathbf{x}', t')$  and trace terms with  $\hat{\mathbf{E}}^{\pm}(\mathbf{x}', t') \hat{\mathbf{E}}^{\pm}(\mathbf{x}', t')$ . The former yield the usual correlation function  $G^{(1)}$  of the radiation field, whereas the latter correspond to nonlinear two-photon effects and yield even order correlation functions [71]. Even in the extremely well-behaved case of a completely coherent pulse the even order correlation functions are vanishing, except one has complete control over the phase of the pulse. Typically, storage-rings and free-electron lasers produce rather chaotic x-ray beams that are not phase-stable. Hence, we neglect the two-photon contributions.

On the other hand, the field correlation functions  $\langle \hat{\mathbf{E}}^{\pm}(\mathbf{x}', t') \hat{\mathbf{E}}^{\mp}(\mathbf{x}', t') \rangle$  are proportional to  $I(t')$ , see Eqs. (7.4), (7.5), where we assume that the spatial variation of the intensity (the beam profile) is negligible. Finally, this yields the density response

up to a prefactor

$$\delta n(\mathbf{x}, t) = \int_{-\infty}^t dt' I(t') \int d^3x' \chi(\mathbf{x}, \mathbf{x}', t, t') \quad (7.49)$$

$$= \int_{-\infty}^t dt' I(t') \langle \Psi_{\text{el}} | \left[ \hat{n}(\mathbf{x}, t), \int d^3x' \hat{n}(\mathbf{x}', t') \right] | \Psi_{\text{el}} \rangle. \quad (7.50)$$

On performing the integral over  $\mathbf{x}'$  in the last expression, one finds that  $\delta n(\mathbf{x}, t) = 0$ . Thus, the linear density response of the  $\hat{\mathbf{A}}^2$  scattering process itself vanishes. Therefore, the fast electron density dynamics induced in  $\hat{\mathbf{A}}^2$  scattering cannot be captured by the linear response electron density propagator  $\chi$ . This finding expresses the fact that  $\chi$  describes linear-order density fluctuations, whereas the density response to non-resonant x-ray scattering is, in general, a higher-order process.

## 7.5. Momentum space imaging: Ultrafast time-resolved Compton scattering

### 7.5.1. Introduction

The scattering signal of time-resolved x-ray diffraction from a wave packet was determined in Sec. 7.2. The example of a hydrogen wave packet illustrated that the diffraction pattern encodes spatial and temporal correlations of the wave packet (see Fig. 7.3). Sec. 7.3 analyzed the role of energy resolution and established the connection of this diffraction pattern with the generalized dynamic structure factor of the electronic wave packet.

However, the question whether the wave packet can be reconstructed in real-time and real-space is still unanswered. The previous results focused on the case of quasi-elastic scattering, in order to come as close as possible to coherent diffractive imaging. In the present section, I take a different approach to this problem. This Section is devoted to a study of the regime of inelastic scattering. It is well known that Compton scattering can recover the electron momentum distribution for stationary electronic systems [21, 120, 135–138]. Ultrafast time-resolved electron (e,2e) spectroscopy of electronic wave packets has been analyzed in Ref. [139]. Here, I propose ultrafast time-resolved Compton scattering (or x-ray ( $\gamma, e\gamma$ ) spectroscopy) to unravel electronic wave packet dynamics in momentum space. This approach recovers the wave packet in real-time and momentum-space. Yet, the reconstruction in real-space is not possible. The derivation follows closely the derivation for the stationary case in Ref. [140].

### 7.5.2. Time-resolved Compton scattering

Compton scattering is a well-known tool to investigate the electron momentum density of a many-body systems [21, 120]. Moreover, Compton scattering has been proposed as a mean to characterize ultrashort x-ray pulses by means of a Compton attosecond streak camera [141]. A typical Compton scattering experiment involves the angle- and energy-resolved measurement of inelastically scattered x-ray photons. Energy-resolved photon scattering measures the double differential scattering cross section (DDSCS). The DDSCS is the probability that a photon is scattered into a given solid angle and a given photon energy interval. Typically Compton scattering is treated within the impulse approximation [135]. In this approximation the electrons are treated as free electrons with a given momentum distribution, which is determined by the atomic or molecular potential. The DDSCS is then proportional to the Compton profile, which is a projection of the 3D electron momentum distribution along the direction of the scattering vector. Here, the electrons are not assumed to move freely, i.e., the impulse approximation is not used. Coincidence measurements of scattered photon and recoil electron are considered, i.e., measurements accessing the triple differential scattering cross section (TDSCS). This allows us to directly obtain the 3D electron momentum distribution [140]. If the recoil electron is not observed, one recovers the Compton profile by averaging over recoil electron measurements. The derivation employs the Dyson orbitals (defined below), as in Ref. [140].

The differential scattering probability  $dP/d\Omega$  and differential scattering cross section  $d\sigma/d\Omega$  differ only by multiplying the incoming photon fluence

$$\frac{dP}{d\Omega} = \mathcal{F} \frac{d\sigma}{d\Omega}.$$

Thus, one can easily obtain the DDSCS from the DSP in Eq. (7.8)

$$\begin{aligned} \frac{d\sigma}{d\Omega d\omega_{\mathbf{k}_s}} &= \left( \frac{d\sigma}{d\Omega} \right)_{\text{Th}} \frac{\omega_{\mathbf{k}_s}}{\omega_{\text{in}}} \sum_f W_1(\omega + E_{\text{el}} - E_f) \\ &\times \left| \int d^3x \langle \Psi_f | \hat{n}(\mathbf{x}) | \Psi_{\text{el}}(\tau_{\text{delay}}) \rangle e^{i\mathbf{Q}\cdot\mathbf{x}} \right|^2. \end{aligned} \quad (7.51)$$

where  $\omega = \omega_{\text{in}} - \omega_{\mathbf{k}_s}$  denotes the energy that is transferred from the photon to the electronic system during the scattering process. The function

$$W_1(\omega) = \frac{\tau_c}{\sqrt{\pi}} e^{-\tau_c^2 \omega^2 / 4}$$

determines the spectral density, and accordingly the bandwidth, of the x-ray pulse. From the DDSCS, one can infer the TDSCS by restricting the summation over final

states to those states, where a recoil electron is emitted into the solid angle  $d\Omega_e$ . This yields the TDSCS

$$\begin{aligned} \frac{d\sigma}{d\Omega d\omega_{\mathbf{k}_s} d\Omega_e} &= \left( \frac{d\sigma}{d\Omega} \right)_{\text{Th}} \frac{\omega_{\mathbf{k}_s}}{\omega_{\text{in}}} \sum_{f|\Omega_e} W_1(\omega + E_{\text{el}} - E_f) \\ &\times \left| \int d^3x \langle \Psi_f | \hat{n}(\mathbf{x}) | \Psi_{\text{el}}(\tau_{\text{delay}}) \rangle e^{i\mathbf{Q}\cdot\mathbf{x}} \right|^2. \end{aligned} \quad (7.52)$$

In the following, let us make the ‘‘sudden approximation’’, i.e., we assume that the recoil electron leaves the system so quickly that the remaining electrons suddenly relax into an ionic state of  $N - 1$  electrons. This means that the recoil electron is not correlated with the electrons in the remaining ion. The recoil electron occupies an unbound state in the potential of the ion. This approximation is justified if the kinetic energy of the recoil electron is large. Thus, we can assume the final state to be of the form

$$|\Psi_f\rangle \approx \hat{c}_{\epsilon,\sigma}^\dagger |\Psi_{n,\bar{\sigma}}^{N-1}\rangle, \quad (7.53)$$

where  $\hat{c}_{\epsilon,\sigma}^\dagger$  is the creation operator for the unbound recoil electron in the potential of the ion, with kinetic energy  $\epsilon$ , spin  $\sigma \in \{\uparrow, \downarrow\}$ , and propagating in the direction of  $\Omega_e$ . The remaining ion is in the  $(N - 1)$ -electron state  $|\Psi_{n,\bar{\sigma}}^{N-1}\rangle$ , where  $\bar{\sigma}$  denotes the spin opposite to  $\sigma$ , and the quantum number  $n$  characterizes the excitation of this state (particle-hole excitations in the independent particle picture, but also higher terms when electron correlations are considered). The final state energy is

$$E_f \approx \epsilon + E_n^{N-1}. \quad (7.54)$$

Inserting final states of the form of Eq. (7.53) into the TDSCS in Eq. (7.52) yields

$$\begin{aligned} \frac{d^3\sigma}{d\Omega d\omega_{\mathbf{k}_s} d\Omega_e} &= \left( \frac{d\sigma}{d\Omega} \right)_{\text{Th}} \frac{\omega_{\mathbf{k}_s}}{\omega_{\text{in}}} \sum_{n,\epsilon,\sigma} W_1(\omega - \epsilon + E_{\text{el}} - E_n^{N-1}) \\ &\times \left| \int d^3x \langle \Psi_{n,\bar{\sigma}}^{N-1} | \hat{c}_{\epsilon,\sigma} \hat{\psi}^\dagger(\mathbf{x}) \hat{\psi}(\mathbf{x}) | \Psi_{\text{el}}(\tau_{\text{delay}}) \rangle e^{i\mathbf{Q}\cdot\mathbf{x}} \right|^2. \end{aligned} \quad (7.55)$$

Observe that  $E_{\text{el}} - E_n^{N-1}$  corresponds to the binding energy of the recoil electron before it was released. We have assumed that the recoil electron leaves the system very quickly, i.e.,

$$\epsilon \gg E_{\text{el}} - E_n^{N-1}. \quad (7.56)$$

Thus, we will neglect the binding energy in the following. We expand  $\hat{\psi}(\mathbf{x})$  in a basis of  $N$  electron spin orbitals  $|\varphi_q\rangle$  such that

$$\hat{\psi}(\mathbf{x}) = \sum_q \varphi_q(\mathbf{x}) \hat{c}_q. \quad (7.57)$$

Moreover, the recoil electron state is not occupied in the initial wave packet. As a consequence, the matrix element in the TDSCS is only nonzero if  $\hat{\psi}^\dagger(\mathbf{x})$  creates the unbound recoil electron state. Thus, we can replace  $\hat{\psi}^\dagger(\mathbf{x})$  by  $\varphi_{\epsilon,\sigma}^*(\mathbf{x}) \hat{c}_{\epsilon,\sigma}^\dagger$  such that  $\langle \Psi_{n,\bar{\sigma}}^{N-1} | \hat{c}_{\epsilon,\sigma}^\dagger \hat{\psi}^\dagger(\mathbf{x}) = \varphi_{\epsilon,\sigma}^*(\mathbf{x}) \langle \Psi_{n,\bar{\sigma}}^{N-1} |$ .

Using the time-dependent Dyson orbitals  $g_{n,\sigma}(\mathbf{x}, \tau_{\text{delay}})$ , defined by

$$g_{n,\sigma}(\mathbf{x}, \tau_{\text{delay}}) = \sum_q \varphi_{q,\sigma}(\mathbf{x}) \langle \Psi_{n,\bar{\sigma}}^{N-1} | \hat{c}_{q,\sigma} | \Psi_{\text{el}}(\tau_{\text{delay}}) \rangle, \quad (7.58)$$

we can express the TDSCS by (cf. Ref. [140])

$$\begin{aligned} \frac{d^3\sigma}{d\Omega d\omega_{\mathbf{k}_s} d\Omega_e} &= \left( \frac{d\sigma}{d\Omega} \right)_{\text{Th}} \frac{\omega_{\mathbf{k}_s}}{\omega_{\text{in}}} \sum_{n,\epsilon,\sigma} W_1(\omega - \epsilon) \\ &\times \left| \int d^3x \varphi_{\epsilon,\sigma}^*(\mathbf{x}) \sum_q \varphi_{q,\sigma}(\mathbf{x}) \langle \Psi_{n,\bar{\sigma}}^{N-1} | \hat{c}_{q,\sigma} | \Psi_{\text{el}}(\tau_{\text{delay}}) \rangle e^{i\mathbf{Q}\cdot\mathbf{x}} \right|^2 \end{aligned} \quad (7.59)$$

$$= \left( \frac{d\sigma}{d\Omega} \right)_{\text{Th}} \frac{\omega_{\mathbf{k}_s}}{\omega_{\text{in}}} \sum_{n,\epsilon,\sigma} W_1(\omega - \epsilon) \left| \int d^3x \varphi_{\epsilon,\sigma}^*(\mathbf{x}) g_{n,\sigma}(\mathbf{x}, \tau_{\text{delay}}) e^{i\mathbf{Q}\cdot\mathbf{x}} \right|^2. \quad (7.60)$$

In the following, we make the strong – but extremely useful – assumption that the recoil electron can be described by a plane wave state. Let the recoil electron state be the plane wave

$$\varphi_{\epsilon,\sigma}(\mathbf{x}) = \frac{1}{\sqrt{V}} \exp(i\mathbf{p}_\epsilon \cdot \mathbf{x}) \alpha(\sigma), \quad (7.61)$$

with momentum  $\mathbf{p}_\epsilon$  pointing to the solid angle element  $d\Omega_e$  and kinetic energy  $\epsilon = p_\epsilon^2/2$ . Substituting this unbound state into Eq. (7.60), the spatial integral yields the Fourier transformation of the Dyson orbital  $\tilde{g}_{n,\sigma}(\mathbf{Q} - \mathbf{p}_\epsilon)$ . In the continuum limit we can replace the summation over the kinetic energy by

$$\sum_\epsilon \rightarrow \frac{V}{(2\pi)^3} \int d\epsilon \sqrt{2\epsilon}.$$

Thus, under the plane wave assumption, the TDSCS becomes

$$\frac{d^3\sigma}{d\Omega d\omega_{\mathbf{k}_s} d\Omega_e} = \left( \frac{d\sigma}{d\Omega} \right)_{\text{Th}} \frac{\omega_{\mathbf{k}_s}}{\omega_{\text{in}}} \int d\epsilon \sqrt{2\epsilon} W_1(\omega - \epsilon) \sum_{n,\sigma} |\tilde{g}_{n,\sigma}(\mathbf{Q} - \mathbf{p}_\epsilon, \tau_{\text{delay}})|^2. \quad (7.62)$$

Defining  $\mathbf{P} := \mathbf{Q} - \mathbf{p}_\epsilon$  and exploiting the completeness of the  $(N-1)$ -electron states in the  $(N-1)$ -electron subspace the crucial expression becomes

$$\sum_{n,\sigma} |\tilde{g}_{n,\sigma}(\mathbf{P}, \tau_{\text{delay}})|^2 = \frac{1}{(2\pi)^3} \iint d^3r d^3r' e^{i\mathbf{P}\cdot(\mathbf{r}'-\mathbf{r})} \sum_{n,\sigma} \sum_{q,q'} \varphi_{q,\sigma}^*(\mathbf{r}) \varphi_{q',\sigma}(\mathbf{r}') \quad (7.63)$$

$$\times \langle \Psi_{\text{el}}(\tau_{\text{delay}}) | \hat{c}_{q,\sigma}^\dagger | \Psi_{n,\bar{\sigma}}^{N-1} \rangle \langle \Psi_{n,\bar{\sigma}}^{N-1} | \hat{c}_{q',\sigma} | \Psi_{\text{el}}(\tau_{\text{delay}}) \rangle \quad (7.64)$$

$$= \langle \Psi_{\text{el}}(\tau_{\text{delay}}) | \hat{\psi}^\dagger(\mathbf{P}) \hat{\psi}(\mathbf{P}) | \Psi_{\text{el}}(\tau_{\text{delay}}) \rangle \quad (7.65)$$

$$= \rho(\mathbf{P}, \tau_{\text{delay}}).$$

Remarkably, we have found the crucial expression in Eq. (7.62) to be simply the instantaneous electron momentum density of the wave packet. As a consequence, the TDSCS depends on the three-dimensional instantaneous electron momentum density, smeared out by the bandwidth of the pulse

$$\frac{d^3\sigma}{d\Omega d\omega_{\mathbf{k}_s} d\Omega_e} = \left(\frac{d\sigma}{d\Omega}\right)_{\text{Th}} \frac{\omega_{\mathbf{k}_s}}{\omega_{\text{in}}} \int d\epsilon \sqrt{2\epsilon} W_1(\omega - \epsilon) \rho(\mathbf{Q} - \mathbf{p}_\epsilon, \tau_{\text{delay}}). \quad (7.66)$$

Observe that  $\mathbf{P} = \mathbf{Q} - \mathbf{p}_\epsilon$  is the momentum that has been transferred to the ion. In order to connect this result with the usual impulse approximation picture [21], we can define the initial momentum of the recoil electron (before the scattering) by  $\mathbf{p}_0 = \mathbf{p}_\epsilon - \mathbf{Q}$ . Then the connection is simply  $\mathbf{p}_0 = -\mathbf{P}$  [140].

Experiments where only scattered photons are detected are of course much simpler to conduct than performing coincidence measurements of scattered photons and recoil electrons. When only solid angle and energy of the scattered photons are measured, the crucial quantity is the DDSCS. In the following, we will average the TDSCS over all possible recoil electron directions, thereby recovering the DDSCS. In this way, we will find the usual Compton profile. For simplicity, we choose the coordinate system in direction of the photon momentum transfer, such that  $\mathbf{Q} = (0, 0, Q)^T$ . Then the momentum  $\mathbf{P} := \mathbf{Q} - \mathbf{p}_\epsilon$  has the squared modulus

$$P^2 = p_\epsilon^2 - Q^2 + 2\mathbf{P} \cdot \mathbf{Q}. \quad (7.67)$$

From Eq. (7.66), we see that

$$\frac{d^2\sigma}{d\omega_{\mathbf{k}_s} d\Omega_{\mathbf{k}_s}} = \left(\frac{d\sigma}{d\Omega}\right)_{\text{Th}} \frac{\omega_{\mathbf{k}_s}}{\omega_{\text{in}}} \int d\Omega_e \int d\epsilon \sqrt{2\epsilon} W_1(\omega - \epsilon) \rho(\mathbf{P}, \tau_{\text{delay}}) \quad (7.68)$$

$$= \left(\frac{d\sigma}{d\Omega}\right)_{\text{Th}} \frac{\omega_{\mathbf{k}_s}}{\omega_{\text{in}}} \int d\Omega_e \int p_\epsilon^2 dp_\epsilon W_1\left(\omega - \frac{p_\epsilon^2}{2}\right) \rho(\mathbf{P}, \tau_{\text{delay}}) \quad (7.69)$$

$$= \left(\frac{d\sigma}{d\Omega}\right)_{\text{Th}} \frac{\omega_{\mathbf{k}_s}}{\omega_{\text{in}}} \int d^3P W_1\left(\omega - \frac{P^2}{2} - \frac{Q^2}{2} + P_z Q\right) \rho(\mathbf{P}, \tau_{\text{delay}}). \quad (7.70)$$

Recall that  $W_1$  is the Fourier transform of the temporal coherence function  $\gamma_{\text{tp}}(t)$ , cf. Sec. 3.2.2. Defining  $W_Q(\omega)$  as the Fourier transform of  $\gamma_{\text{tp}}(t/Q)$  and using the scaling properties of the Fourier transform, we have

$$\frac{d^2\sigma}{d\omega_{\mathbf{k}_s} d\Omega_{\mathbf{k}_s}} = \left(\frac{d\sigma}{d\Omega}\right)_{\text{Th}} \frac{\omega_{\mathbf{k}_s}}{\omega_{\text{in}}} \int d^3P \frac{1}{Q} W_Q\left(P_z + \frac{\omega}{Q} - \frac{Q}{2} - \frac{P^2}{2Q}\right) \rho(\mathbf{P}, \tau_{\text{delay}}). \quad (7.71)$$

We will neglect  $P^2/2Q$  in the following. This is justified because the binding energy of the recoil electron was already neglected. In a simple picture, we may regard

$P^2/2Q$  as the initial kinetic energy of the electron, which may be as well neglected when the binding energy is negligible. We obtain the final expression for the DDSCS

$$\frac{d^2\sigma}{d\omega_{\mathbf{k}_s}d\Omega_{\mathbf{k}_s}} = \left(\frac{d\sigma}{d\Omega}\right)_{\text{Th}} \frac{\omega_{\mathbf{k}_s}}{\omega_{\text{in}}} \int d^3P \frac{1}{Q} W_Q\left(P_z + \frac{\omega}{Q} - \frac{Q}{2}\right) \rho(\mathbf{P}, \tau_{\text{delay}}). \quad (7.72)$$

In the case of a stationary target, one may choose a monochromatic pulse, such that  $W_Q$  can be represented by a delta function. In that case, the last equation yields the usual expression for the Compton profile in the impulse approximation [21, 135].

### 7.5.3. Connection of real- and momentum space densities

In the last section, it was shown how the TDSCS is related to the instantaneous momentum-space density (IMD) of electrons. Measuring the TDSCS yields the IMD, where for the moment we disregard the smearing by the bandwidth of the pulse. What does this result imply for the measurement of the instantaneous real-space density (IRD) of electrons? Recall the definition of the IMD from Eq. (7.65)

$$\rho(\mathbf{P}, \tau_{\text{delay}}) = \langle \Psi_{\text{el}}(\tau_{\text{delay}}) | \hat{\psi}^\dagger(\mathbf{P}) \hat{\psi}(\mathbf{P}) | \Psi_{\text{el}}(\tau_{\text{delay}}) \rangle \quad (7.73)$$

$$= \frac{1}{(2\pi)^3} \iint d^3x d^3x' e^{i\mathbf{P}\cdot(\mathbf{x}'-\mathbf{x})} \langle \Psi_{\text{el}}(\tau_{\text{delay}}) | \hat{\psi}^\dagger(\mathbf{x}) \hat{\psi}(\mathbf{x}') | \Psi_{\text{el}}(\tau_{\text{delay}}) \rangle. \quad (7.74)$$

The Fourier transform of the IMD is

$$\tilde{\rho}(\mathbf{R}, \tau_{\text{delay}}) = \frac{1}{(2\pi)^{3/2}} \int d^3P e^{i\mathbf{P}\cdot\mathbf{R}} \rho(\mathbf{P}, \tau_{\text{delay}}) \quad (7.75)$$

$$= \frac{1}{(2\pi)^{3/2}} \int d^3x \langle \Psi_{\text{el}}(\tau_{\text{delay}}) | \hat{\psi}^\dagger(\mathbf{x}) \hat{\psi}(\mathbf{x} + \mathbf{R}) | \Psi_{\text{el}}(\tau_{\text{delay}}) \rangle. \quad (7.76)$$

Obviously, the Fourier transformation of the IMD does not yield the IRD. Inserting a complete basis of  $N - 1$  electron states  $|\Psi_{n,\sigma}^{N-1}\rangle$  one can express  $\tilde{\rho}(\mathbf{R}, \tau_{\text{delay}})$  in terms of the Dyson orbitals

$$\tilde{\rho}(\mathbf{R}, \tau_{\text{delay}}) = (2\pi)^{-3/2} \sum_{n,\sigma} \int d^3x g_{n,\sigma}^*(\mathbf{x}, \tau_{\text{delay}}) g_{n,\sigma}(\mathbf{x} + \mathbf{R}, \tau_{\text{delay}}) \quad (7.77)$$

$$= (2\pi)^{-3/2} \sum_{n,\sigma} R_{n,\sigma}(\mathbf{R}), \quad (7.78)$$

where  $R_{n,\sigma}$  is the autocorrelation function of the Dyson orbital  $g_{n,\sigma}$ . The Fourier transform of the IMD is the sum over autocorrelation functions of the Dyson orbitals. The IRD, in contrast, is given by the absolute square of the Dyson orbitals

$$\rho(\mathbf{x}, \tau_{\text{delay}}) = \langle \Psi_{\text{el}}(\tau_{\text{delay}}) | \hat{\psi}^\dagger(\mathbf{x}) \hat{\psi}(\mathbf{x}) | \Psi_{\text{el}}(\tau_{\text{delay}}) \rangle = \sum_{n,\sigma} |g_{n,\sigma}(\mathbf{x}, \tau_{\text{delay}})|^2. \quad (7.79)$$

This demonstrates that one does not recover the IRD from the IMD, cf. the discussion in Ref. [21].

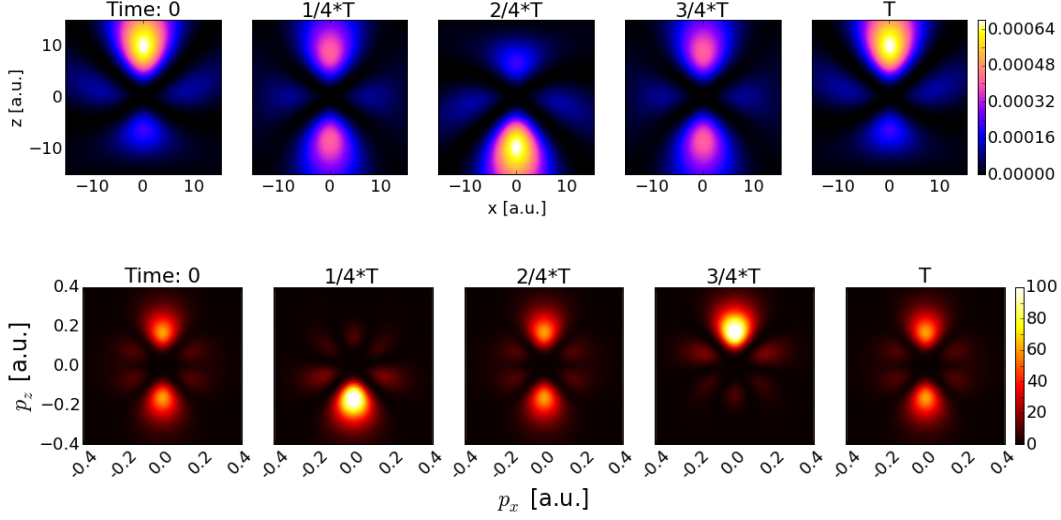


Figure 7.5.: The hydrogen 3d-4f wave packet.

*Upper panel:* Instantaneous real-space electron density (IRD)  $\rho(\mathbf{x}, \tau_{\text{delay}})$ . Shown are 2d slices in the  $(x, 0, z)$ -plane at times  $\tau_{\text{delay}}$  in steps of fourths the oscillation period  $T$ . (Identical to Figs. 5.1 and 7.2)

*Lower panel:* Instantaneous momentum-space electron density (IMD)  $\rho(\mathbf{p}, \tau_{\text{delay}})$ . Shown are two-dimensional slices in the  $(p_x, 0, p_z)$ -plane for at the same time steps as above.

#### 7.5.4. Application to hydrogen 3d-4f wave packet

In this subsection, time-resolved Compton scattering is applied to the hydrogen 3d-4f wave packet, already familiar from Sec. 7.2.2. Calculating the instantaneous momentum density, we determine the DDSCS of Eq. (7.72) for this wave packet.

The IMD of the wave packet can be directly calculated from the analytical expressions of the hydrogen wave functions in momentum space  $\varphi_{n,l,m}(\mathbf{p}) = \langle \mathbf{p} | \varphi_{n,l,m} \rangle$ . Expressed in spherical coordinates  $(p, \vartheta, \varphi)$  of the momentum vector  $\mathbf{p}$ , the momentum space wave functions of hydrogen are [142, 143]

$$\varphi_{n,l,m}(\mathbf{p}) = F_{n,l}(p) Y_{l,m}(\vartheta, \varphi), \quad (7.80)$$

where

$$F_{n,l}(p) = -(-i)^l n^2 2^{2(l+1)} l! \left[ \frac{2}{\pi} \frac{(n-l-1)!}{(n+l)!} \right]^{1/2} \frac{n^l p^l}{(n^2 p^2 + 1)^{l+2}} C_{n-l-1}^{l+1} \left( \frac{n^2 p^2 - 1}{n^2 p^2 + 1} \right),$$

and  $C_N^\nu(x)$  denote the Gegenbauer polynomials. Note that the factor  $-(-i)^l$  contributes a phase factor to the wave packet and cannot be omitted. The 3d-4f wave

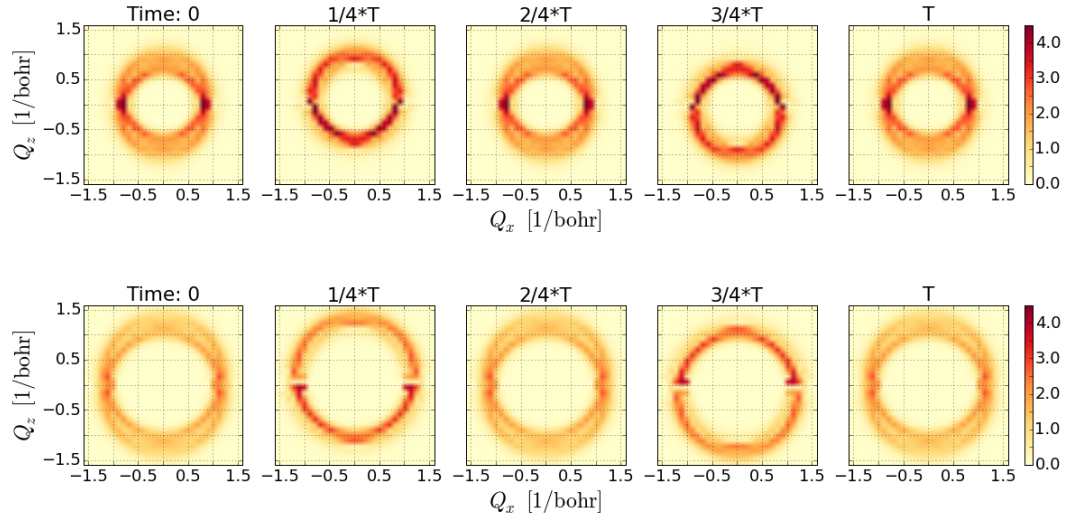


Figure 7.6.: Double differential scattering cross section  $d^2\sigma/d\omega_{\mathbf{k}_s}d\Omega_{\mathbf{k}_s}$  for time-resolved Compton scattering from the 3d-4f wave packet of hydrogen:  $(Q_x, 0, Q_z)$ -plane in  $Q$ -space in units of  $(\frac{d\sigma}{d\Omega})_{\text{Th}}$ . The Energy transfer is  $\omega = 10$  eV (*upper panel*) and  $\omega = 20$  eV (*lower panel*). The  $Q_x, Q_z$ -range extends from  $-3$  to  $3 \text{ \AA}^{-1}$ .

packet in momentum space is given by

$$\langle \mathbf{p} | \Psi_{\text{el}} \rangle = \frac{1}{\sqrt{2}} \varphi_{3,2,0}(\mathbf{p}) + \frac{1}{\sqrt{2}} \varphi_{4,3,0}(\mathbf{p}). \quad (7.81)$$

The lower panel in Fig. 7.5 shows 2d slices the instantaneous momentum-space electron density  $\rho(\mathbf{p}, \tau_{\text{delay}})$  at different times. Comparing with the real-space electron density in the upper panel in Fig. 7.5, one sees how the momentum space density reflects the oscillation of the real-space density. When, at first, electrons are concentrated in the upper region in real-space, their momentum is rather weak and balanced. While the real-space density flows down in the second step, the momentum density reaches its maximum in the down direction. When, at half the oscillation period, the electrons are concentrated in the lower region, the momentum distribution has become balanced again because the momentum is changing its direction.

In the following, we are going to make the restrictive assumption that the x-ray pulse is sufficiently monochromatic to treat  $W_Q$  as essentially a delta function. This means we simplify the DDSCS in Eq. (7.72) to the usual expression [21, 135]

$$\frac{d^2\sigma}{d\omega_{\mathbf{k}_s}d\Omega_{\mathbf{k}_s}} = \left( \frac{d\sigma}{d\Omega} \right)_{\text{Th}} \int d^2p \frac{1}{Q} \rho(p_x, p_y, \frac{\omega}{Q} - \frac{Q}{2}, \tau_{\text{delay}}), \quad (7.82)$$

where we also used  $\omega_{\mathbf{k}_s}/\omega_{\text{in}} \approx 1$ . To justify this simplification, note that the error in replacing  $W_1$  by a delta function in Eq. (7.70) is small. In Ref. [88] a 1 fs x-ray pulse was used to image the 3d-4f wave packet. This pulse length corresponds to a bandwidth  $\sim 1$  eV or .037 a.u., a scale on which the IMD varies slowly. Furthermore, the width of  $W_Q$  is proportional to  $Q^{-2}$ . This means  $W_Q$  approaches a delta function for sufficiently large  $Q$ . Thus, the approximation introduces only small errors. Using the approximation one acquires a notion of the scattering pattern from time-resolved Compton scattering.

Recall that Eq. (7.82) has been formulated in a coordinate system in  $\mathbf{Q}$ -direction, such that  $\mathbf{Q} = (0, 0, Q)$ . One needs to perform a coordinate transformation to calculate the DDSCS for momentum transfer vectors in the  $(Q_x, 0, Q_z)$ -plane. Expressing  $(Q_x, Q_z)$  in polar coordinates  $(Q, \varphi)$ , we can write Eq. (7.82) as

$$\frac{d^2\sigma}{d\omega_{\mathbf{k}_s}d\Omega_{\mathbf{k}_s}} = \left(\frac{d\sigma}{d\Omega}\right)_{\text{Th}} \iint dp_x dp_y \frac{1}{Q} \frac{1}{|\cos\varphi|} \rho(p_x, p_y, p_Q, \tau_{\text{delay}}), \quad (7.83)$$

where  $p_Q = \left(\frac{\omega}{Q} - \frac{Q}{2}\right)/(\cos\varphi) - p_x \tan\varphi$ .

In Fig. 7.6, the DDSCS is shown for energy transfer  $\omega = 10$  eV and  $\omega = 20$  eV. The DDSCS reflects the oscillation of the wave packet. Observe that for  $\varphi = \pi/2$  and  $3\pi/2$  the division by the cosine causes a singularity that causes the bright spots on right and left in the figure. The calculations have been performed on a uniform  $Q$ -space grid, with  $30 \times 30$  grid points. The  $p_x$  and  $p_y$ -values have been discretized with 60-grid points in the range from  $-1.2$  to  $1.2$  atomic units.

In Fig. 7.7, the DSCS  $d\sigma/d\Omega_{\mathbf{k}_s}$  is shown. The DDSCS is integrated over a  $\omega_{\mathbf{k}_s}$ -interval corresponding to a energy resolution of  $\Delta\omega = 1$  eV and  $\Delta\omega = 10$  eV, respectively. This result corresponds to the intensity pattern in x-ray scattering experiments.

It is interesting to compare Fig. 7.7 with Fig. 7.3. These figures result from two completely different approaches: in [88] the crucial transitions were bound-to-bound transitions, whereas in the time-resolved Compton scattering we consider only bound-to-free transitions. In particular, we have made a plane wave assumption for the recoil electron state. In Ref. [88] the energy transfer was minimized by the spectral window function, whereas the Compton scattering relies on a large energy transfer. Yet, both patterns match conspicuously, in the sense that the scattering signal at the large  $Q$  values in Fig. 7.3 resembles the Compton scattering pattern. It has a ring-like structure that oscillates up and down, like the pattern in Fig. 7.7 (note the different  $Q$  range in the figures). The elastic scattering signal in Fig. 7.3 is concentrated in the center of the diffraction signal [88]. This similarity may be a peculiarity of atomic hydrogen: the Rydberg states converge for  $n \rightarrow \infty$  to unbound Coulomb states for  $E \rightarrow 0$ , and in a single-electron system the recoil electron is never

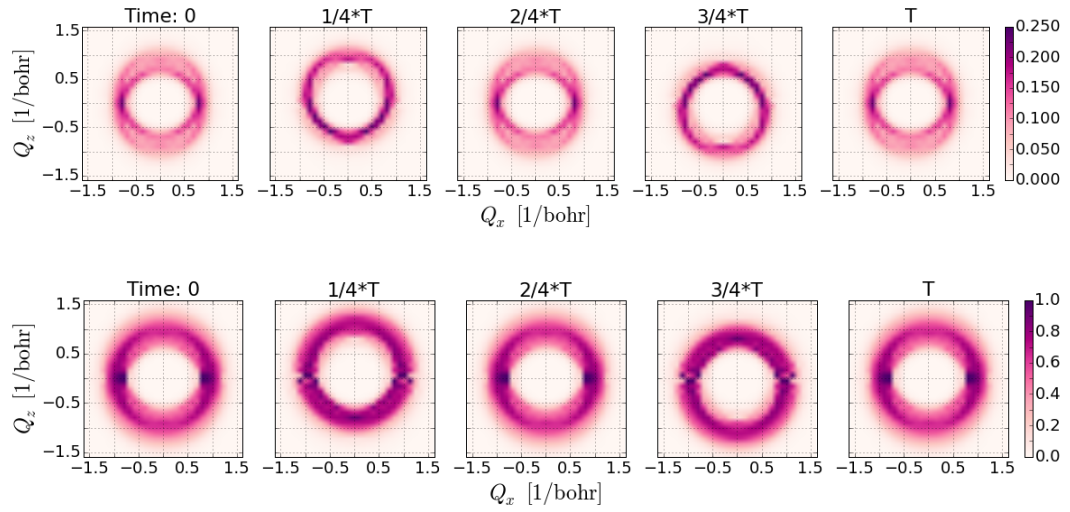


Figure 7.7.: Single differential scattering cross section  $d\sigma/d\Omega_{\mathbf{k}_s}$  for time-resolved Compton scattering from the 3d-4f wave packet of hydrogen: DDSCS integrated over a  $\omega_{\mathbf{k}_s}$ -interval (corresponding to energy resolution),  $(Q_x, 0, Q_z)$ -plane in  $Q$ -space in units of  $(\frac{d\sigma}{d\Omega})_{\text{Th}}$ . *Upper panel*: 1 eV interval, centered at  $\omega = 10$  eV. *Lower panel*: 10 eV interval, from  $\omega = 10$  eV to  $\omega = 20$  eV.

correlated to the remaining ion, i.e., the sudden approximation is always valid.

Heuristically, it has always been plausible that Fig. 7.3 reflects the electron momentum. Finally, a rigorous explanation for this effect is offered by the striking similarity with the scattering signal from time-resolved Compton scattering. Most importantly, the connection of inelastic scattering with the momentum density of the wave packet explains the oscillation period of the diffraction pattern and the violation of Friedel's law.

# Chapter 8.

## Compton scattering in single molecule coherent diffractive imaging

In this chapter I present a rigorous ab initio treatment of incoherent scattering under typical single molecule imaging conditions. My extension of the XATOM toolkit to include incoherent scattering has been used to calculate the presented data. This chapter is based on the article [4]:

SLOWIK, SON, DIXIT, JUREK AND SANTRA [New J. Phys. 16, 073042 \(2014\)](#).

### 8.1. Introduction

#### Basics of single molecule imaging with XFELs

One of the groundbreaking applications of x-ray free-electron lasers (XFELs) is expected to be the imaging of the structure of single molecules with atomic resolution [144–146].

*Why the necessity to resolve molecular structures with atomic resolution?* At the root lies the structure-function relationship: The structure of a molecule defines its function. Being of particular importance for biological systems, this relationship is the cornerstone of the field of structural biology. To comprehend the function of biological macromolecules it is essential to unravel their structure. A potential application is the design of new drugs targeting these molecules. A further application may be the understanding of energy harvesting molecules with the prospect of designing better photovoltaic devices.

*Why the necessity to image single molecules?* In fact, x-ray and electron crystallography have been extremely successful in the last 100 years [113, 114]. X-ray crystallography has resolved the majority of currently known protein structures [147]. However, the success of crystallography is irrevocably subject to the availability of crystals. Unfortunately, numerous interesting proteins, such as membrane pro-

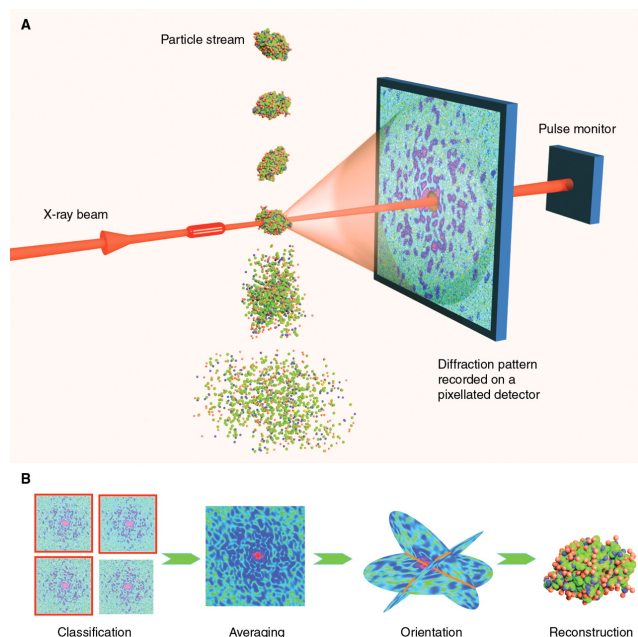


Figure 8.1.: Scheme of single molecule CDI experiment at an XFEL.

(A) The x-ray beam hits the target, scattered photons are detected with a pixel array detector. The target is so strongly ionized that it Coulomb explodes after each shot. (B) The data from many shots is classified into images from similar orientation of the target, averaged and the orientation is determined. Finally, phase reconstruction yields the 3d structure.

Taken from (Gaffney, Chapman Science **316**, 1444) [144]. Reprinted with permission from AAAS. © 2007 American Association for the Advancement of Science.

teins, do not form crystals. A recent breakthrough is the novel technique of serial femtosecond crystallography (SFX) using XFELs [148–150]. It has led to the determination of a previously unknown biomolecular structure [151] and has paved the way to time-resolved studies with Ångström resolution [152–155]. SFX promises to mitigate the problem of crystallization by requiring smaller crystals, which are often easier to grow. The imaging of single molecules would make the difficult crystallization completely unnecessary. So far, imaging of non-crystalline targets with XFEL radiation has been demonstrated with about 30-40 nanometer resolution on single viruses [156] and living bacteria [157].

*Why the need for XFELs?* In crystallography the x-ray radiation scatters on crystals, which results in a diffraction pattern of sharp Bragg spots. X rays generated by synchrotron radiation at storage rings have the necessary fluence and degree of

spatial coherence. In single molecule imaging there is solely the x-ray scattering from a single molecule. Consequently, the scattering signal is continuous and very weak. The emerging x-ray free-electron lasers (XFELs) [6–11] offer coherent x-ray pulses with unprecedentedly high fluence. In this way one expects to obtain enough x-ray scattering signal from single molecules. Moreover, XFELs feature ultrashort x-ray pulses with a few-femtosecond pulse duration. This permits one to outrun the Coulomb explosion [158, 159].

*What is the Coulomb explosion?* The Coulomb explosion is the ionization-induced dynamics of the atoms in the molecule during and after the x-ray pulse [158–162]. Due to the extremely high intensity of XFEL pulses, many x-ray photons are absorbed causing a cascade of ionization events in the molecule. The remaining positively charged ions repel each other, which causes the molecule to disintegrate on an ultrafast time scale of tens of femtoseconds [158, 160–162]. Hence it is named Coulomb explosion. There are several ionization mechanisms that play a role. The most important ones are direct photoionization with subsequent Auger decay and electron impact ionization. Further ionization mechanisms are shake-up and shake-off processes [163–165], internal field ionization [166–168] and Compton scattering [158].

*How does radiation damage affect the imaging?* It is believed that with sufficiently fast x-ray pulses one can outrun the Coulomb explosion [158–162]. In this so-called “diffract-before-destruct” approach, one collects the diffraction data before the nuclear dynamics changes the molecular structure sensitively. The degradation of the scattering pattern due to electronic rearrangements caused by ionization is called electronic radiation damage [169–172].

*What is the imaging method?* Coherent diffractive imaging (CDI) is a lensless imaging technique for the 3-dimensional reconstruction of nanoscale structures [144–146, 174]. CDI can reach a spatial resolution on the order of the wavelength of the radiation. Since we consider spatially coherent hard x rays, atomic resolution (of about  $1 \text{ \AA} = 10^{-10} \text{ m}$ ) is feasible. It is noteworthy that electron diffraction is a complementary and competing technique, especially for very small molecules [175, 176]. The simple basic principle of single molecule x-ray CDI is illustrated in Fig. 8.1. The target molecule is injected into a highly coherent XFEL beam. When the beam scatters from the molecule the diffraction pattern is recorded. During this measurement process the molecule is destroyed by the Coulomb explosion. To gain sufficient diffraction data from all orientations of the molecule, many diffraction patterns from identical copies of the target molecule have to be collected. The reconstruction of the 3d structure can then be performed numerically.

*How can one reconstruct the structure?* The elastically (or coherently) scattered photons are related to the structure of the target. We found in Eq. (6.40) that the scattering pattern is the squared modulus of the Fourier transform of the electron density. The diffraction pattern of each orientation yields a 2d cut of the 3d sphere of

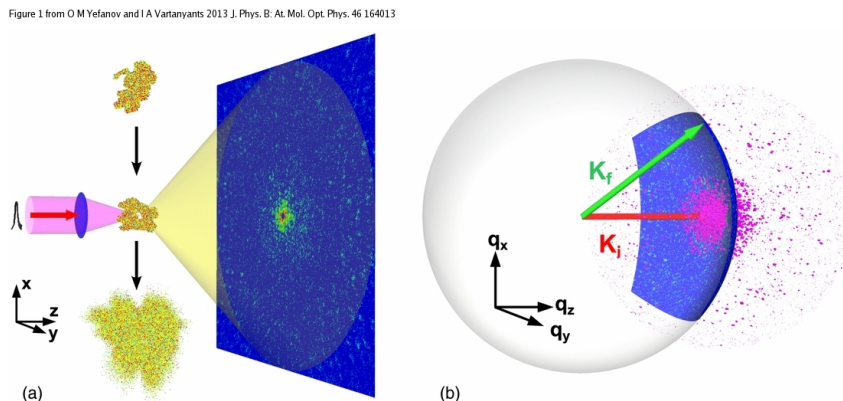


Figure 8.2.: Coherent diffractive imaging. (a) Diffraction from the sample in real-space results in a 2d diffraction pattern. (b) The diffraction pattern lies on the Ewald sphere in reciprocal space and is a cut of of the 3d intensity pattern.

Figure taken from (Yefanov, Vartanyants *J. Phys. B* **46**, 164013) [173].

© 2013 IOP Publishing Ltd.

intensities in reciprocal space, see Fig. 8.2. Because one measures only intensities in reciprocal space, the phases are lost. Collecting measurements from all orientations one may sample the entire 3d Fourier space. Because the orientation of the sample is typically unknown, one needs to retrieve the sample orientation [173, 177–179]. Finally, the missing phases in reciprocal space have to be recovered. This is called the phase-problem, familiar from crystallography [180]. In single molecule imaging one may exploit the continuous diffraction pattern to solve the phase-problem. By oversampling the diffraction pattern one may extract sufficient information to reconstruct the phases [145, 181–183]. Inverse Fourier transformation then yields the electron density, from which one deduces the atomic positions. In this way, the previously unknown structure is reconstructed from many the diffraction patterns.

### Motivation for studying Compton scattering in CDI

Information about the structure of the target is encoded in the coherent x-ray scattering pattern.<sup>1</sup> Surprisingly, the unavoidable incoherent x-ray scattering signal in a single molecule imaging experiment is usually completely neglected. Carrying no structural information, incoherent scattering degrades the quality of the signal. There are probably two main reasons that incoherent scattering has not been a mat-

<sup>1</sup>Note that in this chapter we may use coherent and elastic scattering interchangeably, as well as incoherent and inelastic scattering.

ter of interest in most of the literature. First, in crystallography there are Bragg reflections, which strongly enhance the coherent scattering signal. As a consequence, one can safely neglect the incoherent scattering in crystallography. In single molecule imaging the diffraction pattern is continuous. Thus, there is no reason to neglect the incoherent scattering a priori. Second, CDI experiments performed on mesoscale targets have not suffered from considerable background. But these experiments have been performed at a resolution of several tens of nanometers [156]. Estimations of the incoherent scattering contribution in hydrodynamic models of carbon clusters have indicated its influence at higher resolution [184, 185]. In fact, we will find that there is a strong incoherent background at atomic (Ångström) resolution. Unfortunately, the presently used imaging pixel array detectors [99, 100, 186, 187] are not designed to energetically distinguish the coherent scattering from the incoherent scattering, which is shifted in photon energy. Consequently, filtering out the coherent signal in experiment is not feasible in the near future.

In summary, incoherent scattering degrades the quality of the signal for CDI experiments. This means quantitative understanding of the incoherent scattering signal is indispensable for future experiments, facility design, and development of data processing algorithms. The present results may contribute some new facets to discuss which XFEL machine developments are beneficial for imaging [188, 189].

## 8.2. Formalism of high-intensity x-ray scattering

### 8.2.1. The regime of ionization induced extreme matter states

The x-ray wavelength determines the regime of possible spatial resolution in CDI. Since 12.4 keV photon energy correspond to 1 Å wavelength, several keV photon energy are required for imaging with atomic resolution. CDI is based on the nonresonant scattering formalism from Sec. 2.1.4 governed by the  $\mathbf{A}^2$ -interaction Hamiltonian

$$\hat{H}_{\text{int}} = \frac{\alpha^2}{2} \int d^3x \hat{\mathbf{A}}^2(\mathbf{x}) \hat{n}(\mathbf{x}). \quad (8.1)$$

At the given photon energies it is justified to neglect resonant scattering for biological molecules. Biological molecules consists mostly of light elements, carbon being the most abundant after hydrogen. These elements have typically K-shell binding energies of several hundred eV. Consequently, the photon energy for CDI imaging lies far above the absorption edges.

However, XFELs break new grounds in x-ray-matter interactions because of the unprecedented high x-ray fluence. The dominating process at several keV photon energy is photoabsorption, see Fig. 8.3. The ionization dynamics (during and after the x-ray pulse) expose matter to extreme conditions far from equilibrium [22, 192]. Consequently, we have to include the ionization and relaxation dynamics in our

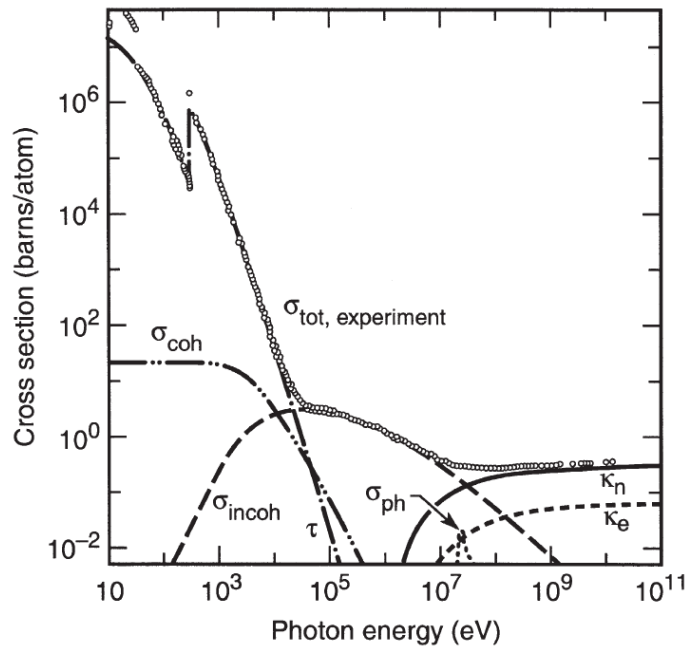


Figure 8.3.: The total photon cross section  $\sigma_{\text{tot}}$  in carbon as a function of incoming photon energy. The contributions of different processes are distinguished:  $\tau$  photoabsorption,  $\sigma_{\text{coh}}$  coherent (elastic) scattering,  $\sigma_{\text{incoh}}$  incoherent (Compton) scattering. Processes irrelevant for this thesis are:  $e^+e^-$  pair production in the nuclear field  $\kappa_n$  and electron field  $\kappa_e$  (triplet production), as well as nuclear photoabsorption  $\sigma_{\text{ph}}$ .

Reprinted with permission from (Hubbell, Gimm, Øverbø, J. Phys. Chem. Ref. Data **9**, 1023) [190], cf. x-ray data booklet [191]. ©1980, AIP Publishing LLC.

model to obtain realistic results. The situation is dramatically different from third-generation synchrotron-radiation sources, where the probability that a single atom absorbs more than one x-ray photon is negligibly small. In contrast, XFEL pulses naturally achieve the saturation x-ray absorption [172, 192–196]. Atoms exposed to XFEL radiation are excited to highly charged states, it is even possible that all electrons are subsequently stripped off the atom [193]. In an experiment on xenon [194], charge states of  $\text{Xe}^{36+}$  were formed with 1.5 keV photons. Remarkably, the absorption of a single photon may lead to the ejection of several electrons. The absorption of a photon results in a cascade of (ultrafast) relaxation processes. Most importantly in light elements ( $Z \lesssim 30$ ), K-shell holes decay via Auger decay. In the high-intensity case of XFEL pulses, additional photons may be absorbed during

a decay cascade. The complex nature of all possible pathways is a challenge for numerical simulation [197]. A realistic simulation of CDI experiments has to take these ionization dynamics into account. This demands a suitably chosen formalism. The applicability of perturbation theory is questionable under conditions where the ground state may be completely depleted. This chapter serves as an outline of a formalism for nonresonant x-ray scattering in a strongly ionization driven system.

### 8.2.2. Differential scattering probability

The system is strongly driven by the dominating photoabsorption process. This is described by the " $\mathbf{p} \cdot \mathbf{A}$ " Hamiltonian, defined in Sec. 2.1.4. Note that the alteration of electronic structure – the so-called electronic radiation damage – has to be distinguished from the Coulomb explosion (the disintegration of molecular structure). Here, we assume a sufficiently short pulse duration to neglect structural dynamics [158]. We consider only electronic radiation damage, which cannot be avoided at high x-ray fluence.

We will consider the scattering induced by the " $\mathbf{A}^2$ " Hamiltonian as a small perturbation. In this subsection, an expression for the scattering probability similar to the ionization-free case will be derived. The practical treatment of the ionization dynamics is described in the following subsection. We write the total Hamiltonian as

$$\hat{H} = \hat{H}_{\text{el}} + \hat{H}_{\text{rad}} + \hat{H}_{\mathbf{p} \cdot \mathbf{A}} + \hat{H}_{\mathbf{A}^2} = \hat{H}_0 + \hat{H}_{\mathbf{A}^2}. \quad (8.2)$$

Let us assume for the moment that we have solved the time-dependent Schrödinger equation for the driven system. Then we have found the time evolution operator  $\hat{U}_0(t, t_{\text{in}})$  with

$$\frac{d}{dt} \hat{U}_0(t, t_{\text{in}}) = -i \hat{H}_0 \hat{U}_0(t, t_{\text{in}}), \quad \text{with} \quad \hat{U}_0(t_{\text{in}}, t_{\text{in}}) = \mathbb{1}. \quad (8.3)$$

Treating the scattering in first order perturbation theory, the full time evolution operator  $\hat{U}(t, t_{\text{in}})$  is

$$\hat{U}(t, t_{\text{in}}) = \hat{U}_0(t, t_{\text{in}}) - i \int_{t_{\text{in}}}^t dt' \hat{U}_0(t, t') \hat{H}_{\mathbf{A}^2} \hat{U}_0(t', t_{\text{in}}). \quad (8.4)$$

The system is prepared long before the scattering ( $t_{\text{in}} \rightarrow -\infty$ ) in the initial state  $\hat{\rho}_{\text{in}} = \hat{\rho}_{\text{in}}^X \otimes \hat{\rho}_{\text{in}}^{\text{el}}$ . In a typical experimental setup the incoming beam is filtered out and only scattered photons are measured. As in Sec. 6.3, we employ the projection operator onto a scattered photon mode as observable

$$\hat{\mathcal{O}}_{\mathbf{k}_s} = \hat{P}_{\mathbf{k}_s, \lambda_s} \otimes \hat{\mathbb{1}}_{\text{el}}. \quad (8.5)$$

$\hat{P}_{\mathbf{k}_s, \lambda_s}$  is the projection operator onto all multimode Fock states with one photon in the mode  $(\mathbf{k}_s, \lambda_s)$ . The differential scattering probability is given by

$$\frac{dP}{d\Omega} = \sum_{\lambda_s} \frac{V\alpha^3}{(2\pi)^3} \int \omega_{\mathbf{k}_s}^2 d\omega_{\mathbf{k}_s} P(\mathbf{k}_s). \quad (8.6)$$

$P(\mathbf{k}_s) = \text{Tr}(\hat{\rho}_f \hat{O}_{\mathbf{k}_s})$  is the expectation value of  $\hat{O}_{\mathbf{k}_s}$  in the state  $\hat{\rho}_f$  of the total system, given by

$$\hat{\rho}_f = \lim_{\substack{t_f \rightarrow \infty \\ t_{in} \rightarrow -\infty}} \iint_{t_{in}}^{t_f} dt_1 dt_2 \hat{U}_0(t_f, t_1) \hat{H}_{\hat{\mathbf{A}}_2} \hat{U}_0(t_1, t_{in}) \hat{\rho}_{in} \hat{U}_0^\dagger(t_2, t_{in}) \hat{H}_{\hat{\mathbf{A}}_2} \hat{U}_0^\dagger(t_f, t_2). \quad (8.7)$$

So far the derivation has been analogous to the ionization-free case in Sec. 6.3. At this point, it is important to emphasize the differences. In the case with ionization, the time-evolution can entangle the electronic and radiation systems. This is most easily understood for the case of a single incoming photon: if the photon is absorbed and an electron ionized the state of the radiation system changes drastically. In this case the radiation and electronic system are strongly correlated. In the following, we will see that under typical experimental conditions the photonic and electronic degrees of freedom can be disentangled. The detailed derivation is performed in Appendix 8.A.

Let us assume, for simplicity, that the molecule is initially in its electronic ground state

$$\hat{\rho}_{in}^{el} = |\Psi_0\rangle\langle\Psi_0|. \quad (8.8)$$

We express the initial state of the radiation system in a coherent state representation

$$\hat{\rho}_{in}^X = \int \prod_{(\mathbf{k}, \lambda)} d^2\alpha_{\mathbf{k}, \lambda} P(\{\alpha_{\mathbf{k}, \lambda}\}) |\{\alpha_{\mathbf{k}, \lambda}\}\rangle\langle\{\alpha_{\mathbf{k}, \lambda}\}|, \quad (8.9)$$

where  $P(\{\alpha_{\mathbf{k}, \lambda}\})$  is the Glauber-Sudarshan  $P$ -function [198]. We assume that the  $P$ -function has Gaussian form [71]

$$P(\{\alpha_{\mathbf{k}, \lambda}\}) = \prod_{\mathbf{k}, \lambda} \frac{1}{\pi \langle \hat{n}_{\mathbf{k}, \lambda} \rangle} e^{-\frac{|\alpha_{\mathbf{k}, \lambda}|^2}{\langle \hat{n}_{\mathbf{k}, \lambda} \rangle}}. \quad (8.10)$$

Glauber has shown that the  $P$ -function takes on such a Gaussian form, with increasing number of statistically independent, arbitrary, stationary sources which excite multiple modes of the radiation field [198]. Because of the random excitation of the field the corresponding density operator describes a chaotic radiation field; in fact, it cannot have second or higher order of coherence. Most importantly, it has been shown that the x-ray radiation field produced by a SASE FEL can be described by

a Gaussian  $P$ -function [199, 200]. The Gaussian  $P$ -function has the useful property that all higher-order correlation functions can be expressed in terms of the first-order correlation function. The first-order correlation function of the SASE FEL can be modelled as quasi-stationary and quasi-monochromatic. This means we can describe the pulse by the average intensity  $I(t)$  and the temporal coherence function  $\gamma(\tau)$ , i.e.,

$$G^{(1,1)}(t_1, t_2) = 4\pi\alpha I\left(\frac{t_1+t_2}{2}\right)\gamma_{\text{tp}}(t_2 - t_1), \quad (8.11)$$

where the temporal coherence function  $\gamma_{\text{tp}}(\tau) = e^{-\tau^2/\tau_c^2} e^{i\omega_{\text{in}}\tau}$  defines the coherence time  $\tau_c$  of the pulse. In particular, we will assume that the coherence time is so short, the temporal coherence function is essentially a delta function in time. This assumption is justified by the fact that SASE FEL pulses have a spiky structure with coherence time in the subfemtosecond regime. Moreover, we assume only sequential one-photon absorption, which is a reasonable approximation [192, 195]. Note that the scattered photons must interfere coherently, thus  $t_1$  and  $t_2$  must lie within the coherence time.

Finally, from a lengthy derivation (see Appendix 8.A) the scattering probability is obtained

$$\begin{aligned} P(\mathbf{k}_s) &= \lim_{\substack{t_f \rightarrow \infty \\ t_{\text{in}} \rightarrow -\infty}} \sum_{\lambda_s} \frac{2(2\pi)^2}{V} \iint d^3x_1 d^3x_2 \frac{1}{\omega_{\mathbf{k}_s} \omega_{\text{in}}} \alpha |\epsilon_{\text{in}}^* \cdot \epsilon_{\mathbf{k}_s, \lambda_s}|^2 e^{i\mathbf{Q} \cdot (\mathbf{x}_1 - \mathbf{x}_2)} \\ &\times \int_{t_{\text{in}}}^{t_f} dt \frac{I(t)}{\omega_{\text{in}}} \int_{-\infty}^{\infty} d\tau e^{-\tau^2/\tau_c^2} e^{i(\omega_{\text{in}} - \omega_{\mathbf{k}_s})\tau} \\ &\times \text{Tr} \left( \hat{\rho}_{\text{el}}(t) e^{i\hat{H}_{\text{el}}\tau/2} \hat{n}(\mathbf{x}_2) e^{-i\hat{H}_{\text{el}}\tau} \hat{n}(\mathbf{x}_1) e^{i\hat{H}_{\text{el}}\tau/2} \right) \end{aligned} \quad (8.12)$$

where

$$\begin{aligned} \hat{\rho}_{\text{el}}(t) &= \sum_a \left( \frac{4\pi\alpha}{\omega_{\text{in}}^2} \right)^a \int_{t_{\text{in}}}^t dt_{A_a} \int_{t_{\text{in}}}^{t_{A_a}} dt_{A_{a-1}} \cdots \int_{t_{\text{in}}}^{t_{A_2}} dt_{A_1} I(t_{A_1}) \cdots I(t_{A_a}) \\ &\times e^{-i\hat{H}_{\text{el}}(t-t_{\text{in}})} \hat{\mathcal{I}}(t_{A_a}) \cdots \hat{\mathcal{I}}(t_{A_1}) |\Psi_0\rangle \langle \Psi_0| \hat{\mathcal{I}}^\dagger(t_{A_1}) \cdots \hat{\mathcal{I}}^\dagger(t_{A_a}) e^{i\hat{H}_{\text{el}}(t-t_{\text{in}})}. \end{aligned} \quad (8.13)$$

The electronic state includes any numbers of photoionization events. The resulting relaxation processes are included in the interactions through the electronic Hamiltonian. Note that in this approach we have rigorously performed the ensemble average over the field. No separation of the ensemble average for the scattering and the ionization dynamics has been necessary. Most importantly, we have found an expression for the x-ray scattering probability that is similar to the ionization-free formulation. The final expression exhibits the familiar density-density correlations, the time-dependence on the system is contained in the electronic state of the system. In the next subsection, a practical method for the calculation of the electronic state is considered.

### 8.2.3. Rate equation approach for electronic system

The previous subsection has shown that x-ray scattering at high-intensity depends on a complex electronic state, depending on the electronic dynamics induced by photoabsorption and relaxation processes in the molecule. It is still an open question to find rigorous and numerically feasible methods to determine the electron dynamics resulting from a strong driving by a high-intensity x-ray pulse. Possible approaches for a rigorous treatment are the theory of open quantum systems [201, 202] and quantum kinetical approaches [203–208], based on density matrix theory or the nonequilibrium Green’s functions technique.

However, empirical evidence shows that rate equation approaches successfully reflect the experimental situation [160, 172, 192, 195]. Thus, we employ a rate equation approach for the electronic dynamics, tracking the populations  $P_I$  of electronic configuration  $I$ . The transitions between the possible electronic configurations  $\{I\}$  are represented by a set of coupled rate equations (also known as “Pauli master equation”)

$$\frac{d}{dt}P_I(t) = \sum_{I' \neq I} [\Gamma_{I' \rightarrow I}P_{I'}(t) - \Gamma_{I \rightarrow I'}P_I(t)], \quad (8.14)$$

where  $\Gamma_{I' \rightarrow I}$  is the rate for a transition from configuration  $I'$  to  $I$ . The Pauli master equation for the x-ray interaction with molecules can be derived from the Bloch-Redfield equation under certain assumptions [209]. In general, rate equations emerge in many physical situations. The validity of the Pauli master equation is often derived from the averaging over many degrees of freedom (e.g., the bath in an open system) [201, 210–212]. For systems with many degrees of freedom it can also be derived from certain assumptions on the interactions [213, 214]. Recently, the first investigations on the role of atomic coherences and consequences of non-markovian behaviour were carried out [215–218]. A crucial assumption in the presented derivation has been the incoherence of the x-ray pulse. With the emergence of coherent self-seeded FEL sources, non-markovian behaviour that cannot be captured by the rate equation approach may become important. This has to be analyzed elsewhere.

Having determined the populations of the electronic configurations from the rate equation approach, the differential scattering signal is defined by

$$\frac{d\mathcal{I}}{d\Omega_{\mathbf{k}_s}} = \int dt j(t) \sum_I P_I(t) \frac{d\sigma}{d\Omega_{\mathbf{k}_s}} \Big|_I. \quad (8.15)$$

Here,  $j(t)$  is the photon flux at time  $t$  of the incident x-ray pulse and  $\frac{d\sigma}{d\Omega_{\mathbf{k}_s}} \Big|_I$  the differential scattering probability of the  $I$ -th electronic configuration. In addition to photoabsorption the accompanying relaxation processes Auger decay and fluorescence are included in the model. We neglect the ionization by Compton scattering

in the rate equation description because the population dynamics are clearly dominated by photoabsorption. In the regime considered here, this is justified because the photoabsorption cross section is about one order of magnitude larger than the total Compton cross section. For example, at  $\omega_{\text{in}} = 10$  keV we obtain from our calculations for a neutral carbon atom in its ground state configuration a total Compton scattering cross section  $\sigma_{\text{Compton}} = 2.7$  barn (cf. [219]) and a total photoabsorption cross section  $\sigma_{\text{abs}} = 41.6$  barn.

In large molecules or clusters electron impact ionization can become a major source of ionization [160, 162, 220–224]. We do not treat electron impact ionization. Thus, our present results rather underestimate the scattering signal from ionized electrons (see below). We also neglect electron recombination that might attenuate the ionization [160, 225, 226].

Altogether, the differential scattering cross section of the  $I$ -th configuration contains the coherent and incoherent scattering from bound electrons (see Eq. (8.22) below) and the Compton scattering from free electrons (see Eq. (8.27) below), cf. [184, 185, 227, 228],

$$\left. \frac{d\sigma}{d\Omega_{\mathbf{k}_s}} \right|_I = \left( \frac{d\sigma}{d\Omega} \right)_{\text{Th}} \left( |f_I(\mathbf{Q})|^2 + S_I(\mathbf{Q}) + N_I^{\text{free}} \right). \quad (8.16)$$

Here,  $N_I^{\text{free}}$  denotes the number of free electrons in configuration  $I$ .  $f_I(\mathbf{Q})$  and  $S_I(\mathbf{Q})$  are the atomic form factor and the static structure factor of configuration  $I$ , respectively.

## 8.3. Form and structure factors

### 8.3.1. Formalism

As already mentioned, the nonresonant scattering is governed by the  $\mathbf{A}^2$ -interaction Hamiltonian

$$\hat{H}_{\text{int}} = \frac{\alpha^2}{2} \int d^3x \hat{\mathbf{A}}^2(\mathbf{x}) \hat{n}(\mathbf{x}). \quad (8.17)$$

Because in the rate equation approach only the populations of electronic configurations are considered, we may consider the electronic system to be in a stationary state  $|\Psi_0\rangle$  (at the instant of the scattering event). Moreover, according to Eq. (8.12) the differential scattering probability can be calculated for this state as in the stationary case. After the scattering event the electronic system will be in the state  $|\Psi_F\rangle$ . An incoming x-ray photon of energy and momentum  $(\omega_{\text{in}}, \mathbf{k}_{\text{in}})$  transfers energy  $\omega = \omega_{\text{in}} - \omega_s$  and momentum  $\mathbf{Q} = \mathbf{k}_{\text{in}} - \mathbf{k}_s$  to the electronic system, thereby making the transition to the scattered photon state  $(\omega_s, \mathbf{k}_s)$ . As described in Sec. 6.3 one obtains the double differential scattering cross section (DDSCS) from Fermi's

golden rule [21], yielding

$$\frac{d^2\sigma}{d\Omega_{\mathbf{k}_s} d\omega_s} = \left(\frac{d\sigma}{d\Omega}\right)_{\text{Th}} \frac{\omega_s}{\omega_{\text{in}}} \sum_F \delta(E_F - E_0 - \omega) \left| \int d^3x \langle \Psi_F | \hat{n}(\mathbf{x}) | \Psi_0 \rangle e^{i\mathbf{Q}\cdot\mathbf{x}} \right|^2. \quad (8.18)$$

Recall,  $(\frac{d\sigma}{d\Omega})_{\text{Th}} = \alpha^4 \sum_{\lambda_s} |\boldsymbol{\epsilon}_{\mathbf{k}_s, \lambda_s}^* \cdot \boldsymbol{\epsilon}_{\mathbf{k}_{\text{in}}, \lambda_{\text{in}}}|^2$  denotes the Thomson scattering cross section (TSCS). In this chapter we will assume that the x-ray pulse is sufficiently monochromatic to neglect the bandwidth of the x-ray pulse.

Within the independent-particle approximation there is only one electron involved in the scattering process. This electron is independent from the other electrons, i.e., there are no correlations. Within this approximation the final electronic state can be written

$$|\Psi_F\rangle = \hat{c}_f^\dagger \hat{c}_i |\Psi_0\rangle. \quad (8.19)$$

We have used the creation (annihilation) operator  $\hat{c}_p^\dagger$  ( $\hat{c}_p$ ) of the spin-orbital  $|\varphi_p\rangle$  with energy  $\varepsilon_p$ , see Sec. 2.1.2. Furthermore, we assume the initial state to be a single Slater determinant

$$|\Psi_0\rangle = \hat{c}_{p_1}^\dagger \dots \hat{c}_{p_N}^\dagger |0\rangle. \quad (8.20)$$

Expanding the electron density operator  $\hat{n}(\mathbf{x}) = \sum_{p,q} \varphi_p^\dagger(\mathbf{x}) \varphi_q(\mathbf{x}) \hat{c}_p^\dagger \hat{c}_q$ , we can express the DDSCS in terms of the spin orbitals

$$\begin{aligned} \frac{d^2\sigma}{d\Omega_{\mathbf{k}_s} d\omega_s} = & \left(\frac{d\sigma}{d\Omega}\right)_{\text{Th}} \frac{\omega_s}{\omega_{\text{in}}} \left( \delta(\omega) \left| \sum_i \int d^3x \varphi_i^\dagger(\mathbf{x}) \varphi_i(\mathbf{x}) e^{i\mathbf{Q}\cdot\mathbf{x}} \right|^2 \right. \\ & \left. + \sum_f^{\text{unocc.}} \sum_i^{\text{occ.}} \delta(\varepsilon_f - \varepsilon_i - \omega) \left| \int d^3x \varphi_f^\dagger(\mathbf{x}) \varphi_i(\mathbf{x}) e^{i\mathbf{Q}\cdot\mathbf{x}} \right|^2 \right), \quad (8.21) \end{aligned}$$

where the index  $i$  runs over all occupied spin-orbitals in the initial state  $|\Psi_0\rangle$ , and the index  $f$  over all unoccupied spin-orbitals in  $|\Psi_0\rangle$ . Keeping the solid angle element  $d\Omega_{\mathbf{k}_s}$  fixed, the DDSCS determines the spectrum of the scattered radiation.

The photon detectors used in coherent diffractive imaging experiments are not designed to resolve the photon energy [99, 100, 186, 187]. Consequently, only the energy integrated DDSCS is experimentally accessible. Integrating the DDSCS over  $\omega_s$  yields the differential scattering cross section

$$\frac{d\sigma}{d\Omega_{\mathbf{k}_s}} = \left(\frac{d\sigma}{d\Omega}\right)_{\text{Th}} (|f(\mathbf{Q})|^2 + S(\mathbf{Q})). \quad (8.22)$$

Coherent (elastic) scattering is governed by the form factor

$$f(\mathbf{Q}) = \int d^3x \sum_i^{\text{occ.}} \varphi_i^\dagger(\mathbf{x}) \varphi_i(\mathbf{x}) e^{i\mathbf{Q}\cdot\mathbf{x}}. \quad (8.23)$$

Incoherent (inelastic) scattering is characterized by the static structure factor

$$S(\mathbf{Q}) = \int d\omega_s \frac{\omega_s}{\omega_{\text{in}}} \sum_f^{\text{unocc.}} \sum_i^{\text{occ.}} \delta(\varepsilon_f - \varepsilon_i - \omega) \left| \int d^3x \varphi_f^\dagger(\mathbf{x}) \varphi_i(\mathbf{x}) e^{i\mathbf{Q}\cdot\mathbf{x}} \right|^2. \quad (8.24)$$

The free electrons that are created during the pulse by photoionization or relaxation processes will also contribute to the scattering signal [158, 184, 185]. In general the free electrons have a highly nonthermal kinetic energy distribution [224]. The fast photoelectrons with 10 keV energy have a velocity of  $\sim 600 \text{ \AA/fs}$ , which means they stay inside a  $1 \mu\text{m}^2$  focal spot for several femtoseconds. Keeping in mind that a free electron with 100 eV energy travels about  $60 \text{ \AA/fs}$ , it becomes apparent that the free electron cloud will expand during the pulse to a volume with a radius much larger than  $10 \text{ \AA}$ . Consequently, coherent scattering from the free electrons will only be important at very low resolution. Here, we make the assumption that unbound electrons are well described by plane wave states  $\varphi_{\text{unb}}(\mathbf{x}) = V^{-1/2} e^{i\mathbf{p}\cdot\mathbf{x}} \chi_s$ . Scattering without changing the plane wave state can occur for zero momentum transfer  $\mathbf{Q} = 0$  only. Thus, neglecting the small scattering angle regime, we can neglect elastic scattering from free electrons.

On the other hand, incoherent scattering from free electrons is possible for all scattering angles. Replacing  $\sum_f$  by  $\frac{V}{(2\pi)^3} \int d^3p'$  the static structure factor of an unbound electron with momentum  $\mathbf{p}$  follows from Eq. (8.24)

$$S(\mathbf{Q}) = \int d\omega_s \frac{\omega_s}{\omega_{\text{in}}} \frac{V}{(2\pi)^3} \int d^3p' \delta(\varepsilon_{\mathbf{p}'} - \varepsilon_{\mathbf{p}} - \omega) \frac{1}{V^2} \left| \int d^3x e^{i(\mathbf{Q}+\mathbf{p}-\mathbf{p}')\cdot\mathbf{x}} \right|^2. \quad (8.25)$$

Using the trick  $\left| \int d^3x e^{i(\mathbf{Q}+\mathbf{p}-\mathbf{p}')\cdot\mathbf{x}} \right|^2 = V(2\pi)^3 \delta(\mathbf{Q} + \mathbf{p} - \mathbf{p}')$  [12] and performing the  $\omega_s$  integral with  $\varepsilon_{\mathbf{p}} = p^2/2$  yields

$$S(\mathbf{Q}) = \int d^3p' \frac{\omega_{\text{in}} + p^2/2 - p'^2/2}{\omega_{\text{in}}} \delta(\mathbf{Q} + \mathbf{p} - \mathbf{p}') = \frac{\omega_{\text{in}} - \mathbf{p} \cdot \mathbf{Q} - Q^2/2}{\omega_{\text{in}}}. \quad (8.26)$$

The final photon energy is  $\omega_s = \omega_{\text{in}} - \mathbf{p} \cdot \mathbf{Q} - Q^2/2$ . There are two energy shifts. The usual Compton shift  $Q^2/2$  for a resting electron [12]. At XFEL photon energies of several keV photon, the Compton shift is negligible  $\omega_s \approx \omega_{\text{in}} [1 + \alpha^2 \omega_{\text{in}} (1 - \cos \theta)]^{-1} \approx \omega_{\text{in}}$ . Moreover, there is an electron momentum dependent Doppler shift  $\mathbf{p} \cdot \mathbf{Q}$ . For slow electrons this induces also a very small change in the final photon energies. For the fast photoelectrons it becomes measurable if  $\mathbf{p}$  and  $\mathbf{Q}$  line up. We will assume that  $\omega_s \approx \omega_{\text{in}}$ . Under these approximations, the static structure factor of configuration  $I$  counts the number of unbound electrons

$$S(\mathbf{Q}) = N_I^{\text{free}}. \quad (8.27)$$

### 8.3.2. Static structure factor in the Waller-Hartree approach

Calculating the static structure factor can be quite cumbersome because it involves unoccupied spin-orbital calculations. For small energy transfers the Waller-Hartree approximation [229] can simplify the calculation of Eq. (8.24) significantly. Let the energy transfer  $\omega$  be small with respect to  $\omega_{\text{in}}$ , then one may assume  $\omega_s/\omega_{\text{in}} \approx 1$ . Moreover, the change of the momentum transfer vector due to the change of  $\omega_s$  is minute. Approximately  $\mathbf{Q}$  is the same as in elastic scattering  $\mathbf{Q} \approx \mathbf{k}_{\text{in}} - k_{\text{in}}\mathbf{k}_s/k_s$ . The static structure factor then reads

$$S(\mathbf{Q}) = \int d\omega \sum_f^{\text{unocc.}} \sum_i^{\text{occ.}} \delta(\varepsilon_f - \varepsilon_i - \omega) \iint d^3x d^3x' \varphi_f^\dagger(\mathbf{x}) \varphi_i(\mathbf{x}) \varphi_f(\mathbf{x}') \varphi_i^\dagger(\mathbf{x}') e^{i\mathbf{Q} \cdot (\mathbf{x} - \mathbf{x}')}. \quad (8.28)$$

Using the completeness of the spin-orbitals  $\sum_f^{\text{unocc.}} |\varphi_f\rangle \langle \varphi_f| = \mathbb{1} - \sum_j^{\text{occ.}} |\varphi_j\rangle \langle \varphi_j|$ , one finds

$$\sum_f^{\text{unocc.}} \varphi_f^\dagger(\mathbf{x}) \varphi_f(\mathbf{x}') = \delta(\mathbf{x} - \mathbf{x}') - \sum_j^{\text{occ.}} \varphi_j^\dagger(\mathbf{x}) \varphi_j(\mathbf{x}'). \quad (8.29)$$

Finally, we obtain the static structure factor

$$S(\mathbf{Q}) = Z - \sum_j^{\text{occ.}} \sum_i^{\text{occ.}} \left| \int d^3x \varphi_j^\dagger(\mathbf{x}) \varphi_i(\mathbf{x}) e^{i\mathbf{Q} \cdot \mathbf{x}} \right|^2, \quad (8.30)$$

where  $Z$  denotes the number of electrons in  $|\Psi_0\rangle$ . Remarkably, the final electronic states do not enter in this equation; all summations are carried out over spin-orbitals occupied in the initial state  $|\Psi_0\rangle$ .

Introducing a suitable averaging over initial Slater determinants the static structure factor can be transformed into a form suitable for numerical implementation. The details are given in Appendix 8.B. One finds

$$\langle S(\mathbf{Q}) \rangle_{\text{det}} = Z - 2 \sum_{n_j, l_j} \sum_{n_i, l_i} \langle \eta_j \eta_i \rangle_{\text{det}} \sum_L (2L+1)(2l_j+1) \left| R_{n_j l_j n_i l_i}^L(Q) C_{l_j 0 L 0}^{l_i 0} \right|^2, \quad (8.31)$$

where  $\eta_i \in \{0, 1\}$  denotes the occupation number of spin-orbital  $\varphi_i$ ,  $C_{l_j 0 L 0}^{l_i 0}$  is a Clebsch-Gordan coefficient, and  $R_{n_j l_j n_i l_i}^L(Q)$  (defined in Eq. (8.86)) is an integral of the radial wave functions and the spherical Bessel functions.

### 8.3.3. Static structure factor from explicit integration

Without making the Waller-Hartree assumption, the static structure factor can be calculated directly by performing the  $\omega_s$ -integration in Eq. (8.24). As in the previous

subsection we average over the initial Slater-determinants and recast Eq. (8.24) into a form that can be readily evaluated numerically, cf. Appendix 8.B. This subsection is an extension of Ref. [230].

Introducing as before the occupation numbers, averaging Eq. (8.24) over all possible initial Slater determinants for open shells yields

$$\langle S(\mathbf{Q}) \rangle_{\text{det}} = \int d\omega_s \frac{\omega_s}{\omega_{\text{in}}} \sum_{f,i} \langle (1 - \eta_f) \eta_i \rangle_{\text{det}} \delta(\epsilon_f - \epsilon_i - \omega) \left| \int d^3x \varphi_f^\dagger(\mathbf{x}) \varphi_i(\mathbf{x}) e^{i\mathbf{Q}\cdot\mathbf{x}} \right|^2. \quad (8.32)$$

Observe that  $1 - \eta_f$  gives only a nonzero contribution if  $|\varphi_f\rangle$  is an initially unoccupied orbital. We need to determine the average of the probability that  $|\varphi_i\rangle$  is occupied (“a particle”) while  $|\varphi_f\rangle$  is unoccupied (“a hole”)

$$\langle (1 - \eta_f) \eta_i \rangle_{\text{det}} = \langle \eta_i \rangle_{\text{det}} - \langle \eta_f \eta_i \rangle_{\text{det}}. \quad (8.33)$$

The average of pairs of occupation numbers has been determined in Eq. (8.79). For bound-to-free transitions we have the simple relation  $\langle (1 - \eta_f) \eta_i \rangle_{\text{det}} = \langle \eta_i \rangle_{\text{det}}$  because  $|\varphi_f\rangle$  has  $\eta_f = 0$  in all initial states. The same holds for bound-to-bound transitions where the shell of  $\varphi_f$  is empty in all initial states. However, for bound-to-bound transitions where  $\varphi_f$  lies in a initially open shell we have to take the  $\langle \eta_f \eta_i \rangle_{\text{det}}$  term into account. As an example, consider the bound-to-bound transition of a  $1s$ -electron into an empty  $2p$ -orbital in  $1s^2 2s^2 2p^2$  carbon:  $\langle (1 - \eta_{2p}) \eta_{1s} \rangle_{\text{det}} = 1 - \frac{1}{3}$ , which is not equal to  $\langle \eta_{1s} \rangle_{\text{det}} = 1$ .

The matrix element in Eq. (8.32) is evaluated in Appendix 8.B, see Eq. (8.88). Finally, the averaged static structure factor reads

$$\begin{aligned} \langle S(\mathbf{Q}) \rangle_{\text{det}} &= \int d\omega_s \frac{\omega_s}{\omega_{\text{in}}} 2 \sum_{n_f, l_f} \sum_{n_i, l_i} \delta(\omega_s - \omega_{\text{in}} - \epsilon_i + \epsilon_f) \langle (1 - \eta_f) \eta_i \rangle_{\text{det}} \\ &\quad \times \sum_L (2L + 1)(2l_i + 1) \left| R_{n_f l_f n_i l_i}^L(Q) C_{l_i 0 L 0}^{l_f 0} \right|^2. \end{aligned} \quad (8.34)$$

Compare this result with the Waller-Hartree approximation in Eq. (8.31). The crucial difference is that in the Waller-Hartree approximation only initially occupied orbitals play a role. Here, in contrast, the sum over  $n_f, l_f$  extends over all unoccupied states. Additionally, there is the integral over the final photon energy. However, the delta function restricts  $\omega_s$  to a fixed value for a given  $\varphi_f$ ; or vice versa, when integrating over a  $\omega_s$ -grid the delta-function restricts the possible final states  $\varphi_f$ . Moreover, we have made no approximation about the momentum transfer vector  $\mathbf{Q}$ . In the Waller-Hartree approximation  $\mathbf{Q}$  is approximated by the elastic scattering momentum transfer, where  $k_s = k_{\text{in}}$ . Here, we use the exact  $\mathbf{Q} = \mathbf{k}_{\text{in}} - \mathbf{k}_s$ .

In the special case that one considers only bound-to-free transitions one can further simplify Eq. (8.34). For bound-to-free transitions one has

$$\langle (1 - \eta_f) \eta_i \rangle_{\text{det}} = (1 - \langle \eta_f \rangle_{\text{det}}) \langle \eta_i \rangle_{\text{det}} = \left( 1 - \frac{N_{n_f, l_f}}{2(2l_f + 1)} \right) \frac{N_{n_i, l_i}}{2(2l_i + 1)}, \quad (8.35)$$

where  $N_{n_i, l_i}$  is the total number of electrons in the  $(n_i, l_i)$  subshell. This results in

$$\begin{aligned} \langle S(\mathbf{Q}) \rangle_{\text{det}} &= \int d\omega_s \frac{\omega_s}{\omega_{\text{in}}} \sum_{n_f, l_f}^{\text{free}} \sum_{n_i, l_i} \delta(\omega_s - \omega_{\text{in}} - \epsilon_i + \epsilon_f) N_{n_i, l_i} \left( 1 - \frac{N_{n_f, l_f}}{2(2l_f + 1)} \right) \\ &\times \sum_L (2L + 1) \left| R_{n_f l_f n_i l_i}^L(Q) C_{l_i 0 L 0}^{l_f 0} \right|^2. \end{aligned} \quad (8.36)$$

### 8.3.4. The XATOM toolkit

The expressions of the form and structure factors depend on the electronic wave functions. Thus, one needs to solve the electronic structure problem. The electronic structure calculations in this chapter were performed using the XATOM toolkit [231]. XATOM has been presented in Ref. [172]. This code for x-ray atomic processes calculates photoabsorption cross sections, fluorescence rates, Auger decay rates, as well as coherent scattering cross sections.

For the present work, we have extended the XATOM to calculate inelastic x-ray scattering cross sections. We have implemented the static structure factor within the Waller-Hartree approximation Eq. (8.31), as well as full energy integrated one Eq. (8.34).

XATOM solves the electronic structure problems for x-ray atomic processes using the Hartree-Fock-Slater model [172, 232, 233]. In this independent-particle model the mean-field Hamiltonian is

$$\hat{H}_{\text{HFS}} = -\frac{1}{2} \nabla^2 - \frac{Z}{|\hat{\mathbf{x}}|} + \int \frac{n(\mathbf{x}')}{|\hat{\mathbf{x}} - \mathbf{x}'|} d^3 x' + V_x(\hat{\mathbf{x}}), \quad (8.37)$$

where  $Z$  is the nuclear charge, the electron density  $n(\mathbf{x}) = \sum_i \varphi_i^\dagger(\mathbf{x}) \varphi_i(\mathbf{x})$  is a sum over occupied spin-orbitals, and  $V_x$  is the Slater exchange potential

$$V_x(\mathbf{x}) = -\frac{3}{2} \left[ \frac{3}{\pi} n(\mathbf{x}) \right]^{1/3}.$$

Furthermore, the Latter tail correction [234] is applied to the potential. Making the central field approximation, the Hamiltonian is angular momentum averaged to impose spherical symmetry. Thus, the solution of the Schrödinger equation can be expressed by a radial term  $u_{nl}$ , a spherical harmonic  $Y_{lm}$ , and a spin function

$$\varphi_{nlms}(\mathbf{x}) = \frac{u_{nl}(r)}{r} Y_{lm}(\Omega_{\mathbf{x}}) \begin{pmatrix} \delta_{s,+1/2} \\ \delta_{s,-1/2} \end{pmatrix}, \quad (8.38)$$

where  $u_{nl}$  with  $n = 1, 2, \dots$  characterizes bound states and continuum states are given by a  $u_{\epsilon l}$  with  $\epsilon > 0$ . The radial wave function  $u_{nl}$  for bound states is calculated by the XATOM code using the generalized pseudospectral method on a nonuniform grid. For unbound states  $u_{\epsilon l}$  is determined by numerically solving the radial Schrödinger equation for given  $\epsilon$  with the fourth-order Runge-Kutta method on a uniform grid. To evaluate integrals with bound and unbound wave functions XATOM uses a spline interpolation to map wave functions from the nonuniform to the uniform grid. For more details consult Ref. [172]. Open-shell systems, like carbon, are treated by averaging over all possible Slater determinants associated with an initial configuration.

## 8.4. Coherent and incoherent scattering from atomic carbon

I investigate the nonresonant incoherent x-ray scattering from atomic carbon, which is after hydrogen the most abundant element in biomolecules.

### 8.4.1. The spectrum of scattered photons

Fig. 8.4 shows the spectrum of x rays, scattered incoherently from a neutral carbon atom, for an incoming photon energy of 10 keV and a scattering angle of  $\theta = 60^\circ$ . Note that the detector geometry in coherent diffractive imaging experiments at XFELs allows scattering angles up to maximally  $\theta \lesssim 70^\circ$  [186, 187]. The spectrum was obtained from calculating the integrand in Eq. (8.36). Fig. 8.4 shows the continuous Compton spectrum of ionizing bound-to-free transitions. The next subsection shows that at  $\theta = 60^\circ$  the bound-to-bound transitions are negligible. At slightly less than 300 eV energy transfer one clearly identifies the carbon K-edge. K-shell Compton scattering only plays a minor role. The spectrum is peaked at a photon energy shift of about 100 eV, and scattering events with an energy shift of less than 200 eV are dominant. As a result it seems to be nearly impossible to filter out the incoherently scattered photons, because the Compton spectrum largely overlaps with the  $\sim 0.1\% - 1\%$  bandwidth of the x-ray pulse. This implies that only the static structure factor is accessible in experiment.

### 8.4.2. Comparison of Waller-Hartree approach and direct integration

The static structure factor can be calculated within the Waller-Hartree approximation as explained in Sec. 8.3.2 or by direct integration of the DDSCS as described Sec. 8.3.3. Fig. 8.5 compares the results of both methods, which show a good agreement. The slight deviation at large scattering angles is a direct result of the Waller-Hartree approximation. Both results coincide, when one replaces the exact  $\mathbf{Q}$  in the integrated DDSCS with the elastic  $\mathbf{Q}$ . In contrast to the Waller-Hartree

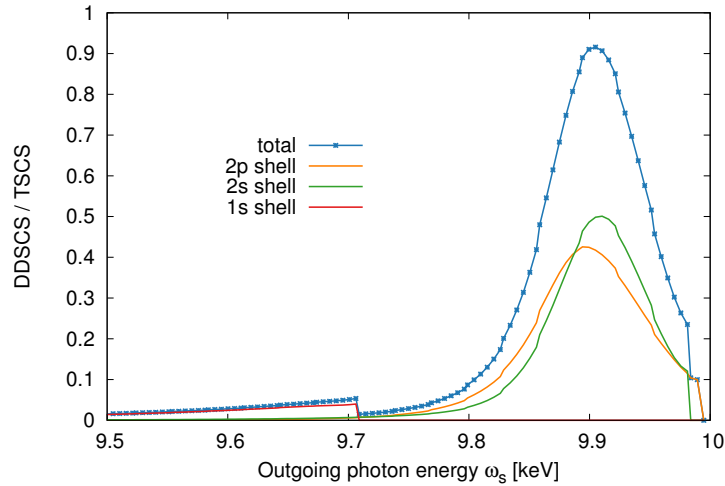


Figure 8.4.: The continuous Compton spectrum of ionizing bound-to-free transitions for  $\omega_{\text{in}} = 10$  keV and  $\theta = 60^\circ$ , contributions of the atomic orbitals are distinguished. Determined from the double differential scattering cross section (DDSCS) of a carbon atom in the ground state in units of the Thomson scattering cross section (TSCS).

Figure taken from (Slowik *et al.*, NJP **16**, 073042) [4] (line styles adapted).

©2014 IOP Publishing Ltd and Deutsche Physikalische Gesellschaft.

approach one has to determine all final states to use Eq. (8.34). This allows, however, to separate the contribution of bound-to-free and bound-to-bound transitions [235]. We find that bound-to-bound transitions play a minor role, although they are not negligible. The present result for carbon agrees with the exact analytical calculation for hydrogen in Ref. [135]. Moreover, the integration of the DDSCS allows a simple model for a photon energy resolving detector. Assuming that the detector accepts only photons up to a maximal energy shift  $\omega$  one may simply integrate the DDSCS from  $\omega_{\text{in}}$  to  $\omega_{\text{in}} - \omega$ . The incoherent scattering signal with and without energy resolution is shown in Fig. 8.6. For this calculation the effect of electronic radiation damage has not been included. Fig. 8.6 shows the effect of photon energy resolution, however it becomes noticeable only at very large scattering angles and for high photon energy resolution. A relative bandwidth of 1% corresponds to 100 eV in the present case, such that higher energy resolution is not desirable. This result confirms the conclusion of the last subsection that one cannot filter out the incoherent scattering. Anyway, existing pixel array detectors are not designed for energy resolution [99, 100, 186, 187]. Accordingly, we employ the Waller-Hartree approach, which is numerically much more favourable, to perform the calculations

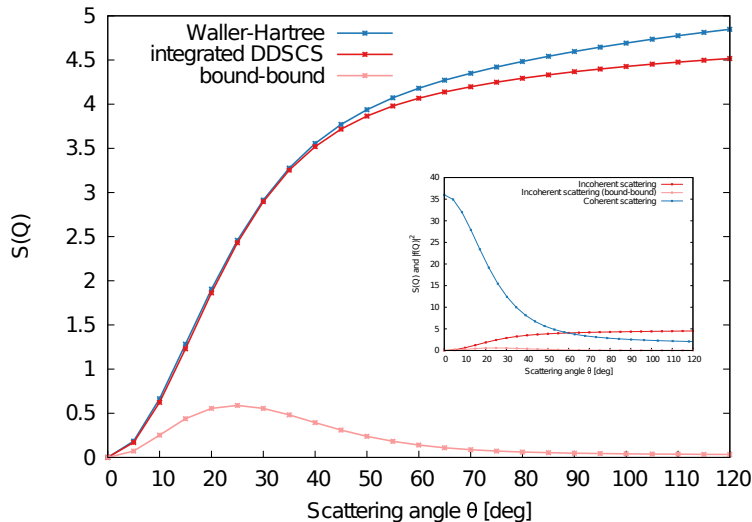


Figure 8.5.: The static structure factor for neutral carbon with  $\omega_{\text{in}} = 10$  keV. The Waller-Hartree approach is compared with numerical integration of the DDSCS. The contributions of bound-to-bound transitions for the latter method are shown. The inset shows the incoherent scattering  $S(\mathbf{Q})$  compared to the coherent (elastic) scattering  $|f(\mathbf{Q})|^2$ . Adapted from Fig. A1 from (Slowik *et al.*, NJP **16**, 073042) [4].

in the remainder of this chapter.

### 8.4.3. Scattering pattern of a single carbon atom

Finally, we are in the position to determine the scattering pattern of a carbon atom according to Eq. (8.15). Fig. 8.7 shows the scattering pattern of a carbon atom resulting from a 10 fs long, flat top x-ray pulse with  $\omega_{\text{in}} = 10$  keV. The total scattering pattern is decomposed into a coherent scattering signal and the incoherent background signal. The incoherent background has two contributions, which are distinguished in the figure. First, the Compton scattering on electrons that are bound in the ionic configurations during the ionization dynamics. Secondly, scattering on unbound (“free”) electrons that are emitted from the atom during the pulse.

Fig. 8.7(a) shows the scattering pattern for a fluence of  $10^{14}$  photons/ $\mu\text{m}^2$ . This fluence is particularly interesting because it corresponds to the currently available fluence at LCLS of  $10^{12}$  photons per pulse focused to  $100 \times 100$  nm<sup>2</sup>. The background signal becomes substantial at high resolution. In fact, the background becomes stronger than the signal at a scattering angle  $\theta \approx 55^\circ$ , corresponding to 1.36 Å resolution. At this fluence, the background signal is dominantly caused by inelastic

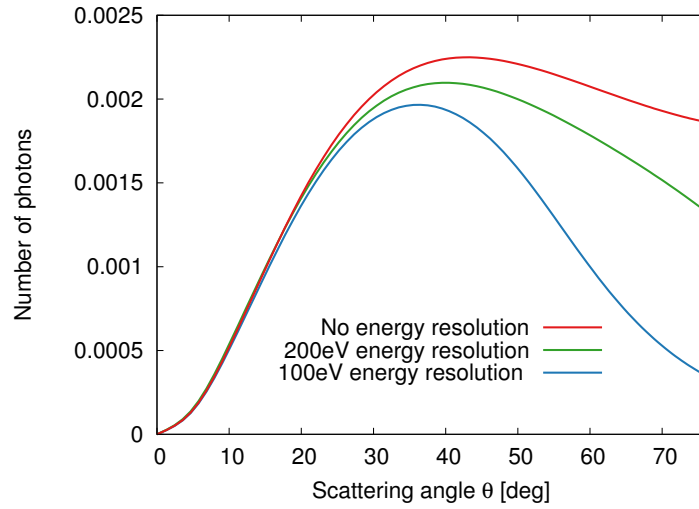


Figure 8.6.: The incoherent scattering signal of a carbon atom for  $\omega_{\text{in}} = 10$  keV, a 10 fs pulse with  $10^{14}$  photons  $\mu\text{m}^{-2}$ . Here, the effect of electronic radiation damage is not yet included. Photon energy resolution is modeled by integrating the DDSCS from  $\omega_{\text{in}} - \omega_{\text{res}}$  to  $\omega_{\text{in}}$ , with  $\omega_{\text{res}} = 100$  or  $200$  eV.

scattering from bound electrons. Absorption is not strong enough to strip many electrons off the carbon atom at this fluence. The mean charge of the carbon atom after the pulse is  $+0.75$ .

Fig. 8.7(b) shows the same graph for a fluence of  $10^{15}$  photons/ $\mu\text{m}^2$ . Increasing the fluence increases the background signal from free electrons.

Fig. 8.7(c) shows the case of very high fluence of  $10^{16}$  photons/ $\mu\text{m}^2$ . With recently proposed schemes this fluence might be available at future facilities [188, 189]. In this regime the scattering pattern changes dramatically. The background signal dominates practically throughout the pattern, for scattering angles larger than  $\theta \approx 20^\circ$  ( $3.6$  Å resolution) the background makes  $\geq 50\%$  of the total signal. At this extreme fluence, most electrons are stripped off the atom by the end of the pulse (the mean charge after the pulse is  $+5.37$ ). The dominant contribution to the background signal is caused by scattering on free electrons. At higher scattering angles there is also a strong contribution from inelastic scattering on bound electrons.

Fig. 8.7(d) shows the percentage of coherently scattered photons in the total scattering signal for all three cases.

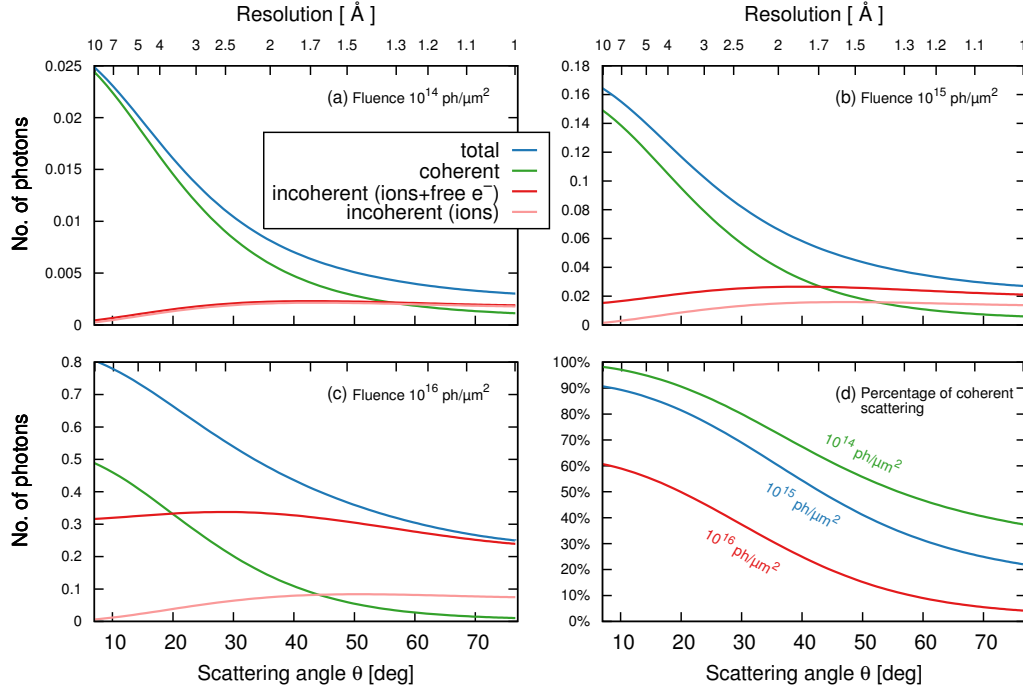
In Fig. 8.8 the scattering pattern is presented for photon energies 12.4 keV and 3.5 keV. The fluences and other parameters are the same as before.

Fig. 8.8(a) shows the scattering pattern for  $\omega_{\text{in}} = 12.4$  keV. We find a substantial

signal degradation at large scattering angles for all fluences. Increasing the fluence degrades the quality of the coherent signal also at small scattering angles. The percentage of the coherent signal drops below 50% at a scattering angle corresponding to 1.3 Å resolution at a fluence of  $10^{14}$  photons/ $\mu\text{m}^2$ , and already 2.9 Å resolution at  $10^{16}$  photons/ $\mu\text{m}^2$ .

Fig. 8.8(b) shows the scattering pattern for  $\omega_{\text{in}} = 3.5$  keV. Interestingly, the dependence on the fluence is even more drastic. This can easily be understood from the photoabsorption cross section, which is about 50 times larger at 3.5 keV than at 12.4 keV. Thus, the strong photoionization gives rise to a strong scattering signal from free electrons. Already at a fluence of  $10^{14}$  photons/ $\mu\text{m}^2$  there is a strong background at small scattering angles. In the forward direction ( $\theta = 0$ ) only about 82% of the scattering signal originates from coherent scattering. But the coherent scattering signal is still prevailing (larger than 60% up to  $\theta \approx 90^\circ$ , i.e., 2.7 Å resolution). In contrast, for  $10^{15}$  photons/ $\mu\text{m}^2$  the coherent scattering signal makes up less than 60% of the total signal and drops below 50% at  $\theta \approx 50^\circ$  (4.2 Å resolution). The most drastic situation is found at a fluence of  $10^{16}$  photons/ $\mu\text{m}^2$ . The background signal is dominating the scattering pattern. Throughout the entire range, the coherent scattering signal contributes less than 40% to the scattering pattern.

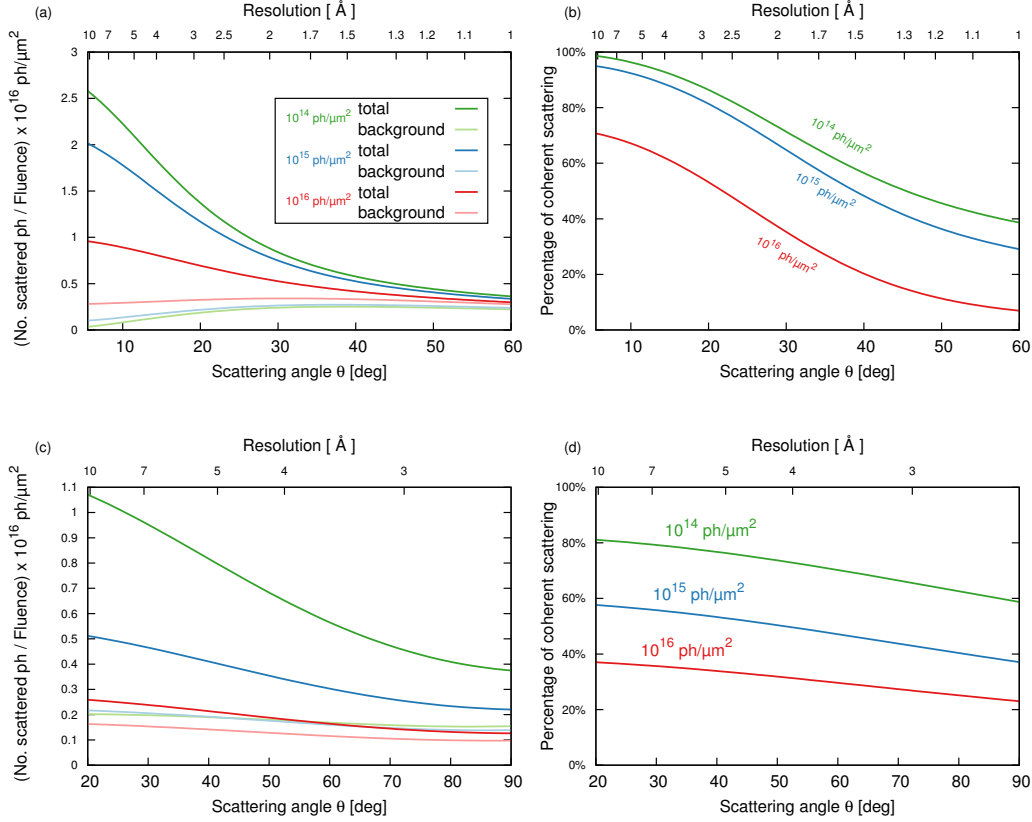
In Fig. 8.9 the pulse duration is varied from 0.1 fs to 100 fs for  $\omega_{\text{in}} = 10$  keV at  $10^{16}$  photons/ $\mu\text{m}^2$ . At large scattering angles the scattering pattern suffers from a dominating background irrespective of the pulse duration. Interestingly, shorter pulses improve the percentage of coherent scattering at small scattering angles or low resolution. This may be considered counterintuitive because a shorter pulse duration at fixed fluence means a higher intensity. In fact, the ionization is decreased, by outrunning the Auger decay and by the production of double core holes, so called “hollow atoms” [172, 193, 196]. For the present case of a single atom, however, making the pulse shorter than one femtosecond has very little consequence.



Photon energy  $\omega_{\text{in}} = 10$  keV.

Figure 8.7.: The number of photons  $dI/d\Omega$  scattered from a carbon atom into a solid angle element  $d\Omega$  for  $\omega_{\text{in}} = 10$  keV. The x-ray pulse is 10 fs long (flat top) and the fluence is (a)  $10^{14}$  photons  $\mu\text{m}^{-2}$ , (b)  $10^{15}$  photons  $\mu\text{m}^{-2}$ , (c)  $10^{16}$  photons  $\mu\text{m}^{-2}$ . The total scattering pattern and its contributions from coherent and incoherent scattering are shown. The incoherent scattering is further decomposed into contributions from bound electrons in the ionic configurations and ionized free electrons. Panel (d) shows the percentage of coherently scattered photons in the total scattering.

Figure taken from (Slowik *et al.*, NJP **16**, 073042) [4] (line styles and key adapted).  
 ©2014 IOP Publishing Ltd and Deutsche Physikalische Gesellschaft.



(a) & (b) Photon energy  $\omega_{\text{in}} = 12.4$  keV.

(c) & (d) Photon energy  $\omega_{\text{in}} = 3.5$  keV.

Figure 8.8.: The scattering pattern for  $\omega_{\text{in}} = 12.4$  keV (panels (a) and (b)) and  $\omega_{\text{in}} = 3.5$  keV (panels (c) and (d)). Panels (a) & (c) show scattering patterns for fluences of  $10^{14}$ ,  $10^{15}$ , and  $10^{16}$  photons  $\mu\text{m}^{-2}$  and 10 fs pulse duration. The number of photons is scaled by  $10^{16}/\text{fluence}$  (in  $\text{ph } \mu\text{m}^{-2}$ ) to fit all lines in the same plot. The contribution of the background from incoherent scattering is shown. Panels (b) & (d) show the percentage of coherently scattered photons.

Figure taken from (Slowik *et al.*, NJP **16**, 073042) [4] (line styles adapted).

©2014 IOP Publishing Ltd and Deutsche Physikalische Gesellschaft.

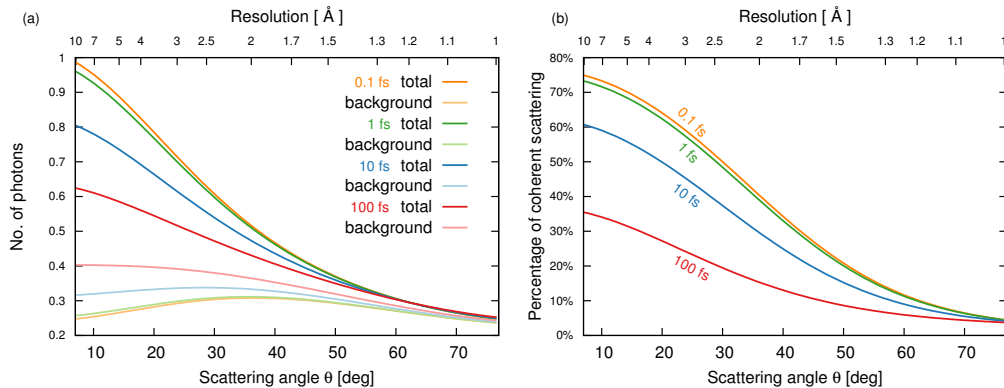


Figure 8.9.: Comparison of the scattering pattern for pulses with different pulse duration. The photon energy is  $\omega_{\text{in}} = 10$  keV, the fluence is  $10^{16}$  photons  $\mu\text{m}^{-2}$ , and the pulse has a flat top profile.

Figure taken from (Slowik *et al.*, NJP **16**, 073042) [4] (line styles adapted).

©2014 IOP Publishing Ltd and Deutsche Physikalische Gesellschaft.

## 8.5. Coherent and incoherent scattering in single molecule imaging

This section addresses the background scattering from large molecules. The reconstruction schemes of single molecule CDI require the mean photon count to exceed a certain threshold. Typically the scheme for structure determination of a single molecule proceeds in three steps [144, 177]:

1. Classification of scattering patterns from the same molecular orientations and averaging patterns of the same class,
2. Determining the relative orientations of the classes,
3. Phase retrieval and reconstruction from the reciprocal space data.

Averaging many images from the same molecular orientation is one way to improve the signal to noise ratio [173, 177, 178, 236–238]. Other methods merge classification and orientation into one step [179, 239, 240]. In any case, dealing with low number of scattered photons is a big challenge for all methods. A mean photon count on the order of 0.1 photons/pixel was indicated as necessary for a successful reconstruction with about 2–3 Å resolution in Refs. [177, 178]. Ref. [179] argued that for small molecules a mean photon count on the order of 0.01 photons/pixel suffices. A common shortcoming of all these thresholds is that they were predicted under simplifying assumptions. In particular, these algorithms completely neglect any electronic radiation damage and any background signal. In this section, I present calculations to

assess the impact of the background scattering on the mean photon count. Moreover, I investigate the dependence of the photon count and the signal quality on the photon energy and x-ray fluence. A systematic determination of optimal machine parameters is important for individual experiments as well as the development of machine upgrades. The problem is to maximize the coherent scattering signal while minimizing the radiation damage and the background signal. Improving the signal to background ratio is also important because we have completely neglected any noise of the signal (See Appendix 8.D.) The noise and the associated photon count distribution are important quantities in the reconstruction algorithms [177, 240]. Moreover, in practice it may be beneficial to use the lowest necessary fluence on the target. In this way, any available surplus power in the XFEL beam could be used to increase the focal spot size of the x-ray beam. A larger focal spot of the x-ray beam improves the hit rate, leading to more efficient use of the XFEL beam and more rapid accumulation of statistically significant data.

Let us estimate the mean photon count scattered by a single molecule into independent pixels (speckles) at high resolution. An independent pixel is the resolution element that corresponds to independent data according to the sampling theorem [145]. Fitting the molecule inside a cube with side length  $2R$ , an independent pixel corresponds to a Q-space area of  $(\pi/R)^2$  [177]. For x-ray wavelength  $\lambda$  the solid angle corresponding to an independent pixel is

$$\Omega_{\mathcal{P}} = \left( \frac{\lambda}{2R} \right)^2. \quad (8.39)$$

For sufficiently short x-ray pulse duration we may neglect any nuclear motion and assume the positions of the atoms to be fixed. In biomolecules such as proteins, carbon is the most abundant element after hydrogen. Consequently the scattering signal will be dominated by the scattering from carbon. Accordingly, we model the molecule as a random distribution of  $N_C$  independent carbon atoms. (For details see Appendix 8.C.) Moreover, we denote the average over independent pixels in the annulus of scattering angle  $\theta$  by  $\langle \cdot \rangle_{\theta}$ . The scattered intensity into a given independent pixel is considered to be approximately constant over the pixel. At sufficiently high resolution – in the regime of Wilson statistics [241] – the average photon number

$$\left\langle \frac{d\mathcal{I}_{\text{mol}}}{d\Omega_{\mathcal{P}}} \right\rangle_{\theta} = \Omega_{\mathcal{P}} N_C \frac{d\mathcal{I}}{d\Omega_{\theta}} \quad (8.40)$$

is proportional to the single atom scattering pattern  $d\mathcal{I}/d\Omega_{\theta}$  given in Eq. (8.15). A detailed derivation is presented in Appendix 8.C. Not surprisingly, the mean number of scattered photons depends on the number of atoms in the molecule. But because the independent pixel (speckle size) also depends on the size of the molecule this

dependence is not direct proportional. Let the molecule have a spherical shape with radius  $R$  and carbon atom density  $\rho_C$ , then the mean photon count is proportional to  $\Omega_{\mathcal{P}} N_C = \frac{\pi}{3} \rho_C \lambda^2 R \propto N_C^{1/3}$ .

Fig. 8.10 illustrates an example with typical parameters for a protein, a molecule of  $R = 10$  nm radius with a carbon atom density of  $\rho_C = 1/15 \text{ \AA}^{-3}$ . It presents the mean photon count per independent pixel of coherently scattered photons and background scattering for  $\omega_{\text{in}} = 10$  keV and 15 keV.

Fig. 8.11 analyzes the mean photon count for different photon energies and x-ray fluences. Moreover, the percentage of the coherent signal in the total scattering signal is shown. As before  $R = 10$  nm and  $\rho_C = 1/15 \text{ \AA}^{-3}$ . In this figure the resolution is fixed at 3 Å and 1.5 Å.

Fig. 8.11(a) shows the average photon count for 3 Å resolution. It shows that a fluence of  $10^{14}$  photons/ $\mu\text{m}^2$  is sufficient to achieve a mean photon count of 0.1 photons/ $\Omega_{\mathcal{P}}$  in the photon energy range of 3–11 keV. An even lower fluence of  $10^{13}$  photons/ $\mu\text{m}^2$  could be used, provided that 0.01 photons/ $\Omega_{\mathcal{P}}$  suffice for a successful reconstruction. The effect of electronic radiation damage is also reflected in this figure. Without radiation damage the coherent scattering signal is independent of  $\omega_{\text{in}}$ . The mean photon count per pixel would then be proportional to  $\omega_{\text{in}}^{-2}$ , reflecting the size of  $\Omega_{\mathcal{P}}$ . Only the lowest fluence case exhibits this behaviour. At the higher fluences the mean photon count is almost constant, with a small peak at 5 keV. The ionization, which is even more pronounced at low photon energy, reduces the coherent scattering. Another sign for the influence of radiation damage is the fact that an increase of the fluence by an order of magnitude does not increase the scattering signal by the same factor.

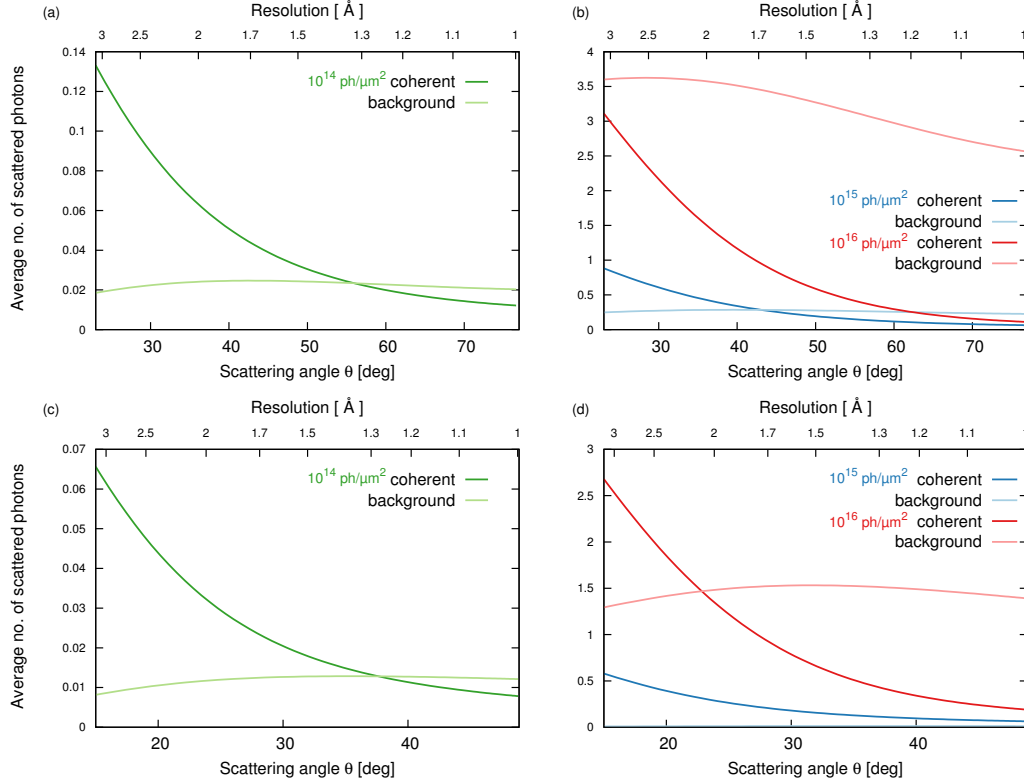
Fig. 8.11(b) shows that the signal quality deteriorates at high fluences. Incoherent scattering on bound electrons sets an upper limit on the percentage of coherent scattering. At higher fluences the background scattering on free electrons worsens the signal quality. Interestingly, the signal quality is much better at higher photon energies, reflecting the lower ionization cross section. Imaging might therefore benefit from using a higher photon energy, because of the improved signal to background ratio.

Similar results are found for imaging with 1.5 Å resolution.

Fig. 8.11(c) shows that in order to reach a mean photon count of 0.1 photons/ $\Omega_{\mathcal{P}}$  a fluence of  $10^{15}$  photons/ $\mu\text{m}^2$  is necessary. The average photon count is not very sensitive to the photon energy, but shows a maximum at 10 keV.

Fig. 8.11(d) shows that the percentage of coherent scattering at 1.5 Å resolution is much lower than at 3 Å resolution. At a fluence of  $10^{16}$  photons/ $\mu\text{m}^2$  there is less than 30% coherent scattering signal in the total photon count for the entire photon energy range of 7–15 keV. For  $10^{15}$  photons/ $\mu\text{m}^2$  the background scattering is

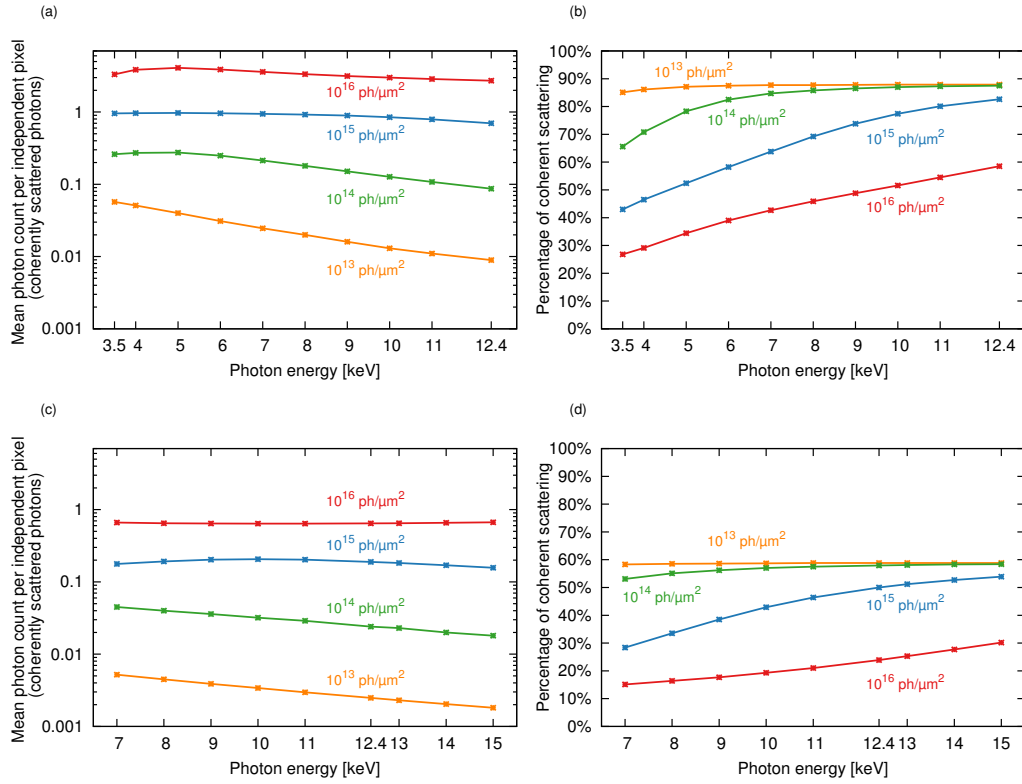
dominating up to 12.4 keV photon energy. Using higher photon energies significantly improves the (fairly low) percentage of coherent scattering. This suggest that using photon energies of about 12.4 keV and higher may be beneficial for high resolution imaging (cf. [188, 189, 242]).



(a) & (b) Photon energy  $\omega_{\text{in}} = 10$  keV.

(c) & (d) Photon energy  $\omega_{\text{in}} = 15$  keV.

Figure 8.10.: The mean photon count per independent pixel at high resolution. Calculated according to Eq. (8.40). The molecule is modeled by radius  $R = 10$  nm and carbon atom density  $\rho_C = 1/15 \text{ \AA}^{-3}$ .



(a) & (b) Resolution  $3 \text{ \AA}$ .  
 (c) & (d) Resolution  $1.5 \text{ \AA}$ .

Figure 8.11.: “Left panels show the average number of coherently scattered photons from a molecule ( $\rho_C = 1/15 \text{ \AA}^{-3}$ , radius  $R = 100 \text{ \AA}$ ) at a fixed resolution, plotted versus the incoming photon energy, for four different fluences. Right panels show the percentage of the coherent scattering signal in the total scattering signal. The resolution is fixed to  $3 \text{ \AA}$  in panels (a) & (b), and to  $1.5 \text{ \AA}$  in panels (c) & (d).”[4] Figure taken from (Slowik *et al.*, NJP **16**, 073042). ©2014 IOP Publishing Ltd and Deutsche Physikalische Gesellschaft.

## 8.A. Differential scattering probability considering high-intensity ionization dynamics

As mentioned in the main text, we write the total Hamiltonian as

$$\hat{H} = \hat{H}_{\text{el}} + \hat{H}_{\text{rad}} + \hat{H}_{\hat{\mathbf{p}} \cdot \hat{\mathbf{A}}} + \hat{H}_{\hat{\mathbf{A}}^2} = \hat{H}_0 + \hat{H}_{\hat{\mathbf{A}}^2}. \quad (8.41)$$

Let us assume for the moment that we have solved the time-dependent Schrödinger equation for the  $\mathbf{p} \cdot \mathbf{A}$ -driven system. Then have a time evolution operator  $\hat{U}_0(t, t_{\text{in}})$  that satisfies

$$\frac{d}{dt} \hat{U}_0(t, t_{\text{in}}) = -i \hat{H}_0 \hat{U}_0(t, t_{\text{in}}), \quad \text{with} \quad \hat{U}_0(t_{\text{in}}, t_{\text{in}}) = \mathbb{1}. \quad (8.42)$$

Treating the scattering in first order perturbation theory, the full time evolution operator  $\hat{U}(t, t_{\text{in}})$  is

$$\hat{U}(t, t_{\text{in}}) = \hat{U}_0(t, t_{\text{in}}) - i \int_{t_{\text{in}}}^t dt' \hat{U}_0(t, t') \hat{H}_{\hat{\mathbf{A}}^2} \hat{U}_0(t', t_{\text{in}}). \quad (8.43)$$

The system is prepared long before the scattering ( $t_{\text{in}} \rightarrow -\infty$ ) in the initial state  $\hat{\rho}_{\text{in}} = \hat{\rho}_{\text{in}}^X \otimes \hat{\rho}_{\text{in}}^{\text{el}}$ . In a typical experimental setup the incoming beam is filtered out and only scattered photons are measured. As in Sec. 6.3, we employ the projection operator onto a scattered photon mode as observable

$$\hat{O}_{\mathbf{k}_s} = \hat{P}_{\mathbf{k}_s, \lambda_s} \otimes \hat{\mathbb{1}}_{\text{el}}. \quad (8.44)$$

$\hat{P}_{\mathbf{k}_s, \lambda_s}$  is the projection operator onto all multimode Fock states with one photon in the mode  $(\mathbf{k}_s, \lambda_s)$ . The differential scattering probability is given by

$$\frac{dP}{d\Omega} = \sum_{\lambda_s} \frac{V\alpha^3}{(2\pi)^3} \int \omega_{\mathbf{k}_s}^2 d\omega_{\mathbf{k}_s} P(\mathbf{k}_s). \quad (8.45)$$

$P(\mathbf{k}_s) = \text{Tr}(\hat{\rho}_f \hat{O}_{\mathbf{k}_s})$  is the expectation value of  $\hat{O}_{\mathbf{k}_s}$  in the state  $\hat{\rho}_f$  of the total system, given by

$$\hat{\rho}_f = \lim_{\substack{t_f \rightarrow \infty \\ t_{\text{in}} \rightarrow -\infty}} \iint_{t_{\text{in}}}^{t_f} dt_1 dt_2 \hat{U}_0(t_f, t_1) \hat{H}_{\hat{\mathbf{A}}^2} \hat{U}_0(t_1, t_{\text{in}}) \hat{\rho}_{\text{in}} \hat{U}_0^\dagger(t_2, t_{\text{in}}) \hat{H}_{\hat{\mathbf{A}}^2} \hat{U}_0^\dagger(t_f, t_2). \quad (8.46)$$

So far the derivation has been analogous to the ionization-free case in Sec. 6.3. At this point, it is important to emphasize the differences. In the case with ionization, the time-evolution can entangle the electronic and radiation systems. This is most

easily understood for the case of a single incoming photon: if the photon is absorbed and an electron ionized, the state of the radiation system changes drastically. In this case the radiation and electronic system are strongly correlated. In the following, we will see that under typical experimental conditions the photonic and electronic degrees of freedom can be disentangled.

Before we determine the action of the time evolution operator on the density operator, we study the action of the  $\mathbf{p} \cdot \mathbf{A}$  term on a state vector. First of all, we assume that x-ray fluorescence is negligible. This is justified if the x-ray photon energy is much higher than any resonant excitations of the target and the electronic system relaxes predominantly via Auger decay. Consequently, we neglect the terms in  $\hat{H}_{\hat{\mathbf{p}} \cdot \hat{\mathbf{A}}}$  that contain the photon creation operator. Let  $|\Psi_i\rangle$  be an eigenstate of  $\hat{H}_{\text{el}}$  and let  $|\{\alpha_{\mathbf{k},\lambda}\}\rangle$  be a multimode coherent state [17, 198], i.e., a collection of eigenstates of the photon annihilation operator. Under these conditions, the action of  $\hat{H}_{\hat{\mathbf{p}} \cdot \hat{\mathbf{A}}}$  on the state  $|\Psi_i\rangle|\{\alpha_{\mathbf{k},\lambda}\}\rangle$  is

$$\hat{H}_{\hat{\mathbf{p}} \cdot \hat{\mathbf{A}}}|\Psi_i\rangle|\{\alpha_{\mathbf{k},\lambda}\}\rangle = \alpha \int d^3x \hat{\psi}^\dagger(\mathbf{x}) \hat{\mathbf{A}}(\mathbf{x}) \cdot \frac{\nabla}{\mathbf{i}} \hat{\psi}(\mathbf{x}) |\Psi_i\rangle|\{\alpha_{\mathbf{k},\lambda}\}\rangle \quad (8.47)$$

$$\approx \sqrt{\frac{2\pi}{V\omega_{\text{in}}}} \sum_{\mathbf{k},\lambda} \alpha_{\mathbf{k},\lambda} \int d^3x \hat{\psi}^\dagger(\mathbf{x}) \frac{\nabla}{\mathbf{i}} \cdot \epsilon_{\text{in}} e^{i\mathbf{k}_{\text{in}} \cdot \mathbf{x}} \hat{\psi}(\mathbf{x}) |\Psi_i\rangle|\{\alpha_{\mathbf{k},\lambda}\}\rangle, \quad (8.48)$$

where we also have assumed that the radiation has a small relative bandwidth, the polarization  $\epsilon_{\text{in}}$  and a mean wavevector  $\mathbf{k}_{\text{in}}$ . Observe, that the free time evolution of this state factorizes

$$e^{-i(\hat{H}_{\text{el}} + \hat{H}_{\text{rad}})t} |\Psi_i\rangle|\{\alpha_{\mathbf{k},\lambda}\}\rangle = e^{-iE_i t} |\Psi_i\rangle|\{\alpha_{\mathbf{k},\lambda} e^{-i\omega_{\mathbf{k}} t}\}\rangle. \quad (8.49)$$

The time evolution of the state  $|\Psi_i\rangle|\{\alpha_{\mathbf{k},\lambda}\}\rangle$  is given by

$$\hat{U}_0(t, t_{\text{in}}) |\Psi_i\rangle|\{\alpha_{\mathbf{k},\lambda}\}\rangle = e^{i\hat{H}_{\text{free}}(t-t_{\text{in}})} \mathcal{T} \exp \left( -i \int_{t_{\text{in}}}^t dt' \hat{H}_{\hat{\mathbf{p}} \cdot \hat{\mathbf{A}}}^I(t') \right) |\Psi_i\rangle|\{\alpha_{\mathbf{k},\lambda}\}\rangle \quad (8.50)$$

$$= \hat{V}_{\text{el}}(t, t_{\text{in}}) |\Psi_i\rangle|\{\alpha_{\mathbf{k},\lambda} e^{-i\omega_{\mathbf{k}}(t-t_{\text{in}})}\}\rangle. \quad (8.51)$$

$\mathcal{T} \exp(\cdot)$  denotes the time-ordered exponential and we have introduced the short hand notation for the action on the electronic part

$$\hat{V}_{\text{el}}(t, t_{\text{in}}) = e^{i\hat{H}_{\text{el}}(t-t_{\text{in}})} \mathcal{T} \exp \left( -i \int_{t_{\text{in}}}^t dt' \sqrt{\frac{2\pi}{V\omega_{\text{in}}}} \sum_{\mathbf{k},\lambda} \alpha_{\mathbf{k},\lambda} e^{-i\omega_{\mathbf{k}}(t'-t_{\text{in}})} \hat{\mathcal{I}}(t') \right), \quad (8.52)$$

which still depends on the state of the radiation field (through the  $\alpha_{\mathbf{k},\lambda}$ ) and the operator that induces the ionization has been abbreviated

$$\hat{\mathcal{I}}(t') = e^{i\hat{H}_{\text{mol}}t'} \int d^3x \hat{\psi}^\dagger(\mathbf{x}) \frac{\nabla}{\mathbf{i}} \cdot \epsilon_{\text{in}} e^{i\mathbf{k}_{\text{in}} \cdot \mathbf{x}} \hat{\psi}(\mathbf{x}) e^{-i\hat{H}_{\text{mol}}t'}. \quad (8.53)$$

### 8.A. Differential scattering probability considering high-intensity ionization dynamics

Note that this decomposition is not true in general, we have exploited the properties of the coherent state.

To use the properties of the coherent states, we express the initial state of the radiation system in a coherent state representation

$$\hat{\rho}_{\text{in}}^X = \int \prod_{(\mathbf{k},\lambda)} d^2\alpha_{\mathbf{k},\lambda} P(\{\alpha_{\mathbf{k},\lambda}\}) |\{\alpha_{\mathbf{k},\lambda}\}\rangle\langle\{\alpha_{\mathbf{k},\lambda}\}|, \quad (8.54)$$

where  $P(\{\alpha_{\mathbf{k},\lambda}\})$  is the Glauber-Sudarshan  $P$ -function [198]. For simplicity, let us assume that the molecule is initial in its electronic ground state

$$\hat{\rho}_{\text{in}}^{\text{el}} = |\Psi_0\rangle\langle\Psi_0|. \quad (8.55)$$

Recall that according to Eq. (8.45), the differential scattering probability depends on

$$\begin{aligned} P(\mathbf{k}_s) = & \lim_{\substack{t_f \rightarrow \infty \\ t_{\text{in}} \rightarrow -\infty}} \sum_{\kappa, \lambda_s} \iint_{t_{\text{in}}}^{t_f} dt_1 dt_2 \left(\frac{\alpha^2}{2}\right)^2 \iint d^3x_1 d^3x_2 \int \prod_{(\mathbf{k},\lambda)} d^2\alpha_{\mathbf{k},\lambda} P(\{\alpha_{\mathbf{k},\lambda}\}) \\ & \times \langle 1_{\mathbf{k}_s} | \langle \Psi_{\kappa} | \hat{U}_0(t_f, t_1) \hat{\mathbf{A}}^2(\mathbf{x}_1) \hat{n}(\mathbf{x}_1) \hat{U}_0(t_1, t_{\text{in}}) | \Psi_0 \rangle | \{\alpha_{\mathbf{k},\lambda}\} \rangle \\ & \times \langle \{\alpha_{\mathbf{k},\lambda}\} | \langle \Psi_0 | \hat{U}_0^\dagger(t_2, t_{\text{in}}) \hat{\mathbf{A}}^2(\mathbf{x}_2) \hat{n}(\mathbf{x}_2) \hat{U}_0^\dagger(t_f, t_2) | \Psi_{\kappa} \rangle | 1_{\mathbf{k}_s} \rangle, \end{aligned} \quad (8.56)$$

where we have inserted a complete set of electronic eigenstates  $\mathbb{1}_{\text{el}} = \sum_{\kappa} |\Psi_{\kappa}\rangle\langle\Psi_{\kappa}|$ . Recall that the observable only counts states with one photon in the mode  $\mathbf{k}_s$ . Using the completeness of coherent states, we can write

$$|1_{\mathbf{k}_s}\rangle\langle 1_{\mathbf{k}_s}| = \sum_{\lambda_s} \int \prod_{\mathbf{l} \neq \mathbf{k}_s} \left( \frac{d^2\beta_{\mathbf{l},\mu}}{\pi} \right) \hat{a}_{\mathbf{k}_s, \lambda_s}^\dagger |\{\beta_{\mathbf{l},\mu}\}\rangle\langle\{\beta_{\mathbf{l},\mu}\}| \hat{a}_{\mathbf{k}_s, \lambda_s}, \quad (8.57)$$

where  $|\{\beta_{\mathbf{l},\mu}\}\rangle$  is any multimode coherent state with  $\beta_{\mathbf{k}_s, \lambda_s} = 0$ , i.e., no photons in the scattered mode. The crucial matrix elements in the last expression can thus be factorized into the electronic and photonic subsystems

$$\begin{aligned} & \langle 1_{\mathbf{k}_s} | \langle \Psi_{\kappa} | \hat{U}_0(t_f, t_1) \hat{\mathbf{A}}^2(\mathbf{x}_1) \hat{n}(\mathbf{x}_1) \hat{U}_0(t_1, t_{\text{in}}) | \Psi_0 \rangle | \{\alpha_{\mathbf{k},\lambda}\} \rangle \\ & = \sum_{\mathbf{q}, \beta} \frac{4\pi}{V\alpha^2} \frac{1}{\sqrt{\omega_{\mathbf{k}_s} \omega_{\mathbf{q}}}} \epsilon_{\mathbf{k}_s, \lambda_s}^* \cdot \epsilon_{\mathbf{q}, \beta} e^{-i(\mathbf{k}_s - \mathbf{q}) \cdot \mathbf{x}_1} e^{-i\omega_{\mathbf{q}}(t_1 - t_{\text{in}})} e^{-i\omega_{\mathbf{k}_s}(t_f - t_1)} \alpha_{\mathbf{q}, \beta} \\ & \times \langle \Psi_{\kappa} | \hat{V}_{\text{el}}(t_f, t_1) \hat{n}(\mathbf{x}_1) \hat{V}_{\text{el}}(t_1, t_{\text{in}}) | \Psi_0 \rangle \cdot \langle \{\beta_{\mathbf{l},\mu}\} | \{\alpha_{\mathbf{k},\lambda} e^{-i\omega_{\mathbf{k}}(t_f - t_{\text{in}})} \rangle. \end{aligned} \quad (8.58)$$

Inserting this result into Eq. (8.56) and using again the completeness for  $|\{\beta_{\mathbf{l},\mu}\}\rangle$

yields the differential scattering probability

$$\begin{aligned}
 P(\mathbf{k}_s) &= \lim_{\substack{t_f \rightarrow \infty \\ t_{in} \rightarrow -\infty}} \sum_{\lambda_s} \int_{t_{in}}^{t_f} dt_1 dt_2 \left(\frac{\alpha^2}{2}\right)^2 \iint d^3x_1 d^3x_2 \int \prod_{(\mathbf{k}, \lambda)} d^2\alpha_{\mathbf{k}, \lambda} P(\{\alpha_{\mathbf{k}, \lambda}\}) \\
 &\quad \sum_{\mathbf{p}, \alpha} \sum_{\mathbf{q}, \beta} \left(\frac{4\pi}{V\alpha^2}\right)^2 \frac{1}{\omega_{\mathbf{k}_s} \sqrt{\omega_{\mathbf{p}} \omega_{\mathbf{q}}}} \epsilon_{\mathbf{p}, \alpha} \cdot \epsilon_{\mathbf{k}_s, \lambda_s}^* \epsilon_{\mathbf{k}_s, \lambda_s}^* \cdot \epsilon_{\mathbf{q}, \beta} e^{-i\mathbf{k}_s \cdot (\mathbf{x}_1 - \mathbf{x}_2)} e^{i\omega_{\mathbf{k}_s} (t_1 - t_2)} \\
 &\quad \alpha_{\mathbf{p}, \alpha}^* \alpha_{\mathbf{q}, \beta} e^{i\omega_{\mathbf{p}} (t_2 - t_{in}) - i\mathbf{p} \cdot \mathbf{x}_2} e^{-i\omega_{\mathbf{q}} (t_1 - t_{in}) + i\mathbf{q} \cdot \mathbf{x}_1} \\
 &\quad \langle \Psi_0 | \hat{V}_{el}^\dagger(t_2, t_{in}) \hat{n}(\mathbf{x}_2) \hat{V}_{el}^\dagger(t_f, t_2) \hat{V}_{el}(t_f, t_1) \hat{n}(\mathbf{x}_1) \hat{V}_{el}(t_1, t_{in}) | \Psi_0 \rangle. \quad (8.59)
 \end{aligned}$$

At this point, we must not forget that  $\hat{V}_{el}$  depends on the properties of the radiation field. Before we can trace over the photonic system (i.e., perform the integral over  $d^2\alpha$ ) we have to make this dependence explicit.

Recall that  $\hat{V}_{el}$  involves a time ordered exponential and can be expressed by

$$\begin{aligned}
 \hat{V}_{el}(t, t_{in}) &= e^{-i\hat{H}_{el}(t-t_{in})} \sum_n (-i\alpha)^n \left(\frac{2\pi}{V\alpha^2}\right)^{n/2} \int_{t_{in}}^t dt_n \int_{t_{in}}^{t_n} dt_{n-1} \cdots \int_{t_{in}}^{t_2} dt_1 \sum_{\mathbf{k}_n, \lambda_n} \cdots \sum_{\mathbf{k}_1, \lambda_1} \\
 &\quad (\omega_{\mathbf{k}_n} \cdots \omega_{\mathbf{k}_1})^{-n/2} \alpha_{\mathbf{k}_n, \lambda_n} e^{-i\omega_{\mathbf{k}_n} t_n} \cdots \alpha_{\mathbf{k}_1, \lambda_1} e^{-i\omega_{\mathbf{k}_1} t_1} \hat{\mathcal{I}}(t_n) \cdots \hat{\mathcal{I}}(t_1). \quad (8.60)
 \end{aligned}$$

To simplify the expressions, we introduce a more compact notation so that the last line is written

$$\hat{V}_{el}(t, t_{in}) = e^{-i\hat{H}_{el}(t-t_{in})} \sum_n (-i\alpha)^n \left(\frac{2\pi}{V\alpha^2}\right)^{n/2} \int_{t_{in}}^t dt^{(n)} \sum_{\mathbf{k}^{(n)}} \frac{\boldsymbol{\alpha}_{\mathbf{k}^{(n)}}}{\sqrt{\boldsymbol{\omega}_{\mathbf{k}^{(n)}}}} e^{-i\omega_{\mathbf{k}^{(n)}} t^{(n)}} \hat{\mathcal{I}}(t^{(n)}). \quad (8.61)$$

Using this short-hand notation, we now inspect the matrix element in the Eq. (8.59) more closely

$$\begin{aligned}
 &\langle \Psi_0 | \hat{V}_{el}^\dagger(t_2, t_{in}) \hat{n}(\mathbf{x}_2) \hat{V}_{el}^\dagger(t_2, t_1) \hat{n}(\mathbf{x}_1) \hat{V}_{el}(t_1, t_{in}) | \Psi_0 \rangle \\
 &= \sum_a \sum_b \sum_c (i\alpha)^a (-i\alpha)^{b+c} \left(\frac{2\pi}{V\alpha^2}\right)^{(a+b+c)/2} \int_{t_{in}}^{t_2} dt_A^{(a)} \int_{t_1}^{t_2} dt_B^{(b)} \int_{t_{in}}^{t_1} dt_C^{(c)} \\
 &\quad \times \sum_{\mathbf{k}^{(a)}} \sum_{\mathbf{k}^{(b)}} \sum_{\mathbf{k}^{(c)}} \frac{\boldsymbol{\alpha}_{\mathbf{k}^{(a)}}^* \boldsymbol{\alpha}_{\mathbf{k}^{(b)}} \boldsymbol{\alpha}_{\mathbf{k}^{(c)}}}{\sqrt{\boldsymbol{\omega}_{\mathbf{k}^{(a)}} \boldsymbol{\omega}_{\mathbf{k}^{(b)}} \boldsymbol{\omega}_{\mathbf{k}^{(c)}}}} e^{-i\omega_{\mathbf{k}^{(a)}} t_A^{(a)}} e^{-i\omega_{\mathbf{k}^{(b)}} t_B^{(b)}} e^{-i\omega_{\mathbf{k}^{(c)}} t_C^{(c)}} \\
 &\quad \times \langle \Psi_0 | \hat{\mathcal{I}}^\dagger(\mathbf{t}_A^{(a)}) e^{i\hat{H}_{el}(t_2-t_{in})} \hat{n}(\mathbf{x}_2) e^{-i\hat{H}_{el}(t_2-t_1)} \hat{\mathcal{I}}(\mathbf{t}_B^{(b)}) \hat{n}(\mathbf{x}_1) e^{-i\hat{H}_{el}(t_1-t_{in})} \hat{\mathcal{I}}(\mathbf{t}_C^{(c)}) | \Psi_0 \rangle. \quad (8.62)
 \end{aligned}$$

We found the dependence of the electronic state on the photonic state in the last expression. This can now be used to trace out the photonic degrees of freedom, i.e.,

### 8.A. Differential scattering probability considering high-intensity ionization dynamics

perform the integral over  $d^2\alpha$  in Eq. (8.59). At this point, we have to specify the state of the radiation system. We assume that the  $P$ -function has Gaussian form [71]

$$P(\{\alpha_{\mathbf{k},\lambda}\}) = \prod_{\mathbf{k},\lambda} \frac{1}{\pi \langle \hat{n}_{\mathbf{k},\lambda} \rangle} e^{-\frac{|\alpha_{\mathbf{k},\lambda}|^2}{\langle \hat{n}_{\mathbf{k},\lambda} \rangle}}. \quad (8.63)$$

Glauber has shown that the  $P$ -function takes on a Gaussian form, with increasing number of statistically independent, arbitrary, stationary sources which generate the radiation field [198]. Because of the random excitation of the field, the corresponding density operator describes a chaotic radiation field. Most importantly, it has been shown that the x-ray radiation field produced by a SASE FEL can be described by a Gaussian  $P$ -function [199, 200]. The correlation function of order  $(N, M)$  is defined by

$$\begin{aligned} G^{(N,M)}(\mathbf{x}_1, t_1; \dots; \mathbf{x}_N, t_N; \mathbf{y}_1, \tau_1; \dots; \mathbf{y}_M, \tau_M) &= \sum_{\mathbf{k}_1 \dots \mathbf{k}_N} \sum_{\mathbf{l}_1 \dots \mathbf{l}_M} (-i)^N (i)^M \left(\frac{2\pi}{V}\right)^{(N+M)/2} \\ &\times \sqrt{\omega_{\mathbf{k}_1} \dots \omega_{\mathbf{k}_N}} \sqrt{\omega_{\mathbf{l}_1} \dots \omega_{\mathbf{l}_M}} \text{Tr}(\hat{\rho}_{\text{in}}^X \hat{a}_{\mathbf{k}_1}^\dagger \dots \hat{a}_{\mathbf{k}_N}^\dagger \hat{a}_{\mathbf{l}_1} \dots \hat{a}_{\mathbf{l}_M}) \\ &\times e^{-i(\mathbf{k}_1 \mathbf{x}_1 - \omega_{\mathbf{k}_1} t_1)} \dots e^{-i(\mathbf{k}_N \mathbf{x}_N - \omega_{\mathbf{k}_N} t_N)} e^{i(\mathbf{l}_1 \mathbf{x}_1 - \omega_{\mathbf{l}_1} \tau_1)} \dots e^{i(\mathbf{l}_M \mathbf{x}_M - \omega_{\mathbf{l}_M} \tau_M)}. \end{aligned} \quad (8.64)$$

We consider the bandwidth to so small that we can replace the prefactors  $\sqrt{\omega_{\mathbf{k}}}$  by  $\sqrt{\omega_{\text{in}}}$ . Inserting the  $P$ -function of Eq. (8.63) into the state of the radiation pulse in Eq. (8.54), we obtain

$$\begin{aligned} G^{(N,M)}(\mathbf{x}_1, t_1; \dots; \mathbf{x}_N, t_N; \mathbf{y}_1, \tau_1; \dots; \mathbf{y}_M, \tau_M) &= \sum_{\mathbf{k}_1 \dots \mathbf{k}_N} \sum_{\mathbf{l}_1 \dots \mathbf{l}_M} (-i)^N (i)^M \left(\frac{2\pi}{V}\right)^{\frac{N+M}{2}} \\ &\times \sqrt{\omega_{\text{in}}^{N+M}} \int \prod_{(\mathbf{k},\lambda)} d^2\alpha_{\mathbf{k},\lambda} P(\{\alpha_{\mathbf{k},\lambda}\}) \alpha_{\mathbf{k}_1, \lambda_{\text{in}}}^* \dots \alpha_{\mathbf{k}_N, \lambda_{\text{in}}}^* \alpha_{\mathbf{l}_1, \lambda_{\text{in}}} \dots \alpha_{\mathbf{l}_M, \lambda_{\text{in}}} \\ &\times e^{-i(\mathbf{k}_1 \mathbf{x}_1 - \omega_{\mathbf{k}_1} t_1)} \dots e^{-i(\mathbf{k}_N \mathbf{x}_N - \omega_{\mathbf{k}_N} t_N)} e^{i(\mathbf{l}_1 \mathbf{x}_1 - \omega_{\mathbf{l}_1} \tau_1)} \dots e^{i(\mathbf{l}_M \mathbf{x}_M - \omega_{\mathbf{l}_M} \tau_M)}. \end{aligned} \quad (8.65)$$

Finally, we exploit the Gaussian form of the  $P$ -function by employing the very useful identity [71]

$$\int d^2\alpha e^{-C|\alpha|^2} \alpha^l (\alpha^*)^m = \delta_{lm} \pi \sqrt{l!m!} C^{-(m+1)}, \quad C > 0. \quad (8.66)$$

From this last identity follows that only terms with  $N = M$  contribute

$$\begin{aligned} G^{(N,M)}(\mathbf{x}_1, t_1; \dots; \mathbf{x}_N, t_N; \mathbf{y}_1, \tau_1; \dots; \mathbf{y}_M, \tau_M) &= \delta_{NM} \left(\frac{2\pi}{V}\right)^N \omega_{\text{in}}^N \sum_{\mathbf{k}_1 \dots \mathbf{k}_N} \sum_{\mathcal{P}} \\ &\times \int \prod_{(\mathbf{k},\lambda)} d^2\alpha_{\mathbf{k},\lambda} P(\{\alpha_{\mathbf{k},\lambda}\}) |\alpha_{\mathbf{k}_1, \lambda_{\text{in}}}|^2 \dots |\alpha_{\mathbf{k}_N, \lambda_{\text{in}}}|^2 \\ &\times e^{i\omega_{\mathbf{k}_1} (t_1 - \tau_{p(1)})} e^{-i\mathbf{k}_1 (\mathbf{x}_1 - \mathbf{x}_{p(1)})} \dots e^{i\omega_{\mathbf{k}_N} (t_N - \tau_{p(N)})} e^{-i\mathbf{k}_N (\mathbf{x}_N - \mathbf{x}_{p(N)})}, \end{aligned} \quad (8.67)$$

where we sum over all  $N!$  permutations of the arguments  $1, \dots, N$ . Moreover, from Eq. (8.66) follows that in the case of a single mode with Gaussian  $P$ -function  $P(\alpha) = \frac{1}{\pi \langle \hat{n} \rangle} e^{-|\alpha|^2 / \langle \hat{n} \rangle}$  one has the moments  $\langle |\alpha|^{2n} \rangle = n! \langle |\alpha|^2 \rangle^n$ . As a result higher-order correlation functions can be reduced to sums of products of the first-order correlation function [71]

$$G^{(N,N)}(t_1, \dots, t_N, \tau_1, \dots, \tau_N) = \sum_{\mathcal{P}} \prod_{j=1}^N G^{(1,1)}(\mathbf{x}_j, t_j, \mathbf{y}_{p(j)}, \tau_{p(j)}). \quad (8.68)$$

Substituting Eqs. (8.68) and (8.62) into Eq. (8.59), we obtain

$$\begin{aligned} P(\mathbf{k}_s) &= \lim_{\substack{t_f \rightarrow \infty \\ t_{in} \rightarrow -\infty}} \sum_{\lambda_s} \iint d^3x_1 d^3x_2 \frac{1}{\omega_{\mathbf{k}_s}} |\epsilon_{in}^* \cdot \epsilon_{\mathbf{k}_s, \lambda_s}|^2 e^{-i\mathbf{k}_s \cdot (\mathbf{x}_1 - \mathbf{x}_2)} \\ &\times \sum_{a,b,c} \delta_{a,b+c} \left( \frac{2\pi}{V} \right) \frac{1}{\omega_{in}^{2(a+1)}} \iint_{t_{in}}^{t_f} dt_1 dt_2 \int_{t_{in}}^{t_2} dt_A^{(a)} \int_{t_1}^{t_2} dt_B^{(b)} \int_{t_{in}}^{t_1} dt_C^{(c)} e^{i\omega_{\mathbf{k}_s}(t_1 - t_2)} \\ &\times \sum_{\mathcal{P}} \prod_{j=1}^{a+1} G^{(1,1)}(\mathbf{x}_j, t_j, \mathbf{y}_{p(j)}, \tau_{p(j)}) \\ &\times \langle \Psi_0 | \hat{\mathcal{I}}^\dagger(\mathbf{t}_A^{(a)}) e^{i\hat{H}_{el}(t_2 - t_{in})} \hat{n}(\mathbf{x}_2) e^{-i\hat{H}_{el}(t_2 - t_1)} \hat{\mathcal{I}}(\mathbf{t}_B^{(b)}) \hat{n}(\mathbf{x}_1) e^{-i\hat{H}_{el}(t_1 - t_{in})} \hat{\mathcal{I}}(\mathbf{t}_C^{(c)}) | \Psi_0 \rangle, \end{aligned} \quad (8.69)$$

where in the argument of the correlation function we have  $t_j \in \{t_2, t_{A_1}, \dots, t_{A_a}\}$  and all  $(b+c+1)!$  permutations of  $\tau_j \in \{t_1, t_{B_1}, \dots, t_{B_b}, t_{C_1}, \dots, t_{C_c}\}$ .

The first-order correlation function of the SASE FEL can be modelled as quasi-stationary and quasi-monochromatic. This means we can describe the pulse by the average intensity  $I(t)$  and the temporal coherence function  $\gamma(\tau)$ , i.e.,

$$G^{(1,1)}(\mathbf{x}_1, t_1, \mathbf{x}_2, t_2) = 4\pi\alpha I\left(\frac{t_1+t_2}{2}\right) \gamma_{tp}(t_2 - t_1) e^{i\mathbf{k}_{in} \cdot (\mathbf{x}_1 - \mathbf{x}_2)}, \quad (8.70)$$

where the temporal coherence function  $\gamma_{tp}(\tau) = e^{-\tau^2/\tau_c^2} e^{i\omega_{in}\tau}$  defines the coherence time  $\tau_c$  of the pulse. We assume that the radiation is spatially coherent in the entire interaction volume, such that the averaged intensity  $I(t)$  does not depend on  $\mathbf{x}_1, \mathbf{x}_2$ . Moreover, we assume that the ionization process is only sensitive to the temporal properties of the pulse, so that  $G^{(N,M)}$  depends only on the time variables of the ionization processes. Thus, we set  $\mathbf{x}_2, \dots, \mathbf{x}_N, \mathbf{y}_2, \dots, \mathbf{y}_M = 0$ . In the following we will assume that the coherence time is so short, the temporal coherence function is essentially a delta function in time. This assumption is justified by the fact that SASE FEL pulses have a spiky structure with coherence time in the subfemtosecond regime. Note that the scattered photons must interfere coherently, and consequently  $t_1$  and  $t_2$  must lie within the coherence time. Moreover, the ionization is assumed to be a sequential process, by choosing all times  $t_{A_1}, \dots, t_{A_a}$  to be mutually different.

This is justified because in the hard x-ray regime each single-photon absorption leads to the population of real atomic states. Thus, we neglect any statistical enhancement of multiphoton absorption, which is a reasonable approximation [192, 195].

Finally, we obtain the scattering probability

$$\begin{aligned}
 P(\mathbf{k}_s) &= \lim_{\substack{t_f \rightarrow \infty \\ t_{in} \rightarrow -\infty}} \sum_{\lambda_s} \frac{2(2\pi)^2}{V} \iint d^3x_1 d^3x_2 \frac{1}{\omega_{\mathbf{k}_s} \omega_{in}} \alpha |\epsilon_{in}^* \cdot \epsilon_{\mathbf{k}_s, \lambda_s}|^2 e^{i\mathbf{Q} \cdot (\mathbf{x}_1 - \mathbf{x}_2)} \\
 &\times \int_{t_{in}}^{t_f} dt \frac{I(t)}{\omega_{in}} \int_{-\infty}^{\infty} d\tau e^{-\tau^2/\tau_c^2} e^{i(\omega_{in} - \omega_{\mathbf{k}_s})\tau} \\
 &\times \text{Tr} \left( \hat{\rho}_{el}(t) e^{i\hat{H}_{el}\tau/2} \hat{n}(\mathbf{x}_2) e^{-i\hat{H}_{el}\tau} \hat{n}(\mathbf{x}_1) e^{i\hat{H}_{el}\tau/2} \right)
 \end{aligned} \tag{8.71}$$

where

$$\begin{aligned}
 \hat{\rho}_{el}(t) &= \sum_a \left( \frac{4\pi\alpha}{\omega_{in}^2} \right)^a \int_{t_{in}}^t dt_{A_a} \int_{t_{in}}^{t_{A_a}} dt_{A_{a-1}} \cdots \int_{t_{in}}^{t_{A_2}} dt_{A_1} I(t_{A_1}) \cdots I(t_{A_a}) \\
 &\times e^{-i\hat{H}_{el}(t-t_{in})} \hat{\mathcal{I}}(t_{A_a}) \cdots \hat{\mathcal{I}}(t_{A_1}) |\Psi_0\rangle \langle \Psi_0| \hat{\mathcal{I}}^\dagger(t_{A_1}) \cdots \hat{\mathcal{I}}^\dagger(t_{A_a}) e^{i\hat{H}_{el}(t-t_{in})}.
 \end{aligned} \tag{8.72}$$

## 8.B. Averaging of $S(\mathbf{Q})$ and simplification for numerical implementation

We recast Eq. (8.30) into a form that can be readily evaluated numerically. If the spin-orbital  $|\varphi_i\rangle$  is occupied in the initial Slater-determinant  $|\Psi_0\rangle$  the occupation number  $\eta_i$  is unity  $\eta_i = 1$ , otherwise the occupation number vanishes  $\eta_i = 0$ . Introducing the occupation numbers the static structure factor becomes

$$S(\mathbf{Q}) = Z - \sum_j \sum_i \eta_j \eta_i \left| \int d^3x \varphi_j^\dagger(\mathbf{x}) \varphi_i(\mathbf{x}) e^{i\mathbf{Q} \cdot \mathbf{x}} \right|^2. \tag{8.73}$$

In the following we introduce an additional averaging  $\langle \cdot \rangle_{\text{det}}$  over the initial Slater determinants  $|\Psi_0\rangle$ . We have assumed the initial state to be a single Slater-determinant. For open-shell atoms we will average over all possible initial occupations of orbitals in the open subshell. Physically, this means we neglect any anisotropy of the initial state, as well as we do not require particularly selected initial states. For example, in carbon we do not consider the spatial orientation of the  $p$ -orbitals, instead we average over all possible initial occupations of  $p$ -orbitals. The averaged static structure factor is

$$\langle S(\mathbf{Q}) \rangle_{\text{det}} = Z - \sum_j \sum_i \langle \eta_j \eta_i \rangle_{\text{det}} \left| \int d^3x \varphi_j^\dagger(\mathbf{x}) \varphi_i(\mathbf{x}) e^{i\mathbf{Q} \cdot \mathbf{x}} \right|^2. \tag{8.74}$$

Before we calculate the static structure factor, we analyze the averaged occupation numbers. First, we determine  $\langle \eta_i \rangle_{\text{det}}$ .

The simplest case is when the  $(n_i, l_i)$  subshell is a closed subshell, i.e., it holds  $2(2l_i + 1)$  electrons. Then we have  $\langle \eta_i \rangle_{\text{det}} = 1$ .

In the case of an open  $(n_i, l_i)$  subshell the number  $\mathcal{N}$  of possibilities to distribute  $N_{n_i, l_i}$  electrons onto the orbitals in the  $(n_i, l_i)$  subshell is

$$\mathcal{N} = \binom{2(2l_i + 1)}{N_{n_i, l_i}}.$$

The averaged occupation number is

$$\langle \eta_i \rangle_{\text{det}} = \langle \eta_{n_i, l_i, m_i, s_i} \rangle_{\text{det}} = \frac{1}{\mathcal{N}} \sum_{\text{det}} \eta_{n_i, l_i, m_i, s_i} = \frac{S_i}{\mathcal{N}}, \quad (8.75)$$

where  $S_i$  denotes the number of initial Slater determinants. There are

$$S_i = \binom{2(2l_i + 1) - 1}{N_{n_i, l_i} - 1}$$

possibilities that  $|\varphi_{n_i, l_i, m_i, s_i}\rangle$  is occupied. This yields

$$\langle \eta_i \rangle_{\text{det}} = \frac{S_i}{\mathcal{N}} = \frac{N_{n_i, l_i}}{2(2l_i + 1)}. \quad (8.76)$$

Now we may look at the average of products of occupation numbers  $\langle \eta_j \eta_i \rangle_{\text{det}}$ . In the simple case  $j = i$  we have  $\langle \eta_i^2 \rangle_{\text{det}} = \langle \eta_i \rangle_{\text{det}}$ , because  $\eta_i \in \{0, 1\}$ . When  $|\varphi_j\rangle$  belongs to a closed shell we have  $\eta_j = 1$  and thus  $\langle \eta_j \eta_i \rangle_{\text{det}} = \langle \eta_i \rangle_{\text{det}}$ . Finally, consider the case  $i \neq j$  and  $|\varphi_j\rangle$  and  $|\varphi_i\rangle$  belong to open shells. If  $|\varphi_j\rangle$  and  $|\varphi_i\rangle$  belong to different subshells, i.e.,  $n_i \neq n_j$  or  $l_i \neq l_j$  the average factorizes

$$\langle \eta_j \eta_i \rangle_{\text{det}} = \langle \eta_j \rangle_{\text{det}} \langle \eta_i \rangle_{\text{det}}. \quad (8.77)$$

If  $|\varphi_j\rangle$  and  $|\varphi_i\rangle$  belong to the same subshell,

$$\langle \eta_j \eta_i \rangle_{\text{det}} = \frac{1}{\mathcal{N}} \sum_{\text{det}} \eta_{n_j, l_j, m_j, s_j} \eta_{n_i, l_i, m_i, s_i} = \frac{S_{ij}}{\mathcal{N}} = \frac{N_{n_i, l_i} (N_{n_i, l_i} - 1)}{(4l_i + 2)(4l_i + 1)}, \quad (8.78)$$

where  $S_{ij}$

$$S_{ij} = \binom{2(2l_i + 1) - 2}{N_{n_i, l_i} - 2}$$

is the number possibilities to distribute  $N_{n_i, l_i}$  electrons in the subshell, such that  $\eta_{n_i, l_i, m_i, s_i} = 1 = \eta_{n_j, l_j, m_j, s_j}$ . In summary, we have

$$\langle \eta_j \eta_i \rangle_{\det} = \begin{cases} 1, & \varphi_i, \varphi_j \text{ in closed shells,} \\ \frac{N_{n_i, l_i}}{2(2l_i+1)}, & \varphi_i \text{ in open shell, } \varphi_j \text{ in closed shell,} \\ \frac{N_{n_i, l_i}}{2(2l_i+1)}, & \varphi_i = \varphi_j \text{ in open shell,} \\ \frac{N_{n_j, l_j}}{2(2l_j+1)} \frac{N_{n_i, l_i}}{2(2l_i+1)}, & \varphi_i, \varphi_j \text{ in open shell, } (n_j, l_j) \neq (n_i, l_i) \\ \frac{N_{n_i, l_i} (N_{n_i, l_i} - 1)}{(4l_i+2)(4l_i+1)}, & (n_j, l_j) = (n_i, l_i) \text{ open, } m_j \neq m_i. \end{cases} \quad (8.79)$$

We observe that as long as  $(m_i, s_i) = (m_j, s_j)$  the average  $\langle \eta_j \eta_i \rangle_{\det}$  depends only on  $n_i, l_i$  and  $n_j, l_j$ .

Similar to Ref. [230] we can now simplify the matrix element in Eq. (8.74). We choose the coordinate system in Q-direction. This means the Q-direction serves as the quantization axis. Then we can expand the exponential term in terms of the spherical Bessel functions  $j_l$  and the spherical harmonics  $Y_{lm}$  [243], with  $r = |\mathbf{x}|$ ,

$$e^{i\mathbf{Q}\cdot\mathbf{x}} = e^{iQr \cos \vartheta} = \sum_{L=0}^{\infty} i^L \sqrt{4\pi(2L+1)} j_L(Qr) Y_{L0}(\Omega_{\mathbf{x}}). \quad (8.80)$$

Assuming a spherically symmetric electronic Hamiltonian (cf. Sec. 8.3.4) the spin-orbitals with quantum numbers  $(n, l, m, s)$  can be decomposed in radial and angular part

$$\varphi_{nlms}(\mathbf{x}) = \frac{u_{nl}(r)}{r} Y_{lm}(\Omega_{\mathbf{x}}) \begin{pmatrix} \delta_{s,+1/2} \\ \delta_{s,-1/2} \end{pmatrix}. \quad (8.81)$$

The crucial matrix element then becomes

$$\langle \varphi_j | e^{i\mathbf{Q}\cdot\mathbf{x}} | \varphi_i \rangle = \int d^3x \varphi_{n_j l_j m_j s_j}^\dagger(\mathbf{x}) e^{i\mathbf{Q}\cdot\mathbf{x}} \varphi_{n_i l_i m_i s_i}(\mathbf{x}) \quad (8.82)$$

$$\begin{aligned} &= \delta_{s_j, s_i} \sqrt{4\pi(2L+1)} \sum_L i^L \int dr u_{n_j, l_j}(r) j_L(Qr) u_{n_i, l_i}(r) \\ &\times \int d\Omega_{\mathbf{x}} Y_{l_j m_j}^*(\Omega_{\mathbf{x}}) Y_{L0}(\Omega_{\mathbf{x}}) Y_{l_i m_i}(\Omega_{\mathbf{x}}). \end{aligned} \quad (8.83)$$

We can simplify the last equation to

$$\langle \varphi_j | e^{i\mathbf{Q}\cdot\mathbf{x}} | \varphi_i \rangle = \delta_{s_j, s_i} \sum_L i^L (2L+1) R_{n_j l_j n_i l_i}^L(Q) \sqrt{\frac{(2l_i+1)}{(2l_j+1)}} C_{l_i 0 L 0}^{l_j 0} C_{l_i m_i L 0}^{l_j m_j}, \quad (8.84)$$

where  $C_{l_1 m_1 l_2 m_2}^{l_3 m_3}$  are the Clebsch-Gordan coefficients and we have used the following identity for the angular integral [243]

$$\int d\Omega_{\mathbf{x}} Y_{l_j m_j}^*(\Omega_{\mathbf{x}}) Y_{LM}(\Omega_{\mathbf{x}}) Y_{l_i m_i}(\Omega_{\mathbf{x}}) = \sqrt{\frac{(2L+1)(2l_i+1)}{4\pi(2l_j+1)}} C_{l_i 0 L 0}^{l_j 0} C_{l_i m_i L M}^{l_j m_j}. \quad (8.85)$$

Moreover, we have introduced the radial integral

$$R_{n_j l_j n_i l_i}^L(Q) = \int dr u_{n_j l_j}(r) j_L(Qr) u_{n_i l_i}(r). \quad (8.86)$$

The expression for the squared modulus of the matrix element becomes

$$\left| \langle \varphi_j | e^{i\mathbf{Q}\cdot\mathbf{x}} | \varphi_i \rangle \right|^2 = \langle \varphi_i | e^{-i\mathbf{Q}\cdot\mathbf{x}} | \varphi_j \rangle \langle \varphi_j | e^{i\mathbf{Q}\cdot\mathbf{x}} | \varphi_i \rangle \quad (8.87)$$

$$= \delta_{s_j, s_i} \sum_L \sum_{L'} i^L (-i)^{L'} R_{n_j l_j n_i l_i}^L(Q) R_{n_j l_j n_i l_i}^{L'}(Q) \quad (8.88)$$

$$\times (2L+1)(2L'+1) C_{l_i 0 L 0}^{l_j 0} C_{l_i m_i L 0}^{l_j m_j} C_{l_j 0 L' 0}^{l_i 0} C_{l_j m_j L' 0}^{l_i m_i}.$$

The Clebsch-Gordan coefficients are only nonzero for  $m_j = m_i$ . Thus, the averaged occupation numbers are independent of  $m_j, m_i$ . Inserting Eq. (8.88) into the expression (8.74) of the averaged static structure factor yields

$$\begin{aligned} \langle S(\mathbf{Q}) \rangle_{\det} &= Z - \sum_{s_j, s_i} \delta_{s_j, s_i} \sum_{n_j, l_j} \sum_{n_i, l_i} \langle \eta_j \eta_i \rangle_{\det} \\ &\times \sum_L \sum_{L'} i^L (-i)^{L'} R_{n_j l_j n_i l_i}^L(Q) R_{n_j l_j n_i l_i}^{L'}(Q) \quad (8.89) \\ &\times (2L+1)(2L'+1) C_{l_i 0 L 0}^{l_j 0} C_{l_i m_i L 0}^{l_j m_j} \sum_{m_j, m_i} C_{l_i m_i L 0}^{l_j m_j} C_{l_j m_j L' 0}^{l_i m_i}. \end{aligned}$$

From the properties of the Clebsch-Gordan coefficients [243] we obtain two useful relations

$$\sum_{m_j, m_i} C_{l_i m_i L 0}^{l_j m_j} C_{l_j m_j L' 0}^{l_i m_i} = (-1)^{l_i - l_j} \frac{\sqrt{(2l_i+1)(2l_j+1)}}{2L+1} \delta_{LL'}, \quad (8.90)$$

and

$$C_{l_i 0 L 0}^{l_j 0} = (-1)^L \sqrt{\frac{2l_j+1}{2l_i+1}} C_{l_j 0 L 0}^{l_i 0}. \quad (8.91)$$

Using these relations we obtain the final result

$$\langle S(\mathbf{Q}) \rangle_{\det} = Z - 2 \sum_{n_j, l_j} \sum_{n_i, l_i} \langle \eta_j \eta_i \rangle_{\det} \sum_L (2L+1)(2l_j+1) \left| R_{n_j l_j n_i l_i}^L(Q) C_{l_j 0 L 0}^{l_i 0} \right|^2. \quad (8.92)$$

## 8.C. Molecular scattering pattern

To a first approximation we can think of complex biomolecules (up to  $\sim 10^5$  atoms) as a random distribution of  $N_C$  independent carbon atoms. For very short pulse duration the atomic positions  $\mathbf{R}_i$  are fixed during the pulse. We assume that scattering at different times adds up incoherently and we average over the populations  $P_{\mathbf{I}}(t)$  of the global electronic configurations  $\mathbf{I} = (I_1, \dots, I_{N_C})$ , where  $I_j$  is the electronic configuration of the  $j$ th atom. The intensity scattered into a given solid angle  $d\Omega_{\mathbf{k}_s}$  can be written

$$\begin{aligned} \frac{d\mathcal{I}_{\text{mol}}}{d\Omega_{\mathbf{k}_s}} = & \left( \frac{d\sigma}{d\Omega} \right)_{\text{Th}} \int dt j(t) \sum_{\mathbf{I}} P_{\mathbf{I}}(t) \left[ \left| \sum_{j=1}^{N_C} f_{I_j}(\mathbf{Q}) e^{i\mathbf{Q} \cdot \mathbf{R}_j} \right|^2 \right. \\ & \left. + \sum_{j=1}^{N_C} (S_{I_j}(\mathbf{Q}) + N_{I_j}^{\text{free}}) \right]. \end{aligned} \quad (8.93)$$

Assuming that the ionization in one atom is statistically independent of the other atoms, the global population factorizes into the individual atomic populations [244]

$$P_{\mathbf{I}}(t) = \prod_{j=1}^{N_C} P_{I_j}(t). \quad (8.94)$$

Under these assumptions the scattering intensity depends only on the single carbon atom population dynamics, see Ref. [244]. Therefore, we need to consider only electronic configurations  $I$  of a single carbon atom, instead of the global configuration  $\mathbf{I}$ .

The last term in Eq. (8.93) characterizes incoherent scattering on bound and ionized electrons. The incoherent summation over single atoms contains no information on the molecular structure. The resulting background signal is

$$\frac{d\mathcal{I}_{\text{bg}}}{d\Omega_{\mathbf{k}_s}} = \left( \frac{d\sigma}{d\Omega} \right)_{\text{Th}} N_C \int dt j(t) \sum_I P_I (S_I(\mathbf{Q}) + N_I^{\text{free}}). \quad (8.95)$$

On the other hand, the first term in Eq. (8.93) derives from the coherent scattering on bound electrons. It reduces to

$$\begin{aligned} \frac{d\mathcal{I}_{\text{el}}}{d\Omega_{\mathbf{k}_s}} = & \left( \frac{d\sigma}{d\Omega} \right)_{\text{Th}} \int dt j(t) \left[ N_C \sum_I P_I |f_I(\mathbf{Q})|^2 \right. \\ & \left. + \left| \sum_I P_I(t) f_I(\mathbf{Q}) \right|^2 \sum_{\substack{i,j \\ i \neq j}} e^{i\mathbf{Q} \cdot (\mathbf{R}_j - \mathbf{R}_i)} \right]. \end{aligned} \quad (8.96)$$

The first term is exactly  $N_C$ -times the coherent scattering signal of a single atom. Furthermore, note that  $f_I(\mathbf{Q})$  and  $S_I(\mathbf{Q})$  are independent of the azimuthal angle and only depend on  $\theta$ , because in our approach is the atom spherically symmetric.

Taking the average  $\langle \frac{d\mathcal{I}}{d\Omega_{\mathbf{k}_s}} \rangle_\theta$  only affects the last term in Eq. (8.96). We consider sufficiently high resolution  $r_{\text{res}} = 2\pi/Q$ . That is, we assume that  $r_{\text{res}}$  is smaller than almost all atom distances  $R_{i,j} = |\mathbf{R}_j - \mathbf{R}_i| > r_{\text{res}}$ . For atom distances larger than the resolution, the phase-factor  $\mathbf{Q} \cdot (\mathbf{R}_j - \mathbf{R}_i) \gg 2\pi$  oscillates strongly and thus  $\langle e^{i\mathbf{Q} \cdot (\mathbf{R}_j - \mathbf{R}_i)} \rangle_\theta = 0$ . On the other hand, we assume that there are no atom distances  $R_{i,j} \ll r_{\text{res}}$ , for which the phase factors would add up coherently. This means, we consider a resolution on the order of the nearest-neighbour distance. In this case we have random phase factors, and their sum corresponds to the average position of a random walk in the complex plane. This results in

$$\left\langle \sum_{\substack{i,j \\ i \neq j}} e^{i\mathbf{Q} \cdot (\mathbf{R}_j - \mathbf{R}_i)} \right\rangle_\theta = 0. \quad (8.97)$$

We considered the case of molecule with 10 nm radius and atom density  $1/15 \text{ \AA}^{-3}$ , corresponding to  $\sim 2.7 \cdot 10^5$  carbon atoms in total. This means there are about  $\sim 8$  atoms within a radius of  $3 \text{ \AA}$  resolution. The nearest-neighbour distance is  $\sim 1.5 \text{ \AA}$ . Assuming that the signal does not vary much over the independent pixel, and combining Eqs. (8.95), (8.96), and (8.97) one obtains Eq. (8.40)

$$\left\langle \frac{d\mathcal{I}_{\text{mol}}}{d\Omega_{\mathcal{P}}} \right\rangle_\theta = \Omega_{\mathcal{P}} N_C \left( \frac{d\sigma}{d\Omega} \right)_{\text{Th}} \int dt j(t) \sum_I P_I(t) \left[ |f_I(\mathbf{Q})|^2 + S_I(\mathbf{Q}) + N_I^{\text{free}} \right], \quad (8.98)$$

$$= \Omega_{\mathcal{P}} N_C \frac{d\mathcal{I}}{d\Omega_\theta}. \quad (8.99)$$

## 8.D. Photon count distribution

In this appendix we take a look at the probability distribution of the photon count. Several stochastic processes have to be considered. So far we have always taken the average of the molecular scattering pattern over a given scattering angle annulus. Considering a random distribution of atoms the intensity in the diffraction pattern is given by a probability distribution. Moreover, the actual number of scattered photons is a stochastic process and consequently subject to noise. The photon count distribution of the coherently scattered photons is a crucial statistical quantity for the image classification in Ref. [177].

Given a random distribution of atoms the probability distribution for the coherent scattering intensity has been given by Wilson [177, 241]

$$p(I) = \frac{1}{\langle I_{\text{coh}}(\theta) \rangle} e^{-I/\langle I_{\text{coh}}(\theta) \rangle}, \quad (8.100)$$

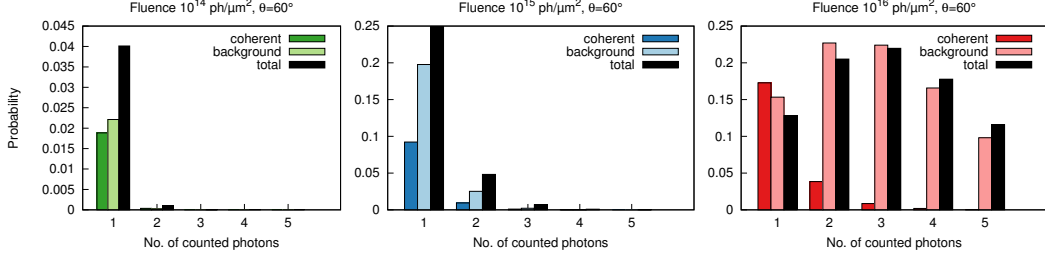


Figure 8.12.: The probability distribution of the photon count at  $\theta = 60^\circ$  and  $\omega_{\text{in}} = 10$  keV for different x-ray fluences. Assuming a random distribution of carbon atoms with  $R = 10$  nm and  $\rho_C = 1/15\text{\AA}^{-3}$ . Shown are the probability distributions of photon counts of coherent scattering, background, and the combined total photon count (see Eqs. (8.102), (8.103), (8.104)).

where  $\langle I_{\text{coh}}(\theta) \rangle$  is the average intensity over the annulus of scattering angle  $\theta$ . Modelling the molecule by a radius  $R$  and a carbon atom density  $\rho_C$ , we have

$$\langle I_{\text{coh}}(\theta) \rangle = \Omega_{\mathcal{P}} N_C \frac{d\mathcal{I}_{\text{coh}}}{d\Omega_{\theta}} = \lambda_{\text{in}}^2 \rho_C R \frac{\pi}{3} \frac{d\mathcal{I}_{\text{coh}}}{d\Omega_{\theta}}, \quad (8.101)$$

where  $\langle I_{\text{coh}}(\theta) \rangle$  denotes the expectation value of coherently scattered photons from a single carbon atom.

Because the sequential scattering of photons is a fundamentally stochastic process the actually detected number of photons is subject to Poisson noise. Combining the Poisson distribution with the intensity distribution in Eq. (8.100) we arrive at the probability distribution to count  $K$  elastically scattered photons in a given independent pixel [177]

$$p_{\text{coh}}(K) = \frac{1}{1 + \langle I^{\text{el}}(\theta) \rangle} \left( \frac{\langle I^{\text{el}}(\theta) \rangle}{1 + \langle I^{\text{el}}(\theta) \rangle} \right)^K. \quad (8.102)$$

Finally, we have to combine this with the probability distribution of the background signal. Being isotropic the background is only subject to Poissonian noise

$$p_{\text{bg}}(K) = \frac{(\langle I_{\text{bg}}(\theta) \rangle)^K}{K!} e^{-\langle I_{\text{bg}}(\theta) \rangle}, \quad (8.103)$$

where  $\langle I_{\text{bg}}(\theta) \rangle = \Omega_{\mathcal{P}} N_C \frac{d\mathcal{I}_{\text{bg}}}{d\Omega_{\theta}} = \rho_C R \lambda_{\text{in}}^2 \frac{\pi}{3} \frac{d\mathcal{I}_{\text{bg}}}{d\Omega_{\theta}}$ . Because elastic and background scattering are statistically independent the probability distribution  $p(K)$  to detect  $K$  photons is the convolution of the coherent and background distributions [245]

$$p_{\text{total}}(K) = \sum_{Z=0}^K p_{\text{coh}}(K-Z) p_{\text{bg}}(Z). \quad (8.104)$$

As before we consider the example with  $R = 10$  nm and  $\rho_C = 1/15\text{\AA}^{-3}$ , and assume  $\omega_{\text{in}} = 10$  keV. The average number of photons scattered into an independent pixel  $\Omega_{\mathcal{P}}$  is shown in Fig. 8.10. The probability distribution of the photon count at  $\theta = 60^\circ$  is presented in Fig. 8.12. In Fig. 8.12 we observe that only in the low fluence case the combined probability distribution resembles the photon count distribution of only coherent scattering. In particular at the highest fluence we find that including the background the photon count distribution is governed by the background scattering.

# Conclusion



# Chapter 9.

## Summary and final remarks

The Road goes ever on and on  
Out from the door where it began.  
Now far ahead the Road has gone,  
Let others follow it who can!  
Let them a journey new begin,  
But I at last with weary feet  
Will turn towards the lighted inn,  
My evening-rest and sleep to meet.

---

*(From J.R.R. Tolkien's "The Lord of the Rings")*

In this dissertation, I scrutinized nonresonant x-ray scattering. Using radiation from x-ray free electron lasers (XFELs), nonresonant x-ray scattering is a promising tool for x-ray imaging with atomic spatial and ultrafast time-resolution. XFELs offer completely new perspectives in imaging with atomic resolution. Examples are serial femtosecond crystallography of nanocrystals and coherent diffractive imaging of single molecules, which are expected to have an enduring impact on structural biology. Moreover, the technology of XFELs is rapidly evolving. Attosecond hard x-ray pulses are expected to be available in the future. They will facilitate new experiments on the time-scale of electronic processes in atoms in molecules. The research field of attosecond physics is still young and mostly taking place in the regime of optical photon energies. The direct investigation of electronic processes by transient x-ray spectroscopy or time-resolved x-ray scattering imaging are exciting potential applications of XFELs in this field.

A thorough understanding of the fundamental aspects of ultrafast nonresonant x-ray scattering is necessary to gauge the full potential of present and future x-ray light sources. This dissertation has discussed fundamental as well as practical aspects of nonresonant x-ray scattering.

## Quantum theory of near-field and far-field imaging

I analyzed the theory of propagation-based phase contrast imaging (PCI), which is a near-field imaging method. In Chapter 3 the classical theory of PCI has been adapted. Based on optical scattering, the present approach is conceptually close to the formulation in quantum theory. Moreover, the theory has been formulated for x-ray pulse with quasi-stationary, quasi-monochromatic statistics.

In Chapter 4, I based the theory of phase contrast imaging on quantum theory for the first time. The quantum theory is a rigorous validation of the classical expression, which it fully recovers. Interestingly, there are automatically only contributions from electronically elastic x-ray scattering. The expectation value of a suitable observable, here the Poynting operator, has been determined in first order perturbation theory. The (0,1) term has been demonstrated to fully account for the phase contrast effect. This term, which cannot be obtained from transition probabilities, accounts for the interference of scattered and unscattered photons. The consequences of this quantum theory have been exploited in Chapter 5 for time-resolved imaging.

In the last three chapters, I investigated x-ray scattering in the far-field. In Chapter 6, I uncovered the relation of the expectation value of the Poynting operator with the commonly used transition probabilities. The (1,1) term of perturbation theory has been demonstrated to be responsible for the far-field scattering pattern. This term includes inelastic scattering, which cannot be properly described in classical theory.

## Time resolved imaging of electronic motion

Optical and x-ray imaging of electronic wave packets have recently seen a rapid progress. In anticipation of further developments of femto- and attosecond x-ray sources, I surveyed possibilities to image coherent electronic wave packets via non-resonant x-ray scattering.

In Chapter 5, the quantum theory of phase contrast imaging has been applied to the imaging of electronic motion. It turns out that PCI recovers, in contrast to far-field methods, the instantaneous electron density. Examples for wave packets in the hydrogen atom have been illustrated. Moreover, this method allows, by using tomographic methods, the reconstruction of the 3d electron density and its Laplacian, which contains information on the topology of the electron charge distribution. Future experimental setups might satisfy the technological requirements to perform such experiments.

In the near future, far-field x-ray imaging of coherent wave packets is expected to become feasible. In Chapter 7, I have explored several imaging methods. As was recently discovered, the far-field scattering pattern of electronic wave packets does

---

not encode the instantaneous electron density, but complex spatio-temporal density correlations. Here, an analysis of the role of photon energy resolution in the measurement is provided. In the case of very high resolution, one measures a generalized dynamic structure factor. In the case of no energy resolution, one measures a generalized static structure factor. For static targets the structure factor is known to give information about electronic correlations. Interestingly, it may thus be possible without energy resolution to probe time-dependent electronic correlations.

Moreover, it was demonstrated how time-resolved x-ray scattering experiments can be used to reconstruct a generalized electron density propagator. The full propagator, which characterizes the complete linear response behaviour of the system, may be recovered in special cases. Additionally, a possibility to recover the instantaneous electron density was discovered. X-ray crystallography from a regular arrangement of wave packets automatically filters out the coherent scattering contribution.

Finally, I proposed time-resolved Compton scattering of electronic wave packets. I demonstrated that coincidence measurements of the scattered photon and the recoil electron yield direct access to the instantaneous electron momentum density. If the recoil electron is not observed, the measurement yields the time-dependent Compton profile. Hence, this method gives a direct access to the instantaneous momentum-space density. In many cases imaging in momentum space is equally desirable as imaging in real-space. I illustrated this method in the case of a hydrogen wave packet. Further studies will certainly test the method on more complex systems. Simulations on complex systems should also be easier to perform than simulations of the quasi-elastic diffraction patterns.

### **Incoherent scattering in single molecule imaging**

Coherent diffractive imaging (CDI) of single molecules is one of the key applications of x-ray free electron lasers. It promises to supersede the often impossible crystallization of biomolecules. XFELs offer the required ultrashort x-ray pulses with unprecedented high intensity. CDI relies on the connection of the elastic (coherent) diffraction pattern with the electron density. Inelastic (incoherent) scattering causes an undesirable background signal.

Chapter 8 presents an ab initio study of incoherent x-ray scattering under typical single molecule imaging conditions. Due to the high-intensity regime, the target will be ionized strongly. Here, electronic radiation damage of the strongly driven electronic system is treated in a rate equation approach. Calculations have been performed with the XATOM-toolkit, which I have extended to comprise inelastic scattering. I calculated the elastic and inelastic scattering patterns of the carbon atom for different photon energies and photon fluences. From these results, I estimated the scattering patterns of typical biomolecules. Remarkably, the scattering

patterns exhibit a strong background signal at high fluence and high resolution. Especially, the scattering from unbound electrons is responsible for a large part of the background signal. Therefore, the results recommend higher photon energies for imaging, due to the reduced photoabsorption. Moreover, the results suggest to make the molecular classification and orientation algorithms, which are needed in the reconstruction procedure, ready for strong background signals. With respect to the expected huge impact of single molecule imaging, further refined studies are indispensable. A logical next step would be to include the inelastic scattering cross sections into molecular dynamics simulations of XFEL irradiated systems. Moreover, the scattering from unbound electrons, which has shown its crucial role, has to be investigated in more detail. From a suitable model of the nonequilibrium state of the electron plasma, one could obtain a more refined Compton spectrum from the free electrons.

### **Outlook**

For such a new method like XFEL imaging and in such a young research field like attosecond physics, there remain many open questions. The results presented here are a first step.

Most urgently, the inelastic background in CDI should be further investigated and the algorithms should be adjusted. Moreover, further studies of Compton scattering in the high intensity regime, on heavy elements, are interesting. Possibly, the Compton spectrum could be used as an online analysis tool. It is conceivable, that it contains information about the ionization dynamics and may serve as a mean to reduce the influence of volume integration.

Time-resolved imaging of electronic wave packets is an important aspect in the long-term. Future studies will involve more complex wave packets. Compton scattering is very promising, simulations seem feasible as they do not involve unoccupied states. It would be interesting to analyze the importance of the plane wave assumption, for instance, with TDCIS calculations. In the future, it will also be important to include ionization into the models.

An important development for theory will be to devise a rigorous and practical treatment of the ionization dynamics. A compelling question will be to bring to light the importance of atomic coherences and statistical properties of the radiation pulse in the ionization dynamics. With the emergence of seeded XFEL light sources, it will prove important to quantify the effects of coherent light on the imaging process.

## Acknowledgements

First and foremost, I would like to express my deepest gratitude to my supervisor **Prof. Robin Santra** for giving me the opportunity to be part of the young and vital research field of ultrafast, high-intensity x-ray science. I am much obliged for his excellent guidance in our many discussions, as well as his patience during them. Through his enthusiasm and his scientific curiosity, he provides an excellent research atmosphere. His immediate and meticulous proofreading of manuscripts was always a valuable affirmation of my efforts.

I am very grateful to **Prof. Michael Thorwart** for his kind and readily willingness to write a report on my dissertation. Moreover, I thank **Prof. Harry Quiney** for writing the third report.

It has been my privilege to be student in the International Max Planck Research School for Ultrafast Imaging and Structural Dynamics (IMPRS-UFAST). I thank the coordinators **Anja Bleidorn** and **Sonia Utermann** for the organization of many instructive workshops.

I am indebted to several colleagues for their help and contributions during the last few years. I warmly thank **Sang-Kil Son** for explaining the XATOM-code to me, for his readiness to implement changes quickly, as well as his constant interest in my work. I gratefully acknowledge the fruitful collaboration with **Gopal Dixit**, who always encouraged me to be visionary and taught me important lessons about writing articles. A special thanks goes to **Stefan Pabst** who always had many suggestions to solve scientific problems. Moreover, I appreciate the help of **Clemens Weninger** who introduced me to Python and always lent an ear to my problems.

I benefited immensely from the discussions with **Oriol Vendrell**, **Stefan Pabst**, **Sang-Kil Son**, **Arina Sytcheva**, **Gopal Dixit**, **Antonia Karamatskou**, **Daria Gorelova**, and **Otfried Geffert**. Our debates on physics – mostly during the coffee breaks – made the time of my doctorate a most enjoyable and extremely instructive experience. A special thanks is due to **Antonia Karamatskou** and **Daria Gorelova** for creating a wonderful working atmosphere in the office.

Those who have not been named are not forgotten: it has been my great pleasure to work in the **CFEL theory division**. The international environment was a greatly rewarding experience and I have gained friends from many parts of the world. The scientific discussions we had all the time, made the last years an intense educational experience. I am grateful to **Berit Heiser** for taking care of all bureau-

cratic issues with stunning efficiency.

I owe a dept of gratitude to the many eyes that were looking over the text to reduce mistakes and typos: **Stefan Birkholz**, **Yi-Jen Chen**, **Giulia Frontoni**, **Daria Gorelova**, **Ludger Inhester**, **Zoltan Jurek**, **Antonia Karamatskou**, **Sang-Kil Son**, and **Clemens Weninger**. Their critical proofreading and their great suggestions were extremely helpful and are very much appreciated by me (and the readers, I suppose).

Last but not least, I thank my **family** and **friends**, whom I have probably not dedicated the amount of time they deserve. Most importantly, I would like to thank **Giulia Frontoni** for her steady moral support and her patience.

## **Eidesstattliche Versicherung**

Hiermit erkläre ich an Eides statt, dass ich die vorliegende Dissertationsschrift selbst verfasst und keine anderen als die angegebenen Quellen und Hilfsmittel benutzt habe.

Hamburg, den

Unterschrift



## Bibliography

- [1] Slowik J M and Santra R 2013 [X-ray phase-contrast imaging: the quantum perspective](#) *J. Phys. B: At. Mol. Opt. Phys.* **46**(16) 164016
- [2] Dixit G, Slowik J M and Santra R 2013 [Proposed Imaging of the Ultrafast Electronic Motion in Samples using X-Ray Phase Contrast](#) *Phys. Rev. Lett.* **110**(13) 137403
- [3] Dixit G, Slowik J M and Santra R 2014 [Theory of time-resolved nonresonant x-ray scattering for imaging ultrafast coherent electron motion](#) *Phys. Rev. A* **89**(4) 043409
- [4] Slowik J M, Son S-K, Dixit G, Jurek Z and Santra R 2014 [Incoherent x-ray scattering in single molecule imaging](#) *New J. Phys.* **16**(7) 073042
- [5] Santra R, Dixit G and Slowik J M 2014 [Comment on "How to observe coherent electron dynamics directly"](#) *Phys. Rev. Lett.* **113**(18) 189301
- [6] Ackermann W et al. 2007 [Operation of a free-electron laser from the extreme ultraviolet to the water window](#) *Nat. Photonics* **1**(6) 336–342
- [7] Emma P et al. 2010 [First lasing and operation of an ångstrom-wavelength free-electron laser](#) *Nat. Photonics* **4**(9) 641–647
- [8] Altarelli M et al. 2006 *The European X-Ray Free-Electron Laser Technical Report DESY 2006-097* DESY Hamburg
- [9] Ishikawa T et al. 2012 [A compact X-ray free-electron laser emitting in the sub-ångstrom region](#) *Nat. Photonics* **6**(8) 540–544
- [10] Allaria E et al. 2012 [Highly coherent and stable pulses from the FERMI seeded free-electron laser in the extreme ultraviolet](#) *Nat. Photonics* **6**(10) 699–704
- [11] Ribic P R and Margaritondo G 2012 [Status and prospects of x-ray free-electron lasers \(X-FELs\): a simple presentation](#) *J. Phys. D: Appl. Phys.* **45**(21) 213001
- [12] Santra R 2009 [Concepts in x-ray physics](#) *J. Phys. B: At. Mol. Opt. Phys.* **42**(16) 169801

- [13] Santra R 2012 *Theory of radiation matter interaction* (Universität Hamburg) – Unpublished lecture notes
- [14] Craig D and Thirunamachandran T 1998 *Molecular Quantum Electrodynamics* (Dover Publications)
- [15] Mandel L and Wolf E 1995 *Optical coherence and quantum optics* (Cambridge University Press)
- [16] Cohen-Tannoudji C, Dupont-Roc J and Grynberg G 1989 *Photons and Atoms: Introduction to Quantum Electrodynamics* (Wiley)
- [17] Loudon R 2000 *The Quantum Theory of Light* (Oxford Science Publications) third edition
- [18] Grynberg G, Aspect A and Fabre C 2010 *Introduction to quantum optics: from the semi-classical approach to quantized light* (Cambridge university press)
- [19] Szabo A and Ostlund N 1996 *Modern quantum chemistry* (Dover Publications)
- [20] Fetter A and Walecka J 2003 *Quantum Theory of Many-Particle Systems* (Dover Publications)
- [21] Schülke W 2007 *Electron dynamics by inelastic X-ray scattering* (Oxford University Press Oxford)
- [22] Hau-Riege S 2011 *High-Intensity X-Rays – Interaction with Matter* (Wiley-VCH)
- [23] Gel'mukhanov F and Ågren H 1999 [Resonant X-ray Raman scattering](#) *Phys. Rep.* **312**(3) 87–330
- [24] Ament L J, van Veenendaal M, Devereaux T P, Hill J P and van den Brink J 2011 [Resonant inelastic x-ray scattering studies of elementary excitations](#) *Rev. Mod. Phys.* **83**(2) 705
- [25] Altarelli M 2006 [Resonant X-ray scattering: a theoretical introduction](#) in E Beaurepaire, H Bulou, F Scheurer and J P Kappler (Editors), “Magnetism: A Synchrotron Radiation Approach”, 201–242 (Springer)
- [26] Bandrauk A D, Fillion-Gourdeau F and Lorin E 2013 [Atoms and molecules in intense laser fields: gauge invariance of theory and models](#) *J. Phys. B: At. Mol. Opt. Phys.* **46**(15) 153001
- [27] Stirling W and Cooper M 1999 [X-ray magnetic scattering](#) *J. Magn. Magn. Mater.* **200**(1) 755–773

- 
- [28] Evans P G and Isaacs E D 2006 [Magnetic x-ray microdiffraction](#) *J. Phys. D: Appl. Phys.* **39**(15) R245
- [29] Bjorken J D and Drell S D 1964 *Relativistic quantum mechanics* (McGraw-Hill)
- [30] Nugent K A 2010 [Coherent methods in the X-ray sciences](#) *Adv. Phys.* **59**(1) 1–99
- [31] Paganin D 2006 *Coherent X-Ray Optics* (Oxford University Press)
- [32] Barty A, Nugent K A, Paganin D and Roberts A 1998 [Quantitative optical phase microscopy](#) *Opt. Lett.* **23**(11) 817–819
- [33] Andrews M R, Mewes M O, van Druten N J, Durfee D S, Kurn D M and Ketterle W 1996 [Direct, Nondestructive Observation of a Bose Condensate](#) *Science* **273**(5271) 84–87
- [34] Andrews M R, Townsend C G, Miesner H J, Durfee D S, Kurn D M and Ketterle W 1997 [Observation of Interference Between Two Bose Condensates](#) *Science* **275**(5300) 637–641
- [35] Turner L D, Domen K F E M and Scholten R E 2005 [Diffraction-contrast imaging of cold atoms](#) *Phys. Rev. A* **72** 031403
- [36] Cowley J and Bridges R 1979 [Phase and amplitude contrast in electron microscopy of stained biological objects](#) *Ultramicroscopy* **4**(4) 419–427
- [37] Butler J and Cowley J 1984 [Phase contrast imaging using a scanning transmission electron microscope](#) *Ultramicroscopy* **12**(1) 39–50
- [38] Allman B, McMahon P, Nugent K, Paganin D, Jacobson D, Arif M and Werner S 2000 [Imaging - Phase radiography with neutrons](#) *Nature* **408**(6809) 158–159
- [39] McMahon P J, Allman B E, Jacobson D L, Arif M, Werner S A and Nugent K A 2003 [Quantitative Phase Radiography with Polychromatic Neutrons](#) *Phys. Rev. Lett.* **91** 145502
- [40] Zernike F 1942 [Phase contrast, a new method for the microscopic observation of transparent objects](#) *Physica* **9** 686–698
- [41] Zernike F 1955 [How I discovered phase contrast](#) *Science* **121**(3141) 345–349
- [42] Nagayama K 2014 [Biological Applications of Phase-Contrast Electron Microscopy](#) in J Kuo (Editor), “Electron Microscopy”, Volume 1117 of *Methods in Molecular Biology* 385–399 (Humana Press)

- [43] Schmahl G, Rudolph D, Guttman P, Schneider G, Thieme J and Niemann B 1995 [Phase contrast studies of biological specimens with the x-ray microscope at BESSY \(invited\)](#) *Rev. Sci. Instrum.* **66**(2) 1282–1286
- [44] Weitkamp T 2004 [XWFP: An X-ray wavefront propagation software package for the IDL computer language](#) in “Optical Science and Technology, the SPIE 49th Annual Meeting”, 181–189 (International Society for Optics and Photonics)
- [45] Snigirev A, Snigireva I, Kohn V, Kuznetsov S and Schelokov I 1995 [On the possibilities of x-ray phase contrast microimaging by coherent high-energy synchrotron radiation](#) *Rev. Sci. Instrum.* **66**(12) 5486–5492
- [46] Cloetens P, Barrett R, Baruchel J, Guigay J P and Schlenker M 1996 [Phase objects in synchrotron radiation hard x-ray imaging](#) *J. Phys. D: Appl. Phys.* **29**(1) 133
- [47] Wilkins S, Gureyev T, Gao D, Pogany A and Stevenson A 1996 [Phase-contrast imaging using polychromatic hard X-rays](#) *Nature* **384**(6607) 335–338
- [48] Pfeiffer F, Weitkamp T, Bunk O and David C 2006 [Phase retrieval and differential phase-contrast imaging with low-brilliance X-ray sources](#) *Nat. Phys.* **2**(4) 258–261
- [49] Bravin A, Coan P and Suortti P 2013 [X-ray phase-contrast imaging: from pre-clinical applications towards clinics](#) *Phys. Med. Biol.* **58**(1) R1
- [50] Momose A, Takeda T, Itai Y and Hirano K 1996 [Phase-contrast X-ray computed tomography for observing biological soft tissues](#) *Nat. Med.* **2**(4) 473–475
- [51] Zhao Y et al. 2012 [High-resolution, low-dose phase contrast X-ray tomography for 3D diagnosis of human breast cancers](#) *Proc. Natl. Acad. Sci. USA* **109**(45) 18290–18294
- [52] Beerlink A, Mell M, Tolkiehn M and Salditt T 2009 [Hard x-ray phase contrast imaging of black lipid membranes](#) *Appl. Phys. Lett.* **95**(20) 203703
- [53] Beerlink A, Thutupalli S, Mell M, Bartels M, Cloetens P, Herminghaus S and Salditt T 2012 [X-ray propagation imaging of a lipid bilayer in solution](#) *Soft Matter* **8**(17) 4595–4601
- [54] Walker S M, Schwyn D A, Mokso R, Wicklein M, Müller T, Doube M, Stamparoni M, Krapp H G and Taylor G K 2014 [In vivo time-resolved microtomography reveals the mechanics of the blowfly flight motor](#) *PLOS Biol.* **12**(3) e1001823

- 
- [55] Cloetens P, Ludwig W, Baruchel J, Dyck D V, Landuyt J V, Guigay J P and Schlenker M 1999 [Holotomography: Quantitative phase tomography with micrometer resolution using hard synchrotron radiation x rays](#) *Appl. Phys. Lett.* **75**(19) 2912–2914
- [56] Pradel A, Langer M, Maisey J G, Geffard-Kuriyama D, Cloetens P, Janvier P and Tafforeau P 2009 [Skull and brain of a 300-million-year-old chimaeroid fish revealed by synchrotron holotomography](#) *Proc. Natl. Acad. Sci. USA* **106**(13) 5224–5228
- [57] Mocella V, Brun E, Ferrero C and Delattre D 2015 [Revealing letters in rolled Herculaneum papyri by X-ray phase-contrast imaging](#) *Nat. Commun.* **6** 5895
- [58] Pogany A, Gao D and Wilkins S 1997 [Contrast and resolution in imaging with a microfocus x-ray source](#) *Rev. Sci. Instrum.* **68**(7) 2774–2782
- [59] Teague M R 1983 [Deterministic phase retrieval: a Green’s function solution](#) *J. Opt. Soc. Am.* **73**(11) 1434–1441
- [60] Nugent K A, Paganin D and Gureyev T E 2001 [A Phase Odyssey](#) *Phys. Today* **54** 27
- [61] Schmalz J A, Gureyev T E, Paganin D M and Pavlov K M 2011 [Phase retrieval using radiation and matter-wave fields: Validity of Teague’s method for solution of the transport-of-intensity equation](#) *Phys. Rev. A* **84** 023808
- [62] Born M and Wolf E 1999 *Principles of optics: electromagnetic theory of propagation, interference and diffraction of light* (Cambridge University Press)
- [63] Als-Nielsen J and McMorrow D 2001 *Elements of modern x-ray physics* (John Wiley & Sons)
- [64] Lajunen H, Friberg A T and Ostlund P 2006 [Quasi-stationary plane-wave optical pulses and the van Cittert-Zernike theorem in time](#) *J. Opt. Soc. Am. A* **23**(10) 2530–2537
- [65] Pääkkönen P, Turunen J, Vahimaa P, Friberg A and Wyrowski F 2002 [Partially coherent Gaussian pulses](#) *Opt. Commun.* **204**(1-6) 53–58
- [66] Scully M O and Sargent M 1972 [The concept of the photon](#) *Physics Today* **25**(3) 38–47
- [67] Milonni P W 1976 [Semiclassical and quantum-electrodynamical approaches in nonrelativistic radiation theory](#) *Phys. Rep.* **25**(1) 1–81

- [68] Bosanac S 1998 [Semiclassical theory of Compton and photoelectric effects](#) *Eur. J. Phys. D* **1**(3) 317–327
- [69] Compton A H 1923 [A Quantum Theory of the Scattering of X-rays by Light Elements](#) *Phys. Rev.* **21** 483–502
- [70] Ho P J and Santra R 2008 [Theory of x-ray diffraction from laser-aligned symmetric-top molecules](#) *Phys. Rev. A* **78**(5) 053409
- [71] Glauber R 1963 [The Quantum Theory of Optical Coherence](#) *Phys. Rev.* **130**(6) 2529–2539
- [72] Parrent G B 1959 [On The Propagation Of Mutual Coherence](#) *J. Opt. Soc. Am.* **49**(8) 787–793
- [73] Lahiri M and Wolf E 2010 [Quantum theory of optical coherence of nonstationary light in the space-frequency domain](#) *Phys. Rev. A* **82**(4) 043837
- [74] Krausz F and Ivanov M 2009 [Attosecond physics](#) *Rev. Mod. Phys.* **81**(1) 163
- [75] Corkum P and Krausz F 2007 [Attosecond science](#) *Nat. Phys.* **3**(6) 381–387
- [76] Smirnova O and Ivanov M 2010 [Ultrafast science: Towards a one-femtosecond film](#) *Nat. Phys.* **6**(3) 159–160
- [77] Leone S R et al. 2014 [What will it take to observe processes in 'real time'?](#) *Nat. Photonics* **8**(3) 162–166
- [78] Haessler S et al. 2010 [Attosecond imaging of molecular electronic wavepackets](#) *Nat. Phys.* **6**(3) 200–206
- [79] Goulielmakis E et al. 2010 [Real-time observation of valence electron motion](#) *Nature* **466**(7307) 739–743
- [80] Hockett P, Bisgaard C Z, Clarkin O J and Stolow A 2011 [Time-resolved imaging of purely valence-electron dynamics during a chemical reaction](#) *Nat. Phys.* **7**(8) 612–615
- [81] Tzallas P, Skantzakis E, Nikolopoulos L, Tsakiris G and Charalambidis D 2011 [Extreme-ultraviolet pump-probe studies of one-femtosecond-scale electron dynamics](#) *Nat. Phys.* **7**(10) 781–784
- [82] Woerner M, Zamponi F, Ansari Z, Dreyer J, Freyer B, Prémont-Schwarz M and Elsaesser T 2010 [Concerted electron and proton transfer in ionic crystals mapped by femtosecond x-ray powder diffraction](#) *J. Chem. Phys.* **133**(6) 064509

- 
- [83] Zamponi F, Rothhardt P, Stingl J, Woerner M and Elsaesser T 2012 [Ultrafast large-amplitude relocation of electronic charge in ionic crystals](#) *Proc. Natl. Acad. Sci. USA* **109**(14) 5207–5212
- [84] Wirth A, Santra R and Goulielmakis E 2013 [Real time tracing of valence-shell electronic coherences with attosecond transient absorption spectroscopy](#) *Chem. Phys.* **414** 149–159
- [85] Neidel C et al. 2013 [Probing time-dependent molecular dipoles on the attosecond time scale](#) *Phys. Rev. Lett.* **111**(3) 033001
- [86] Fechner L, Camus N, Ullrich J, Pfeifer T and Moshhammer R 2014 [Strong-Field Tunneling from a Coherent Superposition of Electronic States](#) *Phys. Rev. Lett.* **112**(21) 213001
- [87] Calegari F et al. 2014 [Ultrafast electron dynamics in phenylalanine initiated by attosecond pulses](#) *Science* **346**(6207) 336–339
- [88] Dixit G, Vendrell O and Santra R 2012 [Imaging electronic quantum motion with light](#) *Proc. Natl. Acad. Sci. USA* **109**(29) 11636–11640
- [89] Emma P, Bane K, Cornacchia M, Huang Z, Schlarb H, Stupakov G and Walz D 2004 [Femtosecond and Subfemtosecond X-Ray Pulses from a Self-Amplified Spontaneous-Emission-Based Free-Electron Laser](#) *Phys. Rev. Lett.* **92** 074801
- [90] Zholents A A and Fawley W M 2004 [Proposal for Intense Attosecond Radiation from an X-Ray Free-Electron Laser](#) *Phys. Rev. Lett.* **92** 224801
- [91] Tanaka T 2013 [Proposal for a Pulse-Compression Scheme in X-Ray Free-Electron Lasers to Generate a Multiterawatt, Attosecond X-Ray Pulse](#) *Phys. Rev. Lett.* **110** 084801
- [92] Kumar S, Kang H S and Kim D E 2013 [Attosecond Hard X-ray Free Electron Laser](#) *Appl. Sci.* **3**(1) 251–266
- [93] Chen M C et al. 2014 [Generation of bright isolated attosecond soft X-ray pulses driven by multicycle midinfrared lasers](#) *Proc. Natl. Acad. Sci. USA* **111**(23) E2361–E2367
- [94] Dixit G and Santra R 2013 [Role of electron-electron interference in ultrafast time-resolved imaging of electronic wavepackets](#) *J. Chem. Phys.* **138** 134311
- [95] Remacle F and Levine R 2006 [An electronic time scale in chemistry](#) *Proc. Natl. Acad. Sci. USA* **103**(18) 6793–6798

- [96] Scholes G D, Fleming G R, Olaya-Castro A and van Grondelle R 2011 [Lessons from nature about solar light harvesting](#) *Nat. Chem.* **3**(10) 763–774
- [97] Breidbach J and Cederbaum L 2003 [Migration of holes: Formalism, mechanisms, and illustrative applications](#) *J. Chem. Phys.* **118**(9) 3983–3996
- [98] Shao H C and Starace A F 2013 [Imaging coherent electronic motion in atoms by ultrafast electron diffraction](#) *Phys. Rev. A* **88**(6) 062711
- [99] Strüder L et al. 2010 [Large-format, high-speed, X-ray pnCCDs combined with electron and ion imaging spectrometers in a multipurpose chamber for experiments at 4th generation light sources](#) *Nucl. Instrum. Methods A* **614**(3) 483–496
- [100] Philipp H T, Hromalik M, Tate M, Koerner L and Gruner S M 2011 [Pixel array detector for x-ray free electron laser experiments](#) *Nucl. Instrum. Methods A* **649**(1) 67–69
- [101] Burvall A, Lundström U, Takman P A, Larsson D H and Hertz H M 2011 [Phase retrieval in X-ray phase-contrast imaging suitable for tomography](#) *Opt. Express* **19**(11) 10359–10376
- [102] Bronnikov A V 2002 [Theory of quantitative phase-contrast computed tomography](#) *J. Opt. Soc. Am. A* **19**(3) 472–480
- [103] Kak A C and Slaney M 2001 *Principles of computerized tomographic imaging* (Society for Industrial and Applied Mathematics)
- [104] Bader R and Nguyen-Dang T 1981 [Quantum theory of atoms in molecules-Dalton revisited](#) *Adv. Quantum Chem.* **14** 63–124
- [105] Bader R F 1991 [A quantum theory of molecular structure and its applications](#) *Chem. Phys.* **91**(5) 893–928
- [106] James R 1962 *The Optical Principles of the Diffraction of X-rays* (Ox Bow Press)
- [107] Tanaka S, Chernyak V and Mukamel S 2001 [Time-resolved x-ray spectroscopies: Nonlinear response functions and Liouville-space pathways](#) *Phys. Rev. A* **63**(6) 063405
- [108] Pabst S, Sytcheva A, Moulet A, Wirth A, Goulielmakis E and Santra R 2012 [Theory of attosecond transient-absorption spectroscopy of krypton for overlapping pump and probe pulses](#) *Phys. Rev. A* **86**(6) 063411

- 
- [109] Dutoi A D, Gokhberg K and Cederbaum L S 2013 [Time-resolved pump-probe spectroscopy to follow valence electronic motion in molecules: Theory](#) *Phys. Rev. A* **88**(1) 013419
- [110] Dutoi A D and Cederbaum L S 2014 [Time-resolved pump-probe spectroscopy to follow valence electronic motion in molecules: Application](#) *Phys. Rev. A* **90**(2) 023414
- [111] Bennett K, Biggs J D, Zhang Y, Dorfman K E and Mukamel S 2014 [Time-, frequency-, and wavevector-resolved x-ray diffraction from single molecules](#) *J. Chem. Phys.* **140**(20) 204311
- [112] Bredtmann T, Ivanov M and Dixit G 2014 [X-ray imaging of chemically active valence electrons during a pericyclic reaction](#) *Nat. Commun.* **5** 5589
- [113] Coontz R, Fahrenkamp-Uppenbrink J, Lavine M and Vinson V 2014 [Going from Strength to Strength](#) *Science* **343**(6175) 1091
- [114] [Nature Milestones in Crystallography](#) URL <http://dx.doi.org/doi:10.1038/nature13348>
- [115] Cao J and Wilson K R 1998 [Ultrafast X-ray diffraction theory](#) *J. Phys. Chem. A* **102**(47) 9523–9530
- [116] Ben-Nun M, Cao J and Wilson K R 1997 [Ultrafast x-ray and electron diffraction: theoretical considerations](#) *J. Phys. Chem. A* **101**(47) 8743–8761
- [117] Henriksen N E and Møller K B 2008 [On the theory of time-resolved x-ray diffraction](#) *J. Phys. Chem. B* **112**(2) 558–567
- [118] Lorenz U, Møller K B and Henriksen N E 2010 [Theory of time-resolved inelastic x-ray diffraction](#) *Phys. Rev. A* **81**(2) 023422
- [119] Mancuso A P 2011 *Scientific Instrument Single Particles, Clusters, and Biomolecules (SPB) Conceptual Design Report XFEL.EU TR-2011-007* European XFEL
- [120] Cooper M J 1985 [Compton scattering and electron momentum determination](#) *Rep. Prog. Phys.* **48**(4) 415
- [121] Van Hove L 1954 [Correlations in space and time and Born approximation scattering in systems of interacting particles](#) *Phys. Rev.* **95**(1) 249
- [122] Petrillo C and Sacchetti F 1995 [Electron-electron correlations in diamond: An x-ray-scattering experiment](#) *Phys. Rev. B* **51**(8) 4755

- [123] Watanabe N, Hayashi H, Udagawa Y, Ten-No S and Iwata S 1998 [Static structure factor and electron correlation effects studied by inelastic x-ray scattering spectroscopy](#) *J. Chem. Phys.* **108**(11) 4545–4553
- [124] Schülke W, Schmitz J, Schulte-Schrepping H and Kaprolat A 1995 [Dynamic and static structure factor of electrons in Si: Inelastic x-ray scattering results](#) *Phys. Rev. B* **52**(16) 11721
- [125] Devereaux T, McCormack G and Freericks J 2003 [Inelastic x-ray scattering as a probe of electronic correlations](#) *Phys. Rev. B* **68**(7) 075105
- [126] Trigo M et al. 2013 [Fourier-transform inelastic X-ray scattering from time- and momentum-dependent phonon-phonon correlations](#) *Nat. Phys.* **9** 790–794
- [127] Vrakking M J and Elsaesser T 2012 [X-Ray photonics: X-rays inspire electron movies](#) *Nat. Photonics* **6**(10) 645–647
- [128] Zamponi F, Ansari Z, Wörner M and Elsaesser T 2010 [Femtosecond powder diffraction with a laser-driven hard X-ray source](#) *Opt. Express* **18**(2) 947–961
- [129] Pines D and Nozières P 1966 *The Theory of Quantum Liquids. Vol. 1: Normal Fermi Liquids* (W. A. Benjamin)
- [130] Abbamonte P, Wong G C, Cahill D G, Reed J P, Coridan R H, Schmidt N W, Lai G H, Joe Y I and Casa D 2010 [Ultrafast Imaging and the Phase Problem for Inelastic X-Ray Scattering](#) *Adv. Mater.* **22**(10) 1141–1147
- [131] Abbamonte P, Finkelstein K, Collins M and Gruner S 2004 [Imaging density disturbances in water with a 41.3-attosecond time resolution](#) *Phys. Rev. Lett.* **92**(23) 237401
- [132] Abbamonte P, Graber T, Reed J P, Smadici S, Yeh C L, Shukla A, Rueff J P and Ku W 2008 [Dynamical reconstruction of the exciton in LiF with inelastic x-ray scattering](#) *Proc. Natl. Acad. Sci. USA* **105**(34) 12159–12163
- [133] Abbamonte P, Reed J, Joe Y, Gan Y and Casa D 2009 [Implicit spatial averaging in inversion of inelastic x-ray scattering data](#) *Phys. Rev. B* **80**(5) 054302
- [134] Gan Y, Kogar A and Abbamonte P 2013 [Crystallographic refinement of collective excitations using standing wave inelastic X-ray scattering](#) *Chem. Phys.* **414** 160–167
- [135] Eisenberger P and Platzman P 1970 [Compton scattering of X rays from bound electrons](#) *Phys. Rev. A* **2** 415

- 
- [136] Metz C, Tschentscher T, Suortti P, Kheifets A, Lun D, Sattler T, Schneider J and Bell F 1999 [Three-dimensional electron momentum densities of graphite and fullerene: a comparison](#) *J. Phys.: Condens. Matter* **11**(19) 3933
- [137] Metz C, Tschentscher T, Suortti P, Kheifets A, Lun D, Sattler T, Schneider J and Bell F 1999 [Three-dimensional electron momentum density of aluminum by  \$\(\gamma, e \gamma\)\$  spectroscopy](#) *Phys. Rev. B* **59**(16) 10512
- [138] Sattler T, Tschentscher T, Schneider J, Vos M, Kheifets A, Lun D, Weigold E, Dollinger G, Bross H and Bell F 2001 [Anisotropy of the electron momentum density of graphite studied by  \$\(\gamma, e \gamma\)\$  and  \$\(e, 2 e\)\$  spectroscopy](#) *Phys. Rev. B* **63**(15) 155204
- [139] Shao H C and Starace A F 2013 [Time-resolved ultrafast electron  \$\(e,2e\)\$  momentum spectroscopy](#) *Phys. Rev. A* **87**(5) 050701
- [140] Kaplan I, Barbiellini B and Bansil A 2003 [Compton scattering beyond the impulse approximation](#) *Phys. Rev. B* **68**(23) 235104
- [141] Yudin G, Bondar D, Patchkovskii S, Corkum P and Bandrauk A 2009 [Unified ab initio treatment of attosecond photoionization and Compton scattering](#) *J. Phys. B: At. Mol. Opt. Phys.* **42**(20) 205601
- [142] Podolsky B and Pauling L 1929 [The momentum distribution in hydrogen-like atoms](#) *Phys. Rev.* **34**(1) 109
- [143] Bethe H and Salpeter E 1977 *Quantum Mechanics of One-and Two-Electron Atoms, 1957* (Springer, Berlin)
- [144] Gaffney K J and Chapman H N 2007 [Imaging Atomic Structure and Dynamics with Ultrafast X-ray Scattering](#) *Science* **316**(5830) 1444–1448
- [145] Quiney H 2010 [Coherent diffractive imaging using short wavelength light sources](#) *J. Mod. Opt.* **57**(13) 1109–1149
- [146] Barty A, Küpper J and Chapman H N 2013 [Molecular imaging using x-ray free-electron lasers](#) *Annu. Rev. Phys. Chem.* **64** 415–435
- [147] Protein Data Bank URL <http://www.pdb.org>
- [148] Chapman H N et al. 2011 [Femtosecond X-ray protein nanocrystallography](#) *Nature* **470**(7332) 73–77
- [149] Spence J, Weierstall U and Chapman H 2012 [X-ray lasers for structural and dynamic biology](#) *Rep. Prog. Phys.* **75**(10) 102601

- [150] Patterson B D 2014 [Crystallography using an X-ray free-electron laser](#) *Crystallogr. Rev.* **20**(4) 242–294
- [151] Redecke L, Nass K et al. 2013 [Natively Inhibited Trypanosoma brucei Cathepsin B Structure Determined by Using an X-ray Laser](#) *Science* **339**(6116) 227–230
- [152] Tenboer J et al. 2014 [Time-resolved serial crystallography captures high-resolution intermediates of photoactive yellow protein](#) *Science* **346**(6214) 1242–1246
- [153] Neutze R 2014 [Opportunities and challenges for time-resolved studies of protein structural dynamics at X-ray free-electron lasers](#) *Phil. Trans. R. Soc. B* **369**(1647) 20130318
- [154] Kupitz C et al. 2014 [Serial time-resolved crystallography of photosystem II using a femtosecond X-ray laser](#) *Nature* **513**(7517) 261–265
- [155] Aquila A et al. 2012 [Time-resolved protein nanocrystallography using an X-ray free-electron laser](#) *Opt. Express* **20**(3) 2706–2716
- [156] Seibert M M et al. 2011 [Single mimivirus particles intercepted and imaged with an X-ray laser](#) *Nature* **470**(7332) 78–81
- [157] van der Schot G et al. 2015 [Imaging single cells in a beam of live cyanobacteria with an X-ray laser](#) *Nat. Commun.* **6**
- [158] Neutze R, Wouts R, van der Spoel D, Weckert E and Hajdu J 2000 [Potential for biomolecular imaging with femtosecond X-ray pulses](#) *Nature* **406**(6797) 752–757
- [159] Chapman H N et al. 2006 [Femtosecond diffractive imaging with a soft-X-ray free-electron laser](#) *Nat. Phys.* **2**(12) 839–843
- [160] Hau-Riege S P, London R A and Szoke A 2004 [Dynamics of biological molecules irradiated by short x-ray pulses](#) *Phys. Rev. E* **69**(5) 051906
- [161] Jurek Z, Oszlanyi G and Faigel G 2004 [Imaging atom clusters by hard X-ray free-electron lasers](#) *Europhys. Lett.* **65**(4) 491
- [162] Jurek Z, Faigel G and Tegze M 2004 [Dynamics in a cluster under the influence of intense femtosecond hard X-ray pulses](#) *Eur. J. Phys. D* **29**(2) 217–229
- [163] Carlson T A and Krause M O 1965 [Electron Shake-Off Resulting from K-Shell Ionization in Neon Measured as a Function of Photoelectron Velocity](#) *Phys. Rev.* **140**(4A) A1057

- 
- [164] Omar G and Hahn Y 1992 [Final charge state distribution in the production and decay of hollow Ar](#) *Z. Phys. D – At. Mol. Cl.* **25**(1) 41–46
- [165] Persson P, Lunell S, Szöke A, Ziaja B and Hajdu J 2001 [Shake-up and shake-off excitations with associated electron losses in X-ray studies of proteins](#) *Protein Sci.* **10**(12) 2480–2484
- [166] Gnodtke C, Saalmann U and Rost J M 2009 [Ionization and charge migration through strong internal fields in clusters exposed to intense x-ray pulses](#) *Phys. Rev. A* **79**(4) 041201
- [167] Nakamura T, Fukuda Y and Kishimoto Y 2009 [Ionization dynamics of cluster targets irradiated by x-ray free-electron-laser light](#) *Phys. Rev. A* **80** 053202
- [168] Kai T, Tokuhisa A, Moribayashi K, Fukuda Y, Kono H and Go N 2014 [Intensity of Diffracted X-rays from Biomolecules with Radiation Damage Caused by Strong X-ray Pulses](#) *J. Phys. Soc. Japan* **83**(9)
- [169] Quiney H M and Nugent K A 2011 [Biomolecular imaging and electronic damage using X-ray free-electron lasers](#) *Nat. Phys.* **7**(2) 142–146
- [170] Curwood E, Quiney H and Nugent K 2013 [Determining electronic damage to biomolecular structures in x-ray free-electron-laser imaging experiments](#) *Phys. Rev. A* **87**(5) 053407
- [171] Lorenz U, Kabachnik N, Weckert E and Vartanyants I 2012 [Impact of ultrafast electronic damage in single-particle x-ray imaging experiments](#) *Phys. Rev. E* **86**(5) 051911
- [172] Son S-K, Young L and Santra R 2011 [Impact of hollow-atom formation on coherent x-ray scattering at high intensity](#) *Phys. Rev. A* **83**(3) 033402
- [173] Yefanov O and Vartanyants I 2013 [Orientation determination in single-particle x-ray coherent diffraction imaging experiments](#) *J. Phys. B: At. Mol. Opt. Phys.* **46**(16) 164013
- [174] Vartanyants I A and Yefanov O M 2015 [Coherent X-ray Diffraction Imaging of Nanostructures](#) in O H Seeck and B Murphy (Editors), “X-Ray Diffraction: Modern Experimental Techniques”, (Pan Stanford Publishing)
- [175] Sciaini G and Miller R D 2011 [Femtosecond electron diffraction: Heralding the era of atomically resolved dynamics](#) *Rep. Prog. Phys.* **74**(9) 096101
- [176] Zewail A H 2006 [4D ultrafast electron diffraction, crystallography, and microscopy](#) *Annu. Rev. Phys. Chem.* **57** 65–103

- [177] Huldtt G, Szőke A and Hajdu J 2003 [Diffraction imaging of single particles and biomolecules](#) *J. Struct. Biol.* **144**(1) 219–227
- [178] Bortel G, Faigel G and Tegze M 2009 [Classification and averaging of random orientation single macromolecular diffraction patterns at atomic resolution](#) *J. Struct. Biol.* **166**(2) 226–233
- [179] Fung R, Shneerson V, Saldin D K and Ourmazd A 2009 [Structure from fleeting illumination of faint spinning objects in flight](#) *Nat. Phys.* **5**(1) 64–67
- [180] Giacovazzo C 2013 *Phasing in crystallography: a modern perspective* (Oxford University Press)
- [181] Miao J, Charalambous P, Kirz J and Sayre D 1999 [Extending the methodology of X-ray crystallography to allow imaging of micrometre-sized non-crystalline specimens](#) *Nature* **400**(6742) 342–344
- [182] Miao J, Ishikawa T, Anderson E H and Hodgson K O 2003 [Phase retrieval of diffraction patterns from noncrystalline samples using the oversampling method](#) *Phys. Rev. B* **67**(17) 174104
- [183] Sayre D 2002 [X-ray crystallography: the past and present of the phase problem](#) *Structural Chemistry* **13**(1) 81–96
- [184] Ziaja B, Chapman H, Fäustlin R, Hau-Riege S, Jurek Z, Martin A, Toleikis S, Wang F, Weckert E and Santra R 2012 [Limitations of coherent diffractive imaging of single objects due to their damage by intense x-ray radiation](#) *New J. Phys.* **14**(11) 115015
- [185] Jurek Z, Thiele R, Ziaja B and Santra R 2012 [Effect of two-particle correlations on x-ray coherent diffractive imaging studies performed with continuum models](#) *Phys. Rev. E* **86**(3) 036411
- [186] Mancuso A P, Aquila A, Borchers G, Giewekemeyer K and Reimers N 2013 *Scientific Instrument Single Particles, Clusters, and Biomolecules (SPB) Technical Design Report XFEL.EU TR-2013-004* European XFEL
- [187] Boutet S and Williams G J 2010 [The coherent X-ray imaging \(CXI\) instrument at the Linac Coherent Light Source \(LCLS\)](#) *New J. Phys.* **12**(3) 035024
- [188] Serkez S, Kocharyan V, Saldin E, Zagorodnov I, Geloni G and Yefanov O 2013 [Proposal for a scheme to generate 10 TW-level femtosecond x-ray pulses for imaging single protein molecules at the European XFEL](#) ArXiv preprint arXiv:1306.0804

- 
- [189] Serkez S, Kocharyan V, Saldin E, Zagorodnov I, Geloni G and Yefanov O 2014 [Perspectives of Imaging of Single Protein Molecules with the Present Design of the European XFEL. - Part I - X-ray Source, Beamline Optics and Instrument Simulations](#) ArXiv preprint arXiv:1407.8450
- [190] Hubbell J, Gimm H A et al. 1980 [Pair, Triplet, and Total Atomic Cross Sections \(and Mass Attenuation Coefficients\) for 1 MeV-100 GeV Photons in Elements Z= 1 to 100](#) *J. Phys. Chem. Ref. Data* **9**(4) 1023–1148
- [191] Thompson A, Attwood D, Gullikson E, Howells M, Kortright J, Robinson A et al. 2009 *X-ray data booklet (2009)* (Lawrence Berkeley National Laboratory) URL <http://xdb.lbl.gov>
- [192] Santra R and Young L 2015 [Interaction of Intense X-ray beams with atoms](#) in E Jaeschke, S Khan, J R Schneider and J B Hastings (Editors), “Synchrotron Light Sources and Free-Electron Lasers”, (Springer International Publishing)
- [193] Young L et al. 2010 [Femtosecond electronic response of atoms to ultra-intense X-rays](#) *Nature* **466**(7302) 56–61
- [194] Rudek B et al. 2012 [Ultra-efficient ionization of heavy atoms by intense X-ray free-electron laser pulses](#) *Nat. Photonics* **6**(12) 858–865
- [195] Rohringer N and Santra R 2007 [X-ray nonlinear optical processes using a self-amplified spontaneous emission free-electron laser](#) *Phys. Rev. A* **76** 033416
- [196] Hoener M et al. 2010 [Ultraintense X-ray induced ionization, dissociation, and frustrated absorption in molecular nitrogen](#) *Phys. Rev. Lett.* **104**(25) 253002
- [197] Son S K and Santra R 2012 [Monte Carlo calculation of ion, electron, and photon spectra of xenon atoms in x-ray free-electron laser pulses](#) *Phys. Rev. A* **85**(6) 063415
- [198] Glauber R J 1963 [Coherent and incoherent states of the radiation field](#) *Phys. Rev.* **131**(6) 2766
- [199] Schroeder C 2002 [Photon statistics of the SASE FEL](#) *Nucl. Instr. Meth. Phys. Res. A* **483** 499 – 503
- [200] Gjaja I and Bhattacharjee A 1991 [Effective density matrix for free-electron-laser radiation](#) *Phys. Rev. A* **43** 3206–3209
- [201] Petruccione F and Breuer H P 2002 *The theory of open quantum systems* (Oxford university press)
- [202] Schaller G 2014 *Open Quantum Systems Far from Equilibrium* (Springer)

- [203] Bonitz M 1998 *Quantum kinetic theory* Volume 33 (Teubner)
- [204] Rossi F and Kuhn T 2002 [Theory of ultrafast phenomena in photoexcited semiconductors](#) *Rev. Mod. Phys.* **74**(3) 895
- [205] Axt V and Mukamel S 1998 [Nonlinear optics of semiconductor and molecular nanostructures; a common perspective](#) *Rev. Mod. Phys.* **70**(1) 145
- [206] Kremp D, Bornath T, Bonitz M and Schlanges M 1999 [Quantum kinetic theory of plasmas in strong laser fields](#) *Phys. Rev. E* **60**(4) 4725
- [207] Haug H, Jauho A P and Cardona M 2008 *Quantum kinetics in transport and optics of semiconductors* Volume 2 (Springer)
- [208] Stefanucci G and van Leeuwen R 2013 *Nonequilibrium Many-Body Theory of Quantum Systems: A Modern Introduction* (Cambridge University Press)
- [209] Inhester L 2013 [Auger decay in double core ionized molecules](#). Ph.D. thesis Georg-August-Universität Göttingen
- [210] Quack M 1978 [Theory of unimolecular reactions induced by monochromatic infrared radiation](#) *J. Chem. Phys.* **69**(3) 1282–1307
- [211] Mukamel S 1979 [On the derivation of rate equations for collisionless molecular multiphoton processes](#) *J. Chem. Phys.* **71**(5) 2012–2020
- [212] Mukamel S 1979 [Stochastic reduction for molecular multiphoton processes](#) *J. Chem. Phys.* **70**(12) 5834–5847
- [213] Van Hove L 1954 [Quantum-mechanical perturbations giving rise to a statistical transport equation](#) *Physica* **21**(1-5) 517–540
- [214] Van Hove L 1957 [The approach to equilibrium in quantum statistics: A perturbation treatment to general order](#) *Physica* **23**(1) 441–480
- [215] Kaiser B, Vagov A, Axt V and Pietsch U 2011 [Ultrafast photoionization dynamics at high laser intensities in the xuv regime](#) *Phys. Rev. A* **84**(4) 043431
- [216] Kaiser B, Brand A, Glässl M, Vagov A, Axt V and Pietsch U 2013 [Photoionization of resonantly driven atomic states by an extreme ultraviolet-free-electron laser: intensity dependence and renormalization of Rabi frequencies](#) *New J. Phys.* **15**(9) 093016
- [217] Brand A, Kaiser B, Vagov A, Axt V and Pietsch U 2014 [Non-Markovian behavior of ultrafast coherent ionization dynamics in a crystal exposed to a seeded free-electron-laser pulse](#) *Phys. Rev. A* **89**(6) 063404

- 
- [218] Li Y, Gao C, Dong W, Zeng J and Yuan J 2015 [Quantum coherence in the dynamical excitation, ionization, and decaying of neon gas induced by X-ray laser](#) ArXiv preprint arXiv:1501.02660
- [219] Böke A 2013 [The total incoherent scattering cross sections for low- \$Z\$  elements](#) *Radiat. Phys. Chem.* **83** 34–41
- [220] Kai T 2010 [Single-differential and integral cross sections for electron-impact ionization for the damage of carbon clusters irradiated with x-ray free-electron lasers](#) *Phys. Rev. A* **81**(2) 023201
- [221] Ziaja B, van der Spoel D, Szöke A and Hajdu J 2001 [Auger-electron cascades in diamond and amorphous carbon](#) *Phys. Rev. B* **64**(21) 214104
- [222] Ziaja B, Szöke A, van der Spoel D and Hajdu J 2002 [Space-time evolution of electron cascades in diamond](#) *Phys. Rev. B* **66**(2) 024116
- [223] Ziaja B, London R A and Hajdu J 2005 [Unified model of secondary electron cascades in diamond](#) *J. Appl. Phys.* **97**(6) 064905
- [224] Hau-Riege S P 2013 [Nonequilibrium electron dynamics in materials driven by high-intensity x-ray pulses](#) *Phys. Rev. E* **87**(5) 053102
- [225] Ziaja B, Wang F and Weckert E 2009 [Multi-electron-recombination rates estimated within dense plasmas](#) *High Energ. Dens. Phys.* **5**(3) 221–224
- [226] Ziaja B, Chapman H, Santra R, Laarmann T, Weckert E, Bostedt C and Möller T 2011 [Heterogeneous clusters as a model system for the study of ionization dynamics within tampered samples](#) *Phys. Rev. A* **84**(3) 033201
- [227] Chihara J 1987 [Difference in x-ray scattering between metallic and non-metallic liquids due to conduction electrons](#) *J. Phys. F: Met. Phys.* **17**(2) 295
- [228] Chihara J 2000 [Interaction of photons with plasmas and liquid metals-photoabsorption and scattering](#) *J. Phys.: Condens. Matter* **12**(3) 231
- [229] Waller I and Hartree D R 1929 [On the intensity of total scattering of x-rays](#) *Proc. R. Soc. A* **124**(793) 119–142
- [230] Dixit G and Santra R 2013 Compton scattering cross section within independent-particle model – *Unpublished notes*
- [231] Son S-K and Santra R 2011 XATOM — *an integrated toolkit for x-ray and atomic physics* (CFEL, DESY, Hamburg, Germany)

- [232] Slater J C 1951 [A simplification of the Hartree-Fock method](#) *Phys. Rev.* **81**(3) 385
- [233] Herman F and Skillman S 1963 *Atomic structure calculations* (Prentice-Hall Englewood Cliffs, NJ)
- [234] Latter R 1955 [Atomic energy levels for the Thomas-Fermi and Thomas-Fermi-Dirac potential](#) *Phys. Rev.* **99**(2) 510
- [235] Schnaidt F 1934 [Über das kontinuierliche und diskontinuierliche Compton-spektrum bei Wasserstoff](#) *Ann. Phys. (Berlin)* **413**(1) 89–112
- [236] Bortel G and Faigel G 2007 [Classification of continuous diffraction patterns: A numerical study](#) *J. Struct. Biol.* **158**(1) 10–18
- [237] Bortel G and Tegze M 2011 [Common arc method for diffraction pattern orientation](#) *Acta Crystallogr. A* **67**(6) 533–543
- [238] Tegze M and Bortel G 2012 [Atomic structure of a single large biomolecule from diffraction patterns of random orientations](#) *J. Struct. Biol.* **179**(1) 41–45
- [239] Shneerson V, Ourmazd A and Saldin D 2008 [Crystallography without crystals. I. The common-line method for assembling a three-dimensional diffraction volume from single-particle scattering](#) *Acta Crystallogr. A* **64**(2) 303–315
- [240] Loh N-T D and Elser V 2009 [Reconstruction algorithm for single-particle diffraction imaging experiments](#) *Phys. Rev. E* **80**(2) 026705
- [241] Wilson A 1949 [The probability distribution of X-ray intensities](#) *Acta Crystallogr.* **2**(5) 318–321
- [242] Hau-Riege S P, London R A, Hultdt G and Chapman H N 2005 [Pulse requirements for x-ray diffraction imaging of single biological molecules](#) *Phys. Rev. E* **71**(6) 061919
- [243] Varshalovich D A, Moskalev A and Khersonskii V 1988 *Quantum theory of angular momentum* (World Scientific)
- [244] Son S-K, Chapman H N and Santra R 2011 [Multiwavelength anomalous diffraction at high x-ray intensity](#) *Phys. Rev. Lett.* **107**(21) 218102
- [245] Goodman J W 1985 *Statistical optics* (Wiley-Interscience)